NANOSTRUCTURED TIN OXIDE MATERIALS AS PHOTOANODE FOR DYE SENSITIZED SOLAR CELLS

QAMAR WALI

DOCTOR OF PHILOSOPHY
UNIVERSITI MALAYSIA PAHANG

THESIS CONFIDENTIAL STATUS
UNIVERSITI MALAYSIA PAHANG

DECLARATION OF THESIS AND COPYRIGHT

Author's Full Name: QAMAR WALI

Date of Birth : 5th March 1985

Title : NANOSTRUCTURED TIN OXIDE MATERIALS AS PHOTOANODE FOR DYE SENSITIZED SOLAR CELLS

Academic Session : 2013/2016

I declare that this thesis is classified as:

[ ] **CONFIDENTIAL** (Contains confidential information under the Official Secret Act 1972)

[ ] **RESRICTED** (Contains restricted information as specified by the organization where research was done)

[✓] **OPEN ACCESS** I agree that my thesis to be published as online open access (Full text)

I acknowledge that Universiti Malaysia Pahang reserve the right as follows:

1. The Thesis is the Property of Universiti Malaysia Pahang

2. The Library of Universiti Malaysia Pahang has the right to make copies for the purpose of research only

3. The Library has the right to make copies of the thesis for academic exchange

Certified By:

_____   _____
 Student's Signature   Supervisor's Signature

 AQ6796412   PROF. JOSE RAJAN
Passport Number   Name of Supervisor
Date: 12/7/2016   Date: 12/7/2016

SUPERVISOR'S DECLARATION

We hereby declare that we have checked this thesis and in our opinion, this thesis is adequate in terms of scope and quality for the award of the degree of Doctor of Philosophy in Advanced Materials.

_____
Supervisor's Signature

Full Name   :   JOSE RAJAN
Position   :   PROFESSOR (FACULTY OF INDUSTRIAL SCIENCES & TECHNOLOGY)
Date   :   12 JULY 2016

_____
Co-supervisor's Signature

Full Name   :   MOHD HASBI AB RAHIM
Position   :   DEPUTY DEAN (FACULTY OF INDUSTRIAL SCIENCES & TECHNOLOGY)
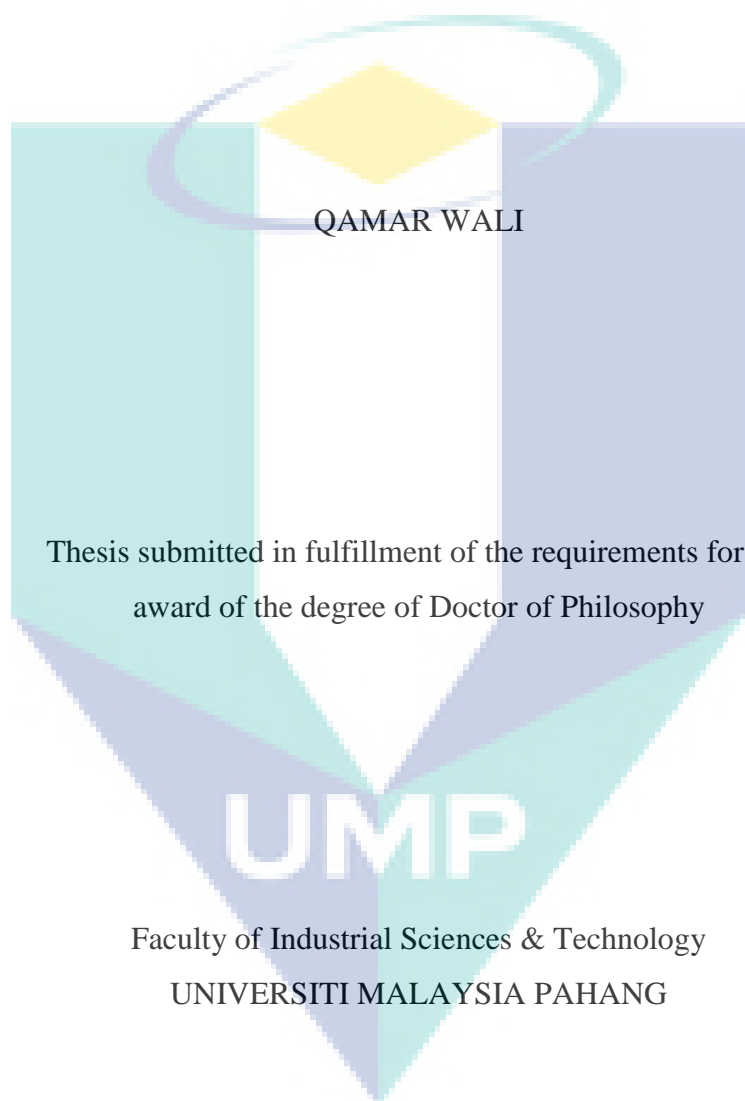Date   :   12 JULY 2016

STUDENT'S DECLARATION

I hereby declare that the work in this thesis is based on my original work except for quotations and citation which have been duly acknowledged. I also declare that it has not been previously or concurrently submitted for any other degree at Universiti Malaysia Pahang or any other institutions.

_____
Author's Signature
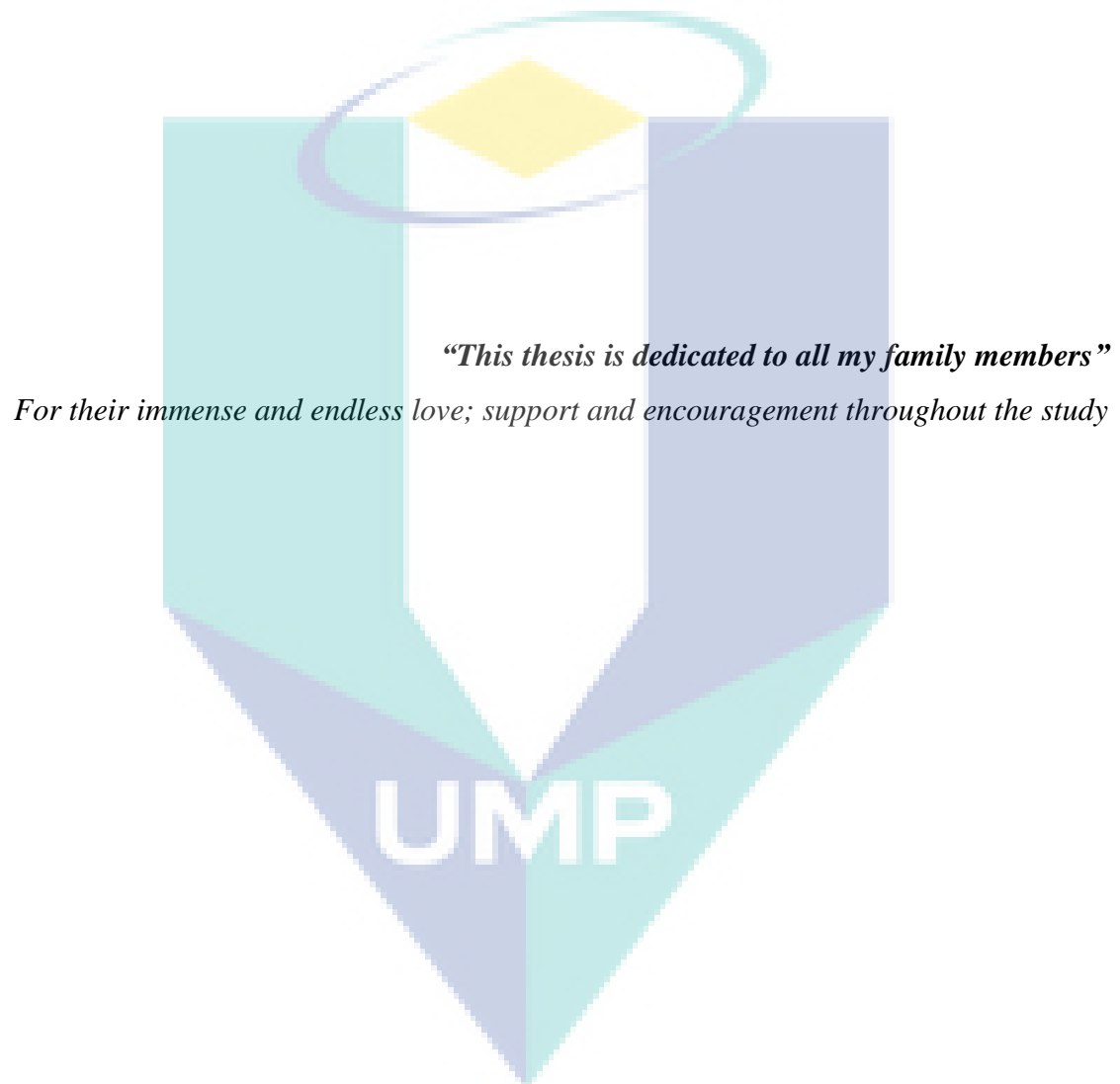
Full Name   :   QAMAR WALI
ID Number   :   PSM13005
Date   :   12 JULY 2016

NANOSTRUCTURED TIN OXIDE MATERIALS AS PHOTOANODE FOR DYE
SENSITIZED SOLAR CELLS

QAMAR WALI

Thesis submitted in fulfillment of the requirements for the
award of the degree of Doctor of Philosophy

Faculty of Industrial Sciences & Technology
UNIVERSITI MALAYSIA PAHANG

JULY 2016

DEDICATION

"This thesis is dedicated to all my family members"

For their immense and endless love; support and encouragement throughout the study

AKNOWLEDGEMENTS

Foremost, I acknowledge the Almighty Allah (SAT) for the strength granted to complete my Ph.D. journey. I would like to express my sincere gratitude to my supervisor Prof. Jose Rajan and co-supervisor Dr. Mohd Hasbi Ab Rahim for their continuous support during my Ph.D. research, for their patience in teaching me, guiding and correcting me and for sharing immense knowledge. My supervisor guidance helped me in all the time of research and writing of this thesis. I could not have imagined having a better advisor and mentor for my Ph.D. study. I could not have reached this stage without his support.

Besides my advisor, I would like to thank the rest of my thesis committee: Prof. Norani Muti Mohamed and Dr. Kafi A. K. M, for their insightful comments and encouragement, but also for the hard question which incented me to widen my research from various perspective

Moreover, I would like to thank to the postgraduate school of my university for awarding me a doctoral scholarship, my faculty members for their support and the technical team of my department for their cooperation in my lab work, my group members especially Azhar Fakhruddin for being so helpful and patient with me.

Last but not the least, I would like to thank my family: my mother and to my brothers who have always been my mentor, siblings for the continuous prayers, sacrifice love and support, and to my dearest wife who has been so patient throughout my study. This would have not been possible without her love and patience through these difficult years.

Qamar Wali, July 2016

iii

ABSTRACT

Photoanode plays vital role in the operation of dye sensitized solar cells (DSSCs) owing to its many fold functions: (i) as a substrate to anchor dye, (ii) enable the bound electron-hole pair formed in the dye to be separated into mobile charge carriers, and (iii) provide a medium to accept and transport the photoinduced electrons. Although TiO_2 nanoparticles (NPs) is the most successful employed photoanode material in DSSCs delivering efficiency (η) ~14.3% due to its high specific surface area (~150 m^2/g), it is characterized by slow electron diffusion and mobility (μ_e). On the other hand, SnO_2 shows an outstanding performance in many electronic devices owing to its higher μ_e. The high μ_e could transport electrons much faster and minimize the charge recombination in the device. From this point of view, SnO_2 is an interesting alternative to that of TiO_2. In this research, NPs and multifunctional NPs-Nanospheres (NPs-NSs) were synthesized hydrothermally by simply varying the hydrothermal annealing temperature from 150 to 200 °C. The multifunctional (NPs-NSs) shows higher crystallinity and superior light scattering in comparison to NPs analogue because of its unique morphology i.e., the size of the spheres in the range of ~800 nm – 1 μm which are comparable to the visible light wavelength. The photovoltaic (PV) parameters include short circuit density (J_{SC}), open circuit voltage (V_{OC}) and η were higher for the multifunctional (NPs-NSs) i.e., 17 mA cm^{-2}, 500 mV and ~4.0% vs. 7, 370 and ~1.3 for NPs analogue, respectively. For the superior charge transport, on the other hand, various one dimensional electrospun nanomaterials were synthesized. A strategy was adopted by just keeping the precursor concentration changing while other constituents of the solution constant. Among them, multiporous nanofibers (MPNFs) resulted in a significantly higher J_{SC} ~18 mA cm^{-2} compared to that of porous NFs (PNFs) ~10 mA cm^{-2} due to 8-10-folds larger surface area of the former, which consequently adsorbed large amount of dye. However, the fill factor (FF) and V_{OC} were limited to (~45-50%) and (~450-500 mV) in pure SnO_2 based DSSCs, respectively. Finally, the lower V_{OC} and FF were enhanced using a composite by incorporating TiO_2 NPs into SnO_2 photoanode via $TiCl_4$ treatment. This technique considerably improved the V_{OC} (from ~500 to 720 mV) and similarly J_{SC} from (~17 to 22 mA cm^{-2}). Though V_{OC} and J_{SC} increased dramatically, the FF was still limited to ~50%. In the second approach, an electrospun composite (SnO_2-TiO_2) NFs was used as photoanode, which yielded V_{OC} (~730 mV) and FF (~60%) simultaneously, closer to that of TiO_2 (V_{OC} ~700-800 mV and FF ~60-68%). Results of this research provide promising directions such as increasing surface area and surface roughness of the composite nanofibers so that efficiency levels for practical applications could be realized.

ABSTRAK

Foto-anod memainkan peranan penting dalam operasi pewarna sensitif sel suria (DSSCs) kerana fungsi kali ganda yang banyak: (i) bertindak sebagai substrat untuk menambat pewarna, (ii) membolehkan pasangan elektron-lubang ditubuhkan daripada pewarna untuk dipisahkan kepada pembawa cas yang boleh bergerak, dan (iii) menyediakan satu medium menerima dan mengangkut elecktron foto-induksi. Walaupun nanopartikel TiO_2 (NPs) adalah bahan foto-anod yang paling berjaya dalam DSSCs yang menyampaikan kecekapan (η) ~14.3% disebabkan oleh kawasan permukaan tertentu yang tinggi (~150 m^2/g), namun ia juga dicategori sebagai penyebaran elektron dan pergerakan yang perlahan (μ_e). Sebaliknya, SnO_2 menunjukkan prestasi cemerlang dalam pelbagai peranti elektronik kerana μ_e yang lebih tinggi. μ_e yang tinggi dapat mengangkut elektron yang lebih cepat and mengurangkan penggabungan semula pertuduhan ke dalam peranti. Dari sudut pandangan ini, SnO_2 adalah satu alternatif yang menarik kepada TiO_2. Dalam kajian ini, NPs dan pelbagai fungsi NPs-sfera nano (NPs-NSs) telah disintesis hidroterma dengan hanya mengubah suhu hidroterma dari 150 to 200 ^{o}C. Pelbagai fungsi (NPs-NSs) menunjukkan penghabluran yang lebih tinggi dan penyerakan cahaya unggul berbanding dengan NPs kerana morfologi yang unik iaitu saiz sfera dalam lingkungan ~800 nm – 1 μm yang boleh dibandingkan dengan panjangan gelombang cahaya yang boleh dilihat. Fotovoltaik (PV) parameter termasuk kepadatan litar pintas (Jsc), voltan litar terbuka(Voc) dan η lebih tinggi untuk pelbagai fungsi (NPs-NSs) iaitu 500 mV dan ~4.0% vs. 7, 370 and ~1.3 kepada NPs. Untuk pengangkutan cai yang lebih tinggi, pelbagai bahan satu nano dimensi elektro-putar telah disintesis. Satu strategi telah diterima pakai hanya berubah kepekatan pelopor manakala juzuk yang lain tidak berubah. Antaranya ,serat-nano yang berliang (MPNFs) meyebabkan J_{SC} ~18 mA cm^{-2} yang lebih tinggi berbanding dengan berliang NFs (PNFs) ~10 mA cm^{-2} kerana 8-10 lipatan kawasan permukaaan yang lebih daripada yang pertama dan dapat menyerap jumlah pewarna yang banyak. Walau bagaimanapun, factor mengisi (FF) dan Voc ada terhad kepada (~45-50%) dan (~450-500 mV) dalam SnO_2 yang tulen berdasarkan DSSCs. Akhirnya, Voc and FF yang lebih rendah telah dipertingkatkan menggunakan komposit yang menggabungkan TiO_2 NPs ke SnO_2 foto-anod melalui rawatan $TiCl_4$. Teknik ini jauh lebih baik Voc from ~500 to 720 mV) dan begitu juga Jsc dari (~17 to 22 mA cm^{-2}). Walaupun Voc dan Jsc meningkat secara mendadak, FF masih terhad kepada ~ 50%. Dalam pendekatan kedua, komposit elektro-putar (SnO_2-TiO_2) NFs telah digunakan sebagai foto-anod, yang mengeluarkan Voc (~730 mV) dan FF (~ 60%) pada masa yang sama, lebih dekat dengan TiO_2 (V_{OC} ~700-800 mV and FF ~60-68%). Hasil kajian ini memberikan arah menjanjikan seperti kawasan permukaan meningkat dan kekasaran permukaan serat-nano komposit supaya tahap kecekapan untuk aplikasi praktikal boleh direalisasikan.

.

TABLE OF CONTENTS

CHAPTER 3   MATERIALS AND METHODS

CHAPTER 4   RESULT & DISCUSSIOIN: MULTIFUNCTIONAL TIN OXIDE NANOSTRUCTURES

CHAPTER 5   RESULT & DISCUSSION: MULTIPOROUS TIN OXIDE NANOFIBERS

CHAPTER 6   RESULTS & DISCUSSION: COMPOSITE TIN OXIDE NANOSTRUCTURES

CHAPTER 7   CONCLUSIONS AND RECOMMENDATIONS

LIST OF TABLES

xi

LIST OF FIGURES

LIST OF SYMBOLS

R_T	Charge transport resistance
R_{CT}	Recombination resistance
R_S	Series resistance
R_{SH}	Shunt resistance
ε	Molar extinction coefficient
τ_n	Electron lifetime
τ_d	Electron transit time
C_μ	Chemical capacitance
A	Absorption
η_{inj}	Electron injection efficiency
η_{cc}	Electron collection efficiency
η	Photoconversion efficiency
P_{max}	Maximum power
P_{th}	Theoretical power
I_{max}	Maximum current
V_{max}	Maximum voltage
μ	Micro
μ_e	Electron mobility
L_n	Diffusion length
L	Photoelectrode thickness
d	Lattice spacing
E_g	Band gap
f	Frequency
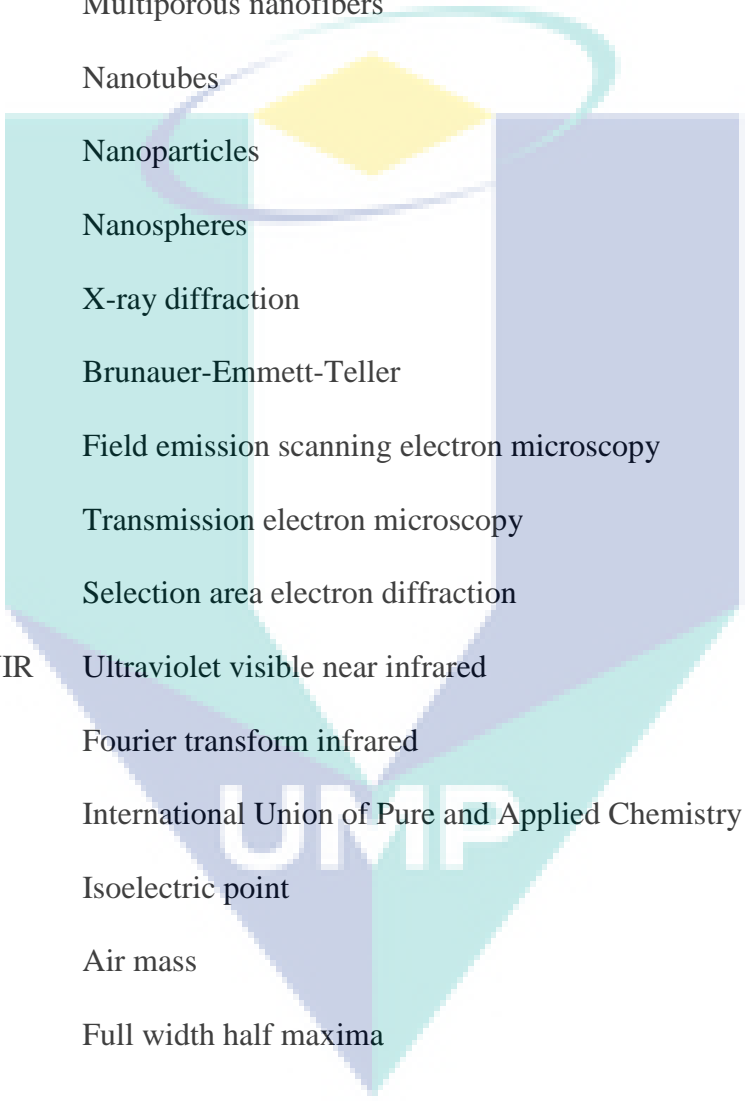
λ	Wavelength
c	speed light in vacuum
W	Watt
mV	Millivolt
ms	Millisecond
k	Kilo
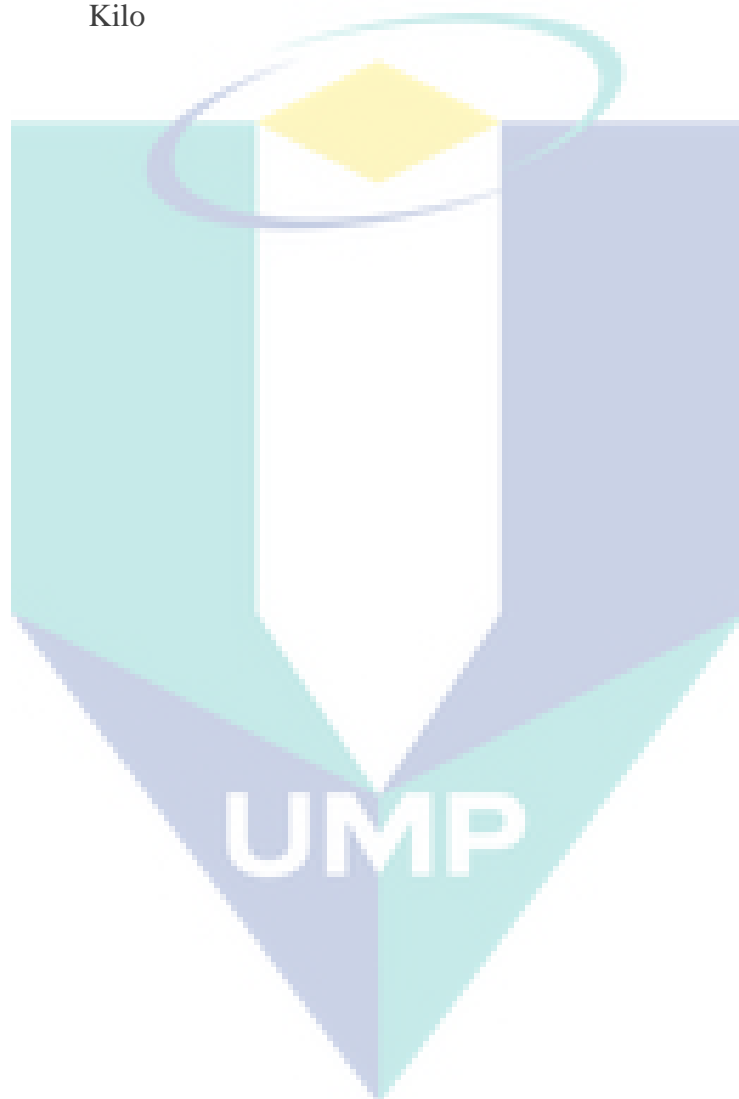
LIST OF ABBREVIATIONS

DSSCs	Dye-sensitized solar cells
MOS	Metal oxide semi-conductor
CE	Counter electrode
WE	Working electrode
FTO	Fluorine doped tin oxide
CB	Conduction band
VB	Valence band
NHE	Normal hydrogen electrode
GNP	Graphene nanoplatelets
I-V	Current-Voltage
J_{SC}	Short circuit current density
V_{OC}	Open circuit voltage
FF	Fill factor
EIS	Electrochemical impedance spectroscopy
LSV	Linear sweep voltammetry
EQE	External quantum efficiency
IPCE	Incident photon to current efficiency
APCE	Absorbed photon to current efficiency
LHE	Light harvesting efficiency
OCVD	Open circuit voltage decay
PV	Photovoltaic
LUMO	Lowest unoccupied molecular orbitals
HOMO	Highest occupied molecular orbitals

1D	One dimensional
NWs	Nanowires
NRs	Nanorods
NFs	Nanofibers
PNFs	Porous nanofibers
MPNFs	Multiporous nanofibers
NTs	Nanotubes
NPs	Nanoparticles
NSs	Nanospheres
XRD	X-ray diffraction
BET	Brunauer-Emmett-Teller
FESEM	Field emission scanning electron microscopy
TEM	Transmission electron microscopy
SAED	Selection area electron diffraction
UV-VIS-NIR	Ultraviolet visible near infrared
FTIR	Fourier transform infrared
IUPAC	International Union of Pure and Applied Chemistry
IEP	Isoelectric point
AM	Air mass
FWHM	Full width half maxima

CHAPTER 1

INTRODUCTION

1.1   BACKGROUND

Dye sensitized solar cells (DSSCs) are classified as third generation organic solar cells because they offer additional functionalities such as flexibility and transparency, which are not offered by the first two generation devices built using single crystalline silicon (first generation) or thin films (second generation). The DSSCs mimic photosynthesis process in which the light absorbed by a green pigment, called chlorophyll, and subsequent photo-induced electron transfer generate fuel (starch). In the DSSCs, dye molecule absorbs light and subsequent charge generation produces PV effect. The DSSCs are called bi-functional solar cells because of its transparency and flexibility-so that they can be used as windows of buildings and automobiles, and generation of photo-current simultaneously (Fakharuddin et al., 2014).

Moreover, DSSCs could be fabricated at low cost, in different colors, on a transparent glass and on flexible substrates which have a huge potential in the commercial market, especially for "low-density" applications such as rooftop solar collector and other small electronic gadgets. Another important feature is its operational hours at both ambient light and full sun condition without much impact on efficiency and also its ability to work at wider angles; while the other traditional solar cells would fail at illumination below a certain range. Thus, DSSCs have a very low cutoff which make them more attractive field in the solar cell technology. The DSSCs could operate between 10 to 14 h

in a day whereas the traditional silicon solar cells merely operate for 6 to 8 hours (Fakharuddin et al., 2014).

Figure 1.1 shows typical functional diagram of a DSSC. The DSSC mainly comprises of a photoanode or working electrode (WE), which is made of metal oxide semiconductor (MOS) deposited on a transparent conducting oxide (TCO) glass substrate (typically fluorine-doped tin oxide, FTO), a thin layer of dye molecules anchored on the MOS film, an electrolyte solution consists of iodide-triiodide (I^-/I_3^-) species, and the cathode substrate made of platinum coated FTO. When light shine on the DSSC, electrons excite from the highest occupied molecular orbital (HOMO) to the lowest unoccupied molecular orbital (LUMO) of the anchored dye molecule. These excited electrons then inject into to the MOS, give rise to the charge separation, resulting electrons diffuse in the conduction band (CB) of the MOS and empty state (holes) in the dye molecule's HOMO diffuse to the electrolyte. The free electrons permeate through the porous MOS and move to the external circuit through the FTO. After passing through the external circuit (load), the electrons return to the system to regenerate the electrolyte component that was used to reduce the oxidized dye molecule (Grätzel, 2003)
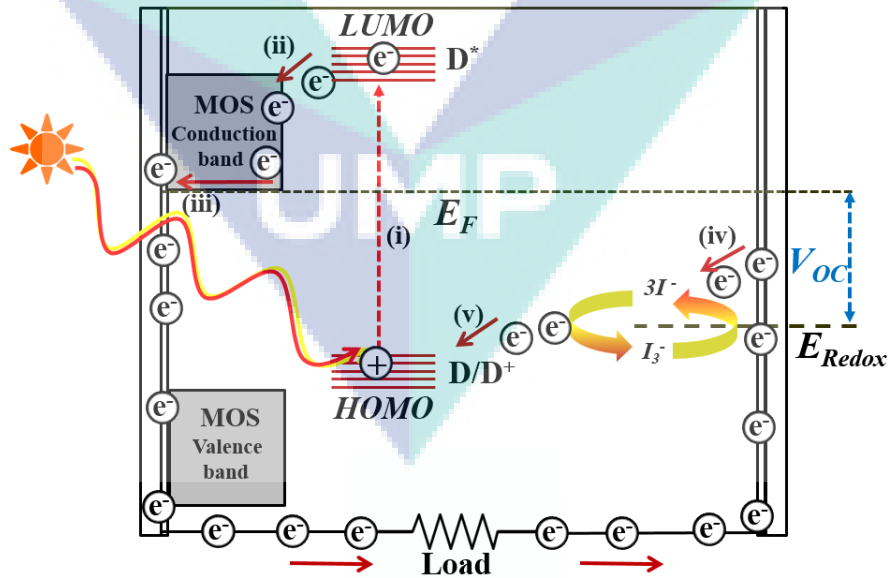
Figure 1.1: Working principle of a DSSC. The V_{OC} is the voltage developed between electrochemical potential (E_{Redox}) of an electrolyte and the fermi energy (E_F) of the MOS. The Process (i), (ii), (iii), (iv), and (v) are explained in chapter 2.

Photoanode or WE play vital role in DSSCs because it not only support the dye molecules, but also accept and transport photoinduced-electrons. The photoanode must possess the following features; (i) high specific surface area for anchoring large amount of dye molecule, (ii) a suitable morphology to support electrons diffusion and additionally scatter light and (iii) a favorable CB alignment (The conduction band of the MOS must be lower than the dye LUMO in order to favor easy electrons injections) with respect to the LUMO of the dye molecule (Jose et al., 2009). In DSSC, TiO_2 mesoporous nanoparticles (NPs) are the most successful employed photoanode resulted in power conversion efficiency (η) of over ~7.1% (O'Regan, 1991) with the combination of (I^-/I_3^-) electrolyte and a ruthenium based dye while the η increased to ~14.3% when a newly introduced cobalt (III/II) electrolyte was used along collaboratively alkoxysilyl-anchor dye of ADEKA-1 and a carboxy-anchor organic LEG4 dye (Kakiage et al., 2015).

Nearly two and half decades of intensive research has been done so far on DSSCs (Hagfeldt et al., 2010), which either introduced new morphologies for the photoanode such as nanotubes (NTs), nanowires (NWs), nanorods (NRs), nanoflowers, nanofibers (NFs), nanobeads, nanochains, nanoribben, and so forth (Zhang and Cao, 2011) or developed different types of sensitizers (Calogero et al., 2015) and electrolytes (Snaith and Schmidt-Mende, 2007). However, these architectures showed poor performance in DSSC owing to the lack of stated key requirements of the photoanode where none of them could offer the required features in a single photoanode. Mesoporous particles in the range of 2-50 nm are extremely important because they have a high specific surface area which anchor large amount of dyes leads to high photon absorption and consequently produce high photocurrent. However, the morphology of these particles severely affects the electron transport; and therefore, a certain number of electron losses during diffusion (Zhang and Cao, 2011). On the other hand, one dimensional nanostructures such as NTs, NRs, NFs and NWs offer superior charge transport and light scattering properties, but anchored less amount of dye owing to their low surface area (Kumar et al., 2012).

Although, various other MOS architectures have been successfully used as a photoanode in DSSCs include Nb_2O_5 (Le Viet et al., 2010), ZnO (Anta et al., 2012), SnO_2 (Kumar et al., 2012) and WO_3 (Zheng et al., 2010) which show competent alternative to TiO_2. For instance, ZnO with similar energy band gap as TiO_2 (E_g ~3.2 eV) and high

isoelectric point (IEP) (at pH ~9) than the later (at pH ~6-7) (Parks, 1965) however, lack of stability restricts its application in DSSCs (Jose et al., 2009). On the contrary, SnO_2 is characterized by high electron mobility (μ_e) of (~250 cm^2 V^{-1} s^{-1} for single crystals and ~150 cm^2 V^{-1} s^{-1} for nanocrystals) compared to that of TiO_2 (μ_e <1 cm^2 V^{-1} s^{-1} in single crystals and ~10^{-5} cm^2 V^{-1} s^{-1} in nanocrystals) with larger E_g ~3.6 eV (Hendry et al., 2004, Zukalová et al., 2005, Tiwana et al., 2011, Hendry et al., 2006, Bedja et al., 1994). The high μ_e could result in a large number of electrons, while the large E_g can support to partly transmit ultraviolet (UV) light and would show stability under UV light (Fungo et al., 2000). Various morphologies of SnO_2 have been used so far as photoanode in DSSCs such as NTs, NPs, nanofloweres and nanospheres (NSs); however, they gave poor performance due to few inherent drawbacks. The most significant one is the low IEP, at pH ~4-5 (Liu et al., 2012, Kay and Grätzel, 2002, Parks, 1965) which leads to absorbing less amount of dye molecules and ultimately result in low photocurrent. Another connected issue is the low conduction band edge of about 300-500 eV below than that of TiO_2 (L A Harris and Wilson, 1978, Scaife, 1980, Bedja et al., 1994), which severely affects the performance of the device, especially open circuit voltage (V_{OC}) and fill factor (FF).

1.2   PROBLEM STATEMENT

Photoanode or WE is at the heart of DSSC. A desirable WE should have (i) high specific surface area to anchor large amount of dye, (ii) a suitable morphology for electron diffusion, electrolyte percolation and superior light harvesting, (iii) a favorable CB alignment with the LUMO of the dye molecule and (iv) high electron conductivity and μ_e to improve charge collection in the device (Zhang and Cao, 2011).

Till date, various MOS have been employed as a WE; however, none of them combine all these required features in a single material. TiO_2, the most successful photoanode material, is characterized by high specific surface area (~150 m^2/g) and suitable CB alignment with the most commercial ruthenium based dyes, however, it is characterized by low μ_e (<1 cm^2 V^{-1} s^{-1}), which results in inferior charge collection. On the other hand, Although SnO_2 offers high μ_e (~250 cm^2 V^{-1} s^{-1}) (Elumalai et al., 2012), its photovoltaic (PV) performance is limited due to a mismatch in band alignment with respect to the most successful dyes and low specific surface area because of its low IEP (at pH ~6-7) (Liu et al., 2012, Parks, 1965). Therefore, innovative approaches are required to improve the performance of the WE by judiciously combining the favorable properties of the above two materials.

1.3   RESEARCH OBJECTIVES

Broad objective of this research is to develop SnO_2 nano morphologies with large surface area, superior light scattering properties and crystallinity; high electron mobility and its composite with other photoanode materials, typically TiO_2, in order to develop highly efficient dye-sensitized solar cells. The specific objectives of this study are as follows in order to achieve the main scientific objective:

1. To develop SnO_2 nanostructure morphologies with large specific surface area (>50 m^2/g), high electron mobility (>1 cm^2 V^{-1} s^{-1}) and desirable light scattering properties.
2. To fabricate SnO_2 based dye-sensitized solar cells using the SnO_2 morphologies and compare their charge transport properties.
3. To tailor the PV parameters of SnO_2 nanostructures by combining the properties of other photoanode materials, typically TiO_2.

1.4 RESEARCH SCOPE

Research activities involved to achieve each objective will be thoroughly elaborated in Chapter 4, 5 and 6. The itemized research activities of each objective are explained as follow:

Scope of objective 1:

a. To synthesize a WE matrix composing of SnO_2 particles of varying sizes by hydrothermal processes such that high surface area and highly scattering particles are in a single ensemble.

b. To synthesize one-dimensional SnO_2 porous NFs (PNFs) by electrospinning technique by controlling solution chemistry so that the charge transport and light harvesting could be simultaneously addressed.

c. To synthesize one-dimensional SnO_2 novel multi-PNFs (MPNFs) by electrospinning in order to have a high surface area for dye adsorption and having superior charge transport characteristics by varying the concentration of the tin precursor in the polymeric solution.

Scope of objective 2:

a. To construct DSSCs using pure SnO_2 NPs as photoanode material and study their PV parameters, particularly, the effect of dye loading and light scattering.

b. To further increase the performance of DSSC in pure SnO_2 NPs, multifunctional (NPs-NSs) employs as a photoanode and study their light scattering and harvesting effect.

c. To fabricate DSSC using one-dimensional pure SnO_2 PNFs and study their PV parameters, mainly, their charge transport and charge collection.

d. To improve the η in one dimensional SnO_2 NFs, a desired MPNFs employ as a photoanode in DSSC, which have a high surface area and also preserving their one-dimensional nature.

Scope of objective 3:

a. To improve the PV parameters in pure multifunctional SnO_2 NSs, TiO_2 NPs-SnO_2 NSs composite develop via a simple solution post-treatment of the prepared electrodes so that to improve the photoanode properties such as physical interconnectivity, electrical conductivity and also to overcome the low conduction band of SnO_2.

b. To further improve the PV parameters of pure SnO_2 MPNFs based DSSCs by employing MPNFs-TiO_2 NPs composite as a photoanode to combine their unique properties in a single WE.

c. To synthesize a composite of SnO_2-TiO_2 NFs via electrospinning to combine the synergistic properties of the both MOS and employ them as photoanode in DSSC.

1.5   STATEMENT OF CONTRIBUTION

At the first stage, SnO_2 multifunctional NPs-NSs were synthesized by optimizing the temperature during hydrothermal reaction. For better charge transport properties, one-dimensional (PNFs and MPNFs) were synthesized using electrospinning process which achieves the first objective. DSSCs were fabricated using the synthesized nanostructures in pure form where the multifunctional NPs-NSs exhibits superior PV parameters particularly J_{SC} (~16 mA.cm^{-2}) with η (~4%) owing to its superior light scattering properties. On the other hand, MPNFs showed significantly higher η (~4.3%) with J_{SC} (~18 mA.cm^{-2}) due to the higher specific surface area and desirable morphology which achieved second objective of this study.

The study also explores the compositing of (i) multifunctional NPs-NSs and MPNFs with TiO_2 NPs and (ii) (SnO_2-TiO_2) NFs composite to overcome the inferior V_{OC} and FF in SnO_2 based DSSCs. These composites are developed to combine the synergistic properties of high μ_e of SnO_2 and favorable CB of TiO_2. Finally, DSSCs parameters were optimized which yielded η ~8% in (SnO_2-TiO_2) NFs and (SnO_2 MPNFs-TiO_2 NPs) composite structure, one of the highest value so far, which achieved the third objective of this study. The active area of the devices were in the range of $12-16$ cm^2.

1.6 THESIS OUTLINE

This thesis is organized as follows: Chapter 1 outlines the research background, problem statement, objectives, scope and research focus. Comprehensive review of the DSSCs and SnO_2 nanostructures are discussed in Chapter 2. Details of methods such as electrospinning and hydrothermal are explained in Chapter 3 and also the characterization techniques for the synthesized products such as X-rays diffraction (XRD); gas adsorption studies, Brunauer-Emmett-Teller (BET), filed emission scanning electron microscopy (FESEM), transmission electron microscopy (TEM), ultraviolet-visible-near-infra-red (UV-VIS-NIR) analysis, current voltage (IV) characteristics curves, incident photon to current efficiency (IPCE) and electrochemical impedance spectroscopy (EIS) analysis. Chapter 4 and 5 highlight the hydrothermally synthesized multifunctional NPs-NSs and electrospun MPNFs and their characterizations and PV parameters, respectively. In chapter 6, a discussion on compositing (NPs-NSs) multifunctional -TiO_2 NPs, (MPNFs-TiO_2 NPs) and composite of (SnO_2-TiO_2) NFs characterizations and their PV parameters. Lastly, Chapter 7 concludes the thesis and provide recommendations for future prospective.

CHAPTER 2

LITERATURE REVIEW

2.1   INTRODUCTION

This chapter presents a brief history of PVs, particularly DSSCs, an overview of the working principle of DSSCs, its various material components, and the progress made in SnO_2 photoanode based DSSCs. The section on SnO_2 based DSSCs elaborates its fundamental properties such as crystal structure, effective mass, μ_e, IEP, and its advantages and disadvantages over other MOS.

2.2   BRIEF HISTORY OF PHOTOVOLTAICS

Edmond Becquerel, a French physicist, was the first to demonstrate the PV effect in 1839 by shinning Pt electrodes coated with AgBr/AgCl inserted in an acidic solution (Becquerel, 1839). The first silicon p-n junction solar cell was developed in 1941 by Russel Ohl of Bell laboratories demonstrating a low η ~1% (Ohl RS., 1941). The η was subsequently improved to ~4.5% and ~6% (Chapin et al., 1954 and Green, M. A. 2009) by the same laboratory in 1953 and 1954, respectively. These devices, termed as 'first generation solar cells', are currently dominating the PV market (>80%) and provides the second highest efficiency solar cells employing its single crystals (η ~27.6% with solar light concentrator and η ~25.0% without it) while η ~20.8% of multicrystalline silicon

solar cells (NREL, 2015). However, silicon based solar cell requires an active layer thickness of ~300 μm to maximize the absorption in the visible region. A complete collection of photogenerated electrons from such thick layer puts stringent conditions on the purity of the materials and thereby increases the manufacturing cost. This brings into account 'second generation solar cells', also called 'thin film solar cells' because that the active material thickness is few microns only. The examples of these types of solar cells are cadmium telluride (CdTe, η ~21.5%) and copper indium gallium diselenide (CIGS, η ~21.7%), currently providing the highest η in single junction solar cells (NREL, 2015). However, the device manufacturing still requires specialized environments those increase its cost/kWh (Fakharuddin et al., 2014).

Primary absorbers in the first and second generation solar cells are crystalline materials with high absorption coefficients, which require high intense solar radiation for its operation. In 'third generation solar cells', molecular absorbers with lower absorption coefficients are employed, the history of which dates back to 19th century (Moser, 1887); i.e., even before the origin of the first two generation solar cells. Systematic efforts to understand the mechanism of the dye sensitization started after a century using RuL_2 $(NCS)_2$ (where L = 2.2-bipyridyl-4,4-dicarboxylic acid dye) (N3) and wide band gap semiconductors such as ZnO and SnO_2 (Vogel et al., 1994, Grätzel, 2009, Memming and Schröppel, 1979). Commercial interest in DSSCs was triggered by the discovery that when N3 dye molecules are anchored to mesoporous TiO_2 nanoparticles and brought in contact with an (I^-/I_3^-) electrolyte gave significantly higher η ~7.1%. This breakthrough, which combined molecular absorbers and nanomaterials, has been a landmark in the history of PVs. One another sharp contrast of the third generation solar cells are that they could be completely solution processable, whereas the first two generations require sophisticated instrumentation for single crystal and thin film growth. Many variations of the solution processable third generation solar cells other than the dye-sensitized (η ~14.3%; (Kakiage et al., 2015)) are perovskite solar cells (η ~20.2%), quantum dot solar cells (η ~9.9%) and organic solar cells (η ~10.6-11.5%) (NREL, 2015).

2.3   WORKING PRINCIPLE AND MATERIAL COMPONENTS OF DSSCS

DSSCs typically consist of a mesoporous MOS film (thickness ~10-20 μm) coated on a conducting glass substrate, which in most cases is FTO coated glass plate. This film form the WE of the DSSCs. The film is then anchored with a molecular absorber (also called sensitizers such as dye) to improve the light absorption characteristics of the MOS film. An electrode, typically Pt coated FTO, is used as counter electrode (CE). The two electrodes are sandwiched together using a 50-60 μm thick spacer. An electrolyte containing a redox couple (for example, I^-/I_3^-) is filled within the gap between two electrodes that act as a hole conducting media (Grätzel, 2009, Wang et al., 2006).

Figure 1.1 (Chapter 1) shows the working principle of DSSC which can be divided into five major processes, (i) light absorption by the dye molecule and generate an exciton (D*), also termed electron-hole (e-h) pair, where electrons excite from the occupied molecular orbital to the unoccupied molecular orbital of dye and leaving behind a hole at the oxidized state (D$^+$). In the second process (ii) the excited electrons are injected into the MOS due to the energy difference between the LUMO of the dye and conduction band (CB) of the MOS and also the latter has a larger density of electron energy states than the former, (iii) diffusion of the photo-induced electrons through the WE material towards the FTO for collection (which depends on the electron diffusion coefficient, the nature of the WE materials and electron-phonon interaction) reaching to the CE (Jose et al., 2009), (iv) The injection of electrons into the electrolyte from the CE and finally, (v) the oxidized dye (D$^+$) is reduced by the electrolyte by accepting one electron from the iodide (I^-) and forms a complex (D… I), here D stands for dye. This complex (D… I) reacts with another iodide and brings the dye to the ground state and form diiodide radical (I_2^-) (Grätzel, 2003, Daeneke et al., 2011, Boschloo and Hagfeldt, 2009). The oxidation of the dye by photon and then its reduction by a redox couple can be described via the following **Eq. (2.1-2.5)** (Pelet et al., 2000, Clifford et al., 2007 and Montanari et al., 2002)

$$D + h\upsilon \longrightarrow D^* \tag{2.1}$$

$$D^* \longrightarrow D^+ + e^-(MOS) \tag{2.2}$$

$$D^+ + I^- \longrightarrow (D{\ldots}I) \tag{2.3}$$

$$(D{\ldots}I) + I^- \longrightarrow D + I_2^- \tag{2.4}$$

$$2I_2^- \longrightarrow I_3^- + I^- \tag{2.5}$$
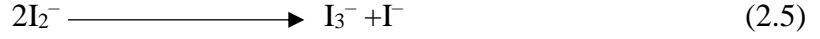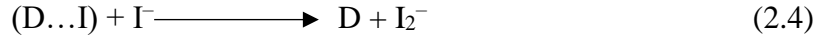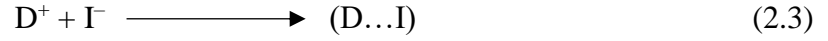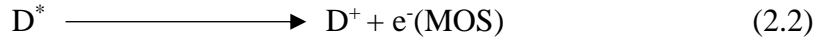
The η of solar cells (DSSC in our case) under 1 sun illumination condition is calculated by the relation $\eta = J_{SC} \times V_{OC} \times FF$, where J_{SC} is the short circuit current density, V_{OC} is the open circuit voltage, and FF is the Fill Factor (Qi and Wang, 2013). The highest η (~14.3%) in DSSCs achieved so far is by employing TiO_2 NPs as MOS owing to their high surface area (~150 m^2/g) along with collaboratively alkoxysilyl-anchor dye of ADEKA-1 and a carboxy-anchor organic LEG4 dye with cobalt based redox system (Kakiage et al., 2015). Various other morphologies such as one-dimensional (NWs, NFs, and NTs etc.), three-dimensional and their composites have been employed as MOS; however, they resulted in inferior PV performance compared to TiO_2 NPs. A detailed comparison of these various MOS materials and their morphologies is given in section 2.4.

2.3.1 Photoanodes (Working Electrode)

Function of the photoanode (or WE) in DSSCs is three-fold: (i) act as a substrate to anchor dyes, (ii) enable the bound electron-hole pair formed in the dye to be separated into mobile charge carriers; and (iii) a medium to transport the photogenerated electrons to the FTO. The role of the WE could be defined by considering the one-dimensional current density for any kind of solar cells (in our case DSSCs), or in general any electronic device, which is given by **Eq. (2.6)**

$$J_{SC} = n(x)\mu_e \nabla F_n(x) \tag{2.6}$$

where $n(x)$ is the concentration of electron in the CB , μ_e is the electron mobility, and $\nabla F_n(x)$ is the gradient in the Fermi levels of the materials across which the electrons flow

(Gregg, 2003). **Eq. (2.6)** defines the key characteristics for a photoanode material: (i) high surface area of the MOS to anchor large amount of dye molecule ($n(x)$), and (ii) superior μ_e to reduce the recombination of photogenerated electrons with the hole spices in the electrolyte.

Many MOS such as TiO_2, SnO_2 and ZnO are employed photoanode in DSSCs (Zhang and Cao, 2011). The crystal structure details of the above MOS and their physical properties are compared in **Table 2.1** and **Table 2.2**, respectively. Among them SnO_2 has high optical transparency and low electrical resistance; therefore, it is an attractive MOS for DSSCs and other optoelectronic devices (Hagfeldt et al., 2010, Das and Jayaraman, 2014) **(Table 2.1)**. Due to its large E_g (~3.6 eV) than that of TiO_2 (~3.2 eV), SnO_2 shows superior stability against UV-light-induced degradation (Tiwana et al., 2011, Boschloo and Hagfeldt, 2009). Second, it is a material of higher μ_e, which for single crystals is ~250 $cm^2\,V^{-1}\,s^{-1}$ and for nanostructures is ~150 $cm^2\,V^{-1}\,s^{-1}$. These values are much higher than that of the single crystal TiO_2 ($\mu_e < 1\ cm^2\,V^{-1}\,s^{-1}$). The high μ_e of SnO_2 than TiO_2 is due to the small effective mass ($0.17m_e$ for SnO_2 and $10m_e$ for TiO_2) (Tiwana et al., 2011, (Kumara et al., 2010).

Table 2.1
Various polymorphs of the three most employed MOS (TiO_2, SnO_2, and ZnO) in DSSCs

MOS	Polymorph	Crystal structure	Lattice parameters
TiO_2(Zhu and Gao, 2014)	Rutile	Tetragonal	a = 4.6 Å, c = 3.0 Å, Z = 2
	Anatase	Tetragonal	a = 3.8 Å, c = 9.5 Å; Z = 4
	Brookite	Orthorhombic	a = 5.5 Å, b = 9.2 Å, c = 5.2 Å, Z = 8
SnO_2 (Das and Jayaraman, 2014)	Rutile	Tetragonal	a = 4.7 Å, c = 3.2 Å
	$CaCl_2$-type	Orthorhombic	a = 4.7 Å, b = 4.7 Å, c = 3.2 Å
	α-PbO_2-type	Orthorhombic	a = 4.7 Å, b = 5.7 Å, c = 5.3 Å
ZnO (Morkoç and Özgür, 2009)	Wurtzite	Hexagonal	a = 2.5 Å c = 6.7 Å
	Zinc blende	Cubic	a = 3.6 (10) Å

Table 2.2
Electrochemical properties of the three selected MOS (TiO₂, ZnO, and SnO₂)

Property	TiO₂	ZnO	SnO₂
Band gap	3.2 eV	3.35 eV	3.6 eV
CB energy min vs. vacuum	-4.1 eV(Polizzotti et al., 2012)	-4.0 eV	-5 eV
VB energy min vs. vacuum	-7.3 eV	-7.35 eV	-8.6 eV
CB orbitals	Ti (3d) (Jose et al., 2009)	Zn (3d) & O (2p) (Jose et al., 2009)	Sn (5s&5p) (Godinho et al., 2008)
Valence band orbitals	O (2p) & Ti (3d)	Zn (3d) (Jose et al., 2009)	O (2p) (Godinho et al., 2008)
Electron mobility	~0.1-1 cm² $V^{-1} s^{-1}$	~200 cm² $V^{-1} s^{-1}$	~100-250 cm² $V^{-1} s^{-1}$
CB effective Mass (light holes)	5-0 m_e (Tiwana et al., 2011)	0.3 m_e (Tiwana et al., 2011)	0.27 m_e (0.3 m_e) (Tiwana et al., 2011)
Charge mobility (bulk)	~1 cm² $V^{-1} s^{-1}$	~ 100-200 cm² $V^{-1} s^{-1}$	~250 cm² $V^{-1} s^{-1}$ (Golnaz Sadoughi, 2013)
Charge mobility (Nano)	~0.1-10^{-2} cm² $V^{-1} s^{-1}$		~125 cm² $V^{-1} s^{-1}$
Isoelectric point	6-7 at pH (Yi-Zhou Zhang, 2013)	~9 at pH (Anta et al., 2012)	4-5 at pH (Yi-Zhou Zhang, 2013)
Effective mass of electrons	9 m_e (1-50 m_e)	0.3 m_e and 0.34 m_e (Morkoç and Özgür, 2009)	0.17 m_e (Kumara et al., 2010)
Effective mass of holes	2 m_e	0.45 m_e and 0.59 m_e (Morkoç and Özgür, 2009)	0.45 m_e
Dielectric constant	114	8.5	12.5

Despite the high surface area, TiO₂ is characterized by slow electron diffusion (~10^{-5} cm² s^{-1}) and lower μ_e (<1 cm² V^{-1} s^{-1}) consequently, resulting in high charge recombination at TiO₂/electrolyte interface (Fakharuddin et al., 2014). The ZnO is

another widely employed photoanode material that has similar band gap (~3.3 eV) to TiO$_2$ while provides higher μ_e than the latter. However, it is chemically unstable with the successful Ru commercial dyes due to the fact that the carboxylic group present in the dye dissolve the ZnO and create Zn^{2+}/dye aggregate, which consequently affect the electrons injection to the MOS (Keis et al., 2000, Jose et al., 2009). Furthermore, SnO$_2$ has a lower CB edge (more positively located i.e., ~300-500 eV) (L A Harris and Wilson, 1978, Scaife, 1980, Bedja et al., 1994) than TiO$_2$ (**Figure 2.1b**) as it is made of lower energy orbitals (s orbitals) (Godinho et al., 2008). The lower CB position enables electron injection from the low lying LUMO sensitizer such as perylene dyes (Ferrere et al., 1997) and PbS quantum dots (Leventis et al., 2010). The incorporation of such sensitizers may lead to utilize near-infrared part of the solar spectrum. Although SnO$_2$ is one of the earliest materials that showed the PV effect in 1980s (Shimura et al., 1986, Memming and Schröppel, 1979), its intrinsic lower CB (~300 eV lower than TiO$_2$) results in routinely achieving low V$_{OC}$ ~500 mV (V$_{OC}$ for TiO$_2$ ~800 mV) despite high J$_{SC}$ ≥15 mA cm^{-2}. Inspired from the high μ_e of SnO$_2$, a number of researchers have attempted doping various transition metals to uplift its Fermi energy level; for example, Zn doped SnO$_2$ resulted in a V$_{OC}$ ~780 mV (Dou et al., 2011). Various semiconductor divalent metal oxides such as Cd, Ni, Cu, and Pb are doped in SnO$_2$ to improve its performance in DSSCs (Kim and Kwon, 2011). Such dopants enhanced the surface area, the dye loading, raised its flat-band potentials, and eventually enhanced the η compared to a pure SnO$_2$ based DSSCs; despite these advancements, η of SnO$_2$ based DSSCs is lower than that of the state-of-the-art TiO$_2$.

Another issue with SnO$_2$ is its low IEP (pH ~4-5) compared to that of TiO$_2$ (pH ~6-7) and ZnO (~pH ~9) (Parks, 1965), which makes weak bonding with the carboxylic groups upon dye anchoring and consequently yielding low photocurrent in DSSCs. Towards this end, a number of SnO$_2$ morphologies other than NPs such as NTs, core-shell structures, and composite nanostructures are employed in DSSCs. These structures provide two advantages; (i) provide larger surface area for dye-loading and (ii) a directed transport path for electron diffusion. Such developments have brought SnO$_2$ to deliver η as high as ~4% in its pure form and 7.6% in hybrid photoanodes (Senevirathna et al., 2007, Docampo et al., 2012, Cojocaru et al., 2013, Duan et al., 2015, Ahn et al., 2014).

2.3.2 Sensitizers or Dye

The photosensitizer is an import part of the DSSCs, which acts as an antenna for the light to absorb. The main function of the sensitizer is to absorb light and generate positive (holes) and negative (electrons) charge carriers simultaneously. The electron inject into the MOS leaving behind a hole in the ground state of the oxidized dye molecule. It basically function like a pump i.e., upon light absorption the dye molecule pumps electron into the MOS and then regenerate from the electrolyte, continue this process over the time (Meyer, 1997). Many sensitizers have been tested as a light absorber, which mainly comprised of synthetic organic dyes, porphyrins, and metal organic complexes. Most of the dyes attached to the MOS via acidic functional groups such as carboxylic or phosphonic acid (Wang et al., 2004). The metal Ruthenium (Ru) based dyes (N719, N3 and N749) are the preferred choice owing to their appropriate ligand and anchoring group with MOS (TiO$_2$, ZnO and SnO$_2$). The sensitizers N719 and N3 yielded η ~10.4%, when tested as a light absorber in the DSSCs. However, a significant amount of potential (0.6 V for I$^-$/I$_3^-$ electrolyte) is lost during regeneration of the oxidized dye molecule (Grätzel, 2009).

Similarly, η ~11.1% has achieved employing black dye (N749) with I$^-$/I$_3^-$ electrolyte in DSSCs due to its 0.2 eV lower electrochemical potential (Chiba, 2006). Although the Ru based sensitizers resulted in a high efficiencies, these dyes are expensive due to their rarity. On the other hand, organic sensitizers (porphyrins, perylenes and phthalocyanines) are another important classes of potential sensitizers for highly efficient DSSCs because these dyes are highly photostable and also offer high light-harvesting capabilities (Imahori et al., 2009). The highest η ~13% was achieved with porphyrin sensitizer accompanied with cobalt (II/III) redox couple (Simon Mathew and Gra¨tzel, 2014). Other numerous sensitizers have been employed as a light absorbers. For instance, metal free indoline dye delivered η ~6.51% (Horiuchi et al., 2004) and η ~2.9% with natural dyes (Calogero et al., 2015).

Generally, the photosensitizers should fulfill the following criteria (i) absorption spectrum should cover a wide range of wavelengths i.e., from near-IR to the visible region of the solar spectrum, (ii) possessing high extinction coefficient, (iii) less dye

aggregation at the MOS surface (iv) have the ability to suppress the electron recombination between electrolyte and MOS, (v) the LUMO of the dye must be higher in energy than the CB of the MOS in order to provide a sufficient driving force of ~0.1-0.2 eV for electron injection (Hara et al., 2003, Hagfeldt and Graetzel, 1995), (vi) the HOMO of the dye should be lower in energy than that of the electrochemical potential of the electrolyte to regenerate the oxidized dye molecule to its original state (Wenger et al., 2010, Kelly and Meyer, 2001, Meyer, 1997), (vii) having carboxylic and phosphonic acid anchoring groups to firmly grafted onto the MOS surface and support an efficient electron injection (Nazeeruddin et al., 2001), (viii) electron transfer from the dye to the MOS must be rapid compared to the recombination with the oxidized dye species (Robertson, 2006), (ix) to withstand with heat and photon in order to ensure long life time i.e., about 10^8 redox turnovers require under a constant exposure to natural sunlight corresponding to 20 years (Calogero et al., 2015, Nazeeruddin et al., 2001), and finally (x) having a reasonable low cost.

2.3.3 Electrolyte (Hole Transport Layer)

In general, an electrolyte must fulfill the following criteria, (i) it should not be participated in the light absorption process so that the maximum sunlight reaches to the dye anchored electrode, (ii) be chemically inert toward all parts of the DSSC in order to avoid any corrosion, (iii) possesses a suitable redox chemical potential (less than 0.2 V energy difference is required between the redox couple and the ground state of the sensitizers in order to provide sufficient driving force for reduction of dye) with respect to the HOMO of the dye and (iv) to withstand high stability at high temperature.

One of the key parameters for the selection of an electrolyte in DSSCs is its redox potential energy, i.e., the reduction potential of the electrolyte, must be at a higher energy than the reduction potential of the dye to regenerate it (**Figure 1.1**) and also to obtain high V_{OC} in the device (Hagfeldt et al., 2010). In conventional DSSC, the two-electron redox couple composed of (I^-/I_3^-) is employed, which is used to regenerate the reduced dye. The electrolyte provides a medium for the charge transport between the CE and the oxidized dye molecule via an ion diffusion mechanism by the following **Eq. (2.7)** (Daeneke et al., 2011, Daeneke et al., 2012)

$$I_3^- + 2e^- \text{ (CE)} \longrightarrow 3I^- \qquad\qquad (2.7)$$

The I^-/I_3^- redox couple is shown to be the best candidate so far, compared to other electrolyte redox couple, in terms of the kinetics of dye interception and electron uptake at the CE (Boschloo and Hagfeldt, 2009). Although η >11% has been achieved so far using the I_3^-/I^- redox couple (Chiba, 2006), this redox system has a few significant drawbacks, viz. (i) it corrodes most catalytic metals on FTO (CE) such as Ag and Pt (Shozo et al., 2009, Koo et al., 2006, Wang et al., 2003b, Olsen et al., 2000) as well as the sealing materials (Koo et al., 2006); and (ii) complex two-electron redox process (Boschloo and Hagfeldt, 2009, Wang et al., 2010, Feldt et al., 2010). In addition, the I^-/I_3^- electrolyte can also absorb the visible light, therefore leading to lower the photocurrent in the device (Martinson et al., 2008, Shozo et al., 2009, Nusbaumer et al., 2003). Furthermore, I^-/I_3^- redox couple has a redox potential of ~0.35 V (versus the normal hydrogen electrode, NHE), and the oxidation potential of the ruthenium based sensitizer is ~1.1 V, consequently, a significant internal potential (~0.4 V) is lost during reduction of the oxidized dye (Boschloo and Hagfeldt, 2009, Pelet et al., 2000).

Thus, it is highly important to explore other alternatives for I^-/I_3^- redox couple. In such scenario, a new disulfide/thiolate redox mediator developed, which possesses negligible absorption of the sun light in the visible range. DSSCs resulted an overall η of 6.4% using this electrolyte (Wang et al., 2010). Daeneke et al. introduced a single electron redox couple consist of ferrocene/ferrocenium (F_c/F_c^+), that yielded η ~7.5%; (Daeneke et al., 2011) however, it suffers from severe electron recombination. An electrolyte redox couple based on copper (I/II) showed inferior performance with the final η ~2.3% (Hattori et al., 2005). A significant rise in η has been achieved when a cobalt (II/III) redox couple was introduced which yielded η ~13% along with porphyrin sensitizer as a light absorber (Simon Mathew and Gra¨tzel, 2014). This tremendous surge in η was because the redox potential of cobalt redox couple is 0.7 V vs. NHE, which is significantly lower than that of I^-/I_3^- electrolyte (0.35 vs. NHE) so that loss-in potential at the dye-electrolyte interface is considerably reduced. Recently, the η of DSSCs reached up to 14.3% using the cobalt electrolyte by tailoring the sensitizer as well as the CE (Kakiage et al., 2015).

It has been shown that Co (III) species diffuse slowly (mass transport almost 1 order of magnitude slower than the I_3^- species) toward the CE. Larger size of Co (III) make it diffuses slowly. This slow diffusion adversely affect the photocurrent (Nelson et al., 2008, Feldt et al., 2010). This slow diffusion of cobalt (III) in DSSCs is recently partially solved by employing graphene nanoplatelets (GNP) grown on Au films as the CE (FTO/Au/GNP) with an overall η ~14.3% and $V_{OC} > 1V$ (Kakiage et al., 2015).

2.3.4 Counter Electrode

Counter electrode in DSSC helps to reduce the electrolyte species in its original state and complete the external circuit for electrons to re-enter the system. The function of the CE in DSSCs is twofold i.e., transfer of external electron to the electrolyte and speed up the electron reaction with the I_3^- species using a catalyst, usually noble metals such as Pt, Ag and Au or carbon materials such as polymers, carbon nanotubes and graphene (Wu and Ma, 2014). For a typical CE, Pt coated (~2 μm thick Pt layer coated usually by sputtering, pyrolysis, electrodeposition and vapor deposition) on the FTO is commonly used because of its high conductivity and catalytic activity. This thin coating of Pt layer on the FTO not only reflect and increase the light harvesting capability after passing through the WE but also serves to catalyze the electrolyte reduction process. The CE materials collect electrons from the external circuit and the catalyst increase the reduction of tri-iodide to iodide at the CE-electrolyte interface (Murakami and Grätzel, 2008). The most frequently used Pt CE is expensive, limited reserves (Wu and Ma, 2014); and it also degrades when in contact with the (I^-/I_3^-) over the time; therefore, affecting the overall performance of DSSCs (Koo et al., 2006).

Other alternatives to Pt based CE have been investigated and employed such as graphene (Wang and Hu, 2012), graphene composite (Peng et al., 2013), activated carbon (Huang et al., 2007), vertically aligned single-walled carbon nanotubes (Dong et al., 2011), multi-walled carbon nanotubes (Yue et al., 2013), cobalt selenide, cobalt sulfide, bismuth sulfide, nickel selenide, MOS (SnO_2 and Nb_2O_5 in the N2 atmosphere) (Wu et al., 2013) and nickel sulfide (Yang et al., 2014b). The carbon nanotubes (CNT) is one of the best alternative to the Pt having high electrical conductivity and catalytic effect. Koo and his co-workers founded that CNT based CE showed more stability than that of Pt

counterpart (Koo et al., 2006). The crucial requirements for the catalysis used in CE are the high electrical conductivity between electrolyte and CE, high catalytic activity, large specific surface area and low charge transfer resistance (R_{CT}) at the electrode/electrolyte interface.

2.4   TIN OXIDE AS PHOTOANODE IN DSSCS

Tin oxide (SnO_2) is an archetypical n-type MOS with high transparency and conductivity, which shows outstanding performance in many electronic devices such as DSSCs (Jarzebski and Marton, 1976, Bedja et al., 1994), lithium ion batteries (Lin et al., 2013), catalysis (Mahmoud and Fouad, 2015b), and gas sensors (Das and Jayaraman, 2014). The SnO_2 crystallizes into the following polymorphs: rutile type ($P4_2/mnm$), pyrite type (Pa3), $CaCl_2$ type (Pnnm), ZrO_2 type orthorhombic phase I (*Pbca*), α-PbO_2 type (*Pbcn*) (Das and Jayaraman, 2014). Among these, the most important naturally occurred polymorph is the cassiterite SnO_2 which crystallizes into rutile tetragonal structure at ambient temperature with space group $P4_2/mnm$. Its crystal structure diagram is shown in **Figure 2.1a**. The unit cell of SnO_2 consists of six atoms: two tin (Sn) and four oxygen atoms where each Sn atom exists at the center of a regular octahedron. Among the various MOS, SnO_2 possess the lowest CB as shown in **Figure 2.1b**. The top of the valence band is made of O (2p) orbital states, whereas the bottom of the CB has Sn (4s) and O (2p) states (Das and Jayaraman, 2014, Godinho et al., 2008). The lattice parameters of SnO_2 are a = b ~4.74 Å, c ~3.18 Å, and the interplanar spacing of the major planes are d_{110} = 3.35 Å, d_{101} = 2.65 Å, d_{200} = 2.37 Å, d_{211} = 1.77 Å, and d_{220} = 1.68 Å, with unit cell volume = 71.54 Å^3 (Das and Jayaraman, 2014).
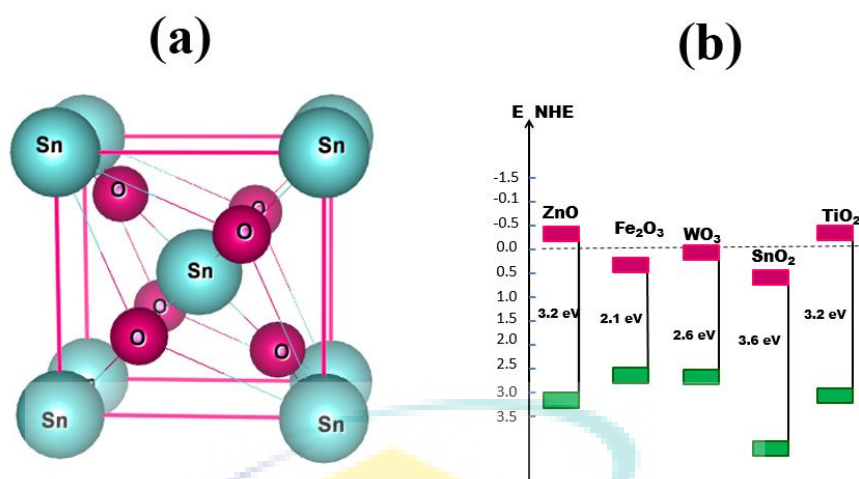
Figure 2.1: (a) Shows the crystal structure of rutile SnO_2, where the big blue atoms are tin and small pink color are oxygen (b) compare the energy band diagram of various MOS.

Source: Reproduced from (Godinho et al., 2008, Vogel et al., 1994)

2.5   DSSCS USING PURE TIN OXIDE NANOSTRUCTURES

Various SnO_2 nanostructures have been employed as a photoanode in DSSC (Liu et al., 2010, Docampo et al., 2012, Teh et al., 2013b, Park et al., 2014, Ganapathy et al., 2014). For instance, NPs for large surface area while NSs for light scattering and harvesting purposes. On the other hand, 1D nanostructures include NRs, NTs and NWs, which are expected to enhance the charge transport properties in the photoanode. Moreover, three dimensional nano morphologies are employed such as flower or mixing of NPs and 1D nanostructures in order to perform dual function in the photoanode of the DSSCs such as large amount of dye loading as well as superior charge transport properties. Various pure SnO_2 morphologies employed as photoanode in DSSCs are listed in **Table 2.3**.

Table 2.3
Photovoltaics parameters of DSSCs of pure SnO$_2$ photoanode based on nanoparticles, one dimensional and core-shell or Nanospheres

Photoanode materials based on SnO$_2$ pure architecture	Dye	J$_{SC}$/mA cm^{-2}	V$_{OC}$/ mV	FF/ %	η/ %	Active area (cm^2)
Nanoparticles pure SnO$_2$ morphologies						
Meso-porous NPs SnO$_2$ (Docampo et al., 2012)	Z907	17.1	450	47	3.7	0.12
SnO$_2$ NPs (Cojocaru et al., 2013)	N719	11.1	517	54	3.1	0.16
nano SnO$_2$-octa SnO$_2$ NPs (Cojocaru et al., 2013)	N719	09.5	437	59	2.4	0.16
SnO$_2$ cuboids (Teh et al., 2013b)	N719	07.5	620	48	2.3	0.12
SnO$_2$ NPs (Duan et al., 2015)	N3	07.9	467	55	2.0	0.20
SnO$_2$ NPs (Gubbala et al., 2008)	N719	11.0	356	36	2.0	0.25
SnO$_2$ NPs (Yang et al., 2014a)	N3	17.2	280	37	1.8	0.20
SnO$_2$ NPs (Teh et al., 2013b)	N719	07.0	590	35	1.4	0.12
SnO$_2$ NPs (Asdim et al., 2014)	N719	8.02	345	49	1.4	0.20
SnO$_2$ crystallites (Kumara et al., 2003)	N3	12.5	330	31	1.3	0.25
SnO$_2$ NPs (Teh et al., 2013a)	N719	3.64	510	55	1.0	0.12
SnO$_2$ NPs (Kim and Kwon, 2011)	Ru 535	7.63	350	43	1.1	no data
SnO$_2$ NPs (Perera et al., 2011)	N719	11.9	347	41	1.7	no data
SnO$_2$ NPs (Qian et al., 2009)	N719	04.9	401	51	1.0	0.16
SnO$_2$ NPs (Ramasamy and Lee, 2010)	N719	04.2	412	53	0.9	0.25
SnO$_2$ NPs (Pang et al., 2012)	N719	02.9	560	52	0.9	0.16

Table 2.3 Continued.

Photoanode materials based on SnO_2 pure architecture	Dye	J_{SC} /mA cm^{-2}	V_{OC}/ mV	FF/ %	η/ %	Active area (cm^2)
SnO_2 NPs (Park et al., 2004b)	N719	06.1	292	37	0.7	no data
SnO_2 NPs (Liu et al., 2005)	N3	11.2	250	26.4	0.7	0.10
SnO_2 NPs (Gu et al., 2014)	N719	05.0	400	33	0.7	0.25
SnO_2 NPs (Krishnamoorthy et al., 2012)	N719	02.4	516	41	0.5	0.15
SnO_2 NPs (Green et al., 2005)		01.7	470	40	0.5	1.0
SnO_2 NPs (Dadkhah and Salavati-Niasari, 2014b)	N719	04.2	330	34	0.5	0.20
SnO_2 NPs (Xu et al., 2014)	N719	02.0	414	50.6	0.4	no data
SnO_2 NPs (Arote et al., 2014)	Rose Bengal	00.9	385	60	0.3	no data
SnO_2 NPs (Snaith and Ducati, 2010)	D102	00.8	0.03	23	0.06	no data
One dimensional pure SnO_2 morphologies						
SnO_2 nano crystal (Aponsu et al., 2013)	D149	09.3	524	50	2.2	0.25
SnO_2 NWs (Gubbala et al., 2008)	N719	05.7	522	50	2.1	0.25
SnO_2 nano grains (Lee et al., 2011)	N719	07.5	465	47.7	1.7	0.22
SnO_2 NFs (Gao et al., 2014)	N719	07.0	506	38	1.3	no data
SnO_2 NRs (Shang et al., 2013)	N719	04.6	530	50	1.2	0.16
SnO_2 NTs (Desai et al., 2013)	N719	08.0	490	27	1.0	no data

Table 2.3 Continued.

Photoanode materials based on SnO$_2$ pure architecture	Dye	J_{SC} /mA cm^{-2}	V_{OC}/ mV	FF/ %	η/ %	Active area (cm^2)
SnO$_2$ NFs (Kumar et al., 2012)	N3	03.0	600	38	0.7	0.28
SnO$_2$ NFs (Gao et al., 2012)	N719	04.5	499	31	0.7	0.18
Core shell or 3 D spheres pure SnO$_2$ morphologies						
SnO$_2$ nanobelt (Mahmoud and Fouad, 2015a)	N719	16.9	690	51	5.7	no data
[a]HM-SnO$_2$ spheres (Park et al., 2014)	N719	12.3	520	58	3.7	0.16
[a]HM-SnO$_2$ spheres (Park et al., 2014)	N719	10.7	560	57	3.4	0.16
SnO$_2$ nano flowers (Kumar et al., 2012)	N3	07.3	700	60	3.0	0.28
SnO$_2$ NPs + NWs (Krishnamoorthy et al., 2012)	N719	09.9	525	49	2.5	0.15
SnO$_2$ NWs-NPs (Gubbala et al., 2008)	N719	06.3	484	53	2.3	0.25
[b]NP- SnO$_2$ spheres (Park et al., 2014)	N719	07.8	490	58	2.2	0.16
[c]Cauliflower-like SnO$_2$ HMS (Ganapathy et al., 2014)	@@	07.5	587	56	2.5	no data
Cauliflower-like SnO$_2$ HMS (Ganapathy et al., 2014)	@@	07.6	551	51	2.1	no data
[d]NP- SnO$_2$ spheres (Park et al., 2014)	N719	06.3	520	56	1.9	0.16
SnO$_2$ crystallite (Senevirathna et al., 2007)	--	10.7	388	42	1.7	0.25
SnO$_2$ nanostructure (Shaikh et al., 2014b)	N719	05.7	510	56	1.6	0.25
SnO$_2$ HNS (Chen et al., 2014)	N179	08.5	495	36	1.5	0.20
SnO$_2$ urchin microsphere (Thapa et al., 2014)	N719	07.6	380	50	1.4	no data
[e]SnO$_2$ MHSs (Qian et al., 2009)	N719	07.4	398	48	1.4	0.16

Table 2.3 Continued.

Photoanode materials based on SnO₂ pure architecture	Dye	J_{SC}/mA cm^{-2}	V_{OC}/ mV	FF/ %	η/ %	Active area (cm²)
NRs based SnO₂ microsphere (Li et al., 2015)	N719	05.3	410	63	1.4	0.13
SnO₂ nanosheets (Bhande et al., 2014)	N719	08.3	430	39	1.4	0.25
Bare SnO₂ meso-porous (Shang et al., 2012)	N719	05.1	549	45	1.3	0.16
Coral-like porous SnO₂ hollow (Liu et al., 2010)		03.6	520	56	1.0	no data
SnO₂ spherical crystallite (Shaikh et al., 2014a)	N719	07.4	320	41	1.0	0.25
Hollow NSs SnO₂ (Wang et al., 2012)	N719	06.4	390	34	0.9	0.2
SnO₂ nanosheets (Xu et al., 2014)	N719	02.4	417	57.3	0.6	no data
Spherical SnO₂ (Liu et al., 2010)		04.2	330	31	0.4	no data
SnO₂ nanoplates (Xu et al., 2014)	N719	01.9	348	35.8	0.3	no data
SnO₂ Nanofloweres (Niu et al., 2014)	N719	05.4	440	43.5	1.0	0.25
SnO₂ microsphere (Liu et al., 2012)	N719	00.5	553	61.5	0.2	0.56
SnO₂ thin film (El-Etre and Reda, 2010)	Erythrosin	00.8	210	40	0.06	1.0

[a] HM = hierarchical mesoporous,

[b] used liquid electrolyte in DSSCs,

[c]@@ = CdS/CdSe/ZnS QDs [d] used solid electrolyte in DSSCs, [e] MHSs stands for multilayered hollow microspheres

2.5.1   NPs-or NSs-based Photoanodes of Large Surface Area

Hydrothermal process is a simple technique to synthesize metal and metal oxides at the nanometer scale. Varieties of nanostructures have been synthesized using this method such as NPs, NRs, NSs, bead type structure, hollow NPs, flower shape and so many others (Dou et al., 2011, Park et al., 2014, Teh et al., 2013b, Ganapathy et al., 2014, Dong et al., 2014, Qian et al., 2009, Yang et al., 2007). In this method, temperature of the reaction typically ranges from ~50-250 ^{o}C to optimize the process conditions for a desired morphology, while the working pressure reach up to 3.0 MPa (O'Regan, 1991, Nazeeruddin et al., 1993). To utilize their high surface area, SnO_2 NPs (surface area ranging from ~44 to 57 m^2/g) have been employed as bi-layered nanostructures (having sizes ~15-20 nm and ~50-150 nm) photoanode and demonstrated η ~4% (Cojocaru et al., 2013). Another report on NPs/NSs by Wang et al., employing SnO_2 NSs by hydrothermal method (surface area of ~64.2 m^2/g) resulted in η ~0.86% using pure NSs which enhanced 8-times (η ~6.02 %) upon $TiCl_4$ aqueous solution treatment. Surprisingly, despite its higher surface area (~64.2 m^2/g), η is lower (~0.86%) than that reported by Cojocaru et al. These results show that the performance of DSSC does not depend on the surface area alone. This is also evidenced by the work of Reda et al. showing that SnO_2 NPs of high surface area (~140 m^2/g) as a photoanode and Erythrosine dye gave η ~0.06% (J_{SC} <1 mA cm^{-2} and V_{OC} of ~200 mV) (El-Etre and Reda, 2010). Similar report by Nan et al. performed a comparative study between bigger size macroporous particles (MPs) possessed less surface area versus smaller NPs of size ~10 nm with high surface area, resulted in a 10% improvement in η in the former based DSSCs despite the fact that the latter possess larger dye loading (Li et al., 2013).

These studies revealed that factors besides surface area such as light scattering and charge collection efficiency (η_{cc}) also contributed to the PV performance. Although NPs usually provides high surface area they are characterized by trap limited electron transport, which eventually limit their performance as shown in **Figure 2.2**. Another issue for the low performance of pure NPs is their poor interconnectivity, which detrimentally reduce the number of photoinduced electrons (Zhang and Cao, 2011, Nelson and Chandler, 2004). Therefore, the progress in NPs based photoanode is

hindered and other alternatives such as 1D nanostructure alone or their composites with NPs are attempted in SnO₂ based photoanode.
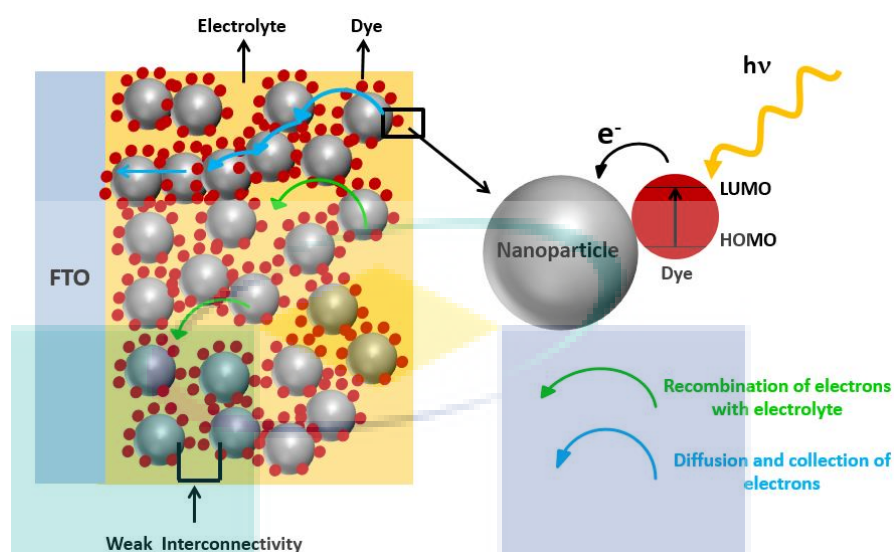
Figure 2.2: Trapping and de-trapping phenomena in NPs based photoanode, where blue arrow shows electron diffusion and the green one shows recombination of electrons with electrolyte species. Electrons can also be lost due to the weak interconnectivity of the successive NPs in the WE.

Source: Reproduced from (Nelson and Chandler, 2004, van de Lagemaat et al., 2000)

2.5.2   One Dimensional Nanostructures Based Photoanode

Eelectrospinning is an effective and easy-to-use technique to fabricate nanofibers with diameters as thin as ~5-20 nm (Ghorani and Tucker, 2015, Dalton et al., 2013, Yarin, 2011, Bellan and Craighead, 2011, Frenot and Chronakis, 2003). The word electrospinning is derived from the term "electrostatic spinning" which uses a polymeric solution for the fabrication of 1D nanostructure such as NTs, NFs, NWs, nanoflowers and even some non-conventional nanostructures at nanometric scale (Thavasi et al., 2008, Kumar et al., 2012, Le Viet et al., 2010, Cavaliere et al., 2013). These nanostructures contain remarkable characteristics such as flexibility, mechanical functionalities i.e., stiffness and tensile strength, and high aspect ratio that make them a superior candidate in a number of devices (Thavasi et al., 2008, Huang et al., 2003). A schematic diagram of the electrospinning procedure is shown in **Figure 3.2,** which mainly consist of three

parts, a high voltage power supply, a capillary tube containing a needle with small diameter also called a spinneret, and a grounded metal collector.

For the formation of the NFs, a high voltage (typically 1-3 kV/cm) is required between the tip of the needle and the grounded conductor to create electrically charge polymeric solution out of the needle and jet it toward the collector surface. The polymeric solution becomes highly charged at such a high voltage-so that the solution droplet at the tip of the needle experiences two major forces i.e., the surface tension and the electrostatic force. As the high voltage leads to increase the intensity of the electric field and cause the semi-spherical surface at the tip of the needle to elongate toward the collector called "Taylor cone". When an electric field reaches to a critical value and the electrostatic force of the charged polymer overcome the surface tension of the Taylor cone, a charged jet erupts from the tip of the needle towards the grounded collector electrode and collected in the form of 1D nanofibers (McCann et al., 2005, Sun et al., 2014, Sawicka and Gouma, 2006, Huang et al., 2003). Many parameters are taken into account during the electrospinning process, including (i) viscosity, conductivity, and surface tension of the polymeric solution, (ii) the distance between the tip of the needle and metal collector, (iii) applied voltage, temperature and humidity inside the electrospinning chamber (Rutledge and Fridrikh, 2007, Inagaki et al., 2012, Li and Xia, 2004).One dimensional nanostructures such as NRs, NWs and NTs are conceived to overcome the poor transport in NPs photoanode in DSSCs. These 1D nanostructures provide a direct path for photoinjected electrons; and therefore, lead to a possibility of the complete electron collection at the WE (Poudel and Qiao, 2012). However, these nanostructures are characterized by inferior surface area that leads to lower dye anchoring. Shang et al. synthesized SnO_2 NRs and NPs in order to compare their performance in DSSCs (Shang et al., 2013). The PV parameters for NRs DSSCs were higher i.e., J_{SC} (~4.58 mA cm^{-2}) than NPs DSSCs (~4.02 mA cm^{-2}) due to its improved electron transport properties. The slight increment in the NRs devices was due to the lower surface area (12.2 m^2/g), which therefore, led to lower dye adsorption than the NPs counterpart (15.1 m^2/g). The charge transport parameters were calculated using bode phase diagram by the following **Eq. (2.8)**

$$\tau_n = \frac{1}{2\pi f_{\max}} \tag{2.8}$$

where τ_n is the electron life time and f_{max} is the mid peak frequency in the bode phase diagram. The calculated τ_n was ~13 ms and ~2.2 ms for NRs and NPs based DSSCs, respectively, a 6 times higher value for NRs due to their 1D nature.

To further elaborate the different performance of the two nanostructure architectures, Akilavasan et al. performed a comparative study of pure SnO_2 NPs and NRs and demonstrated remarkably enhanced performance for NRs based DSSCs. The NRs based DSSCs exhibited enhanced τ_n and reduced recombination, which led to a two-fold improvement in FF, five-fold increase in η, two-fold increment in J_{SC} and also slightly higher V_{OC} (Akilavasan et al., 2014). Still the η based on 1D photoanode DSSCs is far lower therefore, further improvement is required in order to combine the two desire features of the two different morphologies in a single photoanode i.e., NPs for high surface area and 1D nanostructure for reduced electron recombination and faster charge transport.

2.5.3 Three Dimensional Nanostructures

In order to achieve strong light scattering and harvesting properties in the WE, three dimensional (3D) nanostructures, which is composed of submicron nanostructure (size equivalent to that of the wavelength of the visible light) are employed. The 3D nanostructures increase light scattering in the photoanodes, and thereby, improve the η_{cc}. However, owing to their relatively larger sizes than those of NPs, they are characterized by a lower surface area. Recently, Ganapathy et al. reported cauliflower-like SnO_2 hollow microspheres as a WE of the DSSCs and in quantum dot sensitized solar cells, which showed η ~3% and ~2.5%, respectively, using a carbon-based CE . In another report Kumar and colleagues developed 3D flower-shaped structure, where η (~3% with a V_{OC} ~700 mV) has been achieved, which was higher ~4 times compared to that of 1D conventional NFs (0.7%) (Kumar et al., 2012). The SnO_2 nanostructure in pure

form shows inferior performance when tested as a photoanode in the DSSCs therefore, a composite with higher CB MOS is required in order to enhance its low PV parameters.

2.6   COMPOSITE NANOSTRUCTURES OF TIN OXIDE

Various ways have been adopted in order to enhance the performance of pure SnO_2 photoanode in the DSSCs **(Section 2.5 and Table 2.3)**. For instance, making a composite nanostructure of the SnO_2 with other high CB MOS earlier and then utilize as a photoanode material or a fabricating a composite direct via deposition process on the FTO of the DSSCs. Another way to improve the performance is making a core-shell nanocomposite, where the core and shell possessing distinct characteristics. Finally, by incorporating a trace of suitable element to SnO_2 via doping process in order to improve the PV parameter. The SnO_2 composite photoanode employed in DSSCs are tabulated in **Table 2.4**.

Table 2.4
Photovoltaic parameters of composite and doped SnO_2 photoanodes of DSSCs based on NPs, 1D and core-shell or NSs

Photoanode materials based on composite/doped architecture	Dye	J_{SC}/mA cm^{-2}	V_{OC}/ mV	FF/ %	η/ %	Active area (cm^2)
Nanoparticles composite/doped SnO₂ morphologies						
SnO_2 NPs-Al(0.02%)-TiO_2 (Duan et al., 2015)	N3	16.6	650	64	6.9	0.20
Meso-porous SnO_2-MgO (Docampo et al., 2012)	Z907	15.7	670	61	6.4	0.12
Pt-electrode SnO_2/TiO_2 NPs (Sun et al., 2012)	N719	12.5	730	71	6.5	0.25
Carbon-electrode SnO_2 NPs/TiO_2 (Sun et al., 2012)	N719	13.0	740	64	6.2	0.25
SnO_2 MHSs-TiO_2 (Qian et al., 2009)	N719	14.6	664	58	5.7	0.16
SnO_2 NPs-Al(0.01%)-TiO_2 (Duan et al., 2015)	N3	14.6	611	62	5.5	0.20
SnO_2 NPs-$CaCO_3$ (Perera et al., 2011)	N719	11.4	681	69	5.4	no data
SnO_2 NPs/ZnO nanotetrapods (Chen et al., 2010a)	N719	12.0	684	60	5.0	no data
SnO_2 NPs-TiO_2 (Peng et al., 2014)	N719	11.1	641	67	4.7	no data
Commercial SnO_2 NPs/$TiCl_4$ (Wang et al., 2012)	N719	09.7	758	62	4.6	0.2
SnO_2 NPs-TiO_2 (Li et al., 2013)	N719	13.9	670	49	4.4	no data
SnO_2 NPs-Al(0.005%)-TiO_2 (Duan et al., 2015)	N3	11.8	563	66	4.4	0.20
SnO_2 NPs/$TiCl_4$ (Wang et al., 2013b)	N719	12.7	677	50	4.3	0.16
SnO_2 NPs-TiO_2 (Qian et al., 2009)	N719	10.3	665	62	4.2	0.16
SnO_2 NPs- Zn (Shalan et al., 2014)	N719	08.6	756	67	4.2	0.25

Table 2.4 Continued.

Photoanode materials based on composite/doped architecture	Dye	J_{SC}/mA cm^{-2}	V_{OC}/ mV	FF/ %	η/ %	Active area (cm^2)
SnO$_2$ NPs-Al (0.03%)-TiO$_2$ (Duan et al., 2015)	N3	11.5	607	60	4.9	0.20
Mg-SnO$_2$-TiO$_2$ (Pang et al., 2012)	N719	09.7	670	61	4.2	0.16
SnO$_2$ NPs@TiO$_2$ (Gu et al., 2014)	N179	11.5	590	57	3.8	0.25
SnO$_2$ NPs/TiO$_2$ / Cu. anode (Hossain et al., 2011)	Cds/Cdse	17.4	477	45	3.7	0.1199
SnO$_2$ NPs-Ni (Shalan et al., 2014)	N719	07.6	690	69	3.6	0.25
SnO$_2$ NPs/Al (0.02%) (Duan et al., 2015)	N3	12.8	555	51	3.5	0.20
SnO$_2$ NPs/TiO$_2$ /Pt. anode(Hossain et al., 2011)	Cds/Cdse	16.2	458	46	3.4	0.1199
Nano-SnO$_2$-SrTiO$_3$ (24.23%) (Aponsu et al., 2013)	D149	09.5	580	62	3.4	0.25
SnO$_2$ NPs/TiO$_2$ (Duan et al., 2015)	N3	09.3	540	66	3.3	0.20
SnO$_2$ NPs- TiCl$_4$ (Shalan et al., 2014)	N719	06.9	684	70	3.2	0.20
Nano-SnO$_2$-SrTiO$_3$ (27.43%) (Aponsu et al., 2013)	D149	07.6	615	63	2.9	0.25
Nano-SnO$_2$ -SrTiO$_3$ (20.74%) (Aponsu et al., 2013)	D149	08.5	569	60	2.9	0.25
SnO$_2$ NPs/TiO$_2$/Al$_2$O$_3$(Liu et al., 2005)	N3	21.9	440	30	2.9	0.10
SnO$_2$ NPs/Al (0.01%) (Duan et al., 2015)	N3	11.0	512	51	2.8	0.20
SnO$_2$ NPs-TiO$_2$-MgO (Snaith and Ducati, 2010)	D102	06.6	710	59	2.8	no data
SnO$_2$ NPs/ Al (0.005%) (Duan et al., 2015)	N3	09.8	490	55	2.6	0.20
SnO$_2$ NPs-TiO$_2$ (Yang et al., 2014a)	N3	19.7	330	40	2.6	0.20
SnO$_2$ NPs/Al (0.03%) (Duan et al., 2015)	N3	10.0	535	46	2.4	0.20

Table 2.4 Continued.

Photoanode materials based on composite/doped architecture	Dye	J_{SC} /mA cm^{-2}	V_{OC}/ mV	FF/ %	η/ %	Active area (cm^2)
Mg-SnO$_2$ NPs (Pang et al., 2012)	N719	06.7	570	53	2.0	0.16
SnO$_2$ NPs-ZnO (Lee et al., 2010)	N719	06.6	597	62	2.4	0.25
SnO$_2$ NPs/TiO$_2$ NPs (Liu et al., 2005)	N3	20.1	390	26.5	2.1	0.10
Nano-SnO$_2$-SrTiO$_3$ (30%) (Aponsu et al., 2013)	D149	05.3	599	64	2.0	0.25
SnO$_2$ NPs-MgO (Lee et al., 2010)	N719	08.8	447	52	2.0	0.25
Ni-SnO$_2$ NPs (Kim and Kwon, 2011)	Ru 353	07.0	460	58	1.9	no data
Cd-SnO$_2$ NPs (Kim and Kwon, 2011)	Ru 535	08.8	450	46	1.8	no data
Cu-SnO$_2$ NPs (Kim and Kwon, 2011)	Ru 353	06.7	470	57	1.8	no data
SnO$_2$ NPs-MgO (Snaith and Ducati, 2010)	D102	09.5	430	42	1.8	no data
Zn-SnO2 NPs (Kim and Kwon, 2011)	Ru 535	08.5	420	48	1.7	no data
SnO$_2$ NPs-TiO$_2$ (Gu et al., 2014)	N719	05.5	760	45	1.7	0.25
SnO$_2$-MgO (Green et al., 2005)		03.3	710	48	1.2	1.0
SnO$_2$ NPs-NiO (Lee et al., 2010)	N719	03.9	598	52	1.2	0.25
Pb-SnO$_2$ NPs (Kim and Kwon, 2011)	Ru 535	05.8	380	50	1.1	no data
SnO$_2$ NPs-TiO$_2$ (Snaith and Ducati, 2010)	D102	02.5	520	49	0.6	no data
SnO$_2$ NPs-CuO (Lee et al., 2010)	—	00.9	475	70	0.3	0.25

Table 2.4 Continued.

Photoanode materials based on composite/doped architecture	Dye	J_{SC} /mA cm^{-2}	V_{OC}/ mV	FF/ %	η/ %	Active area (cm^2)
One dimensional composite/doped SnO$_2$ morphologies						
SnO$_2$NRs-TiO$_2$ (Song et al., 2013)	N719	19.6	644	68	8.6	0.25
[a]SnO$_2$ NT@TNS/OM-TiO$_2$ (Ahn et al., 2014)	N719	17.1	760	61	7.9	0.16
SnO$_2$ NF-TiO$_2$ (Gao et al., 2014)	N719	20.5	713	48	7.0	no data
SnO$_2$ NRs@TiO$_2$ (Huo et al., 2014)		16.2	780	55	7.0	0.25
SnO$_2$ NFs/ TiCl$_4$ (Wang et al., 2013b)	N719	14.9	702	50	5.4	0.16
Zn -SnO$_2$ -TiO$_2$ 10um (Dou et al., 2011)	N719	13.8	800	59	6.8	0.28
SnO$_2$ NFs-TiO$_2$ (1:1) (Kasaudhan et al., 2014)		13.5	730	63	6.2	0.12
Zn-SnO$_2$-TiO$_2$ nanoflowers 8um (Dou et al., 2011)	N719	10.0	800	63	5.2	0.28
SnO$_2$NTs-TiO$_2$ (Gao et al., 2012)	—	14.7	723	48	5.2	0.18
SnO$_2$-ZnO nanoneedle (Zhou et al., 2014)	N719	09.8	590	57	4.7	0.08
SnO$_2$ NRs-TiO$_2$ NPs (Shang et al., 2013)	N719	10.5	757	`59	4.7	0.16
SnO$_2$ NR-TiCl$_4$ (Kasaudhan et al., 2014)	N719	12.9	650	55	4.6	0.12
SnO$_2$ NFs-TiO$_2$ (Gao et al., 2012)	N719	12.7	742	49	4.6	0.18
SnO$_2$ NWs-TiO$_2$ NPs (Gubbala et al., 2008)	N719	08.6	686	49	4.1	0.25
SnO$_2$ NRs-TiO$_2$ (Huo et al., 2014)	N719	09.9	660	60	4.0	0.25
SnO$_2$ NTs-TiO$_2$ (Desai et al., 2013)	N719	09.9	680	49	3.5	no data
NRs SnO$_2$ /NaOH (Birkel et al., 2012)	N719	08.9	575	61.4	3.1	0.25

Table 2.4 Continued.

Photoanode materials based on composite/doped architecture	Dye	J_{SC} /mA cm^{-2}	V_{OC}/ mV	FF/ %	η/ %	Active area (cm^2)
Zn- SnO$_2$10um (Dou et al., 2011)	N719	06.0	780	62	3.0	0.28
Zn -SnO$_2$ nanoflowers 8um (Dou et al., 2011)	N719	04.5	700	65	2.1	0.28
Core-shell or 3-D composite/ doped SnO$_2$ morphologies						
Five-shell-SnO$_2$-HMSs/ P25 (Dong et al., 2014)	N719	20.1	750	63.2	9.5	0.16
[b]SnO$_2$ HS@TNS/OM-TiO$_2$ (Ahn et al., 2014)	N719	18.2	760	60	8.2	0.16
(SnO$_2$ crystallites)ZnO/ZnO (Kumara et al., 2003)	N3	18.8	660	64	8.0	0.25
SnO$_2$ crystallites /ZnO (Kumara et al., 2003)	N3	16.9	665	65	7.3	0.25
SnO$_2$ crystallite-MgO (Senevirathna et al., 2007)	N719	14.2	758	67	7.2	0.25
Quintuple-shelled/TiO$_2$ (Dong et al., 2014)	N719	17.6	720	56.6	7.2	0.16
SnO$_2$ nanobeans-TiO$_2$ HS (Wang et al., 2015a)		13.0	754	67.2	6.6	no data
SnO$_2$ HNS-TiO$_2$ (Chen et al., 2014)	N719	18.3	744	48	6.5	0.20
SnO$_2$ NPs/NFs-TiO$_2$ (Wang et al., 2013b)	N719	16.8	711	53	6.3	0.16
SnO$_2$ microsphere-TiO$_2$ (Wang et al., 2015b)	N719	14.1	803	55	6.3	0.16
Hollow NSs SnO$_2$/TiCl$_4$ (Wang et al., 2012)	N719	14.6	765	54	6.1	0.2
SnO$_2$ microsphere-TiO$_2$ (Thapa et al., 2014)	N719	14.7	740	56	6.0	no data
SnO$_2$-TiO$_2$ (Shaikh et al., 2014b)	N719	17.0	620	53	5.6	0.25
SnO$_2$ Nanaflowers-TiCl$_4$ (Niu et al., 2014)	N719	12.7	760	58	5.6	0.25
SnO$_2$@TiO$_2$-ZnO nanoplate (Wang et al., 2015c)	N719	15.0	711	51	5.6	0.16

Table 2.4 Continued.

Photoanode materials based on composite/doped architecture	Dye	J_{SC} /mA cm^{-2}	V_{OC}/ mV	FF/ %	η/ %	Active area (cm^2)
SnO_2 microsphere-TiO_2 (Wang et al., 2015b)	N719	12.1	801	54	5.3	0.16
SnO_2 nanosheets-MgO (Bhande et al., 2014)	N719	15.9	690	48	5.3	0.25
SnO_2 nanosheets-$CaCO_3$ (Bhande et al., 2014)	N719	16.0	720	45	5.2	0.25
SnO_2 nanobeans-$TiCl_4$ (Wang et al., 2015a)		11.0	720	65	5.1	no data
SnO_2 microsphere-TiO_2 (Wang et al., 2015b)	N719	10.7	800	59	5.0	0.16
TiO_2-meso-sphere SnO_2-TiO_2 (Shang et al., 2012)	N719	10.6	745	63	5.0	0.16
SnO_2 microsphere-TiO_2 (Wang et al., 2015b)	N719	09.2	792	55	4.0	0.16
Macro SnO_2 (Li et al., 2013)	N719	14.7	690	49	4.9	no data
SnO2 nanobelt-ZnO (Mahmoud and Fouad, 2015a)	N719	15.9	650	47	4.7	no data
NWs based SnO_2/Zn_2SnO_2 HMs (Li et al., 2015)	N719	11.0	590	730	4.7	0.13
Meso-sphere SnO_2-TiO_2 (Shang et al., 2012)	N719	10.9	754	54	4.4	0.16
SnO_2@TiO_2 (Wang et al., 2015c)	N719	`12.7	677	50	4.3	0.16
SnO_2 HMs/TiO_2(600nm) (Chen et al., 2012)	Z907	09.4	662	67	4.1	0.16
Ga-SnO_2 cuboids (Teh et al., 2013b)	N719	07.4	740	73	4.0	0.12
SnO_2 nano-grain -ZnO (Lee et al., 2011)	N719	08.7	648	70	4.0	0.22
SnO_2 nanosheets-ZrO_2 (Bhande et al., 2014)	N719	13.0	690	47	4.0	0.25
Cubic meso-SnO_2/TiO_2 (Ramasamy and Lee, 2010)	N719	10.4	711	51	3.8	0.25

Table 2.4 Continued.

Photoanode materials based on composite/doped architecture	Dye	J_{SC} /mA cm^{-2}	V_{OC}/ mV	FF/ %	η/ %	Active area (cm^2)
[c1]Cauliflower-like SnO$_2$ HMS-TiO$_2$(Ganapathy et al., 2014)	N719	09.0	709	55.6	3.6	no data
SnO$_2$-ZnO (Park et al., 2004b)	N719	07.0	610	83	3.6	no data
Nanocrystalline-SnO$_2$-Zn (Park et al., 2004a)	N719	08.6	590	65	3.3	0.22
SnO$_2$ nanosheets-ZnO (Bhande et al., 2014)	N719	10.2	650	48	3.2	0.25
NWs based SnO$_2$/Zn$_2$SnO$_2$ Ms (Li et al., 2015)	N719	07.2	570	74	3.0	0.13
SnO$_2$ nanocrystallite-ZnO (Shaikh et al., 2014a)	N719	09.5	610	51	3.0	0.25
[c2]Cauliflower-like SnO$_2$ HMS-TiO$_2$ (Ganapathy et al., 2014)	N719	07.8	733	53.3	3.0	no data
SnO$_2$ crystal/KOH (Birkel et al., 2012)	N719	09.4	526	56	2.8	0.25
Nano-SnO$_2$/TiO$_2$ (Ramasamy and Lee, 2010)	-	06.6	707	58	2.7	0.25
TiO$_2$ -SnO$_2$ meso-sphere (Shang et al., 2012)	N719	07.0	683	55	2.7	0.16
Spherical SnO$_2$/NH$_4$OH (Birkel et al., 2012)	N719	09.5	405	41.6	1.6	0.25
Sieve-liked SnO$_2$ sheet/TiCl$_4$ (Teh et al., 2013a)	N719	04.4	610	47.5	1.3	0.12
SnO$_2$ MSs/Zn$_2$SnO$_4$ (Liu et al., 2012)	N719	01.6	707	42.6	0.5	0.56
SnO$_2$/MgO (Tennakone et al., 2003)	--	15.4	654	65	6.0	no data
Sb-SnO$_2$-MgO (Tennakone et al., 2003)	--	07.3	473	65	1.8	no data
nanoSnO$_2$ NPs/TiCl$_4$ (Cojocaru et al., 2013)	N719	11.9	503	59	3.6	0.16

[a] SNT@TNS: SnO$_2$ nanotube-TiO$_2$ nanosheet double-shell nanostructures, OM Organised mesoporous, the device were based on solid electrolyte

[b] SHS@TNS = SnO$_2$ hollow sphere-TiO$_2$ nanosheet double-shell nanostructures, the device were based on solid electrolyte

[c1] Pt counter electrode was used [c2] Carbon nanofibers counter electrodes used

2.6.1 Core-shell Photoanode

Although SnO_2 is a well-known MOS for its high μ_e, a high efficiency DSSCs similar to the state-of-the-art TiO_2 analogues is yet to be seen. This is due to the lower lying CB of SnO_2 which favors electron recombination by the holes present in the electrolyte. Core-shell nanostructure based WE is one of the several strategies to resolve such recombination in SnO_2 based DSSCs. In core-shell structures, SnO_2 serves as a core material because of its higher μ_e whereas the shell is made using insulating oxides or MOS of higher CB (Nb_2O_5, TiO_2, ZnO, MgO, Al_2O_3, Y_2O_3 and ZrO_2) (Prasittichai and Hupp, 2010, Docampo et al., 2012, Palomares et al., 2003, Kay and Grätzel, 2002). The shell serves as an energy barrier at the MOS/electrolyte interface and also improve the dye anchoring due to their higher surface area originating from the high IEP. There are two ways to fabricate a core-shell NPs photoanode as shown in **Figure 2.3** (i) synthesize SnO_2 NPs as a core followed by coating an over layer as a shell on its surface **(Figure 2.3a)** and then employing the material in the photoanodes, and (ii) fabricate SnO_2 NPs photoanode first followed by applying an over layer of a shell on it (**Figure 2.3b**).
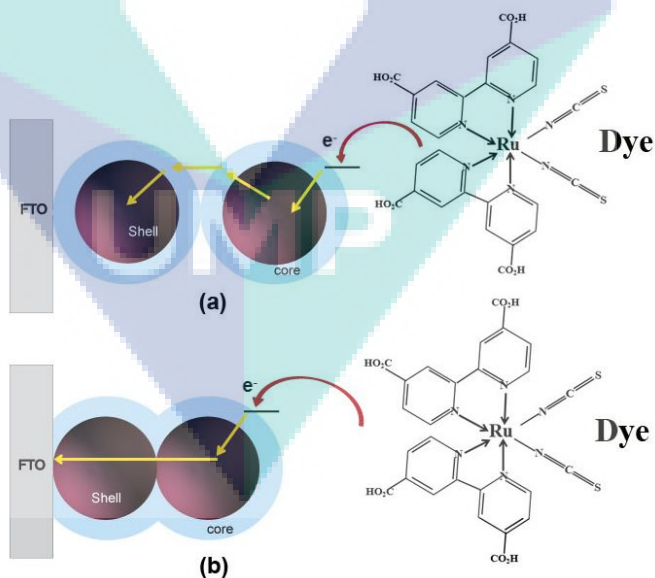
Figure 2.3: Schematic representation of a core-shell photoanodes using two different approaches.

Source: Reproduced from (Chappel et al., 2002, Diamant et al., 2004)

In the first approach, the barrier is formed between successive NPs (serving as a core) and electrolyte whereas, in the second approach the barrier is formed between the core and the electrolyte. The latter has more advantages over the former due to the fact that electron recombination is lower as well as facilitates faster electron transport (Snaith and Ducati, 2010, Zhang and Cao, 2011).

It is important to note that the core and shell material should be chosen to favor a downhill transition i.e., dye's LUMO-shell-core material-FTO. To allow such transition, the CB of the core must be lower than the CB of the shell and the LUMO of the dye molecule must be at a higher energy level than the CB of the shell as shown in **Figure 2.4a**. Electrons can reach to the core material via their injection into the CB of the shell from the dye LUMO followed by downhill movement to the core materials or it can also directly be injected into the core by tunneling process via the shell materials. On the other hand, **Figure 2.4b** illustrates the unfavorable core-shell structure, where the CB of the shell lies at a higher position than LUMO of the dye, and therefore, electrons can only diffuse through tunneling process. Tunneling of electrons can take place when the shell layer is extremely thin (few angstrom thick).

A number of papers reported the core-shell DSSCs, which have shown remarkable improvement in DSSC's parameters. Pang et al. employed SnO_2-ZnO core-shell as a photoanode in DSSCs. Owing to the thin shell layer of ZnO, electron recombination was largely suppressed and achieved five times higher η ~7.3% compared to pure SnO_2 DSSCs (η ~1.3%) (Kumara et al., 2003). It also showed two fold increment in FF and V_{OC} (**Table 2.4**). Similarly, insulating oxides (Al_2O_3 and MgO) and MOS such as, TiO_2 and ZnO are also found to increase the dye loading and the J_{SC} thereby. This is because of the fact that the surface of these insulating oxides is more basic in nature than that of pure SnO_2, which makes the former more favorable with carboxyl groups. This could be evidenced from a study that the pure SnO_2 photoanode have weak coloration, whereas the coloration was strongly enhanced by the systematic increase of TiO_2 NPs thin layer on its surface resulted in enhanced J_{SC}. The differences in coloration could be due to the low acidity and low IEP (pH ~4-5) of
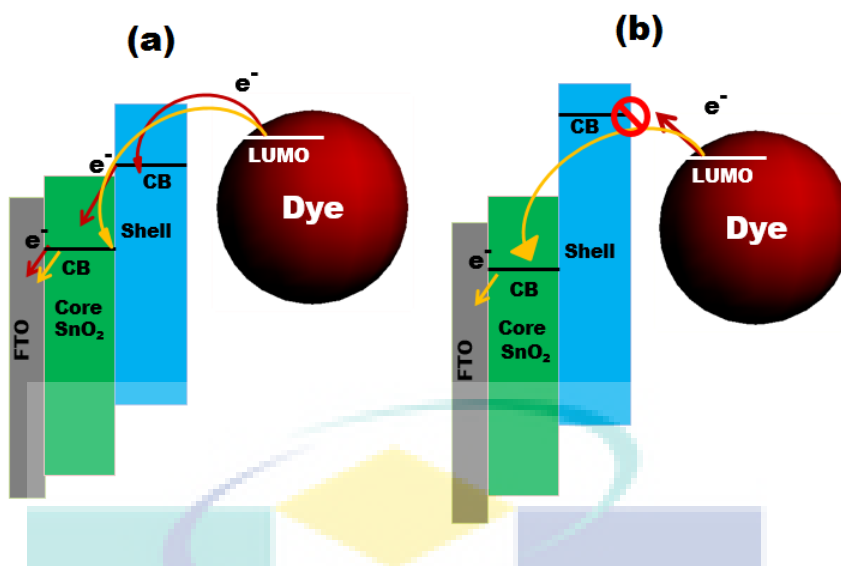
Figure 2.4: Core- shell mechanism (a) depicts the suitable core-shell adjustment where electrons can easily jump to the CB of the shell, then followed to the core material or it can diffuse through the tunneling process while (b) shows unfavorable injection phenomena between dye LUMO and CB of the shell material where electrons can only diffuse via tunneling process.

Source: Reproduced from (Zhang and Cao, 2011)

SnO_2 as compared to the TiO_2 which has IEP (pH ~6-7). Similarly, when SnO_2 photoanode was passivated with SiO_2, a material of lower IPE (pH ~2.0), it resulted in significantly inferior dye loading owing to the more acidic nature of the SiO_2. In contrast, significant improvement in dye adsorption and coloration was achieved when the insulating layers of high IEP, such as MgO (IEP at pH ~12), Al_2O_3 (IEP, at pH ~9) and Y_2O_3 (IEP, at pH ~9) were over coated on SnO_2 surface (Kay and Grätzel, 2002). Thus, a shell layer not only acts as an interfacial barrier for charge recombination but also may affect the dye-loading characteristics of SnO_2 photoanode.

It is obvious that the thickness of a shell layer has a significant effect on the PV performance of core-shell materials based DSSCs. Grätzel et al. reported Y_2O_3 insulating layer on TiO_2 and SnO_2 and showed that an increase in the thickness of the insulating layer give rise to the V_{OC}, however, at the expense of J_{SC}. The diminishing of J_{SC} could be due to the fact that the thickness of insulating layer, although suppress back electrons, it also act as a physical barrier in the tunneling process. However, still the η ~5.2% of DSSCs employing a single shell of insulating oxides around a core of SnO_2 (Kay and Grätzel, 2002) is far lower than the TiO_2 mesoporous NPs based photoanode (14.3%). This brings into account a multi-shell architecture around a single core by Dong Z. et al.

A systematic increase in the number of SnO_2 shells, which enhanced the surface area from ~22 m^2/g in a single shell to ~38 m^2/g in quintuple shells (Dong et al., 2014). It also showed a direct effect on their PV performance; the η increased to 7.18% in quintuple shells from 5.21% in a conventional single shell architecture (all SnO_2 DSSCs WE were passivated with $TiCl_4$ aqueous solution). Although this work reported the highest η in SnO_2 based DSSCs so far, it requires further optimization to elevate the η closer to that of TiO_2 based devices.

2.6.2 Composite (Hybrid Photoanode)

In order to combine the desired features such as large surface area, favored band alignment and directed paths in a single photoanode, composite or hybrid nanostructures are widely employed. Such nanostructures are formed by combining SnO_2 with other MOS of high surface area and CB edge. Chen et al. reported ZnO Nanotetrapods -SnO_2 NPs composite with surface area ~109 m^2/g, notably higher than a pure SnO_2 NP analogue (98.7 m^2/g) and achieved improved η from ~2% to ~6.18%) (Chen et al., 2010b) and other PV parameters are tabulated in **Table 2.4**. In another report by Wang et al. SnO_2 NFs-NPs composites, which achieved η ~6.3%, a ~30% higher than a pure counterpart (~4.30%) (Wang et al., 2013b). Ito et al. also reported a record PV parameters using composite SnO_2 NPs-ZnO submicron particles with a FF ~0.71, a high V_{OC} ~721 mV and η ~6.34% (Ito et al., 2004). These reports suggest that composite WEs tremendously enhanced the PV parameters of DSSCs and can serve as a possible avenue to further enhance the η in SnO_2 DSSCs.

2.6.3 Doped Photoanode

Another way to improve the PV parameters in pure SnO_2 DSSCs, especially the low V_{OC} and FF, is to simply dope SnO_2 with other elements having similar ionic radii (Teh et al., 2013b, Dou et al., 2011, Li et al., 2012). Various transition metals such as Niobium (Nb^{5+} ~0.78 Å) Zinc (Zn^{2+}), Magnesium (Mg^{2+}), Gallium (Ga^{3+} ~0.76 Å), Tungsten (W^{4+}~0.74 Å), Titanium (Ti^{4+}, 0.75 Å) and Indium (In^{3+} ~0.76 Å) are doped in SnO_2 towards this end. Among these, Zn^{2+}, Ga^{3+} and Mg^{2+} showed outstanding

performance when doped with tin (Sn^{4+} ~0.69 Å) (Wali et al., 2015). Dou et al. reported ~20% doping of Zn in SnO_2 and achieved substantial increment in the V_{OC} (~0.78 V in doped and ~0.52 V in pure) (Dou et al., 2011). The Zn doping is expected of replacing some Sn atoms from its crystal structure, which resulted in an upward shift of the Fermi Level of the SnO_2 and consequently achieved a higher V_{OC}.

In a similar report Li et al. compared PV parameters of Zn-doped SnO_2 and pure SnO_2 based DSSCs. The pure SnO_2 photoanodes resulted in V_{OC} ~0.41 V, J_{SC} ~5.10 mA cm^{-2}, FF ~0.53 and η ~1.13%, whereas, doped analogues showed notable improvement (~0.59 V, ~9.22 mA cm^{-2}, ~0.74 and ~4.15%, respectively) (Li et al., 2012). It is revealed that Zn-doped SnO_2 photoanode provide better electron transport and slowed down the recombination with electrolyte, which resulted in improved FF and about 150% enhanced τ_n from ~5.3 ms to ~12.5 ms. Pang et al. reported >200% increment in η in Mg-doped SnO_2 compared to a pure SnO_2 device primarily owing to the increased J_{SC} from ~3 mA cm^{-2} to ~7 mA cm^{-2} (Pang et al., 2012). Teh et al. employed Gallium doped SnO_2 nano-cuboids as a photoanode in DSSCs and achieved a remarkable V_{OC} ~0.74 and FF ~74% without any further surface passivation of the WE (Teh et al., 2013b). The V_{OC} in Ga-doped SnO_2, which is similar to TiO_2, results from the suppression of charge recombination as evidenced by Mott-Schottky analysis in their work. The flat-band potentials consistently shifted upon Ga-doping (-0.34 and -0.81 V for 0 and 5% Ga precursor, respectively), which explains the origin of high V_{OC} and FF in their report.

2.7 CONCLUSIONS

In conclusion, photoanode is the crucial part of the DSSCs due to the fact that it is not only supported the sensitizers but also acts as an electron acceptor and conduct the photo-induced electrons. TiO_2 is the primarily employed photoanode material in the DSSCs owing to its high surface area (~150 m^2/g) and suitable conduction band alignment with the most successful Ruthenium based sensitizers however, it is characterized by a low μ_e (<1 cm^{-2} V^{-1} s^{-1}). On the other hand, SnO_2 offers high μ_e (~250 cm^{-2} V^{-1} s^{-1}) and wider bandgap (~3.6 eV) compared to that of TiO_2 however, it shows 3-4 times lower η ~4% compared to the latter η ~14.3%. In reality, SnO_2 typically results in ~300 mV lower V_{OC} and significantly inferior FF in its pure form than TiO_2 mainly owing to its lower lying conduction band edge (L A Harris and Wilson, 1978). In addition, SnO_2 also results in a lower specific surface area due to its lower IEP (at pH ~4-5) Vs. TiO_2 (at pH ~6-7) resulted in poor dye loading and consequently lower the photocurrent (Kay and Grätzel, 2002). Innovative approaches are required to combine the large surface area of TiO_2 and superior μ_e of SnO_2 in a single photoanode of the DSSCs. Efforts have been made to overcome these limitations by introducing SnO_2 composite nanostructures with other MOS of high CB and doping with suitable transition metals to uplift its Fermi energy level. Such efforts reported a comparable V_{OC} (~780 mV) and FF (~70%) to that of TiO_2 with a maximum η ~7-8% **(Table 2.4)**. Although the η is still lower than the best performing TiO_2 counterpart, recent developments in SnO_2 DSSCs made it the second highest η DSSCs and also paved a way for its further development.

CHAPTER 3

MATERIALS AND METHODS

3.1   INTRODUCTION

This chapter explains research methodology adopted in this study. Briefly, synthesis of SnO_2 NPs and one dimensional nanostructures such as porous nanofibers (PNFs) and multiporous nanofibers (MPNFs) via hydrothermal and electrospinning process, respectively, and also their composites with TiO_2 nanostructures in order to achieve the objectives accomplished during this study. Various techniques are used to study the characteristics of NPs, PNFs, and MPNFs such as XRD for the crystal structure analysis, gas adsorption studies for specific surface area, FESEM and TEM for surface morphology. In addition, procedures to fabricate the DSSCs from the various nano morphologies and details of optical, electrical, and EIS techniques to characterize them are also explained in detail.

3.2   RESEARCH METHODOLOGY

The flow chart of the research methodology is shown in the schematic 1. At first, suitable MOS materials and their desired morphologies were selected from the literature for the photoanode materials in DSSCs. The SnO_2 was selected as a WE material owing to its higher bandgap (~3.6 eV) and μ_e (~100-250 cm^2 V^{-1} s^{-1}). The SnO_2 NPs and multifunctional NPs-nanospheres (NPs-NSs) were the first desired

morphologies to yield high specific surface area and light harvesting properties, which were synthesized using hydrothermal method. The developed materials were employed as a photoanode material in DSSCs. Subsequently, 1D nanostructures (PNFs and MPNFs) were synthesized using electrospinning technique followed by their characterizations and testing as a WE material in DSSCs. Although the multifunctional (NPs-NSs) and MPNFs performed tremendously, the PV parameters still lower than the most employed photoanode TiO_2. To improve the PV performance of DSSCs made by these pure nano morphologies, the multifunctional (NPs-NSs) and MPNFs were post-treated so as to form TiO_2-SnO_2 composite. Finally, (SnO_2-TiO_2) NFs composite is formed by electrospinning to overcome the limitation of previously formed composites. The PV performance of these pure and composite nanomaterials as a WE material in DSSCs was investigated via their electrical, IPCE, OCVD and EIS characterizations.

Schematic 1

Flow chart of the research activities

Selection of material

Tin oxide was the choice for this study

Step1: Synthesis of NPs and multifunctional (NPs-NSs) by hydrothermal

Characterizations by XRD, BET, FESEM and TEM

Fabrication and data analysis of DSSCs

Step 2: Synthesis of PNFs and MPNFs developed by electrospinning process

Characterizations by XRD, BET, FESEM and TEM

Fabrication and data analysis of DSSCs

Step3: Compositing of multifunctional NPs-NSs and MPNFs with TiO_2 NP

Characterizations by XRD, BET, FESEM and TEM

Fabrication and data analysis of DSSCs

Step 4: Composite of (SnO_2-TiO_2) NFs by electrospinning

Characterizations by XRD, BET, FESEM and TEM

Fabrication and data analysis of DSSCs

Conclusions

45

3.3   SYNTHESIS OF TIN OXIDE NANOSTRUCTURES

In this study, two methods were adopted, viz. hydrothermal and electrospinning, in order to develop various SnO_2 nanostructures. The hydrothermal method was used to synthesize NPs and multifunctional (NPs-NSs) while the electrospinning techniques was employed to produce 1D (PNFs and MPNFs) nanostructures and nanocomposite.

3.3.1   Nanoparticle and Nanospheres Via Hydrothermal

High surface area SnO_2 NPs and multifunctional (NPs-NSs) were synthesized using hydrothermal process by optimizing the reaction temperature and pressure. A typical hydrothermal apparatus is shown in **Figure 3.1.** The crystal nucleation and growth occur in a "Teflon" container. The polymer required to have a higher melting point than the reaction temperature in order to avoid any impurity during the processing time.

The size and morphology of the nanostructures formed by this method depend on various parameters such as pressure inside the Teflon, operating temperature, precursor constituents and reaction time. Careful observation and precaution should be kept in mind during the experiment as follows: (i) the solution volume should not exceed 80% than the total volume of the Teflon in order to allow sufficient space for the liquid swelling during reaction time and (ii) the temperature of the reaction should be increased or decreased with a ramping rate of less than 5 ^{o}C/min to avoid any thermal shock. In our experiment, SnO_2 NPs and its multifunctional NPs-NSs were synthesized following a reported method (Wang et al., 2012) with modifications. However, the concentration of the growth solution was kept (16.5 mM) nearly one half than that reported before (32.7 mM) (Wang et al., 2012). In a typical procedure, $SnCl_2 . 2H_2O$ (0.25 g) was mixed with 1 N HCl (0.6 mL), ethanol (6 mL) and DI water (60 mL) and stirred in the sonication bath for an hour. The resultant transparent solution was transferred to an autoclave and kept at a pre-heated furnace at ~150 ^{o}C for ~24 h. After cooling to the room temperature, the solution was centrifuged, washed three times with DI water. After the cleaning process, the sample was dried in the oven at ~70 ^{o}C for overnight. This sample was labelled as "sample 150 ^{o}C". The same procedure was adopted for "sample 180 ^{o}C" and "sample 200 ^{o}C" with increase in the furnace temperature to ~180 ^{o}C and ~200 ^{o}C, respectively.
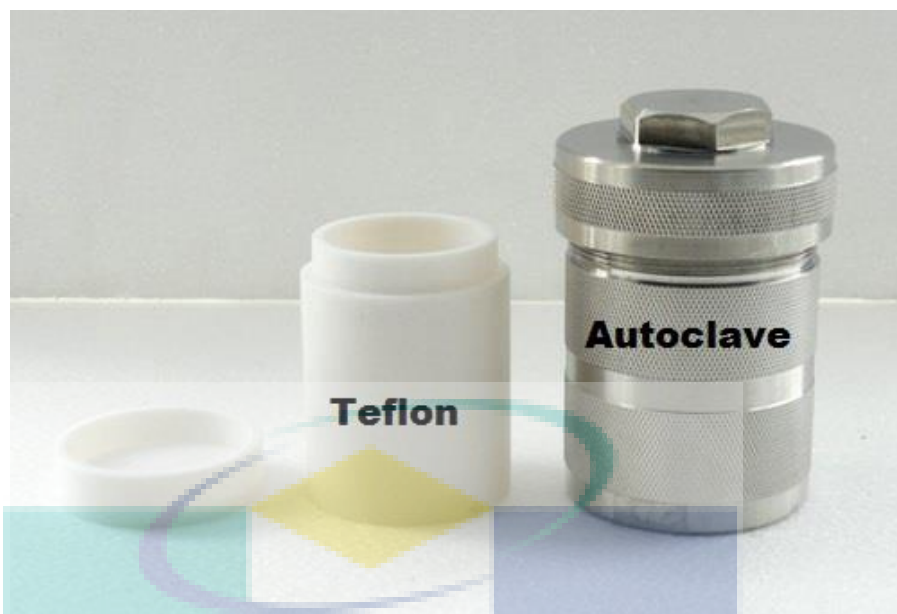
Figure 3.1: Hydrothermal apparatus.

3.3.2   One Dimensional Nanomaterials by Electrospinning

In the present electrospinning method, the starting materials were tin chloride pentahydrate (molecular formula: $SnCl_4.5H_2O$), polyvinylpyrrolidone (PVP) molecular weight = 1300 000, dimethylformamide (DMF) and ethanol; all these chemicals were purchased from Sigma Aldrich. In a typical procedure, 3g of PVP were dissolved in an equal volume ratio (1:1) of ethanol and DMF. To this solution, various concentrations of the tin precursor were dissolved at room temperature until the solution become clear. In brief, the concentrations were 5.5, 7, 8.5, 10, 11.5 mM and are labeled as C_o, C_1, C_2, C_3 and C_4, respectively. The resultant translucent solutions were then transferred to plastic syringe with a gauge (27 $G^{1/2}$) blunted steel needles and loaded to electrospinning. The operating parameters used for the formation of NFs are as follow: applied voltage ~25 kV, the distance between the tip of the needle and the metal collector ~20 cm, the injection flow rate ~0.6 mL h^{-1}, humidity of the chamber ~40-45% and the speed of the rotating metal collector ~1200 rpm. Solid NFs were then collected from the collector and annealed at the temperature ~600 °C for ~3 hours at the heating rate ~0.5 °C min^{-1}. Detail comparison of electrospinning parameters and annealing are listed in **Table 3.1**.

47
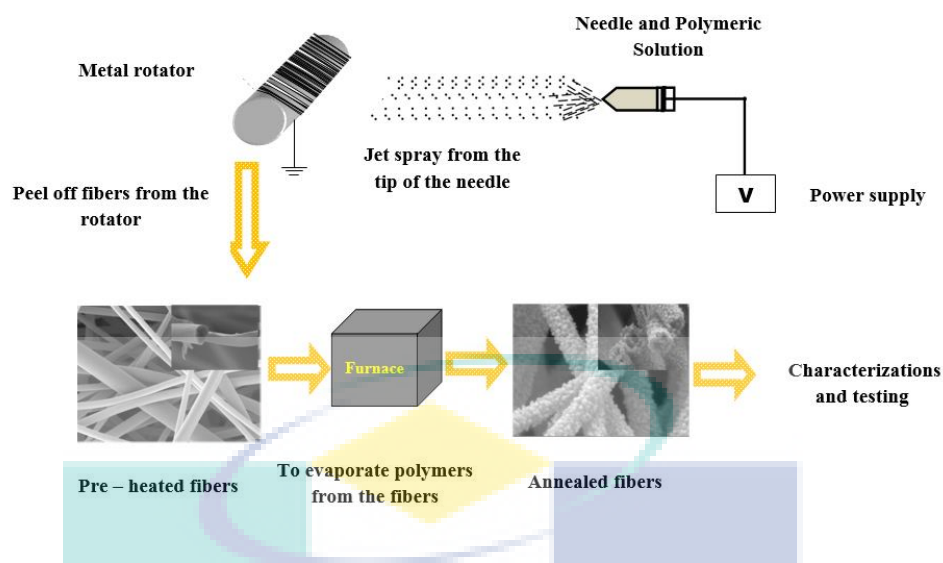
Figure 3.2: Schematic representation of electrospinning process with typical SEM images as-spun nanofibers and their transformation to annealed fibers.

Table 3.1
Operational parameters of electrospinning for synthesis of nanofibers

Sample	Concentration ($SnCl_4$)	Voltage (KV)	Injection (mLh^{-1})	Annealing temp (ºC)	Heating rate (Cº/min)
C_0	5.5 mM	25	0.6	600	0.5
C_1	7.0 mM	25	0.6	600	0.5
C_2	8.5 mM	25	0.6	600	0.5
C_3	10 mM	25	0.6	600	0.5
C_4	11.5 mM	25	0.6	600	0.5

A schematic sketch was drawn of the five types of fibres achieved using electrospinning process. Mainly the formation of these fibres involved three basic steps. Firstly, the prepared polymeric solutions were loaded to electrospinning machine. Secondly, the formed solid fibres were peeled off from the electrospinning collector. Finally, the peeled off fibres were calcined in the furnace at a particular temperature (~600 $^{\circ}$C), which transformed into five different morphologies as shown in the schematic 3.1.
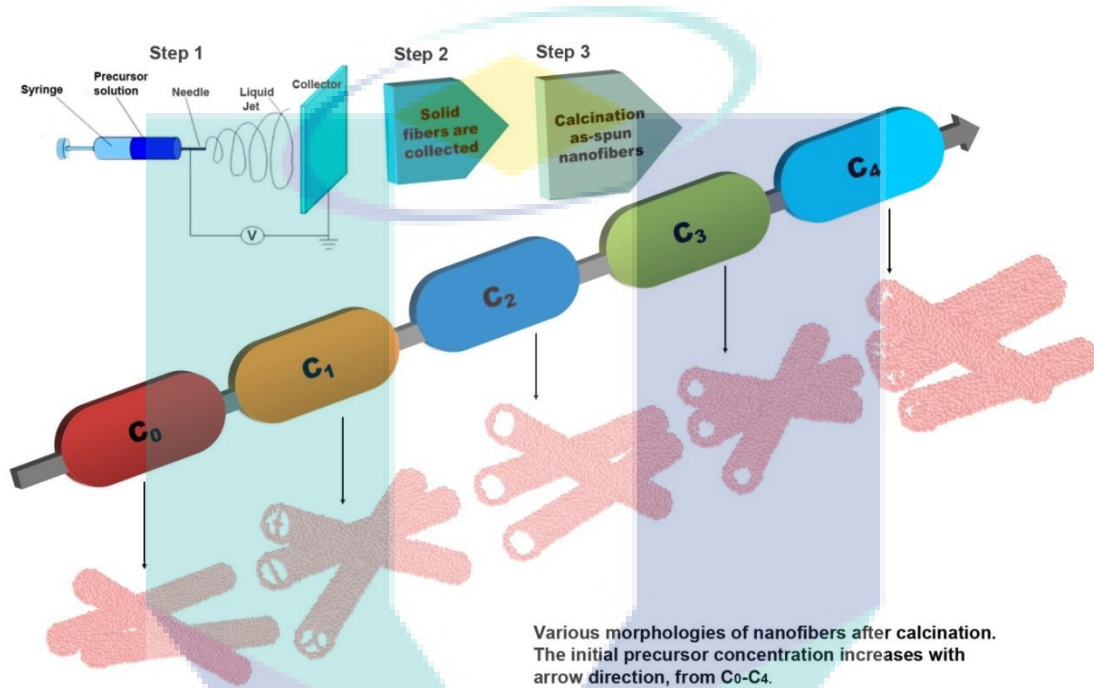
Schematic 3.1: Schematic illustration of the formation of five different morphological nanostructures (C_o-C_4) using electrospinning process.

The diameter distribution and particles size of the synthesized electrospun NFs were measured using Image J software the

3.4   CHARACTERIZATION OF SYNTHESIZED NANOMATERIALS

The materials synthesized were characterized using XRD, gas adsorption measurement BET, FESEM and TEM chemical structure, surface area, and morphology, respectively.

3.4.1   X-rays Diffraction Analysis

Crystal structure and phase of the synthesized nanostructures were examined by (Rigaku Miniflex II X-ray diffractometer employing Cu Kα radiation, λ ~1.5 Å).The XRD is a useful tool to characterize solid crystalline materials, metals, ceramics, minerals and inorganic compounds (Rudman, 1967). It is a nondestructive and rapid technique to find the crystal structure, phase identification, strain, average crystallite size, and even a unit cell dimension and atomic spacing of the crystal structure (McCusker and Baerlocher, 2013). In XRD, high intensity rays are used to determine and find the property of the structure. The wavelength (λ) of the X-rays lies in the range of ~0.0-10 nm of the electromagnetic radiation which include most of the crystals lattice spacing. In brief, monochromatic X-rays hit the target material and interference occur between the scattered radiation, the diffraction condition is explained by Bragg's relation nλ = 2dsinθ. This law simply relates the X-rays 'λ' with scattering angle (θ) and lattice atomic spacing (d) of the crystalline sample. The resulted intensity is plotted versus Bragg angle (2θ). The crystallite size (D) can be calculated using peak width of the intensity plot by Scherrer's **Eq. (3.1)** as follows (Ahn et al., 2004).

$$D = \frac{\kappa\lambda}{B\cos\theta_B} \tag{3.1}$$

In the above **Eq. (3.1)**, λ is the X-ray's wavelength, B is the full width at half maximum (FWHM) of the diffraction peak of XRD pattern, θ_B is the diffraction angle and κ is the Scherer's constant usually taken in the order of (~0.89-1) for a typical crystal. In the XRD measurement the samples were prepared in the powder form and for the substrates (coated

FTOs), the samples were developed in size of (1 cm × 1 cm). The XRD peaks were indexed by comparing with the standard diffraction pattern reported in the powder diffraction cards.

3.4.2 Gas Adsorption Study

Gas adsorption technique was used to investigate the specific surface area (unit: m^2/g) along with pores size and volume of the synthesized nanostructures. The BET surface area analyzers gas adsorption method is the most extensively used standard procedure to determine surface area of the porous materials such as industrial adsorbents, building materials, ceramics, pigments, and catalysts (Brunauer et al., 1940, Brunauer et al., 1938, Sing, 1985). This technique works on the basis of gas adsorption and desorption phenomena on the surface of the porous solid materials. Mostly Argon, carbon dioxide and nitrogen gases are used as an adsorbates to determine the surface area of the solid sample (adsorbent) at absolute temperature (77 K). The BET analysis assumes that adsorption occurs by multilayer formation and that the number of adsorbed layers is infinite at the saturation pressure. In multilayer adsorption, the adsorption space accommodates more than one layer of molecules so that all adsorbed molecules are not in direct contact with the surface layer of the adsorbent. On the other hand, in monolayer adsorption all the adsorbed molecules are in contact with the surface layer of the adsorbent such as Langmuir adsorption.

According to the International Union of Pure and Applied Chemistry (IUPAC), the adsorption isotherms are divided into six types as shown in **Figure 3.3** (Sing, 1985). Type I is the well-known reversible Langmuir adsorption isotherm characterizes by microporous adsorbent and could occur when the adsorbent is monolayer showing sharp rise at initial portion concave to the P/P_o axis. The reversible type II isotherm is the normal form of isotherm obtained with a non-porous or macroporous adsorbent and it isotherm composed of monolayer and multilayer adsorption. For instance, point B (**Figure 3.3**) indicates the stage at which monolayer coverage is complete and multilayer adsorption is seems to start. The reversible type III isotherm is entirely convex to the P/P_o axis over the entire range and therefore it does not show monolayer adsorption (i.e., point B). Type IV isotherm is characterized by its hysteresis loop, which is associated with capillary

condensation taking place in mesopores, and its inferior uptake at the high range P/P_o. Moreover, the initial part of the Type IV isotherm shows monolayer-multilayer adsorption since it exhibits the same pattern as the corresponding portion of the Type II isotherm. Type V isotherm is uncommon where the adsorbent-adsorbate shows weak interaction however, it can be obtained with certain porous adsorbents. In addition, it shows the similar behavior to the Type III isotherm. Furthermore, the Type IV and V behavior are commonly associated with hysteresis, thereby the isotherms are not reproducible on desorption i.e., the desorption path lying higher than the adsorption path. Besides, desorption path rejoins the adsorption path at some lower relative pressure, and an open loop in which measurable amount of a material is irreversibly adsorbed. The closed loop is commonly associated with porous materials. Finally, Type VI isotherm represents stepwise multilayer adsorption on a uniform non-porous surface in which the sharpness of the steps depends on the system and the temperature (Dollimore et al., 1976, Sing, 1985). Generally, the following **Eq. (3.2)** describes adsorption isotherm (Do et al., 2010)

$$\frac{P/P_o}{V(1-P/P_o)} = \frac{1}{V_m C} + \frac{C-1}{CV_m}(P/P_o) \tag{3.2}$$

where V is the adsorbed volume at pressure P and absolute temperature T~77 K; Po is the vapor pressure of a gas temperature T; V_m is the adsorbed gas volume, when the adsorbent surface is covered with a unimolecular layer and is termed the monolayer, C is the constant which is related to the heat adsorption.

Few precautions need to be kept in mind while doing BET analysis. For instance, (i) temperature of N_2 must be monitored (i.e., ~77 K), (ii) N_2 employed as adsorption must be 99.9% pure, (iii) level of the liquid N_2 in the cryostat bath must be kept constant, preferably using an automatic device, and (iv) sample bulb must be immersed to a depth ~5 cm below the liquid N_2 surface.

In the present study, micromeritics ASAP 2020 surface area porosity analyzer was used to determine the specific surface area and pore size distribution of the synthesized SnO_2 nanostructures. Initially blank tube and stopper were weighted (= $x \times$ g) and then

poured appropriate weight of samples into sample tube assy. Next, the sample and tube assy was weighted before degas (= $y \times$ g) followed by degassing the sample tube at ~120 °C for 6 hours. After degassing, weighted the sample and tube assy denoted (= $z \times$ g) with the final weight of the sample after degas (z-x) g. Finally, the degassed samples were run for 4 hours and the BET results was achieved.
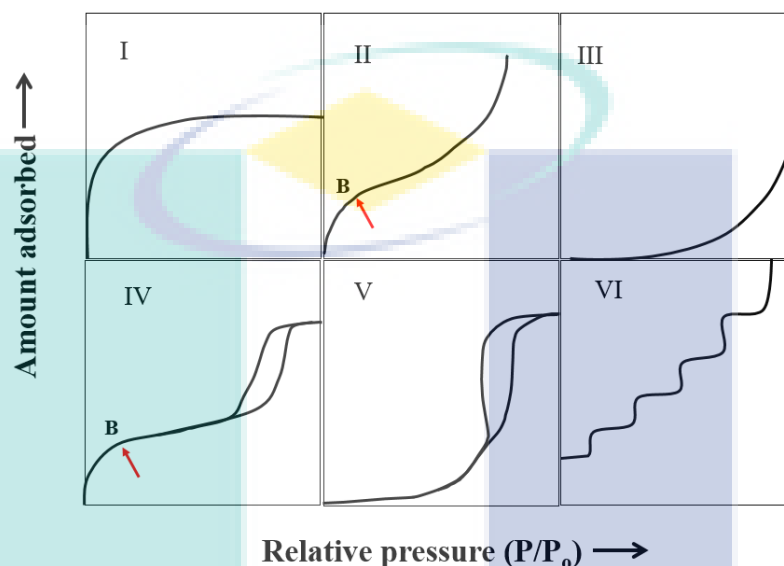
Figure 3.3: Representation of six types of BET gas adsorption isotherms.

Source: Reproduced from (Sing, 1985)

3.4.3 Field Emission Scanning Electron Microscopy Analysis

Surface morphology of the synthesized nanostructures and the photoanode films were investigated by FESEM (JEOL JSM-7600F, USA). It is a vital characterization tool designed to probe the surface of a solid material at the nanoscale range and to measure the elemental investigation of the nanostructures. It offers significantly higher resolution than an optical and electron microscope, and a large depth of focus (Inada et al., 2009). The highly energetic electrons liberated from the source surface and accelerated in a high electric field gradient passes through the electronic lenses. These electronic lenses then focus a narrow energetic electron beam, which excites the target object. After striking the object specimen, secondary electrons are emitted from the target and are detected by a detector to construct an image.

To investigate the surface morphology and roughness of the synthesized (NPs and NFs), the samples were prepared in powder form, while for the photoanodes film, cross-section was prepared using a glass cutter. An extreme care is required during breaking a coated FTO in order to avoid any physical contact with the exposed thin film area. Afterward, the samples were then coated with an enormously thin layer of platinum by sputtering technique to make them conducting and to avoid any possible charging effect during FESEM analysis. The samples were then loaded into the measurement chamber of the FESEM and were examined at a high voltage of about 3-10 kV

3.4.4   Transmission Electrons Microscope

Although FESEM analysis gave sufficient information about the surface morphology of synthesized nanostructures, a more detailed analysis is required to investigate the lattice images, grain size, grain boundaries, and electron diffraction pattern using TEM technique (Kawamoto et al., 2013, Eyre, 1973). The TEM analysis was employed to study the morphology, elemental composition and crystallographic information of the SnO_2 nanostructures in detail. It operates at a much higher voltage (60 -300 kV) than a FESEM (3-10 kV) and static broad beam of electrons with resolution of ~0.2 nm. Moreover, in TEM analysis, an extremely thin specimen is required in order that electrons could easily penetrate and transmit through the specimen.

High resolution TEM (HRTEM) images are formed owing to the phase contrast process. The HRTEM uses both the transmitted and the scattered beams in order to create an interference image. It has been widely and successfully employed tool for analyzing crystal structures and lattice imperfections in various kind of materials on an atomic resolution scale. In addition, it also gives information about the point defects, stacking faults, dislocations, and grain boundaries. Selected area electron diffraction (SAED) provides the crystallographic information about a material from a specific minute volume, unlike XRD which is a bulk analysis characterization. It can shows effectively that the selected materials are amorphous, crystalline or polycrystalline. Furthermore, it gives information about lattice parameter, unit cell details, and any periodicity exist in the materials.

In this experiment, JEOL JEM-ARM300F Transmission Electron Microscope was employed to study the surface features of the SnO_2 nanostructures. For the TEM analysis, samples were used in powder, sonicated in an ultrasonic bath for an hour then investigated under 200 kV operating voltage.

3.5   GENERAL TERMS OF PHOTOVOLTAICS

The cell performance depends on several factors, including J_{SC}, V_{OC}, and FF. All these parameters are illustrated in **Figure 3.4**, which shows a forward bias I-V characteristic curve under standard condition (AM 1.5 G, intensity ~1000 W m^{-2}). In this section, various common terms are explained while analyzing the performance of a solar cell.

Short circuit current density (J_{SC}): The J_{SC} shows the measurement of photocurrent when the photovoltage across the DSSC is zero. It depends on various factors such as number of adsorbed dye molecules on the MOS, light absorption and harvesting capability of the dyes, light intensity, number of photons, charge diffusion, electron injection from the excited dye LUMO to the CB of MOS, and collection of the photo-induced electrons (Ma et al., 2014, Calogero et al., 2015, Haid et al., 2012, Jose et al., 2009). In addition, J_{SC} also strongly depends on the film thickness and morphology used in the photoanode. The factors that affect the J_{SC} includes, the internal resistance of MOS/electrolyte and MOS/MOS interfaces, respectively (Hoshikawa et al., 2005).

Open circuit voltage (V_{OC}): The V_{OC} is the difference between the Fermi level of MOS under illumination and electrochemical potential of an electrolyte when the I_{SC} is zero in the circuit. It is well known that the V_{OC} is increasing with the increase of the energy band gap of MOS due to a positive shift in Fermi level. By neglecting the resistances (R_S and R_{SH}) in **Eq. (3.3- 3.5)** as follows

$$I = I_{ph} - I_d - I_{R_{Sh}}$$
(3.3)

$$I = I_{ph} - I_o \left(e^{\frac{q(V+IR_s)}{\alpha kT}} - 1 \right) - \left(\frac{V + IR_s}{R_{sh}} \right) \tag{3.4}$$

$$I = I_{ph} - I_o \left(e^{\frac{qV}{\alpha kT}} - 1 \right) \tag{3.5}$$

Under open circuit condition, $I = I_{SC} = 0$ and $V = V_{OC}$ by **Eq. (3.6 & 3.7)**

$$\text{So } I_{ph} = I_o \left(e^{\frac{qV_{OC}}{\alpha kT}} - 1 \right) \tag{3.6}$$

$$V_{OC} = \frac{\alpha kT}{q} \ln \left(\frac{I_{ph}}{I_o} - 1 \right) \tag{3.7}$$

V_{OC} depends on the temperature with high negative temperature coefficient. It also depends on the quality of the material because of the saturation dark current I_o and slightly increase with the solar irradiance level.

Fill factor (FF): The FF generally represents the squareness of the IV curve in the DSSC. For an ideal device, it is equal to an unity (100%), a completely rectangle (Qi and Wang, 2013) as can be seen from the green rectangle with a theoretical power (P_{th}), while the maximum achievable power (P_{max}) is the product of maximum voltage (V_{max}) and maximum cell current (I_{max}) presents in the white rectangle or square as shown in **Figure 3.4**. The FF can be strongly affected by the large active area of the photoanode, series ohmic conductive sheet resistance, internal resistances at FTO/MOS interface and at Pt/FTO interface (Hoshikawa et al., 2005, Han et al., 2005), which leads to low collection efficiency at the WE. It also depends on the R_S and R_{SH} values where low R_S value and high R_{SH} could lead to a better FF . The general formula of the FF is given by **Eq. (3.8 & 3.9)** (Gray, 2011)

$$FF = \frac{P_{max}}{P_{th}} \tag{3.8}$$

Where $P_{max} = I_{max} \times V_{max}$ and $P_{th} = I_{SC} \times V_{OC}$

So

$$FF = \frac{I_{max} \times V_{max}}{I_{SC} \times V_{OC}}$$

(3.9)
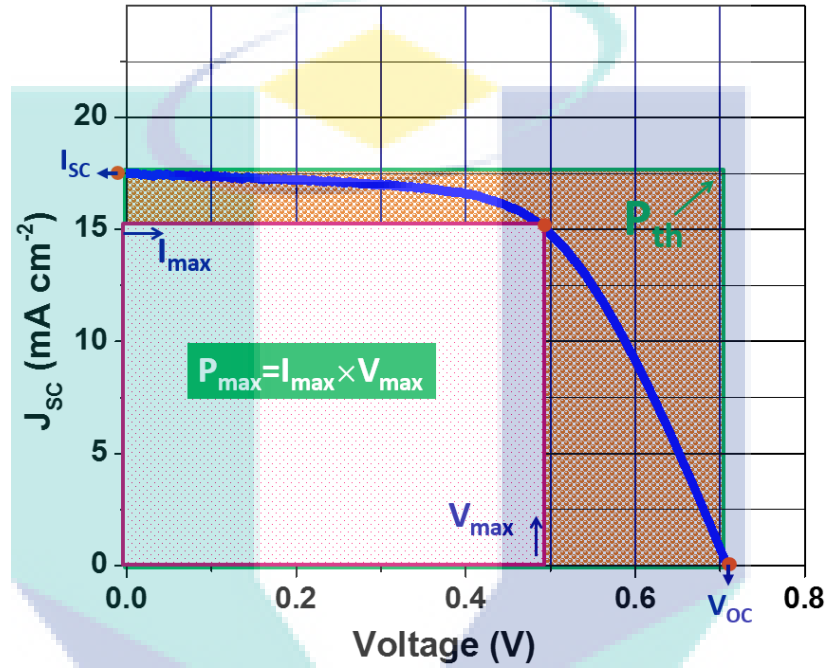
Figure 3.4: Schematic representation of the maximum power obtained in DSSCs characterization and the theoretical or ideal power achievable.

Source: (Qi and Wang, 2013)

Power conversion efficiency (η): The η of DSSCs is the ratio of the P_{max} of the cell to the power of the incident light ($P_{inc} \sim 1000$ W m^{-2}) as represented by **Eq. (3.10 & 3.11)** (Gray, 2011, Ondersma and Hamann, 2013).

$$\eta = \frac{P_{max}}{P_{inc}}$$

(3.10)

where $P_{max} = FF \times J_{SC} \times V_{OC}$ therefore, η is given by

57

$$\eta = \frac{FF \times J_{SC} \times V_{OC}}{P_{inc}} \tag{3.11}$$

Quantum efficiency (QE): The QE is one of the important DSSCs characterization parameters. It provide a ratio between incident light (number of incident photons) to number of electrons collected at WE. If the energy of the incident photon less than the band gap of the WE material, no electron generation occurs resulting in zero QE. Ideally, the curve for QE has a rectangular or square shape, if all the photons absorbed by a solar cells. However, most of the solar cells result in a reduced QE owing to the recombination where charges carriers are incapable to move to the external circuit. The QE is given as a function of either wavelength or energy of the incident light. Generally, two types of QE are considered in solar cells characterizations i.e., External QE (which also called IPCE is explained in the next section) and Internal QE.

Internal QE: It is also termed as absorbed photon to converted electrons (APCE) defined as the ratio of the number of collected charge carriers to the number of photons absorbed by an active area. In other words, the product of η_{inj} and η_{cc} represent APCE or IQE. The IQE contains the information about the fundamental efficiency of exciton dissociation, charge transfer, collection and extraction process (Armin et al., 2014).

Air mass: Any solar cell performance is strongly influenced by the power and intensity of the solar irradiation striking it. The solar power and intensity significantly varying with location on the earth and outer space owing to the length of the light path traverse through the atmosphere (Bird et al., 1983). Therefore, to facilitate an accurate measurement of solar cells a standard solar spectrum and power density have been defined for the measurement on the planet or outer space station. The ratio of any actual path to the shortest path traverse by the sunlight is known as air mass. The radiant solar power per unit area normal to the direction of the sunlight outside the earth atmospheres remains constant refer to air mass zero (AM0) radiation. The Light attenuation is variable when passing through different thickness of the atmosphere and the shortest distance when it is overhead refers as optical air mass unity and the radiation describe as air mass one (AM1). When the sun is at overhead emits light through the atmosphere with path length (L_o) at a zenith angle ($\theta_Z = 0$) refer as AM1. When the sun start moving from the top of the

observer making some angle about 48.2º having length (L) considered standard for measuring the solar cells measuring on the earth surface refer AM 1.5 as shown in the **Figure 3.5** and **Eq. (3.12)**. This standard spectrum refers as AM 1.5 G where 1.5 shows the variation of the angle of sunlight and G represent global when it is in vertical position passing through the atmosphere (Emery, 2005).
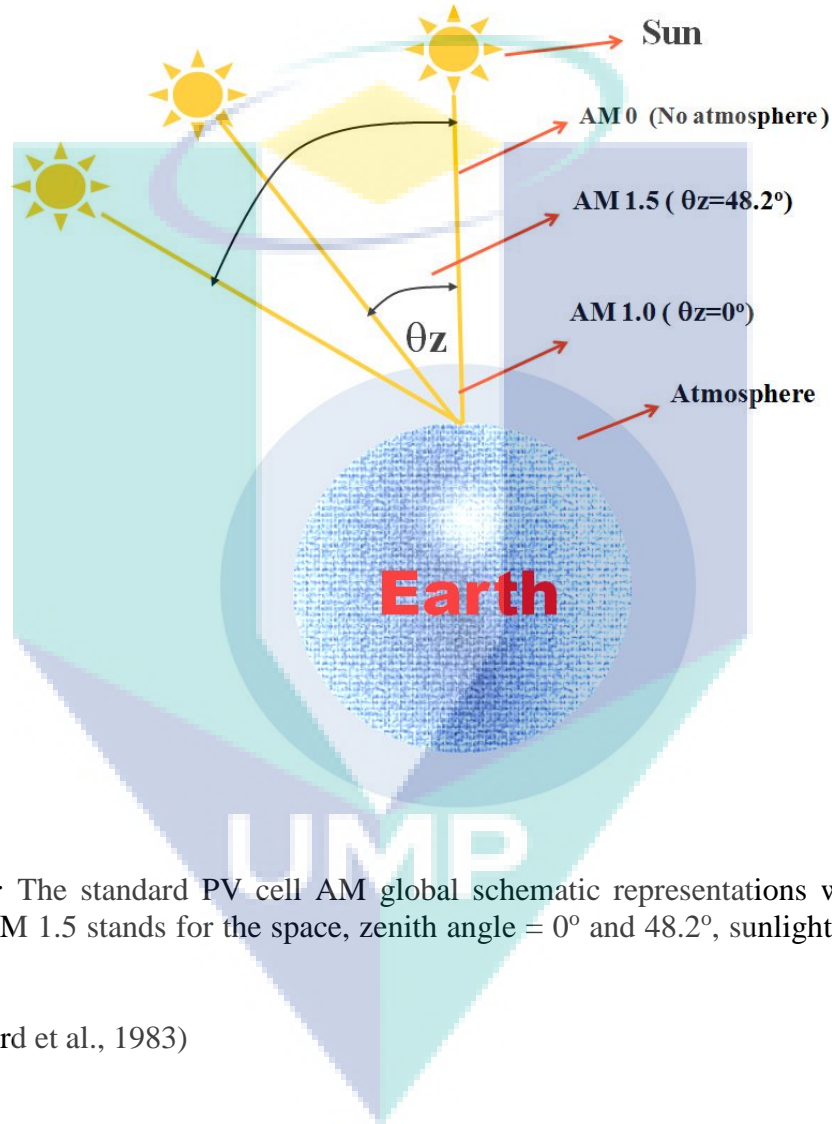
Figure 3.5: The standard PV cell AM global schematic representations where AM0, AM1and AM 1.5 stands for the space, zenith angle = 0º and 48.2º, sunlight striking the earth.

Source: (Bird et al., 1983)

$$Air\ Mass = \frac{Optical\ path\ length\ at\ the\ agnle\ \theta_z}{Optical\ path\ length\ at\ the\ angle\ \theta_z = 0}$$

$$Air\ mass = AM = \frac{L}{L_o} \qquad or$$

$$\text{Air mass} = AM = \frac{1}{Cos\theta_Z} = Sec\theta_Z \tag{3.12}$$

$\theta_Z = 48.2^o$ for AM1.5 G and $\theta_Z = 60^o$ for AM2 with the estimated calculated power intensity of the spectrum 1000 W m^{-2}

3.6   DSSCS FABRICATION AND TESTING

Various steps are required to fabricate DSSC which are explained in the following section. For the testing and measuring of DSSC, UV-VIS-NIR spectroscopy was employed to study the electrodes scattering, light harvesting, and dye loading properties. The current voltage curves were recorded by a potentiostat (Auto lab PGSTAT30, Eco Chemie B.V).

3.6.1   Fabrication Steps of DSSCs

Paste preparation

A standard procedure is adopted to form a printable paste of SnO$_2$ synthesized nanostructure (Yu et al., 2012, Wang et al., 2003a). A sufficient amount (~300 mg each) of SnO$_2$ NPs and multifunctional (NPs-NSs) were dispersed in absolute ethanol followed by stirring in ultrasonic bath to make it a homogenous solution. Pre calculated amount of α-terpinol (α: T, 18 *wt.* %) and ethyl cellulose (E.C, 10 *wt.* %) were added to each solution. The paste making ratio was (SnO$_2$: α-T: E.C, 1: 4.05: 0.5, respectively, measured in mg unit). The above solutions were kept in the sonication bath for an hour in order to mix the ingredients and finally heated on the hot plate at ~70 ^{o}C to evaporate ethanol until a thick slurry was formed. Similar procedure was employed for PNFs, MPNFs, and (SnO$_2$-TiO$_2$) composite fibres paste.

Substrate cleaning and hole blocking layer

Pre-cleaning of substrates (FTOs) is crucial in order to remove any organic impurity on the surface of the FTOs, which may lower the performance of the device. The FTO substrates were pre-cleaned sequentially by distilled water, ethanol and acetone in an ultrasonic bath for 15 min each. The substrates were coated with a dense thin hole blocking layer via a 40 mM aqueous $TiCl_4$ solution treatment (Nazeeruddin et al., 1993, Ito et al., 2006, Ito et al., 2007). The solution was made by adding $TiCl_4$ in distilled water at ~0 ^{o}C and then stirring vigorously for 15 min. The pre-cleaned substrates were immersed in the $TiCl_4$ solution and kept at ~70 ^{o}C in the oven for 30 min to form a dense blocking layer. The $TiCl_4$ treated FTOs were then sintered in the furnace at an optimized ramping program at ~450 ^{o}C for 30 min. The ramping program was as follows: 2 ^{o}C/min until 250 ^{o}C and stay of 10 min followed by 5 ^{o}C/min until 450 ^{o}C and stay of 30 min. Thickness of the films measured from the FESEM images were 17 ± 0.5 µm using FESEM analysis. The fabrication of DSSCs was carried out in the following steps (Ito et al., 2007):

i. Identifying the conducting side of the FTO using multimeter.
ii. Masking the conducting side of the FTO with a scotch tape on the edges in order to pattern the photoanode film.
iii. Applying the synthesized paste on the top of the FTO between the two strips of the scotch tape via a doctor blade to obtain a homogenous layer.
iv. Sintering the thin film coated FTO in the furnace or on the hot plate at the temperature of ~450 ^{o}C for 30 min.
v. Immersing the sintered WE in the dye solution (usually 0.3 mM in ethanol) for 12 h and subsequently rinsing with an ethanol to remove unanchored dye.
vi. Sputtering a thin Pt or other noble metals layer on the FTO to make a CE.
vii. Sandwich the WE and CE together with a ~60 mm thick insulating spacer between them and use clips to hold the two electrodes together.
viii. Filling the gap between the two electrodes with an electrolyte via capillary action or vacuum back filling (for the permanently sealed devices).
ix. Applying a dark mask on the device to define active area and measuring the electrical output of the device.

3.6.2 Spectroscopy Analysis

Absorption properties of the DSSCs are crucial as it yields information about the optical properties such as absorption window and absorption coefficient in these devices. In DSSCs, absorption spectra gives information about the dye-loading, which determine the amount of photocurrent. Generally, UV-VIS-NIR refers to the attenuation of the light spectrum during absorption, reflection or even transmission through the sample. It uses UV (~200-400 nm), VIS (~400-800 nm), and NIR (~750 nm to ~2500 nm) ranges of the electromagnetic spectrum (Schoonheydt, 2010). The source of UV and visible light are usually Deuterium and Tungsten. The UV-VIS-NIR characterization is usually used for liquid solutions, however; solid electrodes and gases are also can be studied (Szalai et al., 2013). The absorption spectrum arises due to the transition of electrons within the molecule from the lower state to the higher states inside the atom using Planck quantum relation

$$E_f - E_i = E_g = hf$$

$$\text{Where } f = \frac{c}{\lambda}$$

$$E_g = \frac{hc}{\lambda}$$

where E_g is the optical band gap, f is the frequency of light , h is the Planck constant, λ is the wavelength of light used, and c is light speed in vacuum.

Light of initial intensity (I_o) passes through the sample of thickness (l) with an intensity (I). The absorbance of light depends on the number of molecule presents in the sample, for instance, concentrated solution has a high absorbance, while diluted one can result in a weak absorbance using a relation $I/I_o = e^{-\alpha l}$. The absorbance of the solution and also the dye loading in our DSSCs are calculated by a relation $A = \varepsilon c l$ where I/I_o is the fraction of the light that remains after passing through the film thickness (l). In the present experiments, absorption spectra of the dye-anchored electrodes and desorbed dye solutions were studied using UV-VIS-NIR spectrophotometer (UV-2600 of Shimadzu with integrated sphere 2600 plus). The dye loading of the anchored photoanodes was

measured by desorption test. The anchored dye was desorbed by immersing it in 0.5 M NaOH solution (1:1, ethanol/DI water) (Nazeeruddin et al., 1993) and then the absorption spectrum of the solution was recorded using a UV-VIS-NIR spectrophotometer. The molar absorption coefficient (ε) of the N3 dye used $1.41 \times 10^4\,\mathrm{Lmol^{-1}\,cm^{-1}}$. Dye loading was measured using desorption test by following **Eq. (3.13)** (Wang et al., 2013a, Yu et al., 2012)

$$\text{Dye loading} = \frac{C \times V}{S} \qquad (3.13)$$

In the above relation, 'V' is the volume of the dye solution, 'S' is the active area of the electrode and 'C' is the concentration of dye which could be find from **Eq. (3.14)**

$$C = \frac{A}{\varepsilon \times l} \qquad (3.14)$$

where A, ε, and l is the absorbance, extinction co-efficient of the dye anchored, and length of the optical path travelled through the cuvette, respectively. In the desorption test the active area was kept (~0.12-0.14 cm^2), volume of the solution (~3-4 mL) and thickness of the cuvette was (1 cm).

3.6.3 Current-Voltage Measurement

Photocurrent (J_{SC})-photovoltage (V_{OC}) measurements were performed using a solar simulator (SOLAR LIGHT, Model 16-S 150) employing single port simulator with power supply (XPS 400) at AM1.5G condition (1000 W m^{-2} & 25 ^{o}C). The J-V curves were measured by a potentiostat (Auto lab PGSTAT30, Eco Chemie B.V). The power of the solar simulator was calibrated to 1000 W m^{-2} via a reference Si cell in order to reduce the possible mismatch between the simulated light and AM 1.5 G in a visible region to <5% and linear sweep voltametery (LSV) was employed as a measurement method. In LSV, a fixed potential range is employed at the WE from a lower limit to upper limit and the response (current) is measured as a function of voltage. The voltage step was 20 mV

and the delay time was kept 50 ms for all the measurements. The photocurrent (J)-photovoltage (V) measurement is an important characterization technique in DSSCs as it provides information about the cell parameters such as V_{OC}, J_{SC}, FF and η (**Figure 3.6**). The shape of the J-V curve clearly reveals the performance of the device at any given illumination condition. The characteristics J-V curve of DSSCs largely depends on accuracy and precision during device fabrication, intrinsic properties of the material, and various interfacial processes within the device.
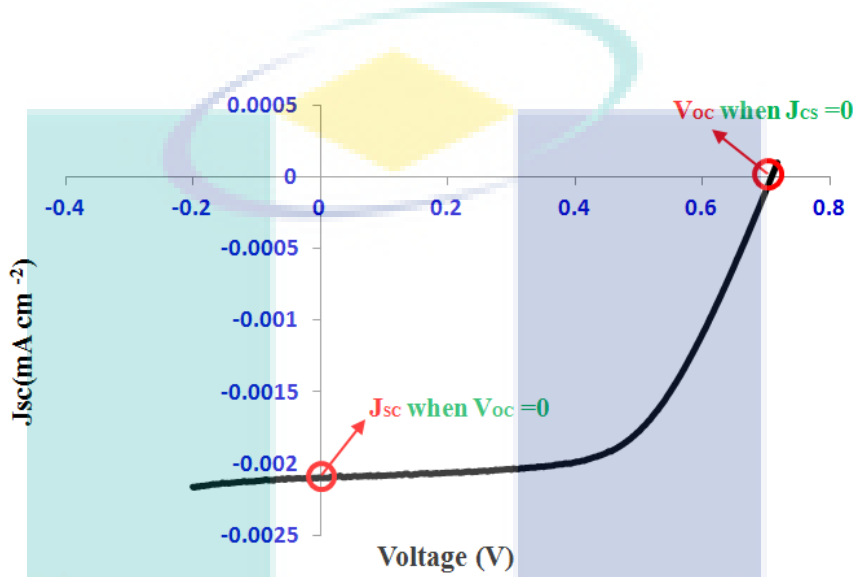
Figure 3.6: A typical IV curve of DSSCs, where J_{SC} and V_{OC} are clearly shown at open and short circuit condition.

Source: Reproduced from (Qi and Wang, 2013, Gray, 2011)

An equivalent model circuit of a DSSC or any PV cell in general can be represented as in **Figure 3.7** (Qi and Wang, 2013, Zekry and Eldallal, 1988, Gray, 2011, Ferber et al., 1998). The basic components of this model are (i) a diode which generates current $I_d = [I_o \, exp \, (qV/\alpha RT)]$, (ii) current due to illuminating of light photons (I_{ph}), (iii) a series resistance (R_s), and (iv) shunt resistance (R_{sh}). The R_s arises from the various sources such as the contact resistance between the MOS layer and FTO, the resistance inside the MOS layer, ohmic losses in the front surface of the cell, impurity concentrations and junction depth. It is considered an important parameter because it affects both the J_{SC} and the maximum power output of the device. For an ideal PV cell, R_s should be zero ($R_s = 0$) while the R_{sh} at infinity ($R_{sh} = \infty$). Generally, **Eq. (3.3 & 3.4)** of the equivalent circuit

model, where I_o represent saturation dark current of the diode at temperature T, I_d is the diode current and I_{Rsh} is the leakage current through a resistor R_{sh}. Under short circuit condition, i.e., when R_s is very small then **Eq. (3.3)** is written as $I = I_{sc} = I_{ph}$ which depends on many factors such as light spectrum, sun irradiance level, area of the solar cells and characteristics of the WE materials.
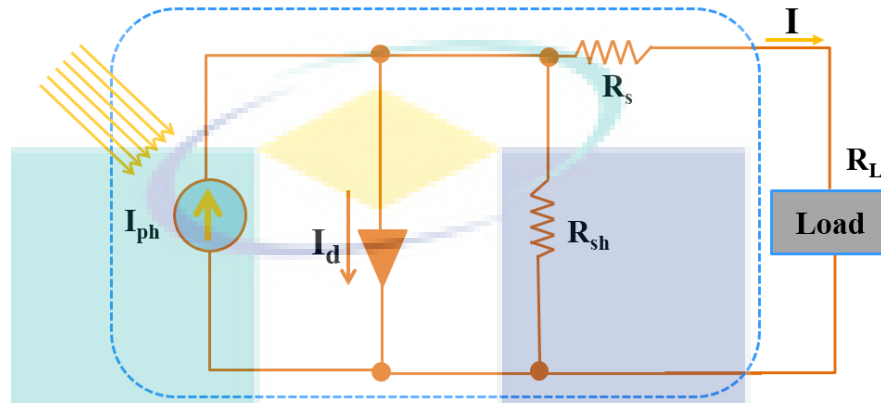
Figure 3.7: An equivalent circuit for a typical solar cell where I_{ph} is the generated current by photons, I_d is the diode current while, R_s and R_{sh} is the series and shunt resistance.

Source: Reproduced from (Qi and Wang, 2013, Zekry and Eldallal, 1988, Gray, 2011, Ferber et al., 1998)

3.6.4 Electrochemical Impedance Spectroscopy

Electrochemical impedance spectroscopy (EIS) analysis has been employed to explore various (electron and ionic) processes taking place in different layers and at their interfaces of the DSSC (Wang et al., 2005, Hoshikawa et al., 2005, Wang et al., 2006, Pitarch et al., 2004). Generally, the word impedance refers to the frequency dependent resistance or in other words, the total opposition (in term of resistor, capacitor and inductor) offer in the circuit to the current flow. Impedance is a complex quantity, which depends on the system as a function of the frequency, which is obtained by varying the frequency of the applied signal.

A theoretical model has been designed to interpret the frequency response of the DSSC as shown in the **Figure 3.8** (Pitarch et al., 2004, Bisquert, 2002, Jose et al., 2009).

Usually, the EIS data consist of a Nyquist plot and two bode phase plots. In the Nyquist plot, three typical frequency peaks are observed, which corresponds to the specific response inside the DSSC. The high-frequency (k Hz range) reflects the charge transfer at the platinized CE, while the response in the intermediate-frequency region (10-100 Hz range) is attributed to the electron transport in the MOS film and the back reaction (sometime also called recombination resistance) at the MOS/electrolyte interface. The low-frequency region (<1 Hz range) attributes to the diffusion in the electrolyte (Kern et al., 2002, Wang et al., 2005, Hoshikawa et al., 2005). In the transmission line (**Figure 3.8**), there are two parallel channels, showing electron transport via MOS and diffusion of redox species through the electrolyte in the pores, respectively. Moreover, various mechanisms take place inside the DSSC as depicts in **Figure 3.8** i.e., (i) electron transfer at the FTO/MOS interface, (ii) electron diffusion through MOS and the charge recombination resistance at the dye anchored MOS/electrolyte interface, (iii) diffusion of iodide/triodide ions present in the electrolyte, and (iv) charge transfer at the Pt coated CE/electrolyte interface and (vi) charge accumulation at different interfaces (Wang et al., 2005, Hauch and Georg, 2001).
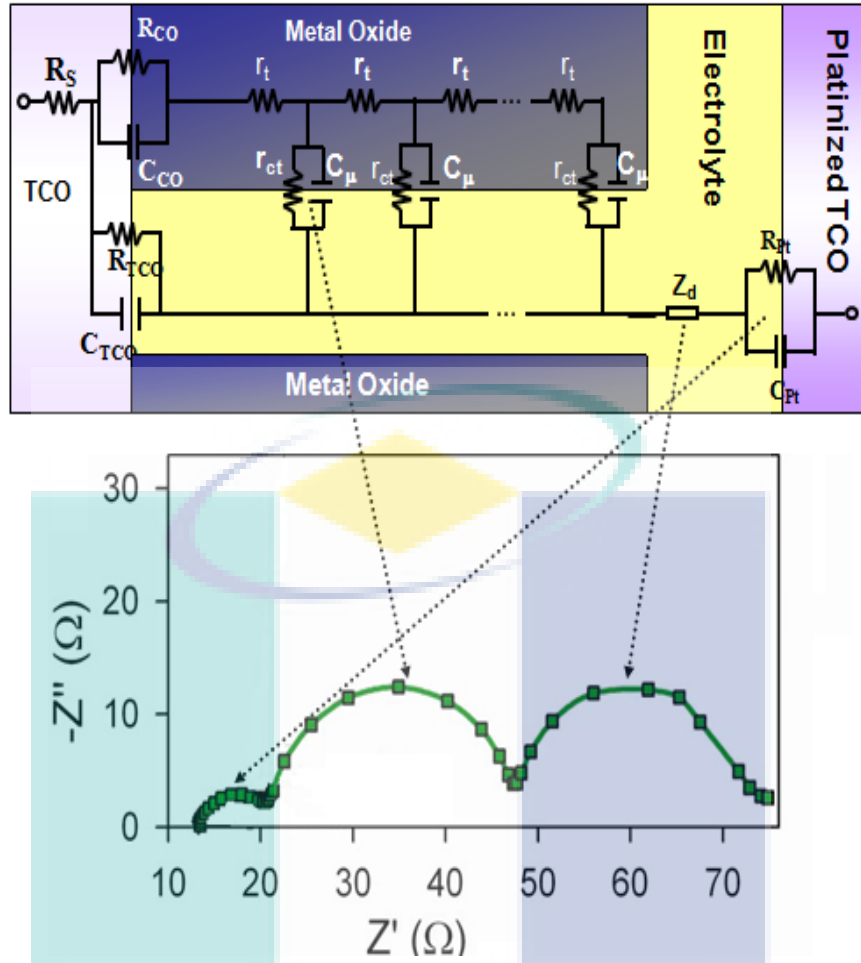
Figure 3.8: A theoretical transmission line model representing various interfaces in the DSSCs in the form of the electrical equivalent circuit. For r_t, r_{ct} and c_μ refer to the text. Z_d is the Warburg element represents Nernst diffusion of I_3^- species in the electrolyte C_{Pt} and R_{Pt} are the double-layer capacitance and the charge transfer resistance at the platinized CE, respectively; C_{TCO} and R_{TCO} are the double-layer capacitance and charge transfer resistance at the exposed FTO/electrolyte interface, respectively; R_{CO} and C_{CO} are the resistance and the capacitance at the FTO/MOS contact, respectively; R_s is the FTO series resistance.

If L is the thickness of the MOS film, the charge transport parameters such as R_T, can be calculated as ($R_T = r_t \times L$ or $r_t = R_T \times A/d$),which offer resistance inside the MOS film, R_{CT} is the total charge transfer resistance between the MOS electrons and electrolyte I_3^- species ($R_{CT} = r_{ct}/L$ or $r_{ct} = R_{CT} \times A \times d$) also called recombination resistance, R_{REC}, and C_μ is the chemical capacitance ($C_\mu = c_\mu \times L$ or $c_\mu = C_\mu/A \times d$), which represents the charge accumulation at the different interfaces inside the DSSC, where 'A' is the active

area of the photoanode and 'd' is the film thickness (Fabregat-Santiago et al., 2002, Wang et al., 2006). These charge transport parameters are calculated from the impedance data (Nyquist and Bode plot) using curve fitting method (Z-view, **Figure 3.9**) by using **Figure 3.8** (Bisquert, 2002). Both the real and imaginary parts were fitted simultaneously using the "calc-modulus" as "data weighing option" at absolute temperature 293 K. The iterations were performed to receive an optimum fit (chi-square $\leq 10^{-5}$) to extract reliable values (Wang et al., 2005, Bisquert, 2008, Jennings et al., 2011, Jose et al., 2009). The charge transport properties of the DSSCs were studied using the Autolab PGSTAT30 employing the NOVA® software. The devices were scanned in a frequency range of 100 kHz to 0.1 Hz for EIS analysis. For electrochemical measurements, the device is kept under dark and an input signal is applied to it. The applied signal is a superposition of a low amplitude sine wave of frequency ω is superimposed on a DC voltage thereby resulting in a current response that shifts with the applied potential. The applied AC signal was varied from 0.4-0.7V.
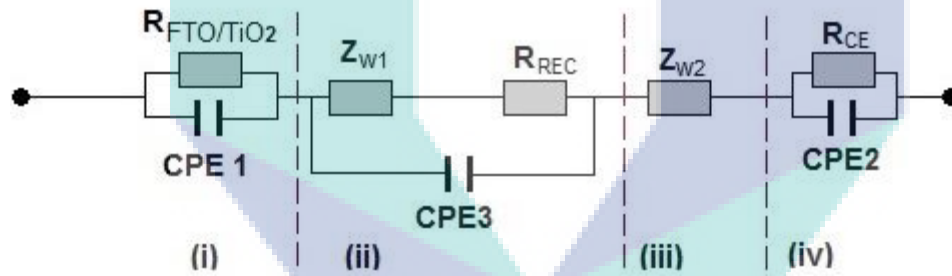
Figure 3.9: A simplified transmission line model used for fitting impedance data.

Source: Reproduced from (Wang et al, 2006 and Fakharuddin A. et al., 2014)

3.6.5 Open Circuit Voltage Decay

Open circuit voltage decay (OCVD) is another important characterization to study the charge recombination and τ_n of DSSC (Zaban et al., 2003). OCVD measures the time-based decay of V_{OC} upon removing the illumination source in DSSC operating at steady state thereby providing a real time measurement of the charge transport parameters through the device. The OCVD measurement is performed in the dark so that no electrons could recombine with oxidized dye molecules as a result electrons can solely recombine with the

tri-iodide species of an electrolyte. The recombination kinetics of electrons can also be verified by plotting τ_n against the V_{OC} as by the following **Eq. (3.15)** (Zaban et al., 2003)

$$\tau_n = -\left(\frac{k_B T}{e}\right)\left(\frac{dV_{OC}}{dt}\right)^{-1} \tag{3.15}$$

where $k_B T$ is the thermal energy e is the elementary positive charge and dV_{OC}/dt represent the decaying of V_{OC} with respect to time.

3.6.6 Incident Photon to Current Efficiency

It is also called incident photon to current efficiency (IPCE), defined as, externally measured ratio of the number of collected charge carriers to the number of incident photons incident on the solar cell as **Eq. (3.16).** It includes the effect of optical losses such as transmission through and reflection of light away from the cell. However, it is often useful to look at the QE of the light that remains after the reflected and transmitted light has been lost. The IPCE is mainly influenced by the three factors: light harvesting efficiency (LHE), electrons injection efficiency (η_{inj}) from the dye's LUMO to the CB of MOS and the (η_{cc}) of the injected electrons at the FTO.

$$IPCE = LHE \times \eta_{inj} \times \eta_{cc} \tag{3.16}$$

where LHE can be expresses as LHE = $1\text{-}10^{-\Gamma\alpha(\lambda)}$, the quantity '$\Gamma$' represents the amount of sensitizer adsorbed on MOS (moles per square centimeter) and 'α' is the absorption cross section of the sensitizer which is measure in unit of $cm^2.mol^{-1}$. Moreover, the J_{SC} can be derived from the IPCE curve by the following **Eq. (3.17)** (Archana et al., 2013).

$$IPCE(\%) = \frac{J_{SC}(mA/cm^2)}{P(mW/cm^2)} \times \frac{1240}{\lambda(nm)} \times 100\% \tag{3.17}$$

The IPCE spectra of the SnO_2 DSSCs (active area ~0.12 cm^2) were recorded using (PEC-S20) instrument. The parameters as follow: start voltage -0.1V, stop voltage 0.8 V with a voltage increment of 0.05 V. The operating mode was DC and the delay time was kept about 100 ms.

3.7 POSSIBLE ERRORS DURING SOLAR CELLS MEASUREMENT

The performance of DSSCs are often over or underestimated owing to various possible errors during characterization including calibration of solar simulator, the measurement time for I-V measurements and IPCE, and the active area determination (Yang et al., 2013). A reliable measurement of the device is crucial to evaluate its performance in order to compare the progress from various groups around the world. Here such common errors are highlighted that can mislead the performance of a solar cell.

3.7.1 Solar Simulator (Light Source)

A solar simulator is use to study the performance of cell under standard condition AM 1.5 G. The xenon lamp used in a solar simulator provide various light intensities, typically up to 1-1.5 sun). Filters are used in the solar simulator to match its spectrum to that of visible sun light. However, as suggested by (Yang et al., 2013) such solar simulators are often characterized by few unwanted sharp atomic peaks at ~450 nm and 650-850 nm as shown in **Figure 3.10**. The high intensity of these peaks results in overestimation of J_{SC} in devices. To avoid such over intensity, the solar simulator is to be calibrated using a standard cell and employing various filters such that the reference cell to generate the same photocurrent as recorded in the first calibration (given in the data sheet). As the sensitizer employed in our study (N3) could cover the range of visible light (300 nm-700 nm), a KG-5 filter is employed to minimize any possibility of overestimation of photocurrent. For sensitizers which possess broader spectral co-efficient such as N 749 (black dye, the spectral response extends to ~850 nm) solar simulator need to be calibrated with KG-3 filter. Another issue with the solar simulator is their aging effect. According to (Yang et al., 2013), the intensity and spectrum of the solar

irradiation vary with its age. The light intensity in our study is calibrated using a Lux meter to 1000 ± 2 W m^{-2}.
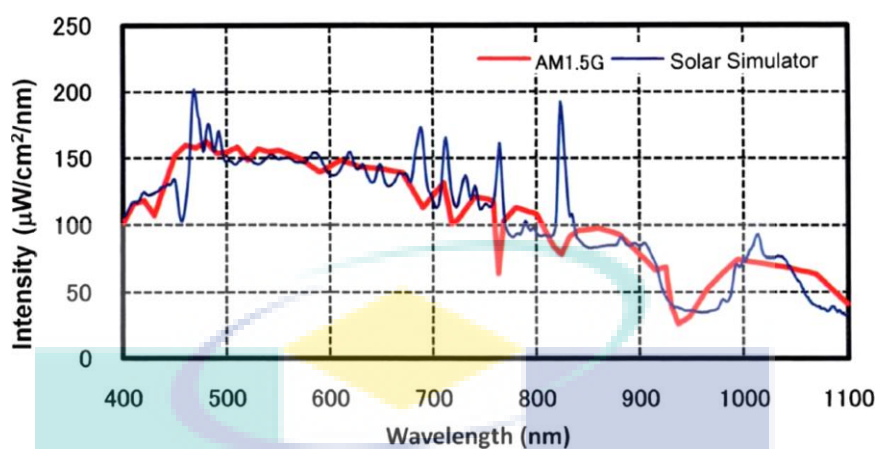
Figure 3.10: Comparative spectra of AM 1.5 G solar light (red) and AM 1.5G solar light from a solar simulator (blue).

Source: Reproduced from (Yang et al., 2013)

3.7.2 Masking and Determination of Active Area

The determination of correct active area is the most important factor while reporting the performance of solar cell. Reporting the DSSCs performance without a mask is a common practice in global research community which often leads to ≥10% over estimation of photocurrent (Hardin et al., 2012, Ito et al., 2006). In a report by (Yang et al., 2013) ~30% over estimation in J_{SC} is observed when a DSSC is tested without a mask compared with a masked device. In the un-masked DSSCs, the incident light is reflected from the FTO substrate back into the TiO$_2$ film and the absorption of light at the edges of the DSSCs would also induce extra solar irradiations as shown in **Figure 3.11**. As the irradiated area by a solar simulator (~2-5 cm^2) is much larger than the active area of the DSSC (~0.12 -0.25 cm^2), the incident light may penetrate from the edges and would cause an over estimation in PV parameters. Covering a DSSC with shaded mask will eliminate such possible error and the PV will be calculated by considering the aperture area of the mask only. The shaded mask however need to completely opaque to block complete light transmission (0%) and minimum light reflection (<5%) in UV to NIR region. A steel mask (~0.3 mm thick) with black surface is recommended to fulfil such criteria. In this study (chapter 4, 5, and 6), a thick mask employed with ~0% transmittance and

71

reflectance as low as 3-4%. Moreover, the aperture area of the mask was smaller than the active area owing to the fact that a larger aperture area than the active area may induce the measurement errors arising from light diffusion, reflection and absorption from the surrounding area.
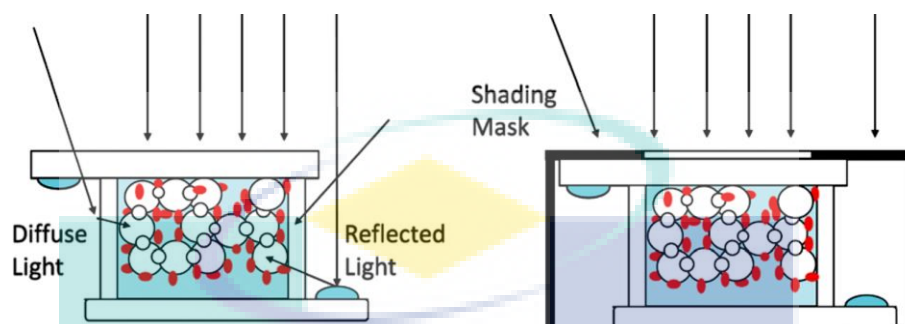
Figure 3.11: The incident solar irradiation on a masked and un-masked DSSC.

Source: Reproduced from (Yang et al., 2013)

3.7.3 Equilibrium Conditions during Steady State Measurements

The steady state measurements of solar cells such as IV and IPCE measurements should be performed when the device under test is in equilibrium. A possible non-equilibrium in the cell, which is caused by a variation in experimental conditions such as temperature, step voltage or the incident light intensity requires a delay time so that the system could reach to equilibrium state. This is crucial as significant dependence of delay time is found on the PV parameters. (Yang et al., 2013) observed 11% over estimation of J_{SC} when the delay time was changed from 5000 ms to 5 ms under the same experimental conditions. The electrolyte plays an important role for a system to reach equilibrium; in electrolytes of high viscosity the slower ion diffusion may induce a large equilibrium time constant, which require a longer delay time. The time constant for a device can be measured by transient photocurrent measurements under the action of a stepwise voltage change. For the DSSCs containing 30-50 mM (I^-/I_3^-) based electrolyte in acetonitrile, a delay time of 50 ms is considered reliable for measurements (Yang et al., 2013). In this study the same delay time (~50 ms) and a voltage step size of 20 mV was used.

3.8   SUMMARY

In summary, chapter 3 discussed the methods such as hydrothermal and electrospinning to synthesize various pure and composite SnO_2 nanostructures (nanoparticles, nanospeheres, and nanofibers) and their various surface (SEM, TEM), chemical (XRD, BET) and optical (UV-VIS-NIR) characterizations. The synthesized materials were then employed as a working electrode material for dye-sensitized solar cells. The procedure to fabricate DSSCs and the calculation of their various PV parameters are discussed in this chapter. Finally, possible errors during cell measurement and routes to overcome these errors are highlighted.
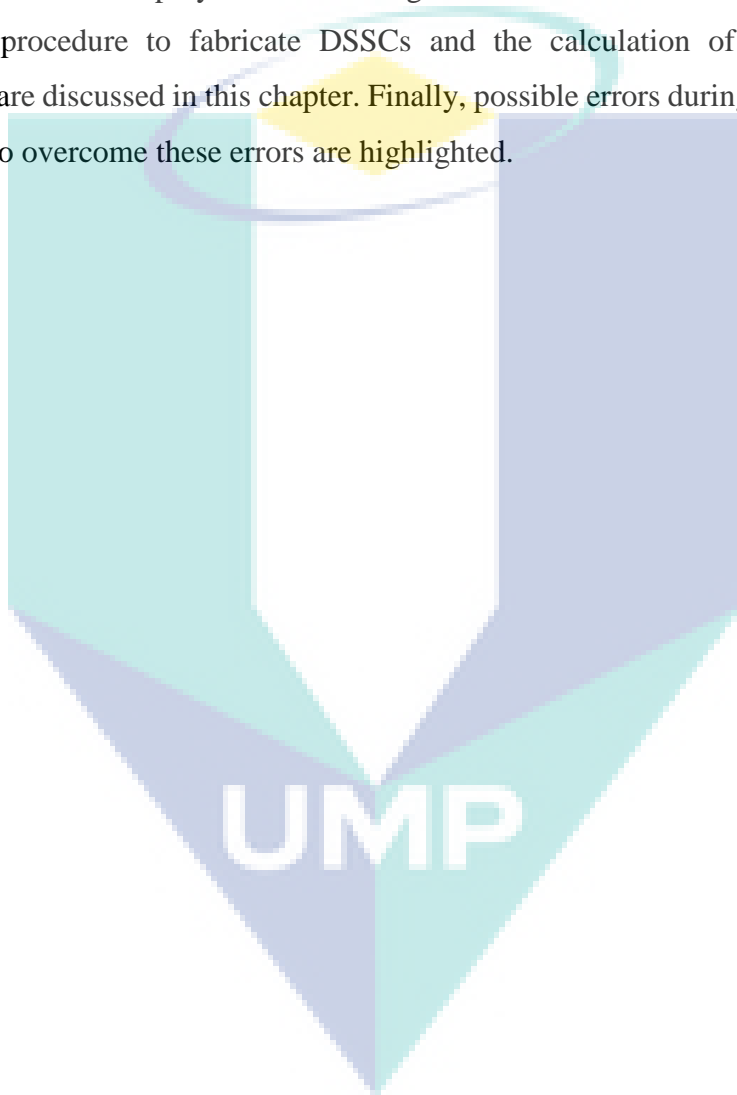
CHAPTER 4

RESULTS & DISCUSSION: MULTIFUNCTIONAL TIN OXIDE NANOSTRUCTURES

4.1   INTRODUCTION

This chapter deals with synthesis of tin oxide NPs and multifunctional (NPs-NSs) in order to achieve a high surface area and superior light harvesting properties by controlling the annealing temperature. The details of synthesis has already been described in Chapter 3 (Section 3.2). The materials thus synthesized were developed into for DSSCs electrodes (See section 3.5) and evaluated their performance. The details of materials characteristics, optical properties of the electrodes developed and results of solar cell testing are described in this Chapter.

4.2   CHARACTERIZATION OF SYNTHESIZED NANOSTRUCTURES

4.2.1   X-rays Diffraction Analysis

Three samples were synthesized at three temperatures, viz. 150, 180, and 200 ºC, which are labeled as sample 150 ºC, sample 180 ºC, sample 200 ºC, respectively. The XRD patterns of these samples show similarity in the peak position and intensity distribution as can be seen in **Figure 4.1**. All the peaks could be indexed to the tetragonal rutile SnO_2 (cassiterite phase, space group $P4_2/mnm$, JCPDS file card # 41-1445). The samples synthesized at lower temperatures (≤ 180 ºC) showed (110), (101) (200), (211) and (301) planes. However, few extra planes (220), (002), (310) and (202) are observed

in the sample synthesized at 200 ºC, which are due to its higher crystallinity. The crystallinity of the materials were evaluated from the FWHM of the major reflections, i.e., (110), (101, and (211) plane employing Scherrer Equation and shown in **Table 4.1**. Clearly, as the temperature increased from 150 to 200 ºC the crystallite size increased from 0.8 to 10.6 nm. The calculated lattice parameters from the XRD patterns are a = b ~4.738 Å and c ~3.187 Å, which are in good agreement with that reported (JCPDS file card # 41-1445). The XRD data of the materials are given in **Table 4.2**.
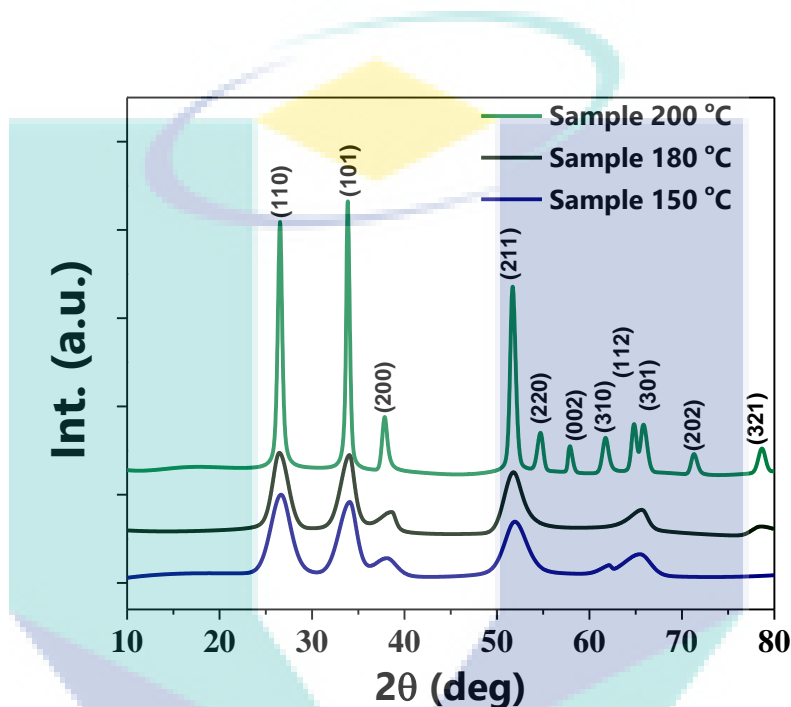
Figure 4.1: XRD pattern of the synthesized samples at three different temperature (150, 180, and 200 ºC).

Table 4.1
FWHM (B) of the three principal (110), (101), and (211) planes and their crystallite sizes of the SnO$_2$ synthesized nanostructures at temperatures (150, 180, and 200 ºC) calculated using Scherrer's Equation

Synthesized samples	(110)		(101)		(211)	
	FWHM (B) deg	Crystallite size (nm)	FWHM (B) deg	Crystallite size (nm)	FWHM (B) deg	Crystallite size (nm)
150 ºC	2.54	0. 78	2.27	1.59	2.85	1.05
180 ºC	1.98	0.99	1.80	1.60	2.34	1.29
200 ºC	0.55	3.02	0.43	10.58	0.67	2.26

Table 4.2

XRD data of the SnO₂ nanostructures synthesized at three temperatures (150, 180, and 200 °C) by hydrothermal method

2θ (degrees)	d(Å)	(hkl)	I/I₀		
			150 °C	180 °C	200 °C
26.46	3.36	(110)	1	1	~0.94
33.82	2.64	(101)	0.91	0.97	1
37.76	2.38	(200)	0.28	0.54	0.43
51.63	1.76	(211)	0.7	0.85	0.77
54.49	1.68	(220)	--	--	0.39
58.00	1.58	(002)	--	--	0.36
61.62	1.50	(310)	0.20	--	0.38
64.71	1.43	(112)	--	--	0.42
65.66	1.42	(301)	0.33	0.56	0.41
71.42	1.32	(202)	--	--	0.34
78.29	1.22	(321)	0.64	0.43	0.35

4.2.2 Morphological Study

The morphologies and surface analysis of the three samples (150, 180 and 200 °C) were studied using FESEM analysis. **Figure 4.2a** shows that the sample 150 °C consists of uniform NPs distribution with a diameter in the range of ~10 to ~30 nm. The particles are distributed in a wide range with less agglomeration revealing porosity in the nanostructure. When the temperature is increased to 180 °C, the FESEM images in **Figure 4.2c** shows a bimodal distribution of spheroidal particles one of which centered at 10-30 nm (as for the sample 150 °C) and the other centred at ~700-800 nm. However, a close examination (**Figure 4.2d**) shows that the basic building blocks of the bigger particle remained at ~10-30 nm. Bigger particles further grow > 1 µm at 200 °C with relatively large size distribution and wider gapes among the individual particles as shown in **Figure 4.2 (e-h)**. Moreover, hollow NPs are also observed having size in a nanometric scale (~50-100 nm). This unique nanostructure "sample 200 °C" having hollow nature and wider gaps among the NPs was further investigated using TEM analysis in order to elaborate its nature.
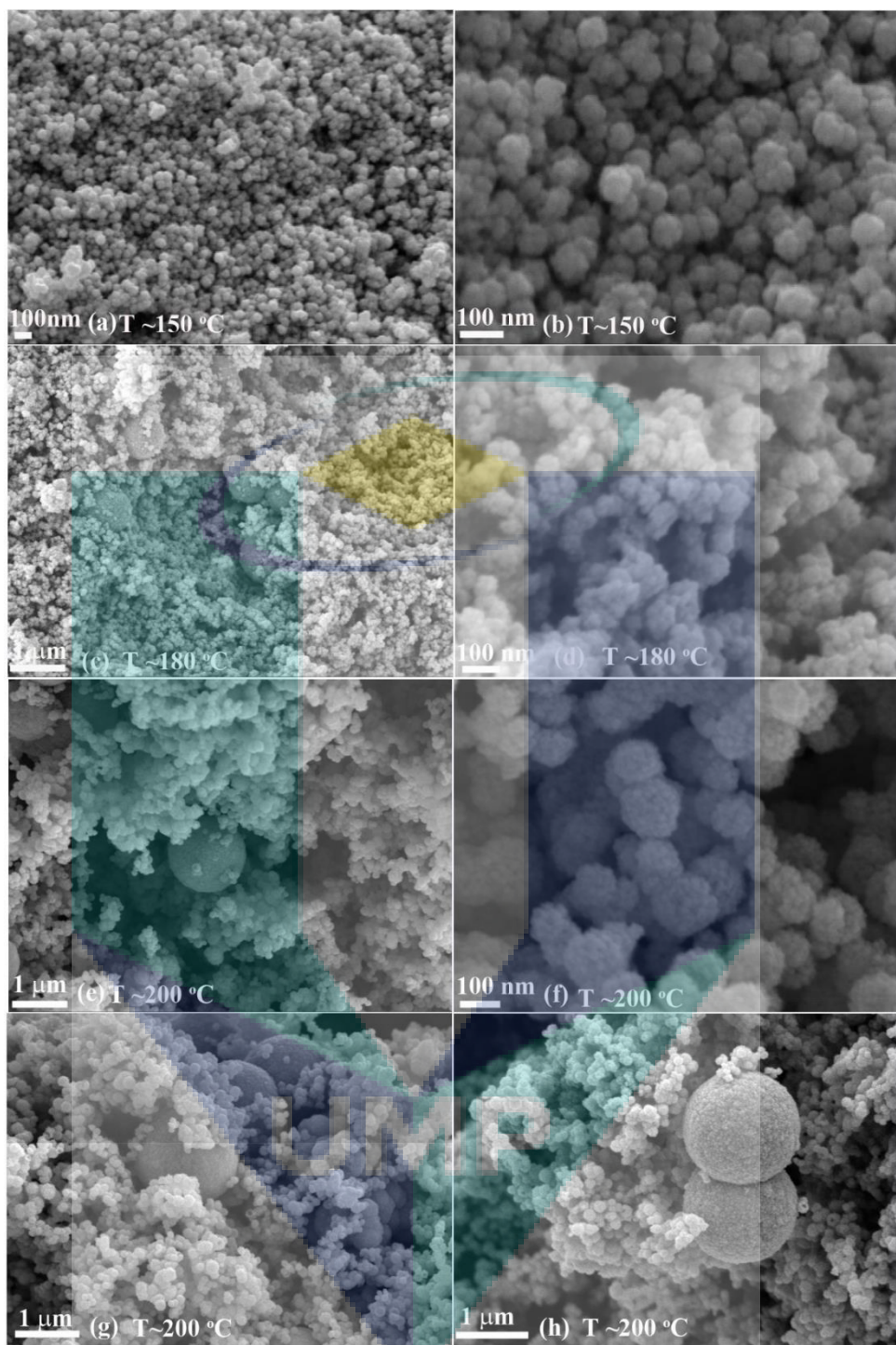
Figure 4.2: FESEM images of the synthesized nanostructures (a & b) "sample 150 °C", (c & d) "sample 180 °C", and (e-h) "sample 200 °C".

It can be observed from **Figure 4.2 (c, g and h)** that the distribution of small NPs and big spheres are not uniform. The proportion of small NPs (~100 nm) are about 70% while is only about 30% for the big spheres (>1 μm). The hydrothermal method exploits that by increasing temperature and pressure, the fundamental properties of water and thus

its abilities as a solvent changes. Important characteristics such as the ionic product, density, thermal conductivity, viscosity, heat capacity and the dielectric constant are all highly pressure, temperature dependent, and by tuning the synthesis parameters, specific solvent properties can be obtained. The theory of hydrothermal process uses simple thermodynamic functions to describe the formation of the nuclei that lead to particles formation and it is described by a process called nucleation. Generally atoms in solvent liquid phase fluctuate due to thermal motion. These fluctuation of atoms lead to the formation of atomic assemblies with local structure similar to solid phase. When stable nuclei have formed in the solid/liquid interface, the particle start growing to form a bigger particle. This leads to re-dissolution of the newly formed particles creating a concentration gradient in the solution. Uniformity of the concentration is reestablished by material diffusion towards the larger particles, thus leading to particle growth called Ostwald ripening. **Figure 4.3a** shows a typical TEM images of the sample 200 $^{\circ}$C. Spherical multifunctional (NPs-NSs) of large size distribution in the range of ~50 nm-1 µm was observed; particles in each particle remain practically constant at ~10 nm. All multifunctional including the smaller ones showed partial transparency to the electron beam; from which it is inferred that the multifunctional are hollow. Hollow nature of the multifunctional (NPs-NSs) could also be observed from SEM (**Figure 4.2g-h**). Crystallinity of the sample was judged from the HRTEM lattice images and SAED patterns, which are shown in **Figure 4.3b**.

The HRTEM images showed multifunctional (NPs-NSs) of defect free nanograins with lattice fringe ~0.34 nm and SAED pattern (shown in the inset of the **Figure 4.3b**) revealed diffraction spots oriented along a circle, where the bright circles represent polycrystalline nature of the structure and could be related to the XRD data. These observations show that the particles are of high crystallinity. In the XRD pattern, sharp and intense peaks of the sample 200 $^{\circ}$C reveals that they are highly crystalline as observed from the HRTEM images and SAED patterns. Smaller particles with superior crystallinity are recommended for efficient charge transport in DSSCs while anchoring large amount of dyes (Archana et al., 2013).
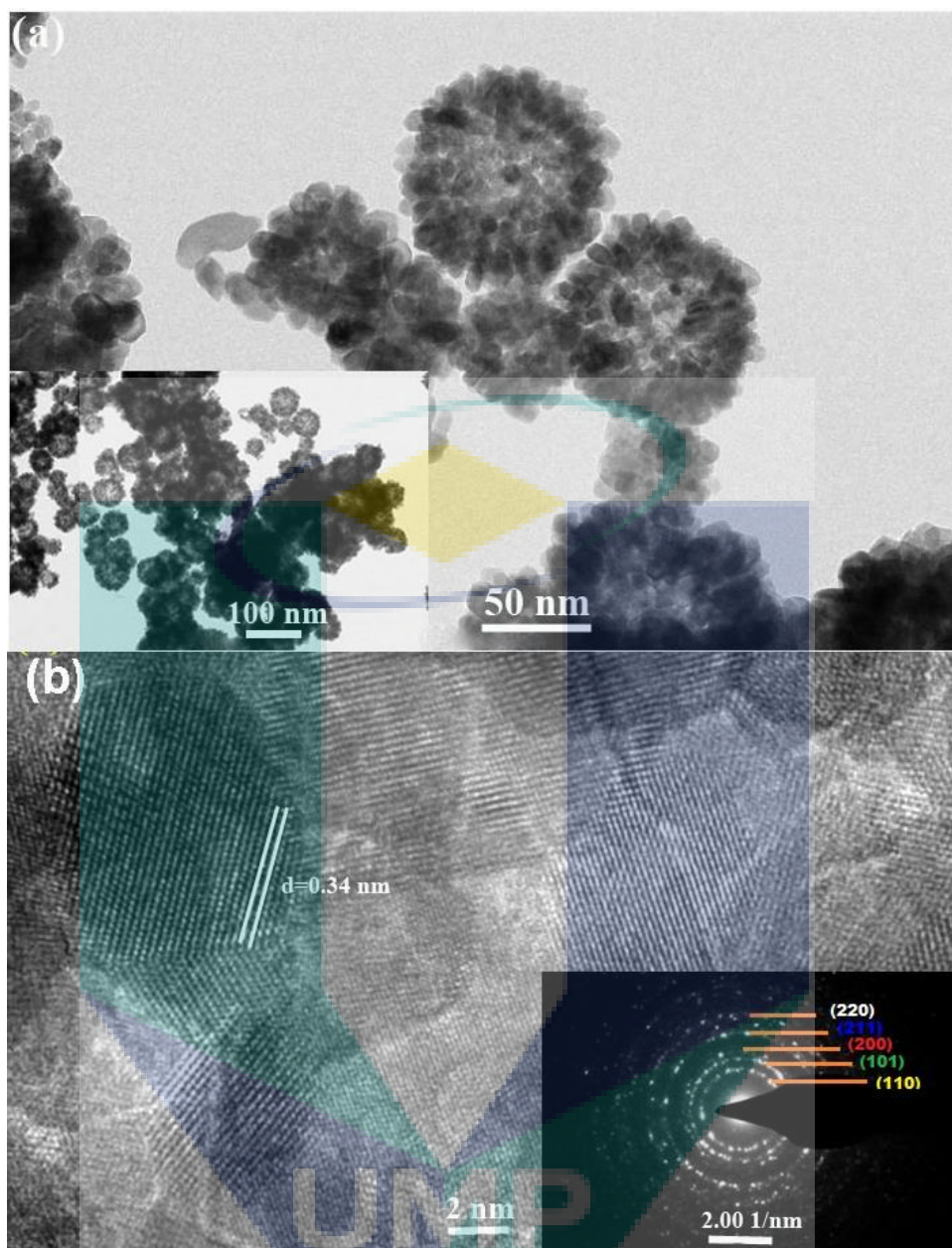
Figure 4.3: TEM images (a) at low magnification and (b) magnified HRTEM and [inset SAED image] of the sample synthesized at 200 °C.

4.2.3 Gas Adsorption Studies

The specific surface area, pore size and volume distribution were studied by BET method in nitrogen adsorption and desorption environment. The particulate properties of the samples, such as surface area, pore size and volume distributions are listed in **Table 4.3**. The BET surface area were ~50, ~46, and ~29 m^2/g, respectively for samples 150, 180, and 200 ^{o}C. The lowering of surface area could be due to the formation of multifunctional (NPs-NSs) at high temperature for samples 180 & 200 ^{o}C. The high surface area and varying pore size are beneficial for the DSSCs as they help in large dye loading and help improving permeations of the electrolyte. Adsorption-desorption isotherm of the three samples correspond to type IV isotherm are shown in **Figure 4.4**. The area under hysteresis loops increased with processing temperature thereby indicating increasing the pore size distribution.

Table 4.3
BET surface area, pore sizes, and pore volume distribution of the synthesized samples at three temperatures

Sample	BET/ m^2/g	Pore size / nm	Pore volume / cm^3/g
Sample150 ^{o}C	50	11.7	0.09
Sample180 ^{o}C	45	13.1	0.15
Sample200 ^{o}C	29	15.1	0.19
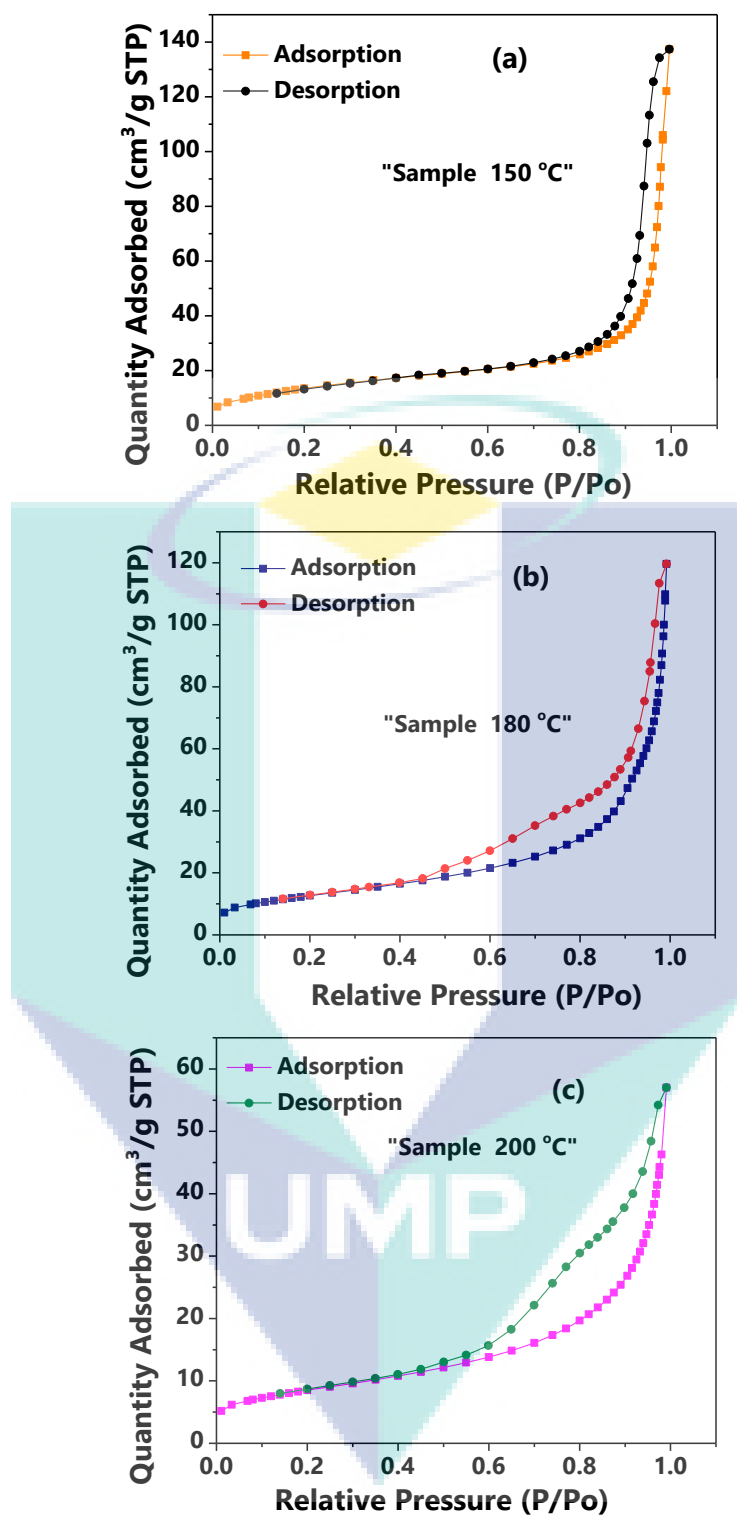
Figure 4.4: Gas adsorption-desorption isotherm curve of (a) sample 150 ºC, (b) sample 180 ºC, and (c) sample 200 ºC.

4.3 DSSCS FABRICATION AND TESTING

4.3.1 Morphology and Thickness of the Electrodes

Figure 4.5 shows a typical FESEM image (sample 200 ºC) showing the cross-section of the electrode of thickness ~8.5-12 µm. The particles were well sintered onto FTO; a closer examination shows sporadic distribution of larger particles as well as their shell structure **(Figure 4.5f)**. The hollow structures retained their initial morphology even after extensive mechanical agitation during the paste making procedure and subsequent thermal annealing. No agglomeration was found in the WE film; ensuring high porosity for electrolyte permeation.
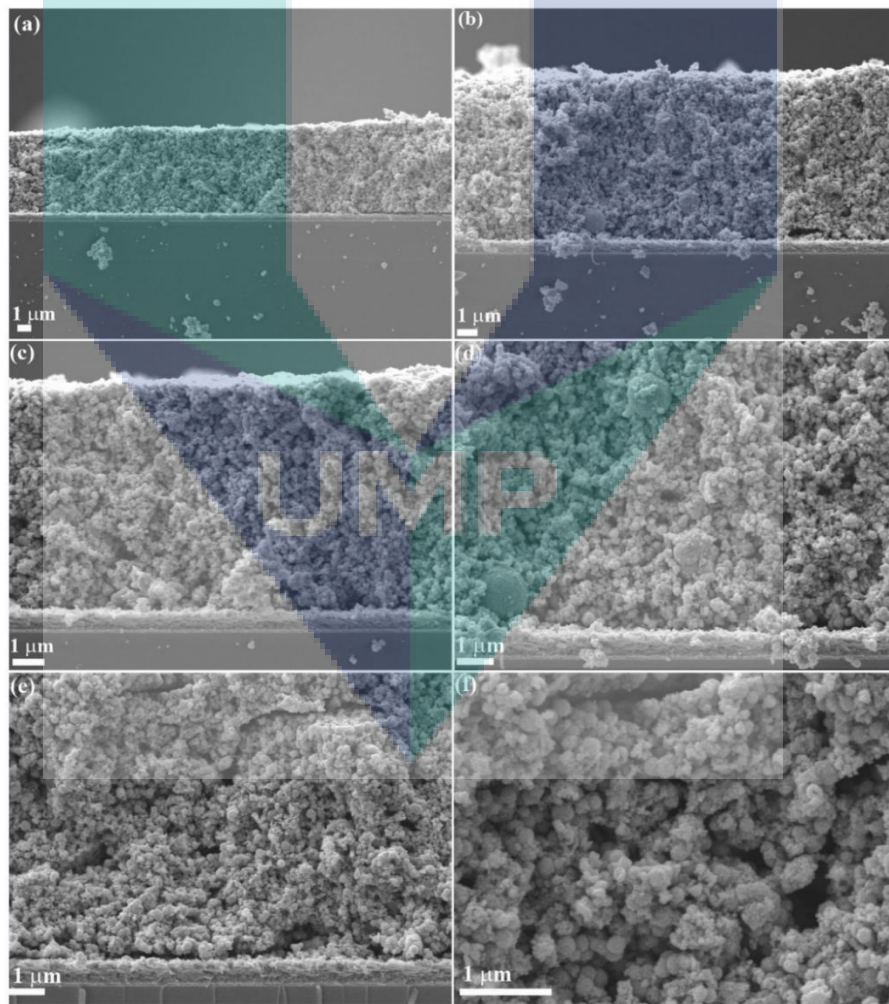
Figure 4.5: SEM cross section of the fabricated DSSC electrode using sample 200 ºC at various magnifications.

4.3.2 Light Scattering Properties of the Dye Anchored Electrodes

The light harvesting properties of the dye-anchored WE were studied by UV-VIS -NIR absorption spectroscopy. The light scattering properties of the electrodes were studied by recording their absorbance **(Figure 4.6)**, transmittance **(Figure 4.7)** and reflectance spectra **(Figure 4.8)**. **Figure 4.6** shows that electrodes of samples 150 and 180 °C showed similar absorbance although slightly improved absorbance was observed for the latter in spite of lower dye-loading. Light scattering by the larger particles is responsible for this increment in absorbance. The electrode of sample 200 °C showed larger absorption cross-section, i.e., the area under the absorbance curve, due to the presence of larger particles in spite of its inferior dye-loading, than that of the other two samples (150 & 108 °C).
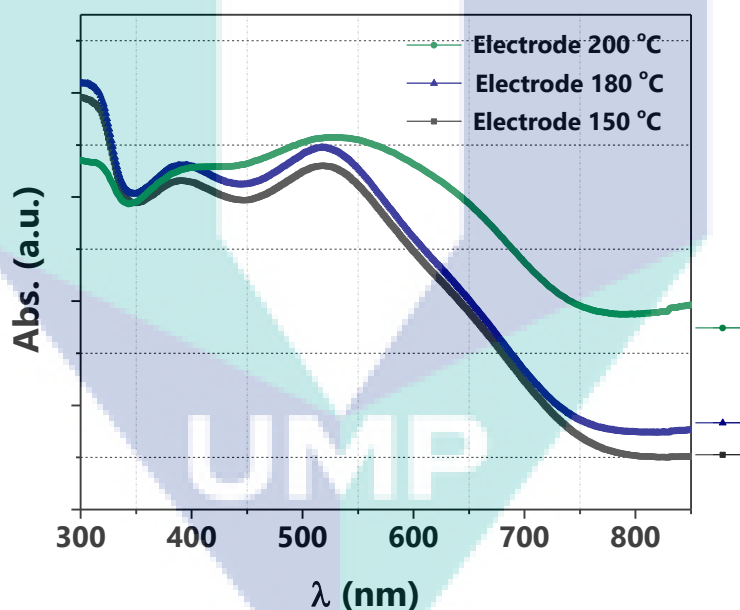
Figure 4.6: Absorption spectra of three dye anchored photoanodes synthesized at different temperatures (150, 180 and 200 °C).

Superior light harvesting property of the electrode 200 °C is more obvious in the transmittance spectra **(Figure 4.7)**. As the size of the particles in sample 200 °C corresponds to the wavelength of the VIS (~360-700 nm) and NIR (~700 nm- ~2.5 μm) regions of the light, therefore, a strong light scattering could be expected. Moreover, the presence of micron and mesoporous sized NPs would increase the reflection of light and eventually

enhance the optical path length for incident photons (Grätzel, 2009). The transmittance of the electrodes were ~34, ~30, and < 10% at the dye's absorption wavelength range for electrodes 150, 180, and 200 °C, respectively. Thus, ~90% of the incident light is absorbed by the electrode 200 °C, whereas considerable portion of the incoming light is transmitted in the other electrodes (150 & 180 °C).
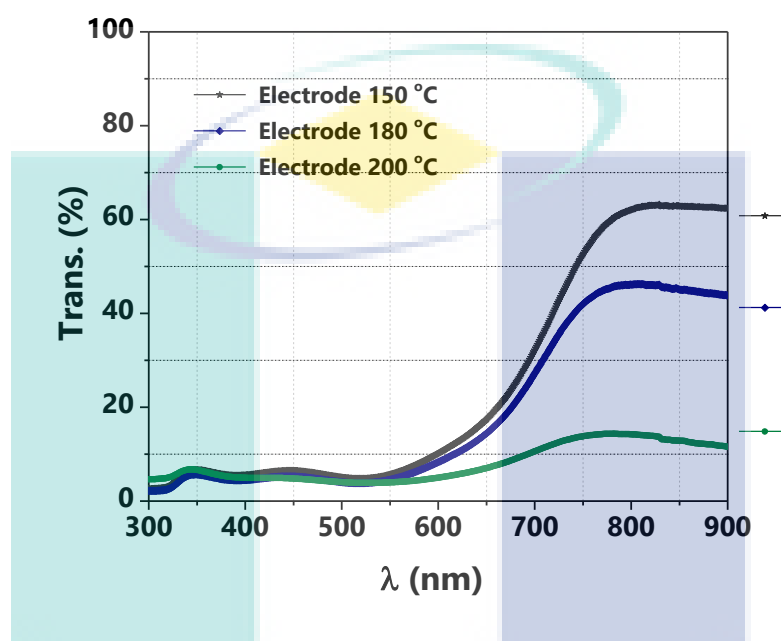
Figure 4.7: Transmission spectra of three dye anchored electrodes.

In a diffuse reflection **(Figure 4.8)**, incident photons are reflected in all directions by the photoanode thereby increasing the LHE. If the internal diffuse reflection is taken into consideration, electrode 200 °C has a higher reflectance >700 nm owing to its comparable size together with macro and mesopores, which is expected to increase the incident light reflected and scattered inside the photoanode. However, if the external reflectance is taken into consideration, the electrode 200 °C possesses lower reflectance in the 350-700 nm range than electrodes 150 and 180 °C. This low reflectance of the electrode 200 °C reveals high absorbance; and therefore, leads to high PV parameters.
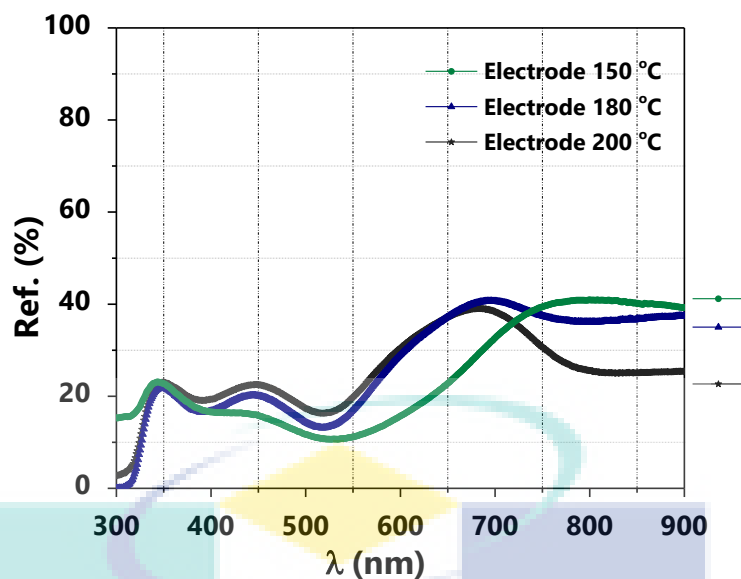
Figure 4.8: Reflection spectra of three dye anchored electrodes (150, 180, and 200 °C).

Dye loading of the dye anchored electrodes was measured by desorption test as shown in **Figure 4.9** (for detail analysis of desorption test refer to Chapter 3, Section 3.6.2). The spectra of the desorbed dye solution show that electrode 150 °C has the highest absorption, while it was the least for 200 °C, respectively. The calculated dye loading values were ~278, ~203, and ~131 nmol.cm^{-2} for (150, 180 and 200 °C electrodes), respectively. The difference in the dye loading is due to the fact that they have difference in BET surface area and also of their varying pores and volumetric size distribution **(Table 4.3)**. It is a well-known fact that small particles possesses high surface area and consequently anchoring large amount of dye and vice versa.
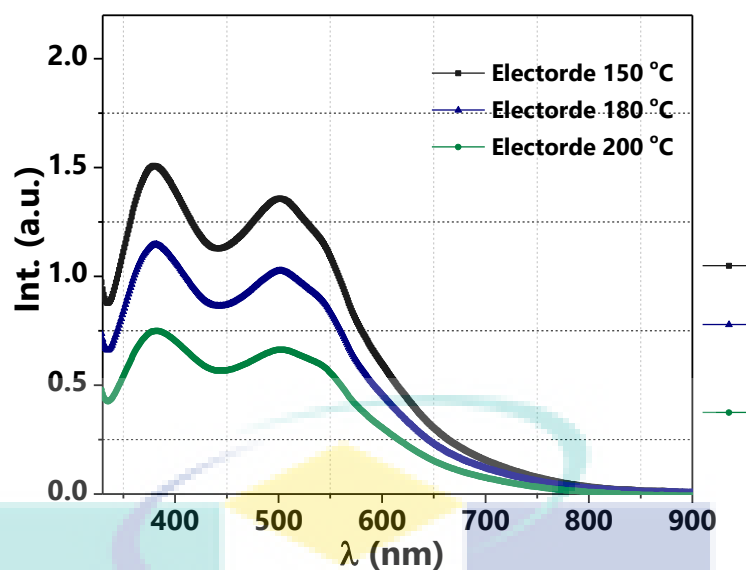
Figure 4.9: Absorption spectra of unloaded dye of electrodes (150, 180, and 200 $^{\circ}$C).

4.4 PHOTOVOLTAICS CHARACTERISTICS OF TIN OXIDE DSSCS

To observe the performance of the NPs and multifunctional (NPs-NSs) as WE in DSSCs, J-V characteristics was performed under a standard solar simulator at 1 sun condition as illustrated in **Figure 4.10**. The PV parameters of DSSCs based on sample (150, 180, and 200 $^{\circ}$C) are tabulated in **Table 4.4**. The η of the DSSCs increased in the order of ($\eta_{DSSC\ 200\ ^{\circ}C} > \eta_{DSSC\ 180\ ^{\circ}C} > \eta_{DSSC\ 150\ ^{\circ}C}$), respectively. The DSSCs 200 $^{\circ}$C showed the highest J_{SC} compared to other two types (DSSC 150 $^{\circ}$C and 180 $^{\circ}$C), which could be attributed to the increased light scattering properties of the former electrode as discussed in the earlier section. The DSSCs 200 $^{\circ}$C showed the comparable η ~4.0% till date using in pure form of SnO_2 with other PV parameters such as (J_{SC} ~16.3 mA cm^{-2}, V_{OC} ~491 mV and FF ~0.50) achieved, so far. For comparison, DSSC based on commercial TiO_2 P25 was also prepared as a reference and its PV parameters are listed in **(Table 4.4)** and IV characteristic curve is shown in **(Figure 4.10)**. Both the DSSCs i.e., DSSC 200 $^{\circ}$C and P25 DSSC resulted in a similar J_{SC} however, the latter has far higher FF and V_{OC}.
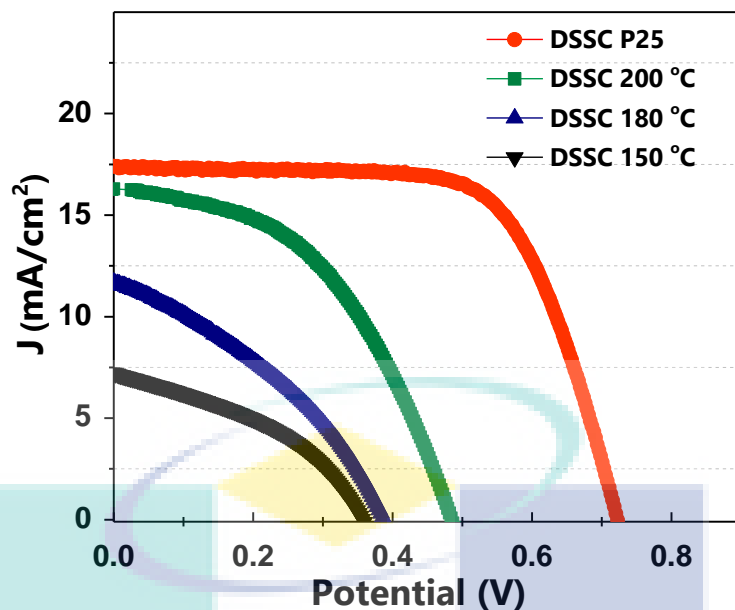
Figure 4.10: PV characteristic curves of DSSCs based on (150, 180, 200 °C, and P25 NPs) at 1 sun condition.

In addition, a systematic improvement in V_{OC} ($V_{OC (DSSC\ 200\ °C)} > V_{OC (DSSC\ 180\ °C)} > V_{OC (DSSC\ 150\ °C)}$) was observed in the three set of devices despite the chemical similarity of the WE material. This increase in V_{OC} could be due to increased light scattering achieved using varying particle size and crystallinity. In terms of FF, DSSCs 200 °C has better value compared to the other two types of (DSSCs 150 °C and180 °C), respectively. This improved FF might be due to the pore widening of the pore-size distribution of the former sample. Chen et al., synthesized mesoporous TiO_2 beads with surface areas up to 108 m^2/g with pore sizes (pore diameters varying from 14.0 to 22.6 nm) *via* a facile combination of sol-gel and solvothermal processes (Chen et al., 2009). In comparison, our fabricated nanostructures possess lower surface area with almost the same pore size distribution and shape diameter, however, the higher J_{SC} could be attributed to the multiple factors including improved light scattering and high μ_e of SnO_2. The observed higher J_{SC} of the DSSCs 200 °C can be credited to (i) the presence of small hollow NPs provide more sites (inner and outer surface) for dye anchoring, whereas micrometer sized spheres offer less grain boundaries therefore, minimize the loss of electrons during transportation and (ii) this type of nanostructures with varying particle size can have more chances for an electrolyte penetration owing to their high porosity.

87

Table 4.4

Photovoltaic parameters of DSSCs (J$_{SC}$, V$_{OC}$, FF, η and dye loading) based on synthesized samples 150, 180, 200 ºC, and P25 NPs, respectively

Devices	J$_{SC}$/ mA cm^{-2}	V$_{OC}$/ V	FF	η/ %	Dye loading/ n mole.cm^{-2}
DSSC 150 ºC	07.2	0.37	0.38	1.02	278
DSSC 180 ºC	11.1	0.40	0.37	1.62	203
DSSC 200 ºC	16.3	0.49	0.50	4.0	131
DSSC P25	16.4	0.72	0.61	7.2	702

4.5 CHARGE TRANSPORT PARAMETERS

Impedance spectroscopy analysis of DSSC 200 ºC was compared with DSSC P25 as shown in **Figure 4.11**. The Nyquist plot of DSSC 200 ºC shows smaller diameter than that of DSSC P25 as can be seen in **Figure 4.11a**, thereby, resulted in a sever electron recombination with the electrolyte species. To further identify the lower performance of DSSC 200 ºC as compared to the TiO$_2$ counterpart, the charge transport parameters were extracted using Z-view software of well-known Bisquert transmission line model (Bisquert, 2002). The DSSC 200 ºC exhibits inferior R$_{CT}$ value, i.e., the value was ~19 Ω for DSSC 200 ºC and ~70 Ω for DSSC P25. On the other hand, DSSC 200 ºC shows surprisingly lower R$_T$ (~10 Ω) and it was very high for DSCC P25 (~43 Ω). It is well known fact that TiO$_2$ NPs possesses detrimental grain boundaries between individual NPs and also characterized by low μ_e thereby leads to higher R$_T$ value (Fakharuddin et al., 2014).

The τ_n was calculated for both DSSCs using the mid frequency of the bode-phase plots **(Figure 4.11b)** using a relation $\tau_n = 1/2\pi f_o$ (Le Viet et al., 2010) where f_o is the maximum frequency at the mid peak. The calculated value of f_o was ~18.0 and ~29.3 Hz, with corresponding τ_n ~8.85 and ~5.3 ms for DSSC 200 ºC and DSSC P25, respectively.
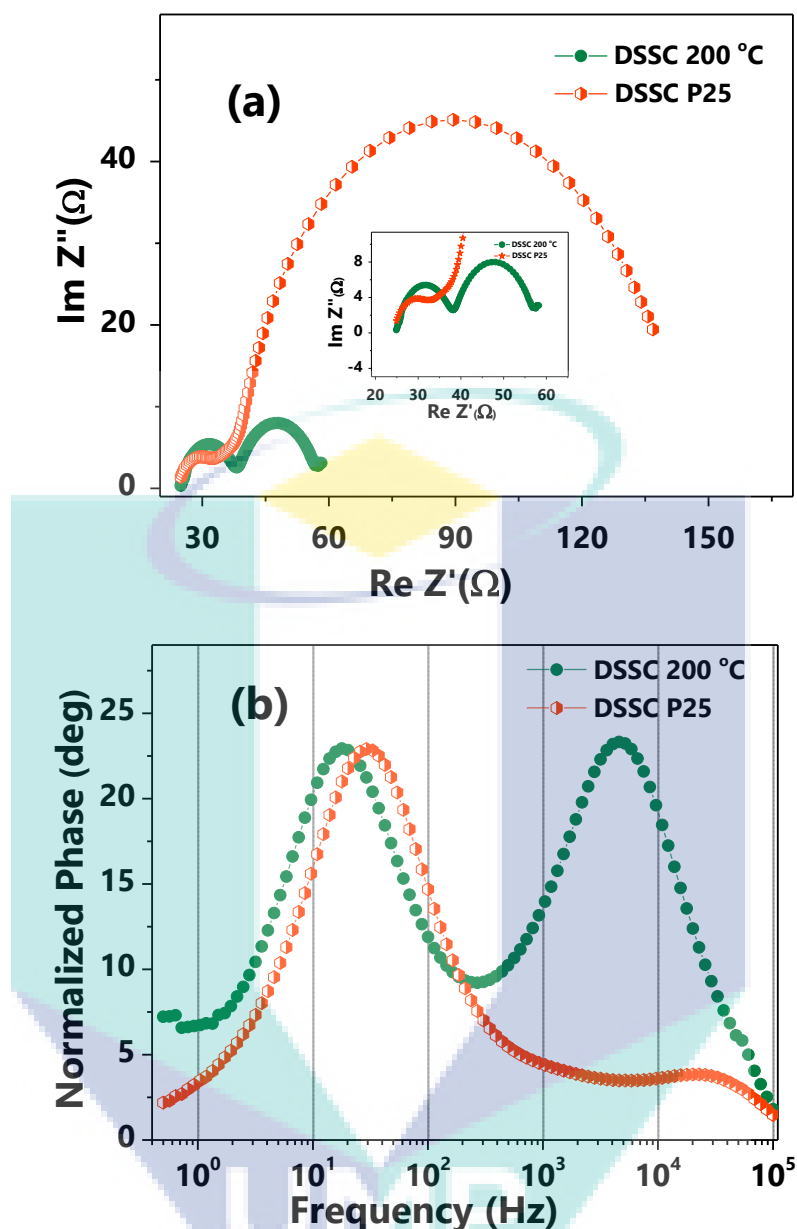
Figure 4.11: (a) Shows the Nyquist plot, while (b) depict bode phase plots of DSSC 200 ºC and DSSC P25.

The difference in η_{cc} of the DSSCs was investigated using the IPCE spectra. **Figure 4.12** compares the IPCE spectra of the DSSC 200 ºC and DSSC P25. The highest IPCE was ~78% for DSSC 200 ºC and ~72% for DSSC P25 at a particular λ ~520 nm near the peak absorbance of the N3 sensitizer. The enhanced IPCE curve of DSSC 200 ºC could be due to the improved light scattering capability of the multifunctional (NPs-NSs) compose of variable particle sizes despite the fact that it resulted in low surface area (~29 m^2/g) and subsequently inferior dye-loading. Furthermore, the *J-V* data was validated from the IPCE

measurements of the DSSCs by calculating the J_{SC} using a relation (**Chapter 3, Eq. 3.17**). The integrated IPCE over the entire wavelength ($\lambda \sim$300-800 nm) was used to calculate the J_{SC} as depicted in **Figure 4.12**. The calculated J_{SC} of the DSSC 200 ºC ($\sim$14 mA cm^{-2}) and PDSSC P25 ($\sim$15 mA cm^{-2}), which agrees with their measured J_{SC} **(Table 4.4)**.

The measured OCVD curves of the DSSC 200 ºC and DSSC P25 are shown in **Figure 4. 13a** while **Figure 4.13b** compares the τ_n of both DSSCs measured from the OCVD curves **(Chapter 3, Eq. 3.15)**. In OCVD curve, both the DSSCs show a similar decaying over the entire time although SnO$_2$ has shown low R_{CT} (i.e., recombination of photo-induced electrons with electrolyte is faster for SnO$_2$ than TiO$_2$). On the other hand, DSSC 200 ºC exhibits comparable τ_n over the low voltage range to that of DSSC P25, however, at a typical voltage of $\sim$300 mV, the calculated τ_n for the former was $\sim$0.7 sec and $\sim$1.5 sec for the latter, respectively.
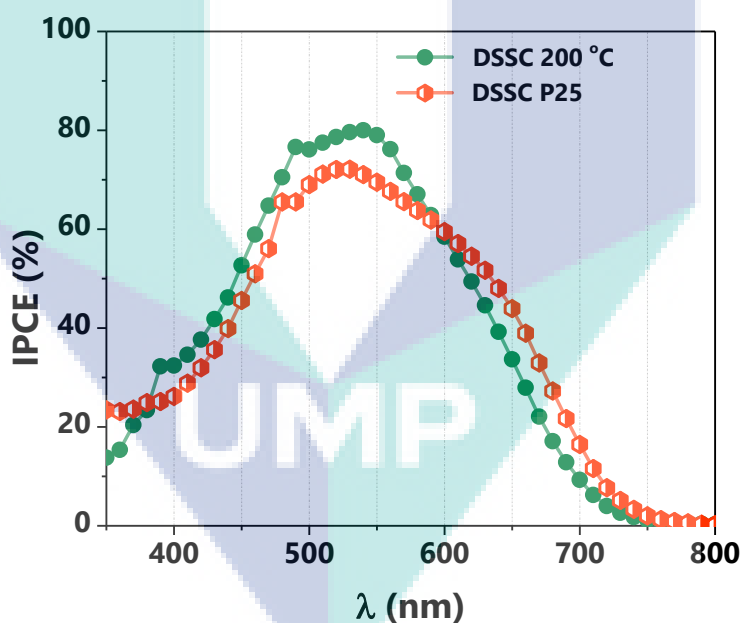
Figure 4.12: IPCE characteristic curve of DSSC 200 ºC and DSSC P25.
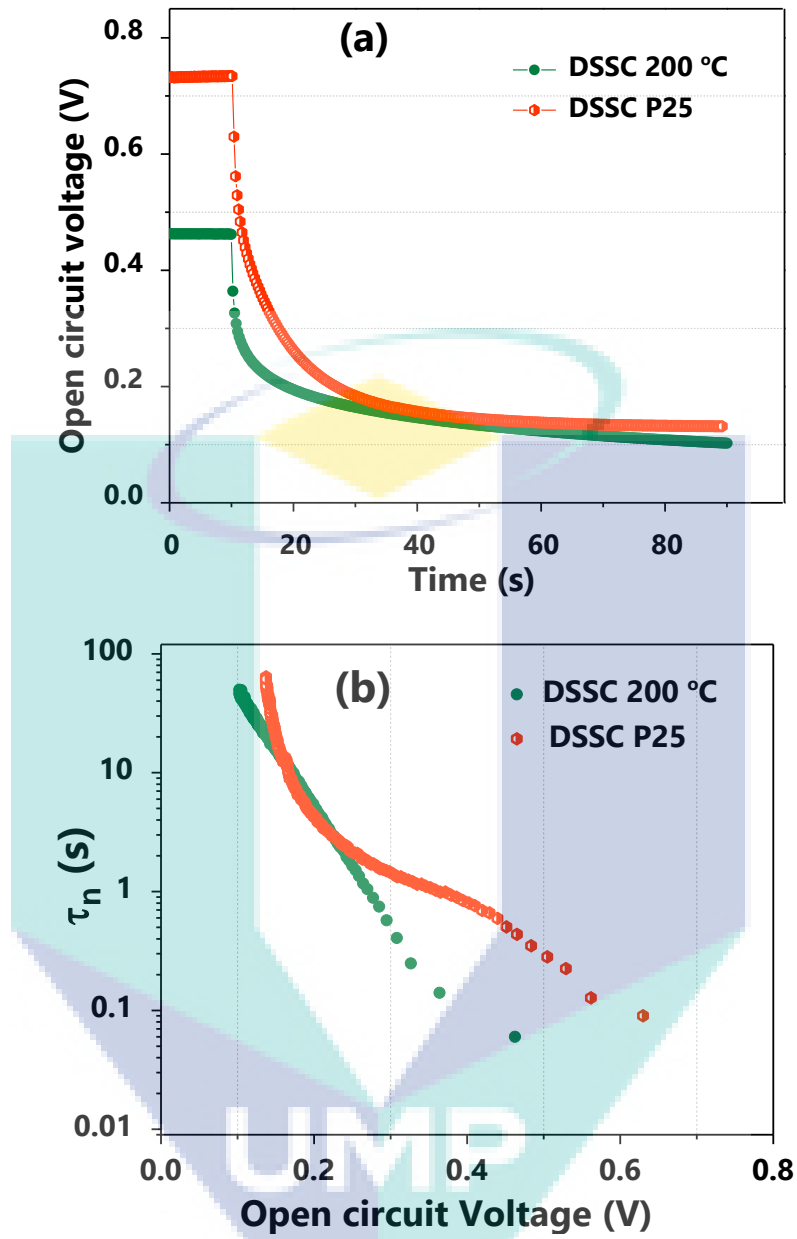
Figure 4.13: (a) Shows the OCVD curve of DSSC 200 °C versus DSSC P25 and (b) illustrates τ_n versus V_{OC} for the respective devices.

4. 6   CONCLUSIONS

In conclusion, although surface area is the crucial factor for the photoanode materials, the additional light scattering and harvesting are playing a vital role. Small NPs synthesized at low temperature (~150 °C) resulted in a highest BET surface area (~50 m^2/g) while lack in light harvesting characteristics. On the other hand, the unique (combination of hollow NPs along with a micron size sphere) morphology synthesized at a higher temperature (~200 °C) performed tremendously when employed as photoanode in DSSCs. This nanostructure possesses the two desired features, i.e., high surface area and superior light scattering capability as can be seen from the light absorption analysis. Moreover, SnO_2 based DSSC showed comparable IPCE and life time to that of TiO_2 counterpart. Finally, the sample 200 °C showed an overall η ~4% with J_{SC} as high as ~16.3 mA cm^{-2}. The overall performance of SnO_2 was lower than TiO_2 counterpart because conduction band and valence band energies of the former are much lower than the latter, which increases the over potential and charge recombination.

CHAPTER 5

RESULTS & DISCUSSION: MULTIPOROUS TIN OXIDE NANOFIBERS

5.1   INTRODUCTION

This chapter describes properties of the solutions used for electrospinning and characteristics of nanofibers thereby obtained. At the first stage, PNFs and MPNFs were synthesized, characterized and subsequently followed by their testing as a WE in DSSCs. Briefly, the MPNFs resulted in a higher specific surface area ~80 m^2/g, many fold to that of PNFs, expected to anchored large amount of dye that can lead to a superior photocurrent.

5.2   CHARACTERIZATION OF ELECTROSPUN NANOFIBERS

5.2.1   Precursor Concentration vs. Viscosity of the Solutions

The synthesis method of the SnO_2 electrospun 1D nanostructures is described in detail (Section 3.3). The tin precursor concentration in the polymeric solution for electrospinning was varied in five steps i.e., 5.5 (C_o), 7.0 (C_1), 8.5 (C_2), 10.0 (C_3) and 11.5 mM (C_4), respectively, where "C" stands for concentration. **Table 5.1** summarizes the precursor concentration and viscosity of the solution used for electrospinning. In the electrospinning polymeric solution, the tin precursor was increased gradually in a systematic way while kept other parameters constant. It is obvious from **Table 5.1** that

an increase in tin precursor concentration in the polymeric solution monotonously raised the viscosity of the solution. **Figure 5.1** shows the % increase in concentration vs. % increase in viscosity of the five solutions (C_o-C_4). It can be observed that the precursor concentration increased sharply from concentration C_o (0%) to C_4 (109.1%). On the other hand, the viscosity of the solution (C_o-C_4) showed a sharp increase with the first addition whereas the magnitude of increase is less pronounced for subsequent additions.

Table 5.1

Characteristics parameters of the electrospinning solution such as precursor concentration, solution viscosity and % increments

Sample label	Precursor Concentration / mM	Solution Viscosity / cP	Increase in precursor / %	Increase in viscosity / %
C_o	5.5	256.7	0	0
C_1	7.0	298.1	27.3	16.1
C_2	8.5	304.9	54.6	18.8
C_3	10	321.5	81.8	25.2
C_4	11.5	344.2	109.1	34.1
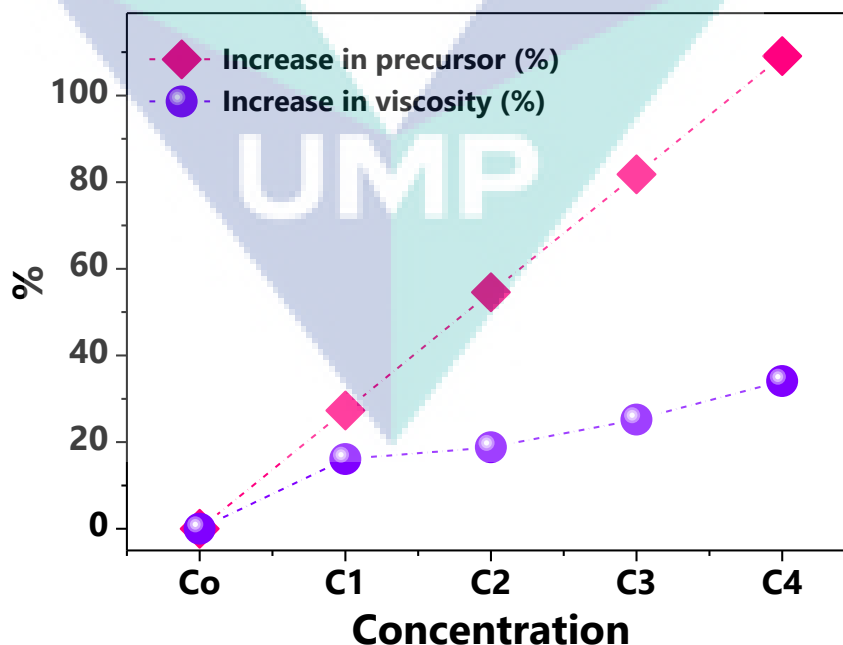
Figure 5.1: Illustration of the % increase in concentration vs. % increase in the viscosity of the five (C_o-C_4) concentration solution.

5.2.2 Crystal Structure of the Annealed Samples

The phase purity and crystallinity of the synthesized electrospun annealed (C_o-C_4) nanostructures were examined using XRD technique with 2θ range from 10 to 80° as shown in **Figure 5.2**. All the peaks in the XRD pattern could be indexed to the tetragonal structure of SnO_2 with space group $P4_2/mnm$. No impurity was found in all five types of synthesized nanostructures and the highest intensity peaks are centered at 2θ ~26.8°, ~32° and ~53° ascribed to (110), (101), and (211) planes, respectively. It can be seen from the Figure that all materials have similar XRD pattern; however, there were few extras planes appeared for C_1 and C_2. These extra planes is expected to be due to the high crystallinity of the respective samples. The calculated values of the lattice parameters were similar i.e., a = b ~4.635 Å and c ~3.165 Å, which are in close agreement with the standard data (JCPDS Card No 41-1445).

The D values of these nanostructures (C_o-C_4) were calculated using Scherrer's Equation **(Eq. 3.1)**. The principal (110) plane of all nanostructures was used to calculate the FWHM by fitting it with a single Gaussian peak. It can be seen from **Table 5.2** that the D is the highest for C_1 and C_3 (~20 nm), while it is the lowest for C_o (~10.6 nm) owing to the difference in their FWHM. Large D are beneficial for superior conductivity (Archana et al., 2009); therefore, the SnO_2 synthesized from the solutions C_1 and C_2 are expected to provide superior charge transport properties.

Crystal structure and the difference in microstructure between the materials were further studied by TEM. Samples from only two concentrations were selected for the TEM analysis C_1 and C_2, because (i) XRD shows similar pattern for all samples, and (ii) these two nanostructures show significantly different morphologies are explained in detail in the next sub-section detailing the FESEM results. **Figure 5.3 (a-b)** and **(d-e)** show TEM images of C_2 and C_1, respectively. A highly porous and hollow structure is visible in both cases. The C_1 were formed with grains of size 10-15 nm which are smaller than the grains forming the C_2 (15-20 nm). The smaller grains and many pores in C_1 could lead to large surface area. The HTREM images **(Figure 5.3 b & e)** of the C_2 and C_1 have clear lattice fringes of ~0.3 nm and ~0.2 nm, assure high crystallinity of these nanostructures, respectively. The smaller lattice fringe for the C_1 could be attributed to its smaller grain

sizes as compared to PNFs. The SAED **(c) and (f) in Figure 5.3)** show concentric circles which are due to polycrystallinity in both nanostructures; however, the C_2 have a relatively spotty pattern. In **Table 5.3**, the lattice spacing determined from XRD and SAED patterns of the respective samples are compared. The extra XRD peaks appeared in the sample C_1 is clearly reflected in its SAED pattern **(Figure 5.3).**
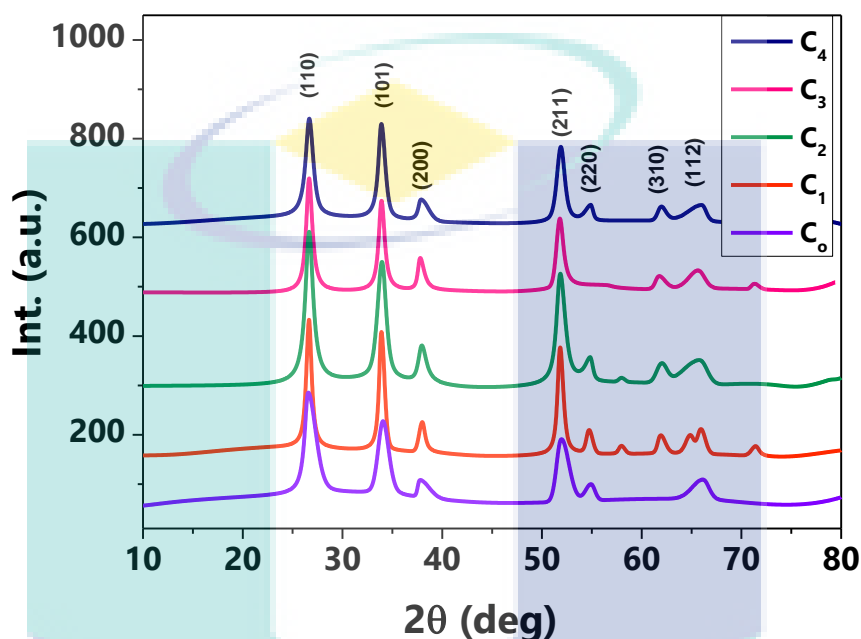
Figure 5.2: XRD pattern of the electrospun annealed (C_o-C_4) nanostructures.

Table 5.2
FWHM, crystallite size, pore size, and pore volume of the synthesized (C_o-C_4) samples

Sample	FWHM (B)/deg	Crystallite size (D)/nm		Pore size/ nm	Pore Volume/ cm^3/g
		XRD	HRTEM		
C_o	1.48	10.6	--	60.7	0.064
C_1	0.79	19.9	~10-15	12.2	0.069
C_2	1.01	15.3	~10-20	16.1	0.071
C_3	0.81	19.0	--	22.5	0.165
C_4	1.04	15.0	--	18.9	0.094
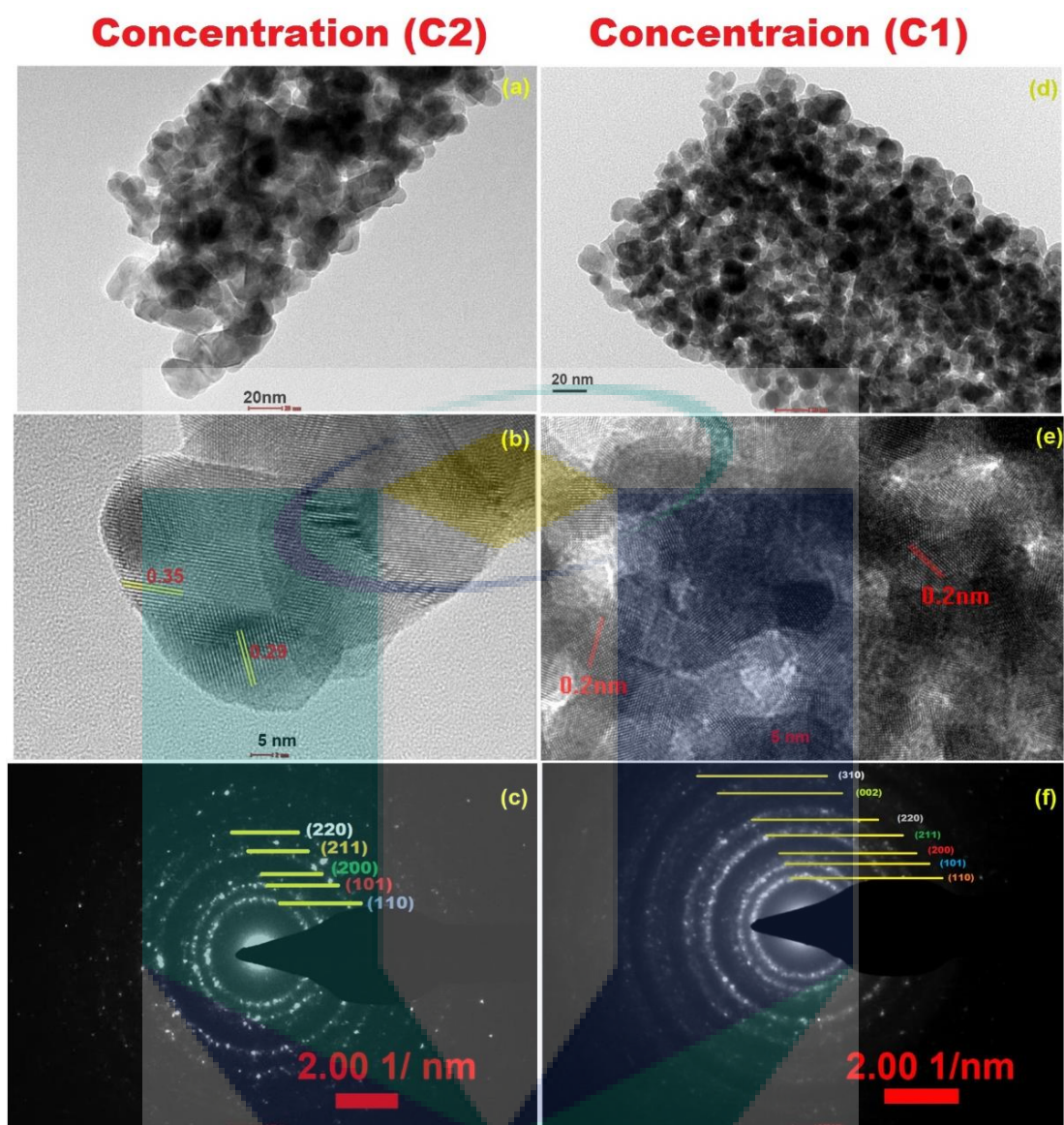
Figure 5.3: TEM images (a) C_2 and (d) C_1 low magnification (b) C_2 and (e) C_1 at high magnification, (c) & (f) SAED pattern of the annealed samples (C_1 & C_2).

Table 5.3
Lattice spacing of the samples (C_1 & C_2) using XRD and TEM techniques

Annealed Sample	XRD Lattice spacing (d) (nm)				HRTEM Lattice spacing (d)
	(110)	**(101)**	**(211)**	**Ave**	
C_1	0.3345	0.2645	0.1764	0.2584	~0.20 nm
C_2	0.3365	0.2639	0.1766	0.259	~0.35 nm

5.2.3   Concentration Dependent Morphology of the Tin Oxide

Conventionally, the tin precursor dispersed electrospun PVP fibrous mats are annealed at between 500 to 600 °C to obtain the pure SnO_2 fibres (Kumar et al., 2012, Gao et al., 2012, Guo et al., 2012, Gao et al., 2014, Fu et al., 2014, Ahn et al., 2013); therefore, the as-spun polymeric fibres were annealed at 600 °C in this study. Surface morphology of the annealed fibers were studied by FESEM analysis. **Figure 5.4** shows FESEM surface morphology of the annealed electrospun nanofibers for samples C_o (a1-a3), C_1 (b1-b3), C_2 (c1-c3), C_3 (d1-d3), and C_4 (e1-e3). For the sample C_o, porous solid NFs were formed with diameter ranging from ~100-170 nm. The FESEM images of the sample prepared from C_o shows that it has a smooth surface morphology; and the higher magnification images show that the nanostructure is composed of grains of ~10-20 nm uniformly distributed throughout the structure with considerable surface roughness. A slightly small increase in the precursor concentration (7 mM, C_1) resulted in a slightly larger diameter (120-190 nm) nanofibers; however, the grains are larger (20-30 nm) as can be seen in the high magnification FESEM images. Further increase the precursor concentration to (8.5 mM, C_2), the resulted fibres have diameters in the range ~160-220 nm, where the surface seems more porous than C_o; however, with smaller particle size than that of C_1. Similar NFs have been achieved to that of C_2 when the tin precursor was increased to 10 mM (C_3). Finally, when the precursor concentration was increased more than double of the initial value (i.e., 11.5 mM, C_4) fibres with a significantly varying diameter (210-340 nm) was resulted, which is in accordance with the previous report on electrospinning of SnO_2 NFs (Kumar et al., 2012). The morphological features of the annealed electrospun NFs (C_o-C_4) are summarized in **Table 5.4**. Image J software was used to measure the particle size and diameter of the NFs.
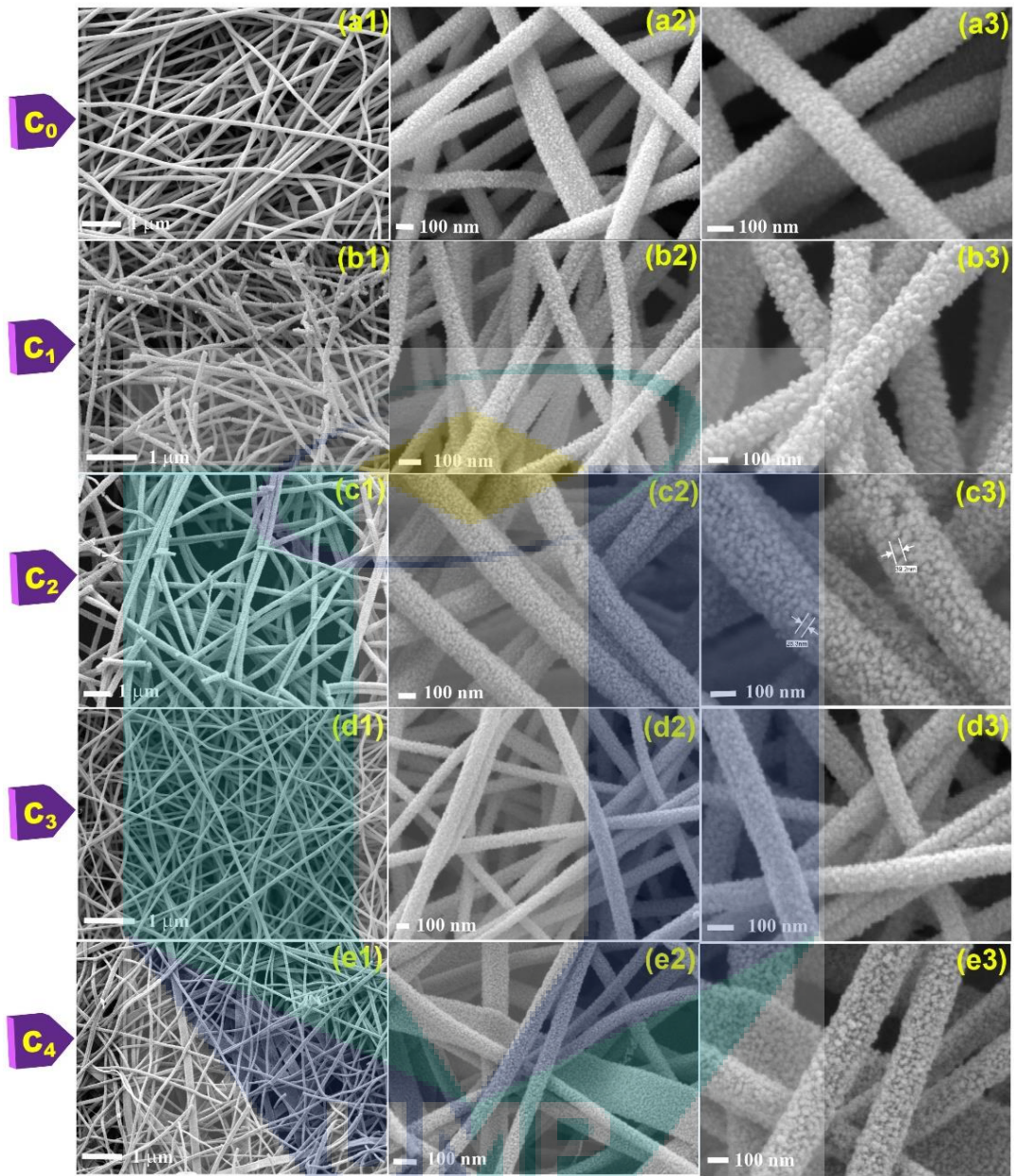
Figure 5.4: FESEM surface morphologies (a1-a3) Show C_o solid NFs, (b1-b3) C_1 MPNFs, (c1-c3 and d1-d3) C_2 and C_3 for PNFs and C_4 (e1-e3) present the formation of porous nanostructure developed by electrospinning.

Table 5.4
Morphology, grain size, and diameter of the annealed electrospun nanostructures

Sample label	Morphology	Diameter distribution /nm	Grain size /nm
C_o	NFs	114-170	10-20
C_1	NFs	124-191	20-30
C_2	NFs	162-224	15-25
C_3	NFs	170-195	10-25
C_4	NFs	213-337	20-30

The cross-sectional FESEM view of the annealed nanofibers of the samples C_o (a1-a3), C_1 (b1-b3), C_2 (c1-c3), C_3 (d1-d3), and C_4 (e1-e3) are shown in **Figure 5.5**. It can be observed that the cross-section of concentration C_o are solid. A slight increase in the precursor concentration (7 mM, C_1) shows that the NFs are transformed to hollow structure and composed of multiple pores inside a single fibre termed multiporous NFs (MPNFs). The number of pores in the MPNFs varied from 2 to 4 with their inner diameters ranging from 30 to 70 nm. Further increase in the precursor concentration (C_2 and C_3) resulted in a hollow structure consist of a single channel per nanofiber named porous NFs (PNFs) having inner diameter ~50-100 nm; i.e., increase in the precursor concentration in samples C_2 and C_3 resulted in significant decrease in the pore diameter and ultimately the pores vanished in the sample C_4. **Table 5.5** shows the features of cross-sectional view of the synthesized nanostructures (C_o-C_4) such as morphology, surface area, and channel's diameter, respectively.
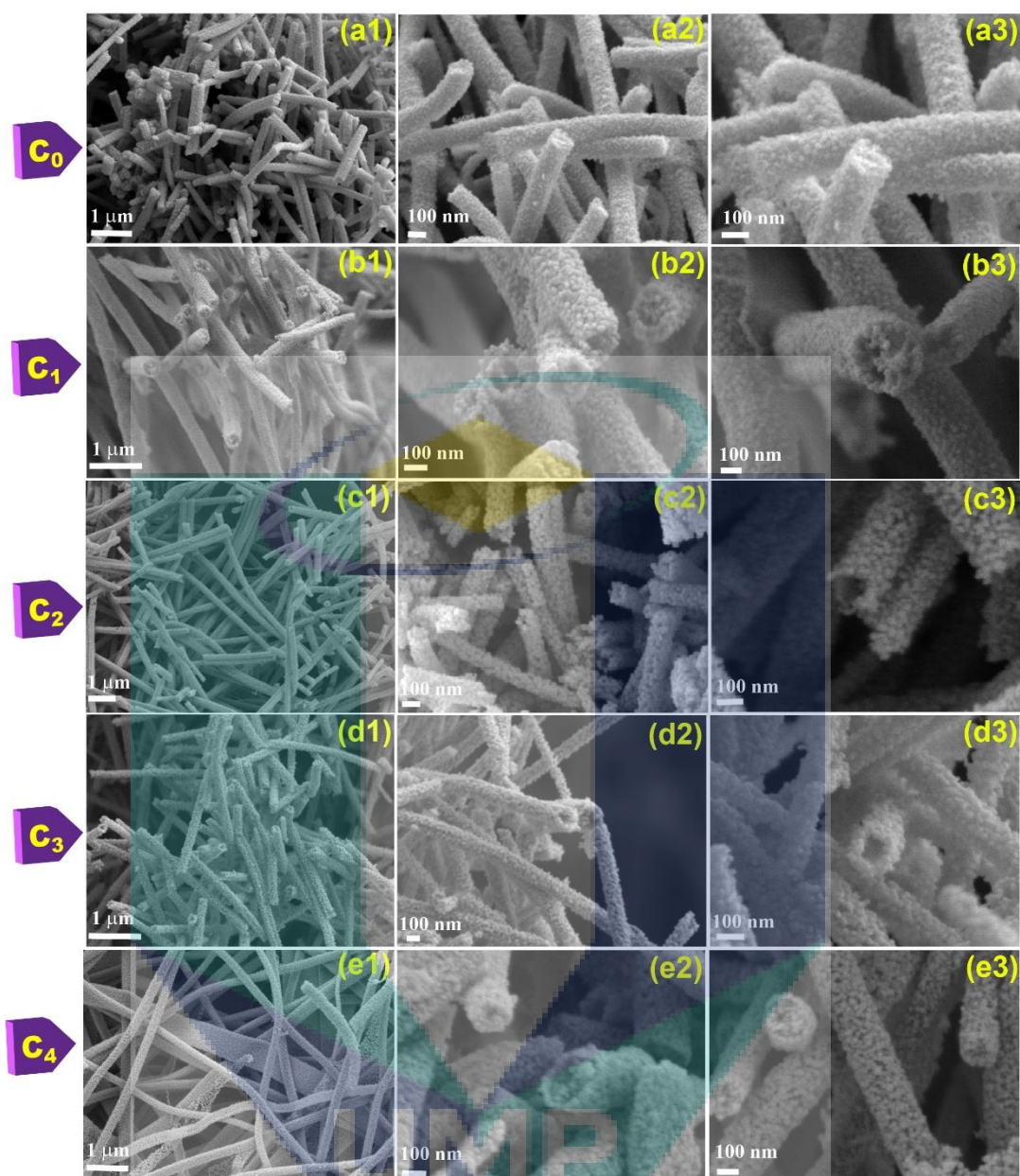
Figure 5.5: FESEM cross sectional view (a1-a3) Show C_o NFs, (b1-b3) depict C_1 MPNFs, (c1-c3 and d1-d3) demonstrate C_2 and C_3 for PNFs and C_4 (e1-e3) present the formation of porous nanostructure developed by electrospinning.

A significant question that needs to be addressed is on the mechanism of formation of variable porosity and the changes in the sizes of the particles composing the fibres withchange in concentration of the precursor. It can be seen that C_o and C_4 resulted in solid NFs, while C_1 and (C_2 & C_3) resulted in PNFs and MPNFs, respectively

Table 5.5
Morphology, channel's diameter, surface area, % increase in surface area of the annealed nanostructures

Sample label	Morphology	Channel's diameter / nm	Surface area /m^2/g	% increase (m^2/g)	Channel
C_o	NFs	--	7	0	0
C_1	MPNFs	30-50	78	1014	$1-4$
C_2	PNFs	50-100	12	71	1
C_3	PNFs	50-100	10	42	1
C_4	NFs	--	10	42	0

To see whether there is any clue about the formation of PNFs and MPNFs, FESEM images of the as-spun fibres were recorded **(Figure 5.6)**. The as-spun polymeric mats had a conventional fibre morphology with similar fibre diameter (~300-400 nm) cross-section and cylindrical surface. i.e., no significant change was observed in the morphology of the as-spun fibres, which appears unable to explain the formation of variable porosity in the annealed fibres.

To further examine whether there is any structural change in the as-spun polymeric fibres, XRD analysis was performed. **Figure 5.7** shows the XRD pattern of the C_o, C_1 and C_2, pure PVP nanofibers without any tin precursor. The XRD pattern of the pure PVP showed a typical amorphous powder diffraction pattern containing a broad and diffused peak at ~23°. Inorganic crystalline phases (judged from the sharp peaks) were observed in the as-spun polymeric samples. To check whether these peaks belong to unreacted tin chloride or tin hydroxide $Sn(OH)_4$ upon hydrolysis of $SnCl_4.5H_2O$, the XRD patterns of these materials were recorded and compared in the **Figure 5.7**. The $Sn(OH)_4$ was synthesized by precipitating a clear $SnCl_4.5H_2O$ aqueous solution using ammonium hydroxide. It is clear from the XRD patterns that the phases in the polymeric fibres are neither from $SnCl_4$ nor from $Sn(OH)_4$. The crystal structure of the phases could not be identified; however, the peaks show a reversal of intensity for C_2 (PNFs) compared to C_1 (MPNFs) indicating the change in orientation of the crystallites, which might be causing variable porosity upon changing the precursor concentration.
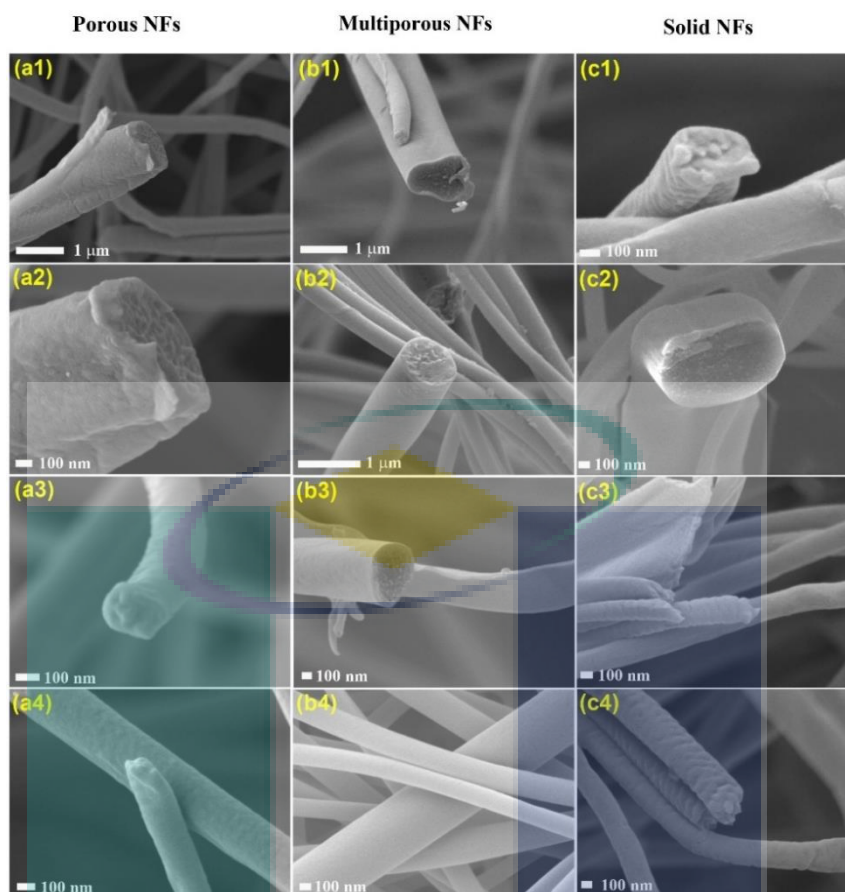
Figure 5.6: FESEM cross section view of the synthesized as spun nanostructure for (a1-a4) PNFs, (b1-b4) MPNFs, (c1-c4) solid NFs at varying magnification level.
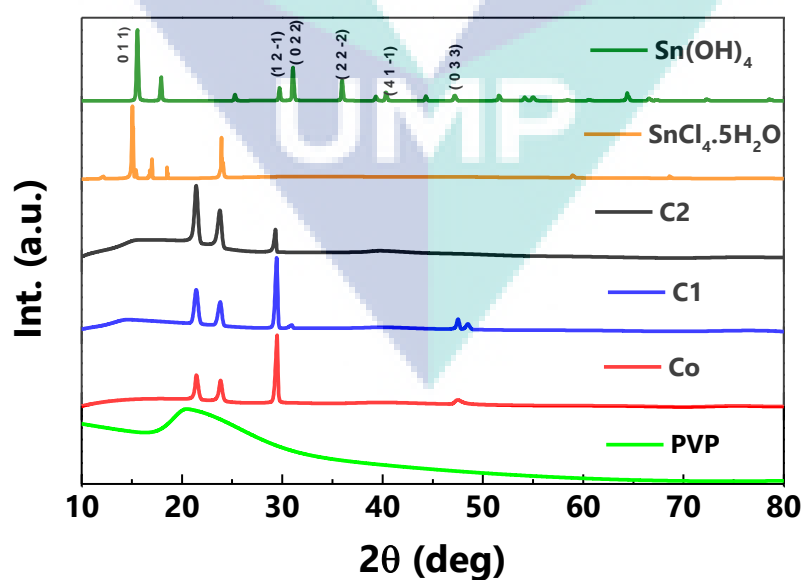
Figure 5.7: XRD pattern of the as-spun fibres of concentration C_o, C_1, and C_2 compared along with pure PVP nanofibers, $SnCl_4.5H_2O$ precursor, and $Sn(OH)_4$.

Furthermore, chemical analysis of the three as-spun (C_o, C_1, and C_2) fibres were made by Fourier transform infrared spectroscopy (FTIR), and compared with PVP fibres and $SnCl_2.5H_2O$ precursor. It can be seen from **Figure 5.8** that the major absorption band lies at ~1630 cm^{-1} for as-spun (C_o-C_1) fibres, PVP fibres, and $SnCl_2.5H_2O$ showing similar functional groups. Another principal absorption band centred (at ~1200 cm^{-1}) was observed for the three as-spun fibres arising from the adsorbed moisture in the sample. Therefore, the FTIR spectra does not convey a profound inference on the chemical structure of the respective fibres.
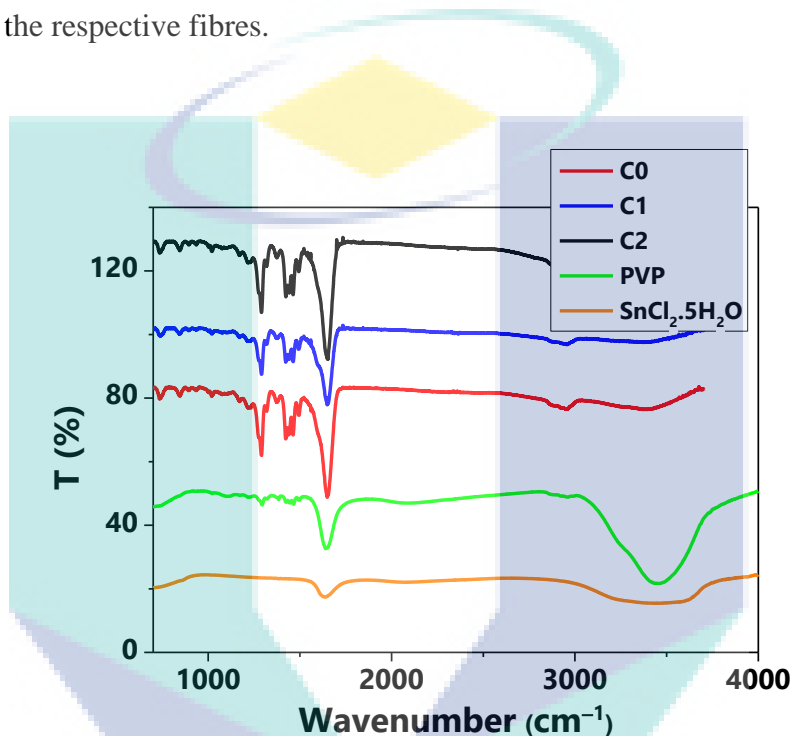
Figure 5.8: FTIR curves of the three (C_o, C_1, and C_2) as-spun fibres along with PVP fibres and $SnCl_2.5H_2O$ precursor.

5.2.4 Gas Adsorption Studies of the Annealed Samples

The surface properties of the above nanostructures were measured using BET surface analyzer. Briefly, the BET surface area of the samples varied in the range of 7-78 m^2/g i.e., C_o ~7, C_1 ~78, C_2 ~12, C_3 ~10, and C_4 ~10 m^2/g. In addition, the difference in the pore size and volume distribution between these nanostructures were studied by adsorption-desorption test in the N_2 atmosphere. **Figure 5.9 (a-e and f)** present the adsorption-desorption isotherms for the samples (C_o-C_4), and pore diameter distribution, respectively. According to the IUPAC classification of adsorption isotherm, type IV

104

curve describe the nanostructure, which composed of mesopores (2-50 nm). The BJH method is commonly employed to determine the volume and size distribution of mesopores and micropores (Rouquerol et al., 1994, Olivier, 1998). Characteristic features of the type IV isotherm plots are its hysteresis loop, which is associated with the filling and emptying of mesopores by a phenomena called capillary condensation (Sing, 1985). In the present experiment, all five types of samples exhibit type IV isotherms, and their average pore and volume size are listed in **Table 5.2**. It is observed that sample C_o contains the highest pore diameter (~60.7 nm) and C_1 the lowest (12.2 nm).

Therefore, to summarize, although various characterizations methods such as SEM, XRD, and FTIR have been conducted in order to understand the formation mechanism of the MPNFs and PNFs, there was no clear evidence obtained using these techniques.
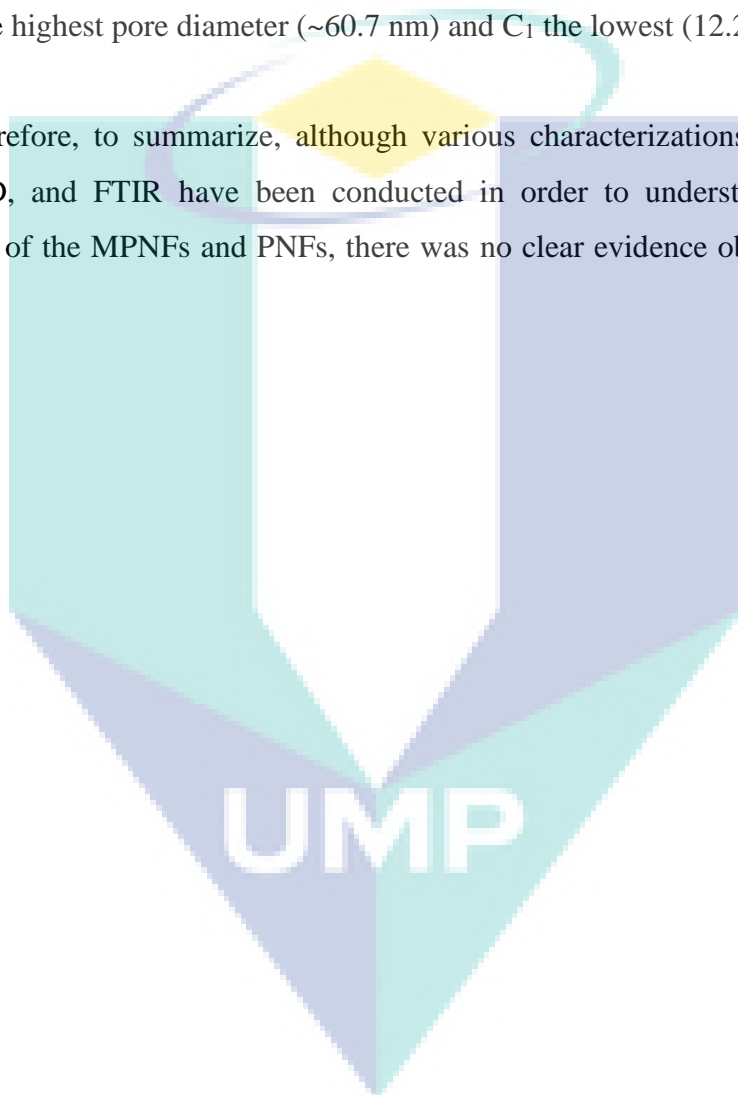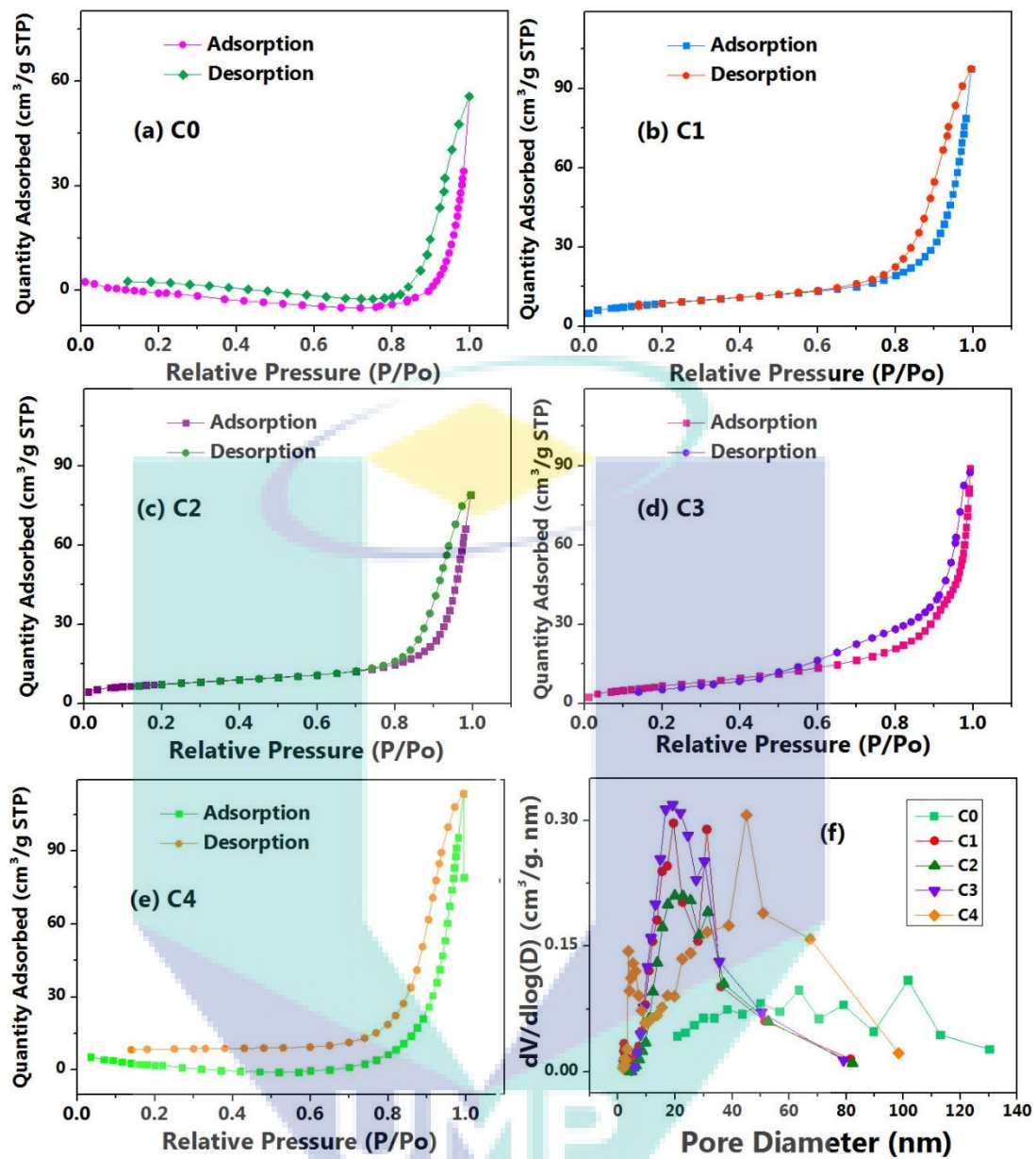
Figure 5.9: Gas adsorption-desorption isotherm curves (a-e) for sample C_o, C_1, C_2, C_3, and C_4, respectively and (b) Pore diameter distribution of the respective samples.

5.3   DSSCS FABRICATION AND TESTING

5.3.1   Morphology and Thickness of the Electrodes

To see any changes in the morphology of the synthesized PNFs and MPNFs after passing through an extensive mechanical agitation during the past making procedure and then thermal annealing, images of the prepared coated electrodes were recorded. In **Figure 5.10**, the FESEM images are displayed showing the cross-sectional view of the photoanodes fabricated using PNFs and MPNFs. Thickness of the films measured from the FESEM images were 17 ± 0.5 µm. It is interesting to note that the PNFs and MPNFs retained their morphologies even after extensive mechanical agitation during the paste making procedure and subsequent thermal annealing. No agglomeration was found in the photoanode film; ensuring high porosity for efficient electrolyte penetration and superior charge transport (Zhang and Cao, 2011)

5.3.2   Light Scattering Properties of the Dye Anchored Electrodes

Light harvesting properties of the dye-anchored WE were studied by UV-VIS - NIR absorption spectroscopy. The light scattering properties of the electrodes were studied by recording their absorbance (**Figure 5.11**) and transmittance (**Figure 5.12**). **Figure 5.11** shows that electrode prepared using PNFs and MPNFs showed similar absorption curve although slightly improved absorbance was observed for the latter due to its high specific surface area.

Superior light harvesting property of the electrode synthesized using MPNFs is more obvious in the transmission spectra (**Figure 5.12**). This is due to the fact that MPNFs are highly porous and contains multichannels inside a single fiber so that it could increase the reflection of light and eventually enhance the optical path length for incident photons (Grätzel, 2009). The transmittance of the electrodes were < 20 and ~40 at the λ ~600-750 nm for MPNFs and PNFs, respectively. Thus, ~80% of the incident light is absorbed by the MPNFs electrode, whereas considerable portion of the incoming light is transmitted in the PNFs electrode.
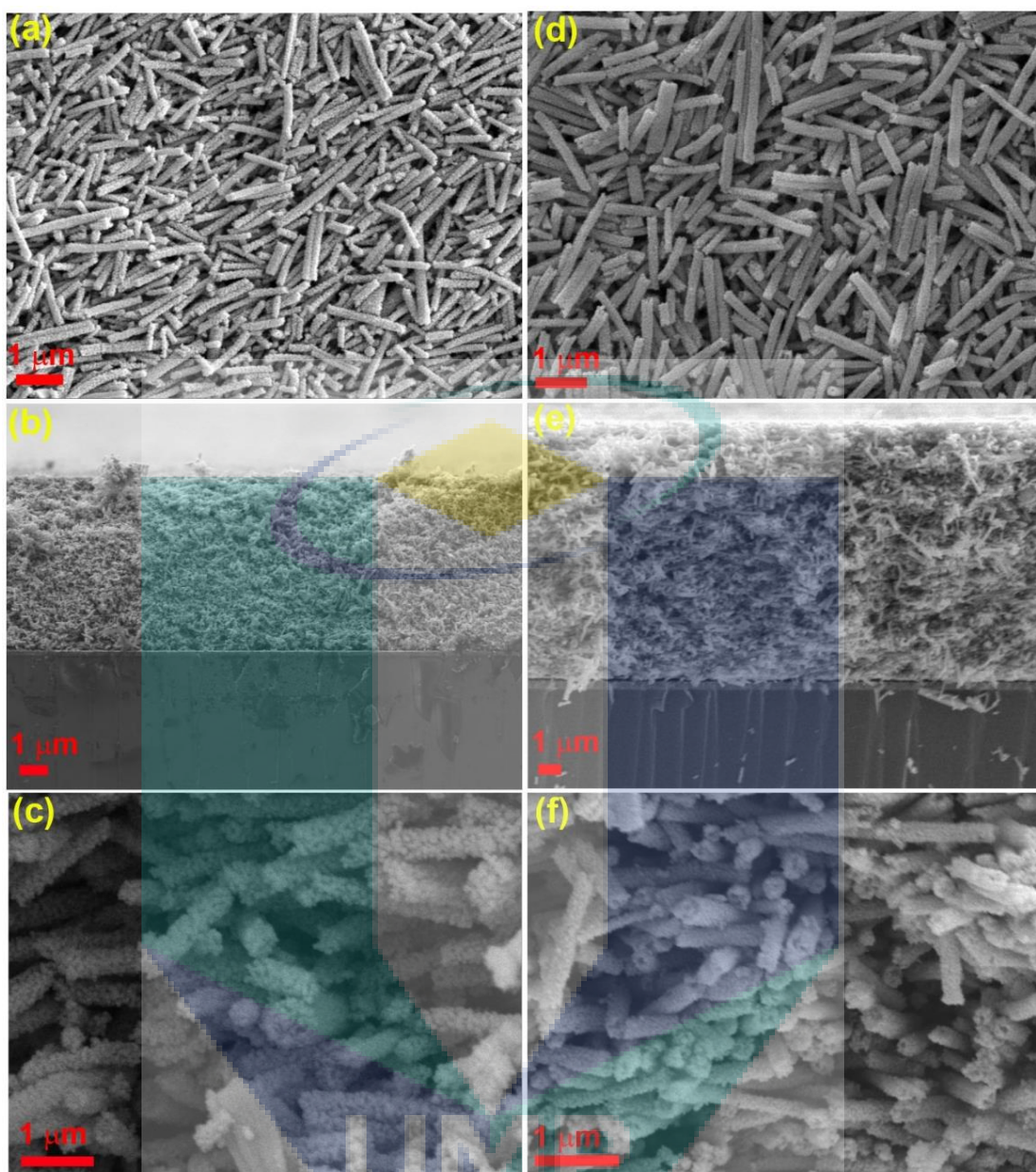
Figure 5.10: FESEM top view of the coated FTO substrates (a & d), while (b & e) and (c & f) illustrate the cross section view at low and high magnification of PNFs and MPNFs electrodes.
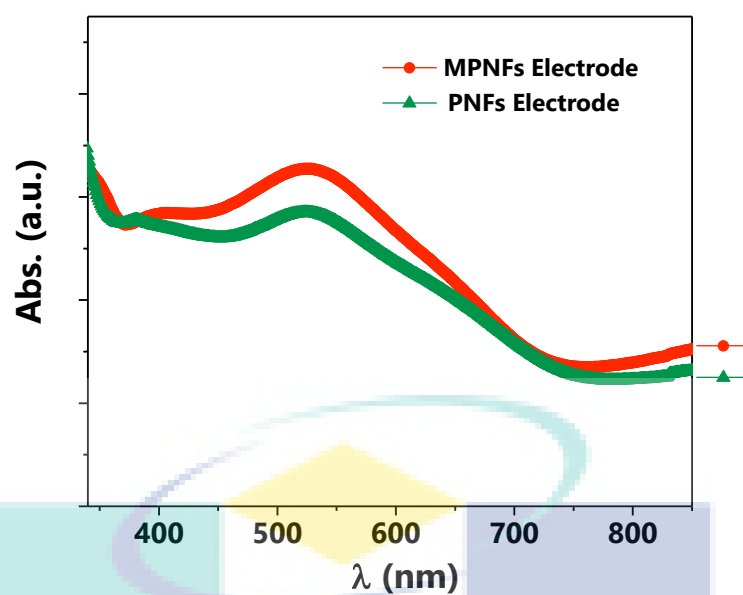
Figure 5.11: Absorption spectra of the PNFs and MPNFs dye anchored electrodes.
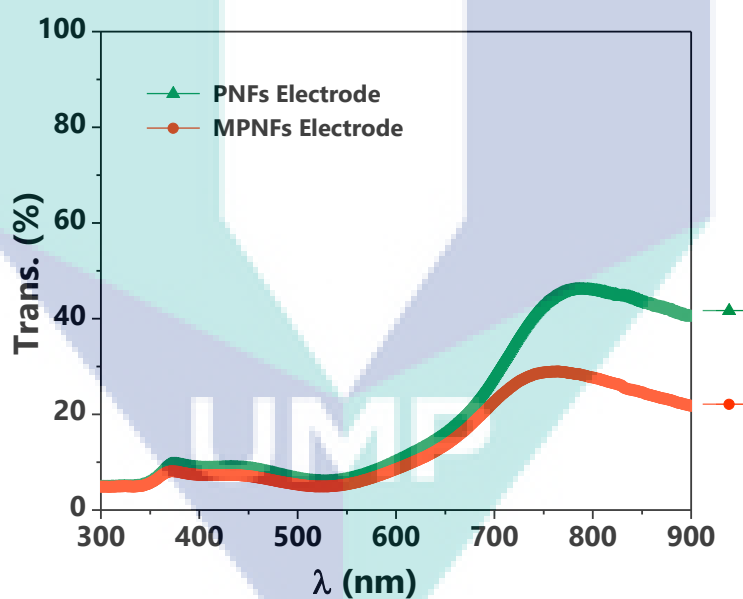
Figure 5.12: Transmission spectra of the PNFs and MPNFs dye anchored electrodes.

The dye-loading on photoanodes was calculated by the desorption test and their curve are shown in **Figure 5.13**. The calculated dye-loading of MPNFs is 3.38×10^{-7} nmole.cm^{-2} which is over 4 times larger than that of PNFs (0.83×10^{-7} nmole.cm^{-2}). The significantly enhanced dye-loading is attributed to the higher surface area of MPNFs. Besides, they have highly porous morphology, i.e., multiple channels inside a single NF,

which ultimately provides more bonding sites on the outer as well as inner side for dye anchoring group as compared to the single channel fiber counterpart. A control electrode of TiO$_2$ was also fabricated using commercial P25 paste. The dye-loading of the P25-based electrode (7.02×10^{-7} mol.cm^{-2}) is twice that of the MPNFs based electrodes owing to its two-fold higher surface area (~100-150 m^2/g) than the later. The lower surface area of the SnO$_2$ MPNFs is owing to the lower IEP (~4 – 5 at pH) thereby make weak bonding to the carboxylic groups of the ruthenium based dyes .On the other hand, TiO$_2$ NPs possess IEP (~6 – 7, at pH) and therefore make a strong bonding group with carboxylic groups with carboxylic group and consequent enhance the dye loading.
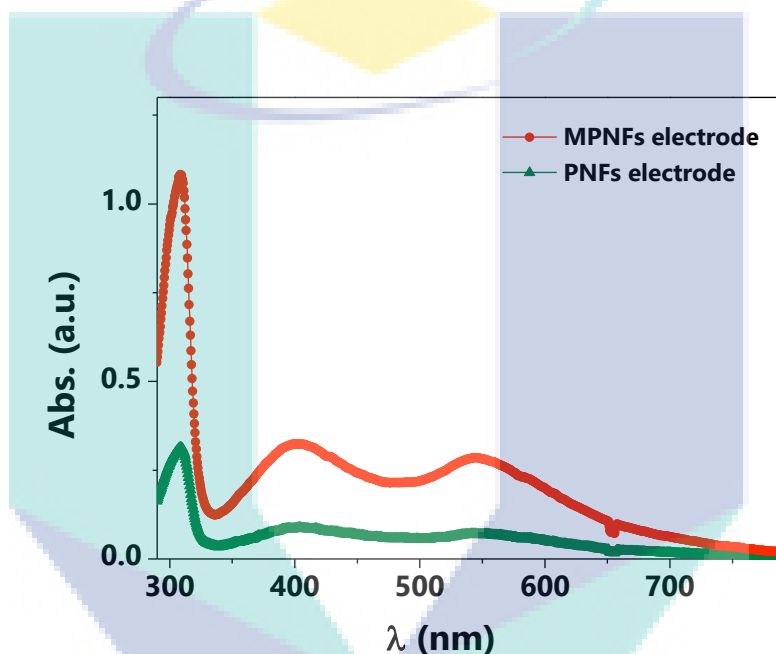
Figure 5.13: UV-VIS-NIR absorption spectra of the desorbed dye of the electrodes fabricated using PNFs and MPNFs.

5.3.3 Photovoltaics Characteristics of Tin Oxide Nanostructures

To realize the effect of increased surface area in MPNFs, photoanodes were fabricated for DSSCs. I-V analysis of the DSSCs are shown in **Figure 5.14** and the corresponding PV parameters are listed in the **Table 5.6**. As expected from high surface area of MPNFs, a high J$_{SC}$ ~18 mA cm^{-2} and η ~4.3% were obtained for the MPNFs DSSCs, while those for PNFs DSSCs are (J$_{SC}$ ~10 mA cm^{-2} and η ~2%). The V$_{OC}$ in MPNFs DSSCs showed an increment of ~0.57 mV as a consequence of the enhanced J$_{SC}$. The FF of both DSSCs remained practically the same (0.49 in MPNFs and 0.45 in PNFs).

As the thickness of both electrodes was same, the presence of multichannels in MPNFs and their smaller D value compared to PNFs, which resulted up to 8 times increased surface area and up to 5 times larger dye loading, is attributed to the higher J_{SC}. A reference P25 DSSC was fabricated to shows its comparison with SnO_2 based DSSCs. The P25 DSSC resulted in η ~7.6% with other PV parameters (V_{OC} ~0.72 V, J_{SC} ~17.4, and FF ~0.61), which shows (~45%) higher V_{OC} and (20%) large FF than the PNFs and MPNFs DSSCs. However, MPNFs DSSC exhibit superior photocurrent than that of TiO_2 based DSSC (**Table 5.6**). The low V_{OC} and FF are the main issues in SnO_2 based DSSCs due to its lower conduction band edge (L A Harris and Wilson, 1978), which results in high electron recombination with the electrolyte species (Kay and Grätzel, 2002, Ferrere et al., 1997, Gubbala et al., 2008). A remedy for this issue has been developed and are explained in the next chapter.
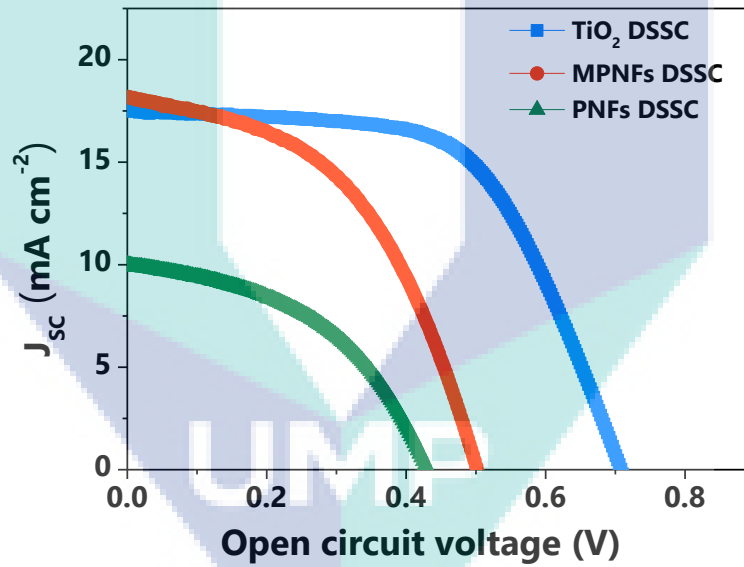
Figure 5.14: Current voltage characteristic curve of DSSCs fabricated using synthesized PNFs, MPNFs and a reference cell based on TiO_2 P25 NPs under standard 1 sun condition with intensity of 1000 W m^{-2}.

Table 5.6

PV parameters, Jsc, Voc, FF, η and dye loading of DSSCs fabricated using PNFs, MPNFs and P25 NPs, respectively (Film thickness of the devices kept at ~17 μm)

DSSCs	J_{SC}/ mA cm^{-2}	V_{OC}/ V	FF	η/ %	Dye loading/ n mole.cm^{-2}
PNFs	10	0.45	0.45	2.0	83
MPNFs	18	0.51	0.49	4.3	338
P25 NPs	17.4	0.72	0.61	7.6	702

5.3.4 Charge Transport Properties of DSSCs

Electrochemical impedance analysis (EIS) is a useful tool used to explore the charge transport and transfer mechanism in the DSSC. The EIS for the PNFs DSSC and MPNFs DSSC was studied under dark condition. The Nyquist and Bode phase plots of both devices are shown in **Figure 5.15**. The intermediate peak in the Nyquist plot **(Figure 5.15a)** of the MPNFs DSSC shows large diameter as compared to that of PNFs DSSC assuring high recombination resistance and consequently resulted long τ_n as $\tau_n = (C\mu \times R_{CT})^{1/2}$ (Bisquert, 2002). In bode phase plot, the MPNFs DSSC peak shifts **(Figure 5.15b)** towards lower frequency than that of PNFs counterpart showing long τ_n. The calculated τ_n for the both devices from mid peak frequency of the bode-phase plots using a relation $\tau_n = 1/2\pi f_o$ (Le Viet et al., 2010) where f_o is the maximum frequency at the mid peak. The calculated values of f_o were ~14 Hz and ~29 Hz with corresponding τ_n ~11 ms and ~5 ms for the MPNFs DSSC and PNFs DSSC, respectively. Long τ_n implies that electrons could survive for a long time in the photoanode material before recombining with electrolyte species and consequently leads to high PV performance (Azhar Fakharuddin, 2014, Zaban et al., 2003). Although both nanostructures are having 1D nature and prepared from the same materials, the better performance of MPNFs over PNFs could be due to its multichannel inside a single fibres.
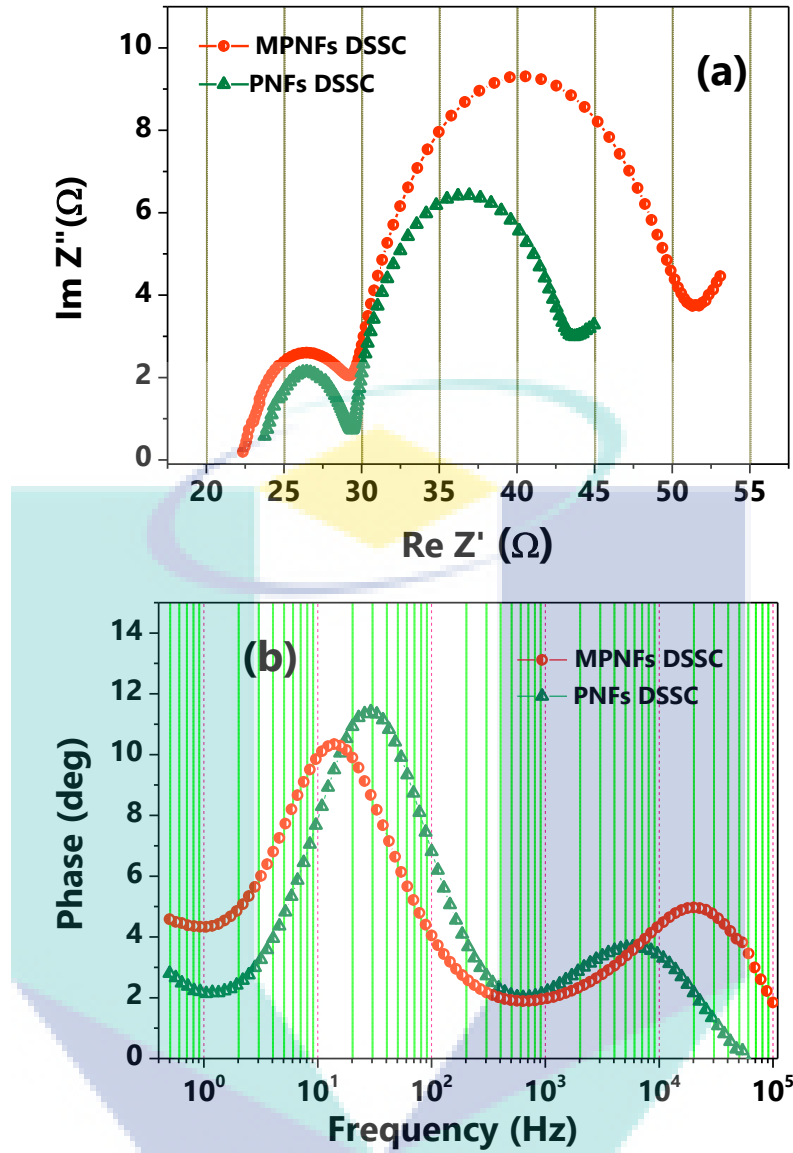
Figure 5.15: (a) Shows Nyquist plot and (b) Bode phased plots for PNFs and MPNFs DSSC.

To further analysis the better performance of the MPNFs DSSC, an OCVD measurement was performed. It is a simple technique to investigate real-time recombination kinetics in DSSCs by changing their equilibrium state from illuminated to dark. **Figure 5.16a** illustrates OCVD curves of the PNFs, MPNFs, and P25 DSSC, respectively. It is evident that the V_{OC} decay rate was significantly lower for MPNFs DSSC as compared to PNFs and P25 DSSC suggesting low recombination of photoexcited electrons. **Figure 5.16b** compared the τ_n of the (PNFs, MPNFs and P25 DSSC), which was calculated using their OCVD curves. The MPNFs DSSC showed the highest τ_n; for example, at 0.3 V, MPNFs gave τ_n ~7 sec whereas it was 2.3 and 1.47 sec

for PNFs and P25 DSSC, respectively. The calculated τ_n for P25 DSSC in our case is similar to that obtained by (Zaban et al., 2003) i.e., (~20 ms-1s) for a P25 NPs based high efficiency DSSCs. The high τ_n observed in SnO$_2$ can be attributed to their 1D morphology as well as improved charge mobility through it.
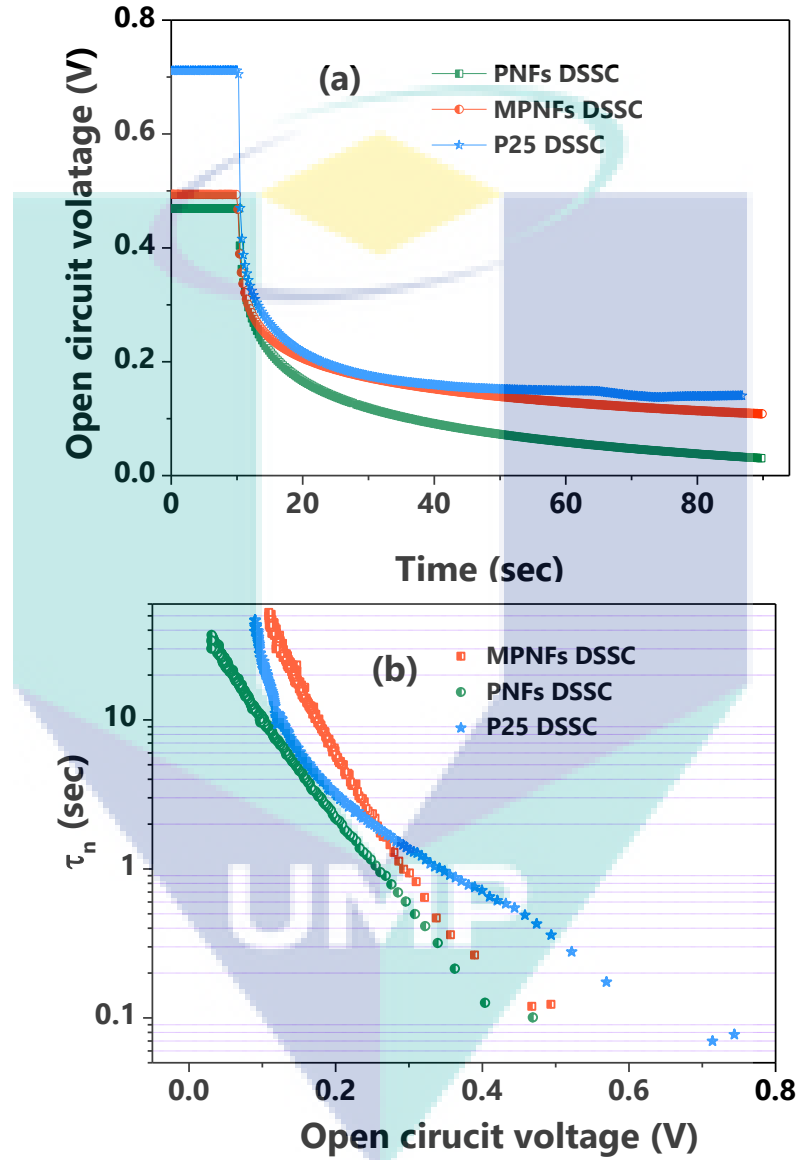
Figure 5.16: (a) Shows OCVD and (b) shows the τ_n calculated from the OCVD curve vs. V$_{OC}$ of the MPNFs, PNFs, and P25 DSSCs.

η_{cc} of the PNFs, MPNFs, and P25 DSSC were compared from τ_n and electron transit time (τ_d) by using an expression $\eta_{cc} = 1/1 + (\tau_n/\tau_d)$ (Cai et al., 2011). It is obvious from **Figure 5.17a** that MPNFs DSSCs showed ~21% increased charge collection than that

of P25 DSSC and slightly improved charge collection against PNFs DSSC in photoanodes of similar thickness (17±0.5 µm). This increment is owing to the fact that the diffusion length $L_n = L\sqrt{R_{CT}/R_T}$; (Wang et al., 2006, Fakharuddin et al., 2014a, Hara and Mori, 2011) i.e., the distance travelled by the photoinjected electrons before they recombine with the electrolyte specie in MPNFs based photoanodes is 2-3 times higher than that of P25 DSSC. The L_n, which is ~70-75 µm in MPNFs DSSC, ~65-70 µm in PNFs and ~30-35 µm in P25 DSSC (**Figure 5.17b**), clearly establishes the nature of the porous nanostructures. Thus, an enhanced τ_n and significantly higher L_n demonstrates the beneficial effects when 1D nanomaterial MPNFs architecture are employed as a photoanode material.
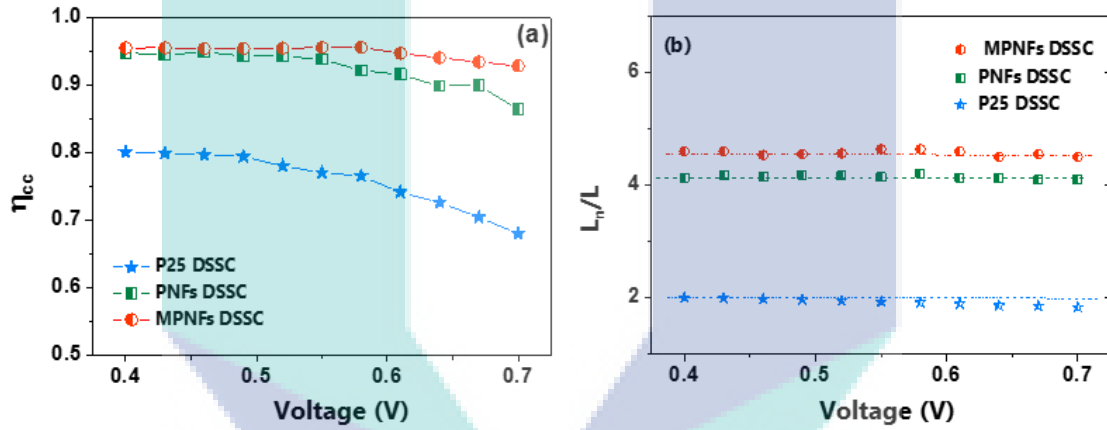
Figure 5.17: (a) Charge collection efficiency of the PNFs, MPNFs, and P25 DSSC (b) electron diffusion length calculated using a well-known electrical equivalent model for the both devices.

Furthermore, to validate the higher photocurrent of the MPNFs DSSCs, IPCE measurement was performed. The IPCE curves of the three devices (PNFs, MPNFs, and P25 DSSC) are shown in **Figure 5.18**, and J_{SC} was calculated **(Chapter 3, Eq. 3.17)**. The integrated IPCE over the entire λ was used to calculate the J_{SC}. The calculated J_{SC} of the MPNFs, PNFs, and P25 DSSC were ~17.8, ~10.3, and ~15.2 mA cm^{-2}, respectively, which agrees closely with their measured J_{SC} from the I-V measurements **(Table 5.6)**. A significant increase in the IPCE of the MPNFs over the others two was observed. The highest IPCE for MPNFs, PNFs, and P25 DSSCs are ~83%, ~57%, and ~68%, respectively. The increased IPCE of the MPNFs DSSCs over the PNFs could be attributed to its significantly larger dye-loading and desirable charge transport characteristics.

However, its dye-loading is only half to that of P25 DSSC thereby indicating that improved J_{SC} of the MPNFs results from both dye-loading and desirable charge transport characteristics.

Moreover, an enhanced light scattering in the case of both MPNFs and PNFs is noticed at $\lambda > 560$ nm which is attributed to the bigger size of 1D porous material than that of P25 particles. An improved charge transport in SnO_2 can be normally expected due to its many fold increased μ_e compared to that of the TiO_2. The charge transport parameters such as L_n, τ_n, and IPCE of the three DSSCs are compared in **Table 5.7**. It is clear from the data that MPNFs DSSC possesses superior charge transport properties over the PNFs as well as P25 DSSC.
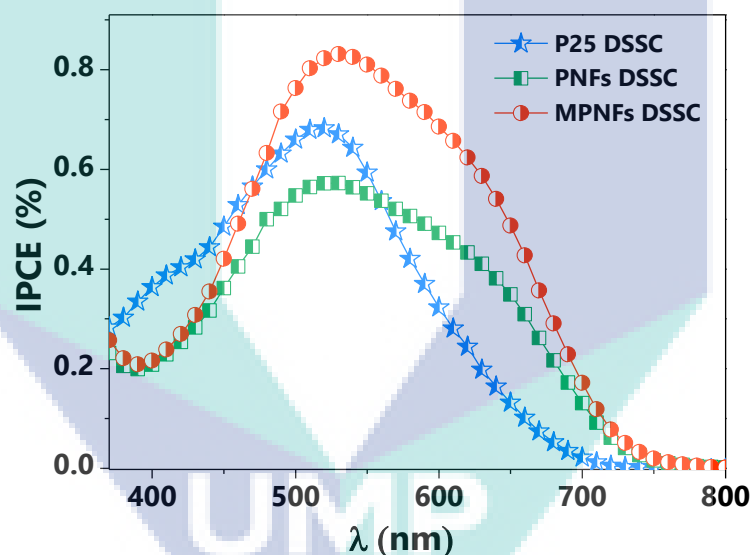
Figure 5.18: Incident photon to current conversion efficiency curves of the PNFs, MPNFs, and P25 DSSCs.

Table 5.7
Charge transport parameters (diffusion length, electron life time using bode phase plot, OCVD, and IPCE) for the PNFs, MPNFs, and P25 DSSC

Devices	L_n (μm)	τ_n (ms) Bode Phase	τ_n (sec) OCVD	IPCE (%)
PNFs DSSC	~68	5	2.3	57
MPNFs DSSC	~72	11	7	83
P25 DSSC	32	5.3	1.47	68

5.4 CONCLUSIONS

In conclusion, while 1D nanostructure routinely produce low surface area, MPNFs showed tremendously high surface area (~80 m^2/g) due to their hollow nature and the presence of multichannel inside a single fiber. High surface area MPNFs adsorbed large amount of dye molecules and therefore achieved a significant high photocurrent. In addition, MPNFs DSSC exhibit significantly superior charge transport properties such as high crystallinity, high IPCE, long diffusion length and long life time to that of PNFs counterpart. An overall final η ~4.3% was achieved using MPNFs as a photoanode material, while PNFs yielded η merely half of it.
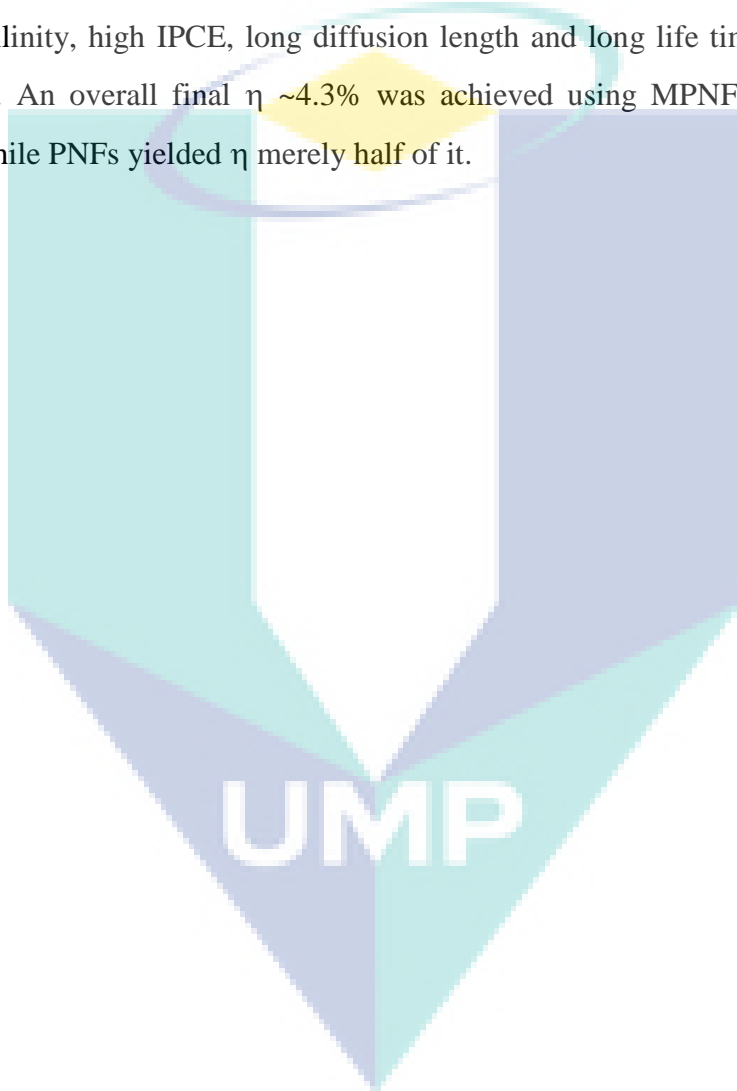
RESULT & DISCUSSION: COMPOSITE TIN OXIDE NANOSTRUCTURES

6.1   INTRODUCTION

This chapter highlights the development of composite nanostructures of SnO_2 and TiO_2 using two different approaches in order to address the lower V_{OC} and FF of pure SnO_2 DSSCs observed in chapter 4 and 5. In the first approach, two types of composite are formed by a solution treatment (i) TiO_2 NPs composited with SnO_2 multifunctional NPs-NSs and (ii) SnO_2 MPNFs- TiO_2 NPs. To further improve the PV parameters in these composites, a composite (SnO_2-TiO_2) NFs is formed by electrospinning. While in the first approach both the TiO_2 and SnO_2 nanostructures are first synthesized from two different precursor solutions, the second approach aim to synthesize a composite from a single precursor solution in order to combine the benefits of the two different materials.

6.2   CHARACTERIZATION OF COMPOSITE NANOSTRUCTURES

6.2.1 Phase and Crystallinity of Composite Nanostructures

The phase and crystallinity of the pure SnO_2 MPNFs and $TiCl_4$ treated electrodes were examined by XRD technique (**Figure 6.1**). The crystal structure of the composite SnO_2 MPNFs showed tetragonal cassiterite phase, space group P4$_2$/*mnm* with lattice parameters a = b = 4.635 Å and c = 3.165 Å. These values match precisely with the

standard data (JCPDS Card No 41-1445). All XRD patterns reflect the existence of pure SnO_2 peaks; however, new peaks emerged in the composite architectures evidencing the presence of TiO_2, particularly at a higher $TiCl_4$ molar concentrations. A new (004) plan is observed at $2\theta \sim 36.48^o$ in the SnO_2-TiO_2 composite, corresponding to anatase TiO_2, the intensity of which increased systematically with increasing TiO_2 NPs concentration, i.e., from 0.1 M to 0.5 M. However, at a higher molar concentration (0.5 M) rutile phase is also observed as evidenced by (110) and (111) peaks at ~ 28 and $\sim 41.61^o$, respectively.

Furthermore, an additional anatase peak (211) at $\sim 54.76^o$ is also observed due to the excess TiO_2 NPs formation using 0.5 M. Electrodes were also prepared using higher $TiCl_4$ molar concentrations such as (~ 0.75 M & 1 M). However, thicker layers tend to vanishes in the $TiCl_4$ solution or crack upon heat treatment as reported previously (Kavan et al., 1993). The major peaks of anatase structure were not seen (in all $TiCl_4$ composite nanostructures) after annealing at ~ 450 ^{o}C due to the fact that the $TiCl_4$ layers are extremely thin (below ~ 250 nm). On the other hand, it is expected that a $TiCl_4$ layer with thickness above ~ 1 μm must have the anatase structure (Kavan et al., 1993). Although characterization to realize the thickness of TiO_2 overlayer is not carried out in our study, the absence of TiO_2 XRD peaks at lower molar concentrations and presence of TiO_2 peaks at high concentration suggest that the systematic change in $TiCl_4$ concentration is correlated with the TiO_2 overlayer thickness as observed by (Kavan et al. 1993).
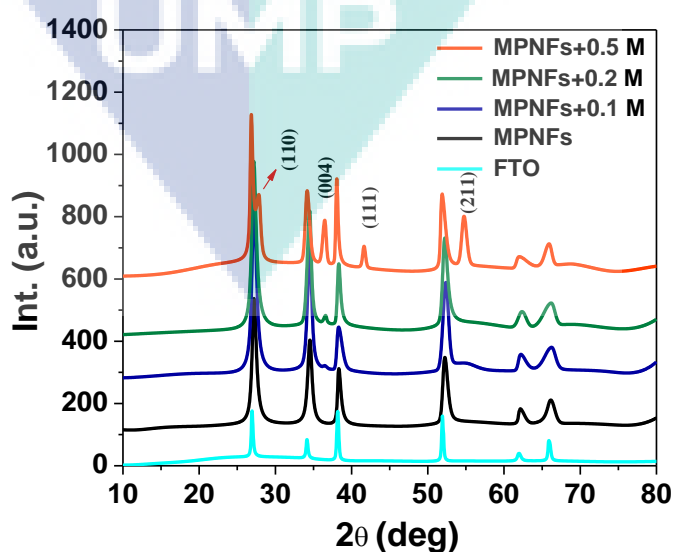
Figure 6.1: XRD pattern of the various treated electrodes along with FTO substrate as a reference.

119

The XRD analysis **(Figure 6.2)** of electrospun (SnO_2-TiO_2) NFs from a single precursor solution also showed principal peaks for SnO_2 such as (110), (101) and (211) however, these peaks are broader than those observed in previous composites (those formed from two different precursor solutions). The composite XRD was also compared with pure SnO_2 NFs and TiO_2 (anatase & rutile) in order to investigate the broadened FWHM of the former. The widening of the composite peaks can be attributed to the combined chemical behavior of SnO_2 and TiO_2.
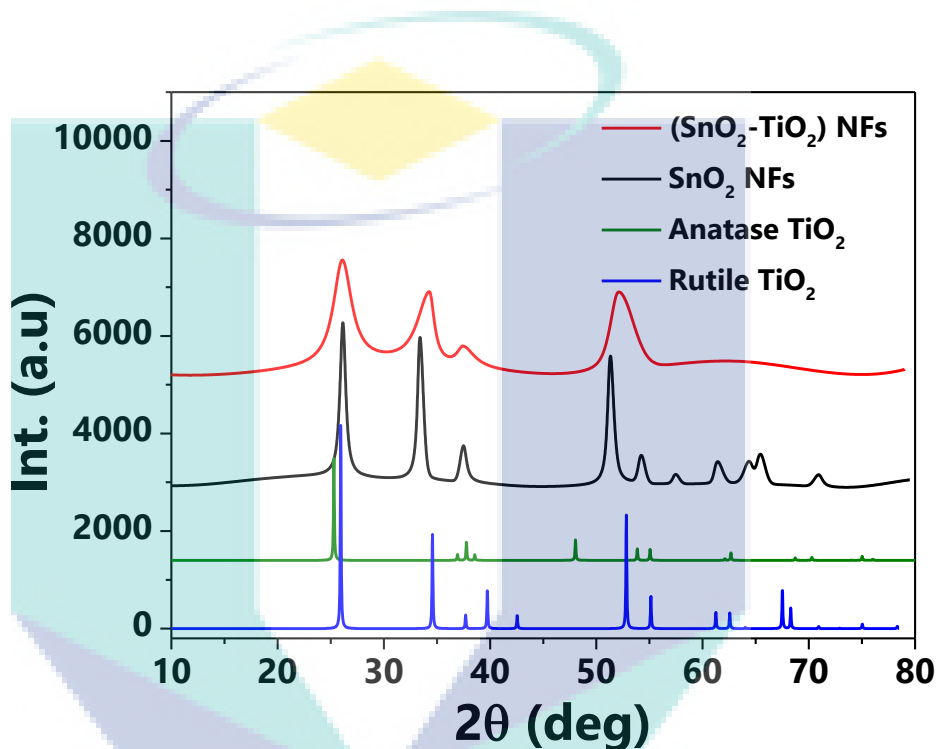
Figure 6.2: XRD pattern of the electrospun (SnO_2-TiO_2) NFs along with pure SnO_2 NFs and TiO_2 (anatase & rutile).

To further understand the variation in the crystallinity of chemically synthesized SnO_2-TiO_2 composite, we employed HTREM and SAED **(Figure 6.3)**. The lattice spacing of the HTREM images are clear throughout the materials and index to ~0.3-0.34 nm, which are in close agreement with both SnO_2 and TiO_2 values. The SAED pattern showed a concentric circles, which reveals that the material is polycrystalline. The bright concentric circles also corroborates to the XRD peaks of the composite NFs. This suggests the key difference between the two types of composites; while the mixing of two types of nanostructures or post-treatment of one (TiO_2) on the surface of another (SnO_2) formed a composite which may still have dominant separate chemical identities, a

composite formed chemically from a single solution, on the other hand, tends to have a single chemical identity and the two different materials are scarcely distinct.
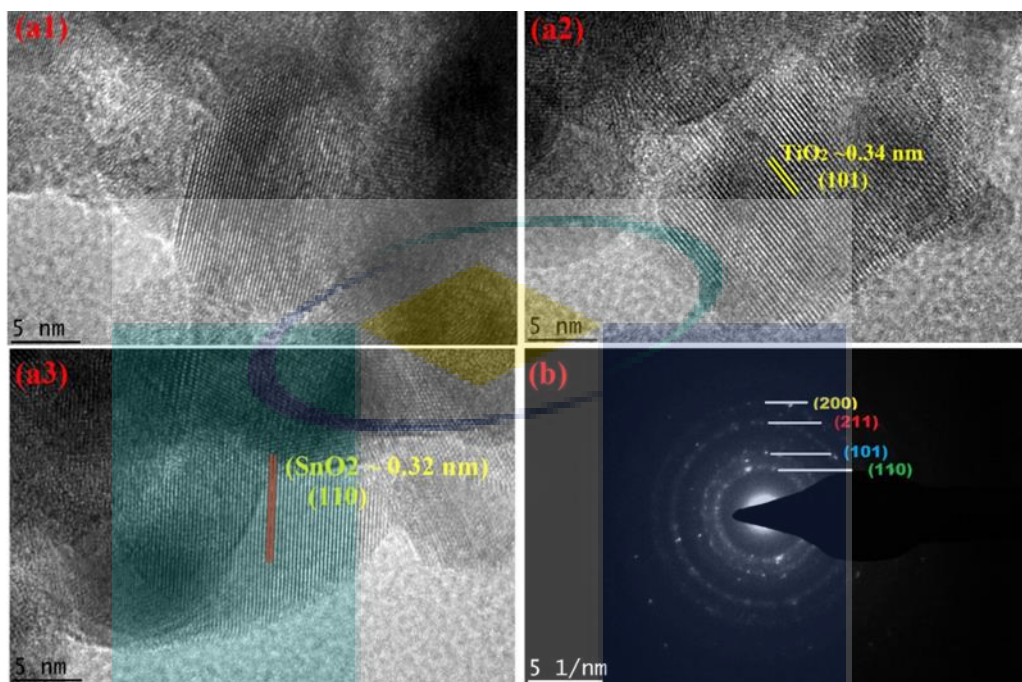
Figure 6.3: HRTEM images show (a1-a3) and (b) SAED pattern of the electrospun (SnO$_2$-TiO$_2$) NFs composite.

6.2.2 Morphological Properties of Composite Photoanodes

As shown in Chapter 5 that the MPNFs yielded significantly higher PV parameters compared to those of PNFs, they have been chosen in order to further tailor their PV performance to match TiO$_2$ counterparts. The calcined MPNFs coated electrodes were treated with various TiCl$_4$ molar concentration (0.1, 0.2 and 0.5 M) aqueous solutions (for detail TiCl$_4$ procedure see Section 3.6.1). The effect of various TiCl$_4$ concentrations on the MPNFs surface morphology is shown in **Figure 6.4**. The pure SnO$_2$ MPNFs exhibit porous morphology; however, upon TiCl$_4$ post treatment, the pores in the MPNFs start to fill **(Figure 6.4d1 & d2)** evidencing the formation of thin TiO$_2$ particles eventually resulting in SnO$_2$-TiO$_2$ nanocomposite. Although the effect is not very apparent for lower TiCl$_4$ molar concentration (0.1 M) treatment, as can be seen from the surface of NFs, which might be due to a conformal TiO$_2$ coating over SnO$_2$ MPNFs surface. The higher concentrations systematically developed nanoparticles of size (~5-10 nm), which not only

formed a thin TiO_2 overlayer on MPNFs but also filled the gaps between them resulting in an improved interconnectivity of the grains.
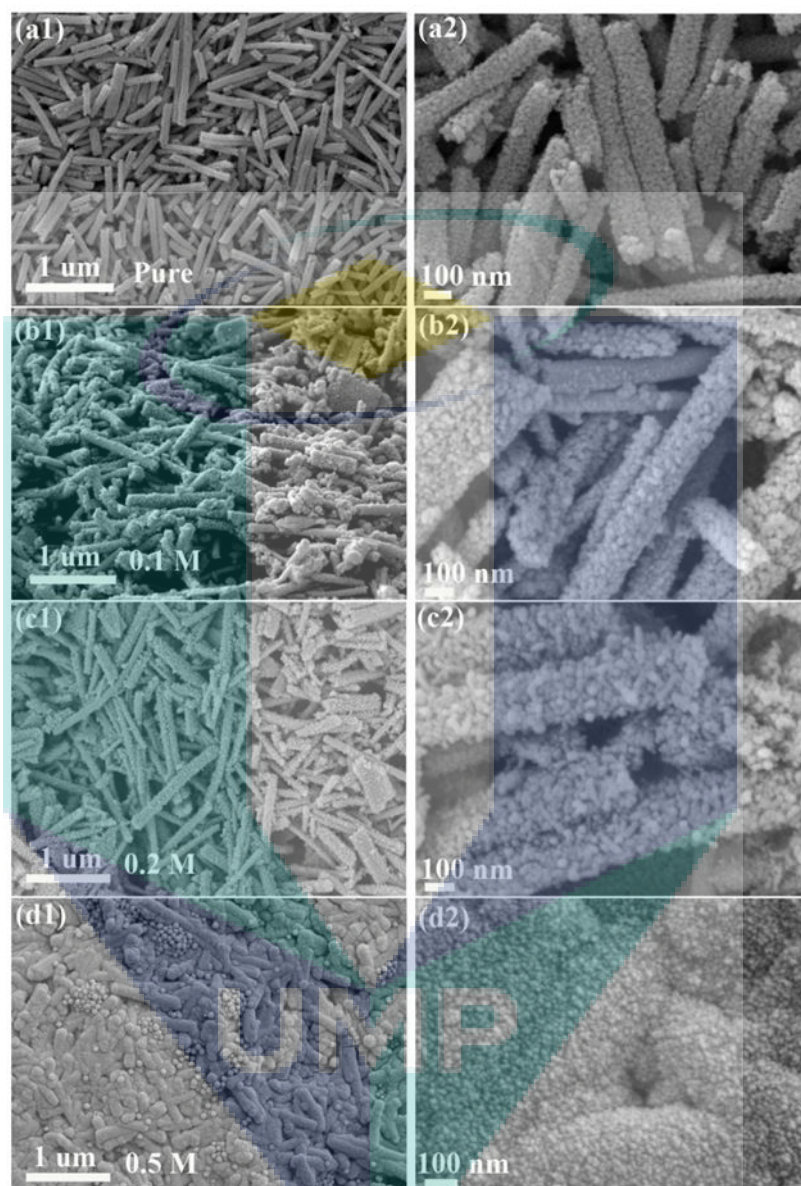
Figure 6.4: FESEM surface images (a1 & a2) show pure SnO_2 MPNFs electrodes and (b1-d2) demonstrate (0.1, 0.2, and 0.5 M) $TiCl_4$ molar concentrations on pure SnO_2 MPNFs electrodes.

An improved physical interconnection i.e., (the voids between the NFs are filling due to the access number of TiO_2 NPs increasing from 0 M to 0.5 M) of NFs in the photoanode film upon $TiCl_4$ post treatment is also clear from their cross sectional images **(Figure 6.5b1-d2)**. Although porosity of the photoanode materials favors electrolyte

penetration and enhance dye uptake, it increases grain boundary density and decrease particle-particle interconnectivity thereby suppresses charge transport properties (Park et al., 1999). TiO$_2$ NPs served as a medium to fill the voids in pure MPNFs (**Figure 6.4d1 & d2**), which is expected to increase the transport properties in the photoanodes of the DSSCs. The decrease in porosity and filling voids can also be seen upon increasing TiCl$_4$ molar concentration (**Figure 6. 4b1-d2**). Interestingly, the SnO$_2$ MPNFs film thickness remains unchanged upon TiO$_2$ NPs via TiCl$_4$ solution process; however, it only filled the gaps between the NFs. This suggest that the overlayer formed by TiCl$_4$ is too thin to be separately realized by FESEM in composite morphology.
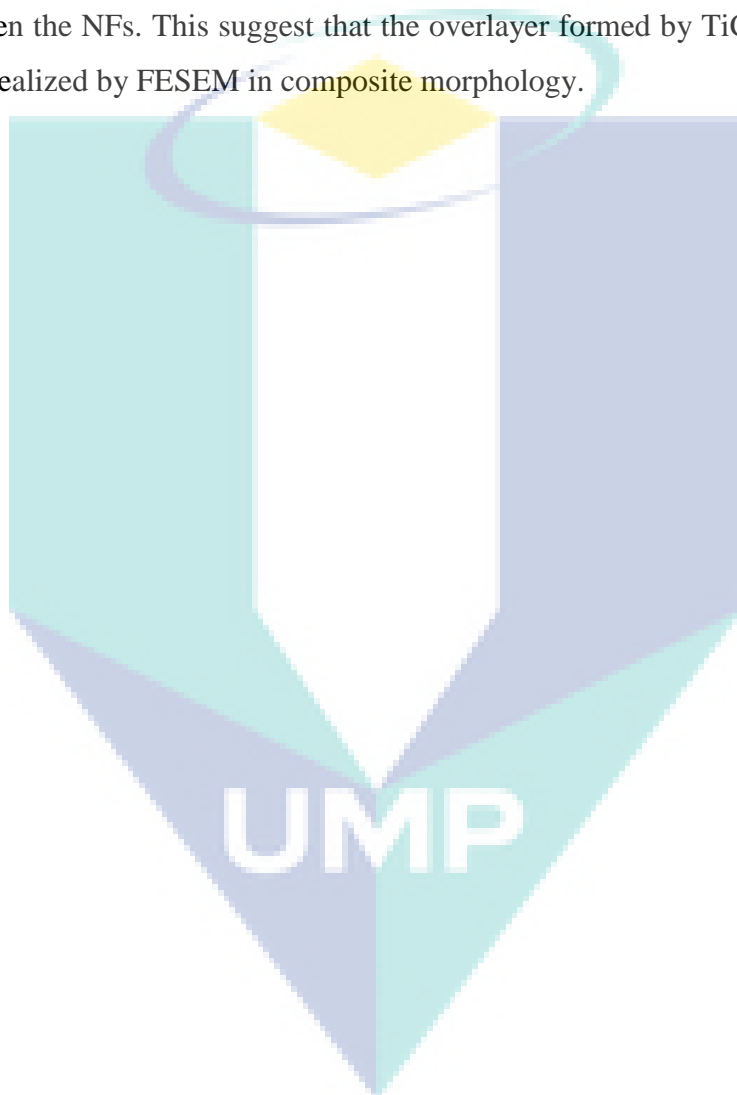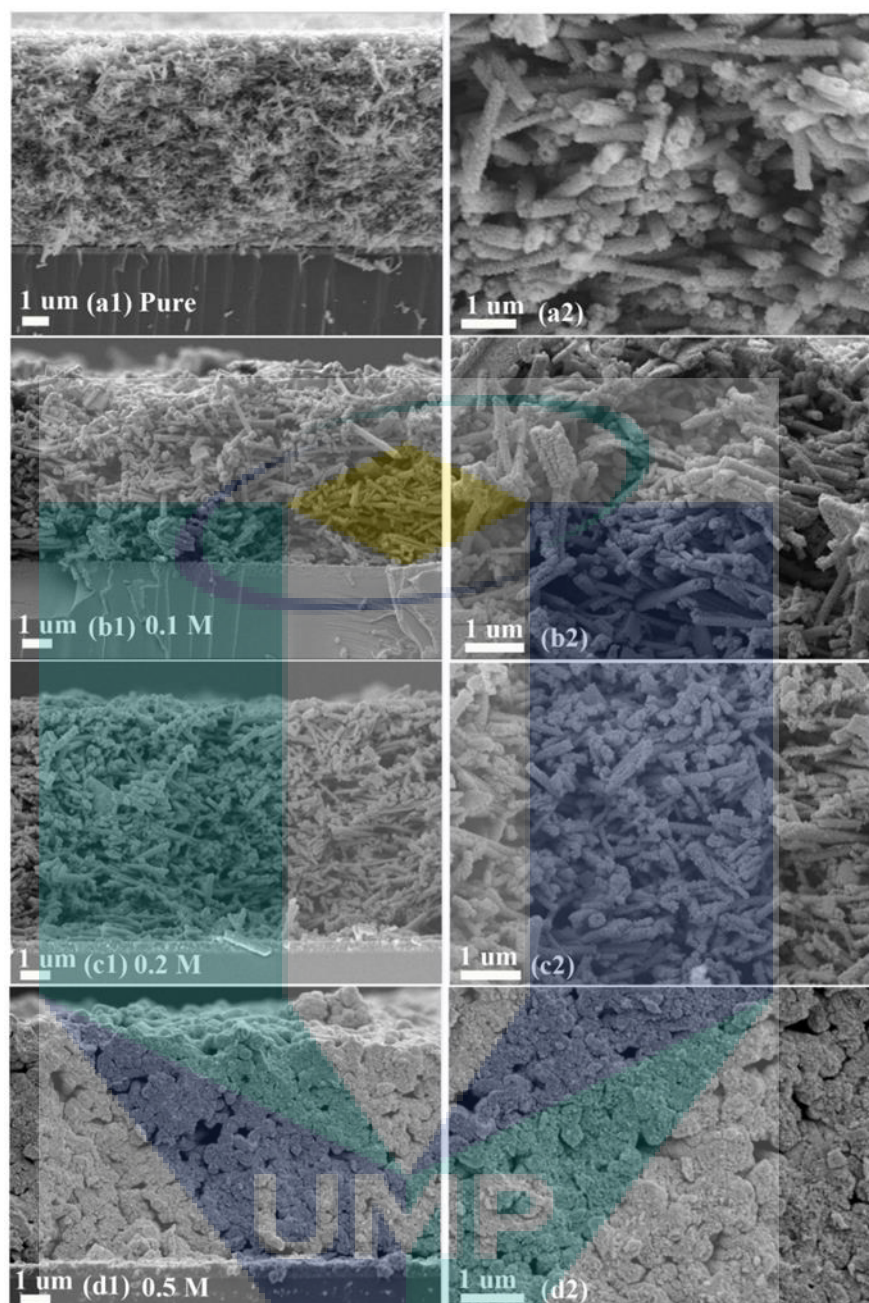
Figure 6.5: FESEM cross-section view of the pure SnO$_2$ MPNFs (a1 & a2) and passivated electrodes (b1-d2) using 0.1, 0.2, and 0.5 M TiCl$_4$ molar concentrations at different magnifications.

6.2.3 Morphological Features of Electrospun Composite

The details of synthesis of electrospun (SnO$_2$-TiO$_2$) nanofibers composite is described in Section 3.3.2. The synthesized electrospun composite nanostructures were examined by FESEM analysis. **Figure 6.6** demonstrates surface morphology of the

annealed composite NFs, which shows smooth surface morphology. The diameter of the fibres ranges between 200-300 nm as can be seen from the higher FESEM magnification images.
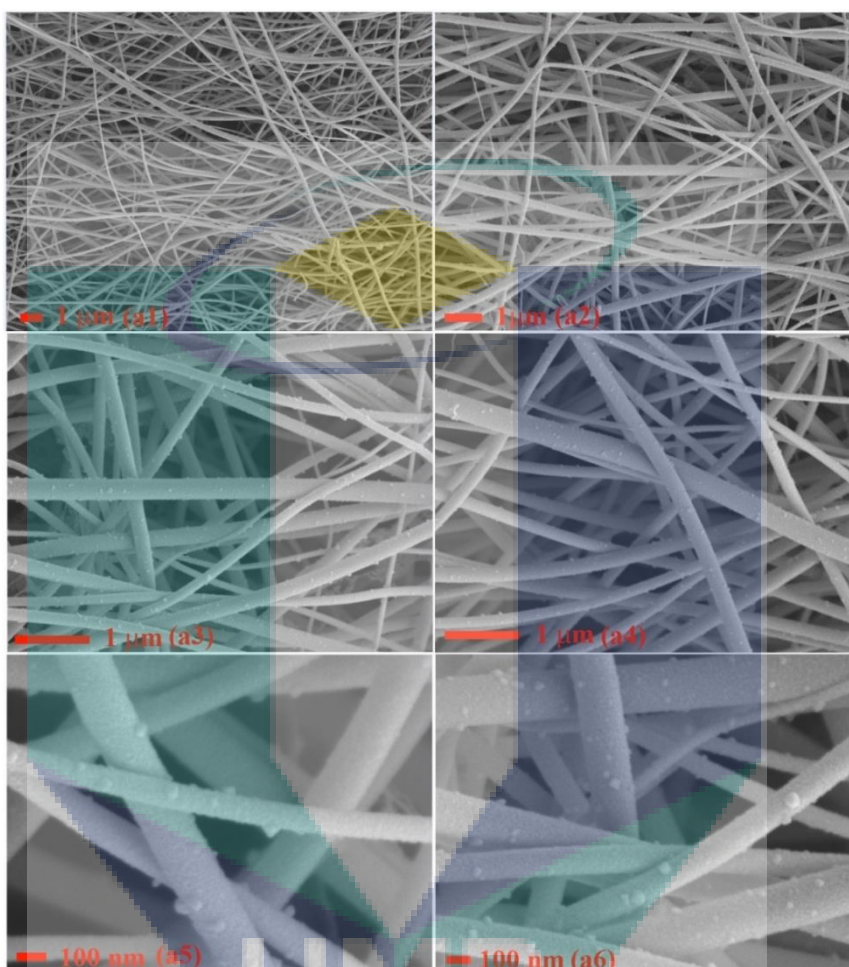
Figure 6.6: FESEM surface morphology images of (SnO$_2$-TiO$_2$) NFs from low to high magnification (a1-a6).

Cross sectional view **(Figure 6.7)** of the synthesized nanocomposites reveal that, contrary to the surface analysis, the composite NFs are in fact hollow in nature, similar to those of MPNFs (explained in chapter 5). This additional feature offered by composite NFs, as typical TiO$_2$ NFs formed by electrospinning are solid and do not offer tubular morphology.
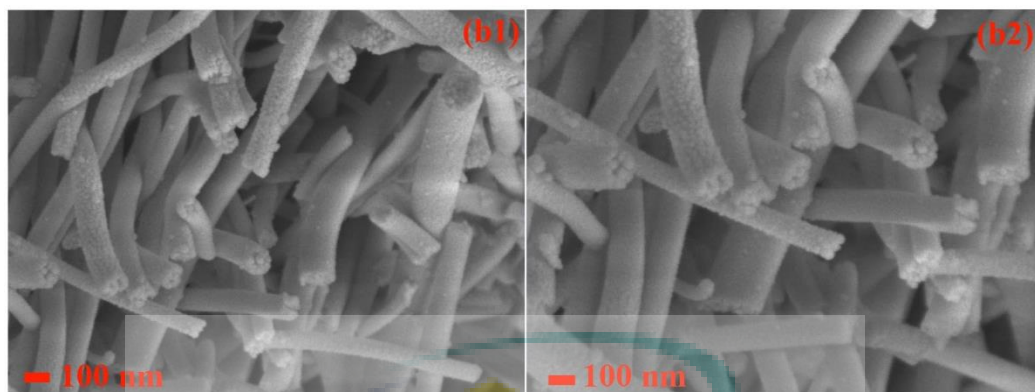
Figure 6.7: FESEM cross sectional morphology images of (SnO$_2$-TiO$_2$) NFs from low to high magnification (b1&b2).

In order to confirm the formation of (SnO$_2$-TiO$_2$) NFs composite EDX analysis was performed. During the EDX measurement different areas were focused and the corresponding peaks are shown in **Figure 6.8a-c**. Both SnO$_2$ and TiO$_2$ can be seen in the synthesized composite nanostructure in the EDX spectrum. In spectrum 1, the quantity of Sn, Ti and O were 9.67, 10.71 and 79.62, respectively, while in spectrum 2, the values were (11.67, 13.48 and 74.85 measured in atomic % for Sn, Ti and O, respectively). Details of the three EDX spectra of the electrospun (SnO$_2$-TiO$_2$) NFs values measured in atomic and weight % are listed in **Table 6.1**.
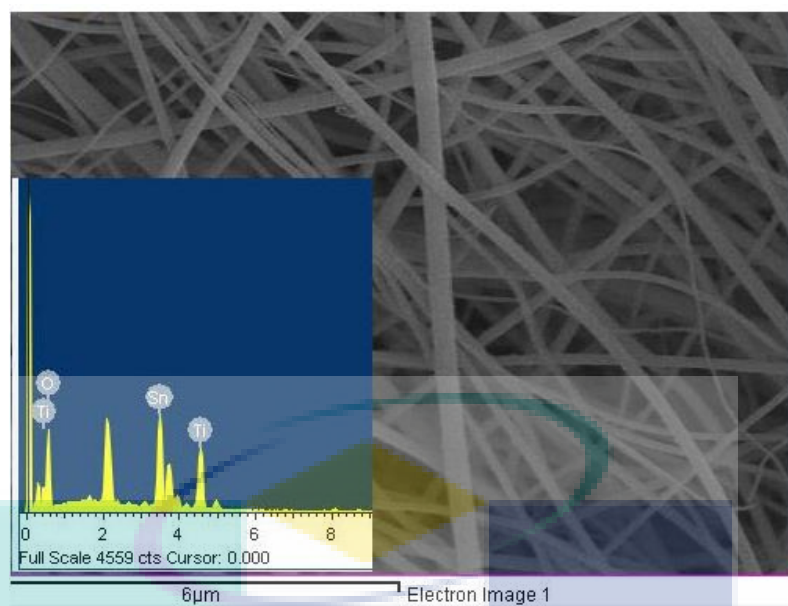
Figure 6.8a: EDX pattern of the electrospun (SnO_2-TiO_2) NFs composite (spectrum 1).
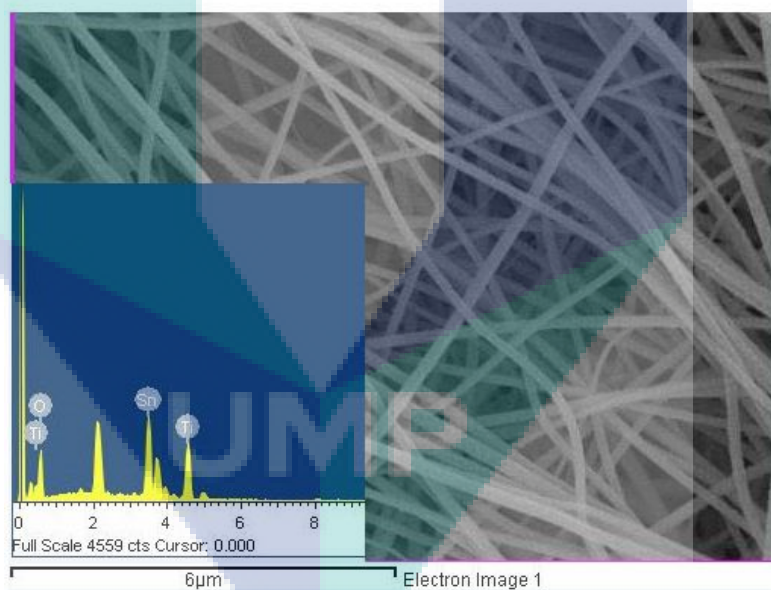
Figure 6.8b: EDX pattern of the electrospun (SnO_2-TiO_2) NFs composite (spectrum 2).
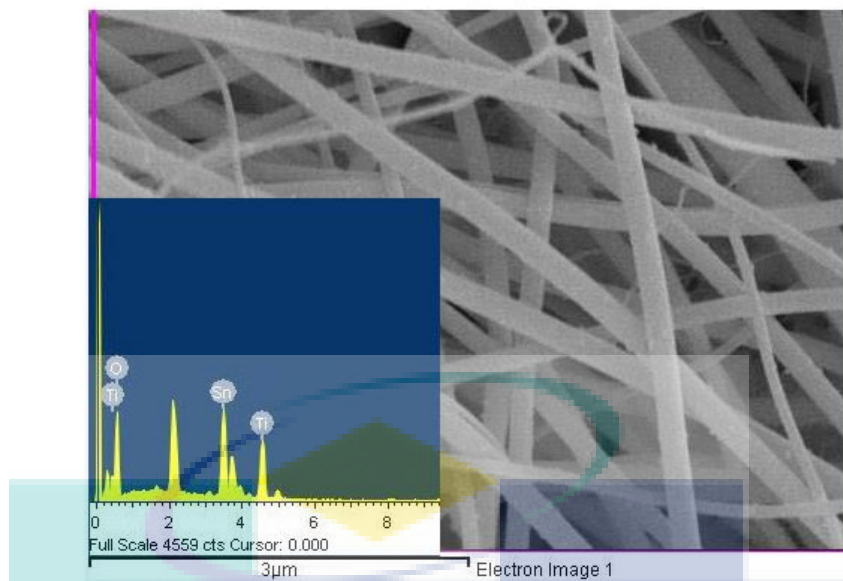
Figure 6.8c: EDX pattern of the electrospun (SnO$_2$-TiO$_2$) NFs composite (spectrum 3).

Table 6.1
EDX weight ratio of electrospun (SnO$_2$-TiO$_2$) NFs nanocomposite using three spectrums focused three distinct areas

(SnO$_2$-TiO$_2$) composite	Tin (Sn)		Titanium (Ti)		Oxygen (O)	
	Weight (%)	Atomic (%)	Weight (%)	Atomic (%)	Weight (%)	Atomic (%)
Spectrum 1	39.10	9.67	17.48	10.71	43.41	79.62
Spectrum 2	42.91	11.67	19.99	13.48	37.10	74.85
Spectrum 3	37.05	8.86	17.37	10.29	45.58	80.85

To further investigate the morphology of (SnO$_2$-TiO$_2$) NFs composite, TEM analysis was performed. **Figure 6.9** shows TEM images of the composite nanostructure at low magnification where highly smooth NFs' surface can be seen, corroborating the findings of FESEM images. The NFs varies in diameter and also shown a partial transparency to an electron beam; from which it is deduced that the NFs are porous. The composite NFs possesses grain size (10-20 nm) and visible grain boundary can be seen throughout the composite material.
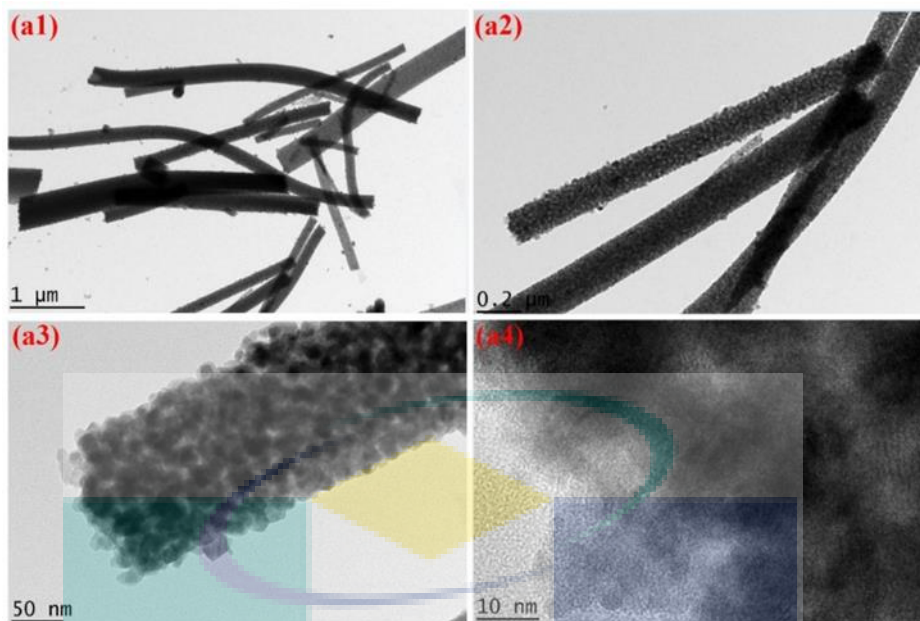
Figure 6.9: (a1-a4) depict TEM images of the electrospun (SnO$_2$-TiO$_2$) NFs composite.

6.3 DSSCS FABRICATION AND TESTING

6.3.1 Dye Loading of the Electrodes

Dye loading of the dye anchored electrodes was measured by desorption test as shown in **Figure 6.10** (for detail analysis of desorption test see Section 3.6.2). The spectra of the desorbed dye solution show that MPNFs electrode treated with 0.5 M concentration exhibit significantly higher dye loading (262 nmole.cm^{-2}) than other molar treatments. The dye loading dramatically decreased for the lower TiCl$_4$ concentration as can be observed from the **Figure 6.10**. Moreover, electrospun SnO$_2$-TiO$_2$ NFs composite electrodes shows inferior dye loading due to the lower surface area while the hydrothermal multifunctional (NPs-NSs) showed dramatic increase when treated with TiCl$_4$. On the other hand, TiO$_2$ P25 surpass the dye loading owing to the nature of these particles which having the highest surface area (~150 m^2/g). Dye loading values of the pure and TiCl$_4$ treated electrodes are listed in **Table 6.2**.
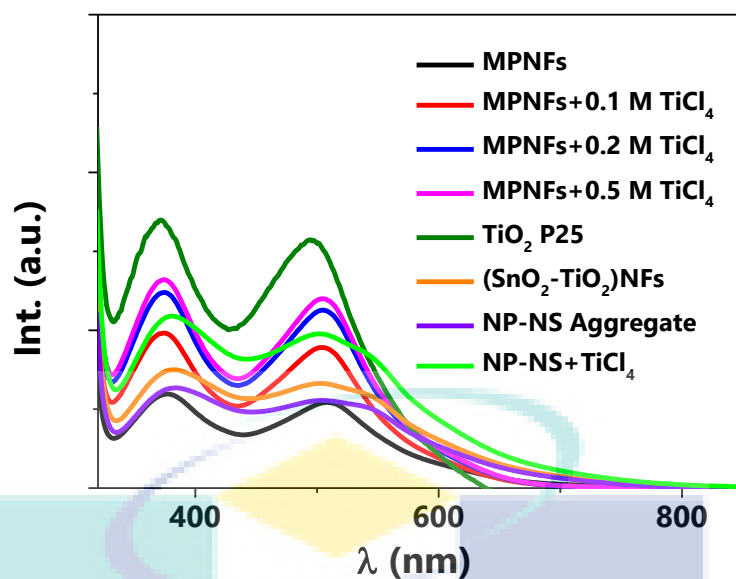
Figure 6.10: UV-VIS-NIR absorption spectra of the desorbed photoanodes for pure SnO_2 MPNFs, multifunctional NPs-NSs, TiO_2 P25 NPs, (SnO_2-TiO_2), and post treated electrodes at different $TiCl_4$ concentrations (0.1, 0.2 and 0.5 M) on MPNFs and multifunctional particles.

6.3.2 Photovoltaics Characteristics of the DSSCs

It has been revealed in Chapter (4 & 5) that hydrothermal multifunctional NPs-NSs and electrospun MPNFs performed notably better than other SnO_2 morphologies and generated a comparable J_{SC} (~17-18 mA cm^{-2}) to that of the TiO_2. However, the V_{OC} (~480-500 mV) and FF (~45-50%) were far lower than that of TiO_2 (typically ≥800 mV & 60-70%) and therefore DSSCs made from their composite photoanodes were investigated.

J-V characteristics of the best performing devices are shown in **Figure 6.11**. The PV parameters of pure and composite DSSCs are listed in **Table 6.2**. It is obvious that the η of the DSSCs increased in the order i.e., multifunctional NPs-NSs ($\eta_{multifunctional\ NPs-NSs\ +TiCl4} > \eta_{multifunctional\ NPs-NSs}$), which showed ~80% higher η (~7.5%) than the parent device **(Table 6.2)**. Although the $TiCl_4$ treated DSSCs yielded a higher J_{SC} (~21%) than the P25 DSSC, a ~20% lower FF of the former restricts its performance than its TiO_2 counterpart. On the other hand, MPNFs electrodes were treated using various $TiCl_4$ concentration, which yielded ($\eta_{MPNFs+0.5\ MTiCl4} > \eta_{MPNFs+0.2\ MTiCl4} > \eta_{MPNFs+0.1\ MTiCl4} > \eta_{Pure\ MPNFs}$).

130

Table 6.2

Photovoltaic parameters of DSSCs (J_{SC}, V_{OC}, FF, η and dye loading based on pure (Multifunctional NPs-NSs and MPNFs), passivated MPNFs electrodes with (0.1, 0.2 and 0.5 M) $TiCl_4$ aqueous solution and an electrospun composite of (SnO_2-TiO_2)NFs

DSSC/ WE	J_{SC}/ mA cm^{-2}	V_{OC}/ V	FF	η/ %	Dye loading/ n mole.cm^{-2}
Pure (NPs-NSs)	16.3	0.490	0.49	4.0	131
Pure MPNFs	17.5	0.491	0.50	4.3	119
MPNFs+0.1 M $TiCl_4$	18.3	0.570	0.50	5.2	192
MPNFs+0.2 M $TiCl_4$	19.1	0.620	0.50	5.9	245
MPNFs+0.5 M $TiCl_4$	22.0	0.720	0.53	7.9	262
(NPs-NSs) +$TiCl_4$	21.33	0.705	0.53	7.5	180
(SnO_2-TiO_2) NFs	16.0	0.732	0.64	7.5	173
P25 NPs	17.49	0.730	0.60	7.6	745

The pure MPNFs showed an enhanced J_{SC} (~18 mA cm^{-2}) however, limited in V_{OC} (~470-500 mV) and FF (~45-50%). Initially, the MPNFs electrode was treated with 0.1 M $TiCl_4$, which increased the J_{SC} (From 18 mA cm^{-2} to 18.3 mA cm^{-2}), V_{OC} (~490 mV to 570 mV) and a slightly increase in FF was observed with overall η of ~5.2% with a subsequent 0.2 M $TiCl_4$ solution post-treatment dramatically increased the V_{OC} up to ~620 mV with a marginal increase in the J_{SC} and FF that resulted a final η of ~5.9%. Nonetheless, the η was still far lower than the most successful employed MOS TiO_2 (~14.3%). Finally, the pure MPNFs electrode was passivated with higher $TiCl_4$ molar concentration (0.5 M), which resulted in an exceptional η ~8% with V_{OC} ~720 mV close to that of TiO_2 based DSSCs in our experiments (~730 mV) and yielded notably higher J_{SC} ~22 mA cm^{-2} (J_{SC} of TiO_2 ~17 mA cm^{-2}). Upon further increase in $TiCl_4$ concentration the post-treated photoanode films cracked during the hydrolysis process or upon sintering which is in close agreement with the reported results (Kavan et al., 1993). It appears that the $TiCl_4$ post-treatment only increases the V_{OC} and J_{SC} significantly and has only a minor impact on the FF of the devices. The increment in J_{SC} is attributed to the enhanced dye loading upon $TiCl_4$ post-treatment **(Figure 6.10)** which also have its impact on V_{OC}. Similar improvements in J_{SC} are observed by (Park et al., 1999 and Barbé et al., 1997). The achieved FF (~45-50%) of SnO_2 is still far lower than that of TiO_2 (~60-70%).

From the comparative experiments of pure SnO_2 multifunctional NPs-NSs and MPNFs based DSSCs and their $TiCl_4$ post-treated analogues it is obvious that SnO_2 possesses lower IEP (at pH, ~4-5) and thereby make weak bonding to the carboxylic groups of the ruthenium based dyes. The week bonding consequent in inferior dye anchoring and eventually lower J_{SC}. On contrary, TiO_2 has a high IEP (at pH, ~6-7) therefore make a strong bonding group with carboxylic groups. Thus, the increase in J_{SC} values of the SnO_2 electrodes passivated with $TiCl_4$ solution can be understood from the surface passivation which changes adsorption properties of pure SnO_2 resulting in higher amount of dye loading **(Figure 6.10)** and a surge in J_{SC}.

Another significant improvement in composite photoanodes is the increase in V_{OC}. The lower V_{OC} (~470-500 mV) in pure SnO_2 CB is due to its lower CB than TiO_2 with respect to the most successful ruthenium based sensitizers **(Chapter 2, Figure 2.1)**. The increase in V_{OC} in SnO_2 photoanodes upon $TiCl_4$ post-treatment is attributed to the formation of a TiO_2 NPs thin layer. The physical barrier reduces electron back recombination from SnO_2 CB to dye or with electrolyte so that to increase the number of accommodated electron in the CB of the SnO_2 and eventually enhance the lower V_{OC} as reported. There are two possible electron injection routes for the photoinjected electrons to be injected from the dye's LUMO to the CB of SnO_2, (i) it can pass direct to SnO_2 through the TiO_2 NPs thin layer via tunnelling or (ii) it may first jump into the TiO_2 CB and then into SnO_2 CB owing to the downhill transition. As the V_{OC} and the J_{SC} are correlated **(Eq. 6.2)** (Nazeeruddin et al., 1993, Rosenbluth and Lewis, 1989, Kumar et al., 1992), The above studies showed that $TiCl_4$ post treatment on the pure SnO_2 nanostructures electrodes only improved the V_{OC} and J_{SC}, however the FF remained unchanged throughout the study. The enhancement in V_{OC} and J_{SC} reveals that the injection efficiency of photogenerated electrons into MOS and the blocking behaviour of the MOS-electrolyte interface is improved as also observed by (Kavan et al., 1993).

In order to combine the synergistic properties of SnO_2 higher μ_e and TiO_2 favourable CB in a single photoanode in DSSCs, electrospun (SnO_2-TiO_2) NFs composites were developed. The DSSCs made using the composite NFs resulted in FF ~64%, similar to that of TiO_2 NPs and a similar V_{OC} ~732 mV, however, a slightly decrease in the J_{SC} is noticed **(Figure 6.11)**.
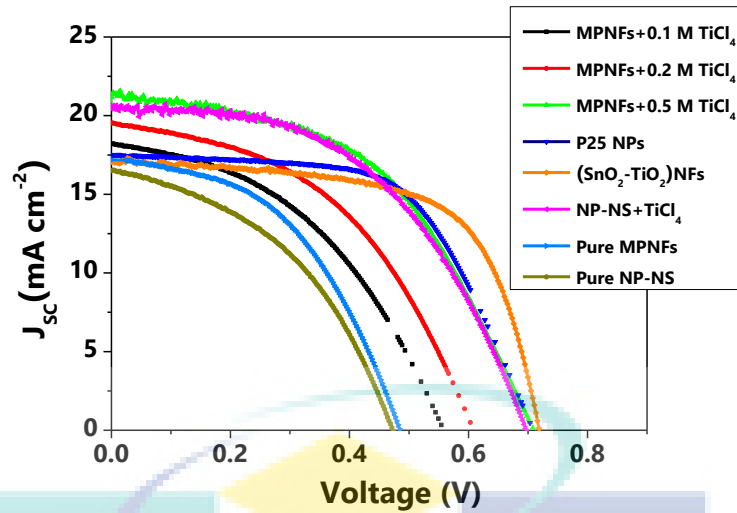
Figure 6.11: Current voltage characteristics curves of DSSCs based on (multifunctional NPs-NSs & MPNFs), passivated MPNFs electrodes with (0.1, 0.2 and 0.5 M) $TiCl_4$ aqueous solution, and electrospun composite of (SnO_2-TiO_2) NFs.

6.3.3   Origin of High Open Circuit Voltage

DSSCs based on pure SnO_2 yielded in inferior PV parameters owing to its lower V_{OC} and FF using conventional electrolyte (I^-/I^-_3) and ruthenium based sensitizers. These two quantities effect the performance of device as $= V_{OC} \times J_{SC} \times FF$. Higher V_{OC} could be achieved if there is a balance between the photoinjected electrons from the LUMO of the dye molecule into the CB of SnO_2 and the transfer of electrons from the CE to an electrolyte. The increase in V_{OC} is due to the suppression of the back reaction at the SnO_2-electrolyte interface, which originates between the CB electrons and I_3^- species of the electrolyte. Although MOS surface is covered with the dye, the I_3^- species either could penetrate the dye and recombine with the CB electrons of the MOS or access the unanchored exposed MOS surface where the dye molecule are not anchored by the following (**Eq. 6.1**) (Nazeeruddin et al., 1993)

$$I_3^- + 2e_{CB}^-(MOS) \rightarrow 3I^- \tag{6.1}$$

It is well known fact that the photoinjected electrons combine faster in SnO_2 photoanode owing to its lower CB than TiO_2 when conjugated with most ruthenium based dyes. However, the increase in the V_{OC} in SnO_2 electrode upon $TiCl_4$ post-treatment could

133

be due to the minimized loss in potential between the LUMO of the dye because of an upward shift in CB of SnO_2-TiO_2 composite. Moreover, the thin TiO_2 layers formed by $TiCl_4$ treatment on the surface of the SnO_2 electrodes sufficiently hinder the recombination of photoinjected electrons with I_3^- species resulting in higher V_{OC} for the passivated electrodes **Eq. (6.2)** (Rosenbluth and Lewis, 1989, Kumar et al., 1992, Nazeeruddin et al., 1993).

$$V_{OC} = \frac{kT}{e}\left(\frac{J_{inj}}{n_{cb}k_{rec}[I_3^-]}\right) \tag{6.2}$$

where kT is the thermal energy, e is the elementary charges, J_{inj} is the injected electron flux, $k_{rec}[I_3^-]$ is the rate constant of I_3^- reduction and n_{cb} is the CB electron density or concentration of electron in the CB in the dark. Another reason for an enhanced V_{OC} could be the injection rate in composite NFs i.e., as an electron can easily jump to the TiO_2 CB as compared to that of SnO_2 CB as discussed earlier (Chapter 2).

6.4 CHARGE TRANSPORT PROPERTIES

The achieved high V_{OC} and the suppression of electron recombination by $TiCl_4$ blocking layer were evaluated from the charge transport parameters using EIS technique. The Nyquist plot of the DSSCs show three semi-circles. The first small circle of Nyquist plot at high frequency region (>1k Hz) represents the charge transport resistance, while the recombination of electrons at the dye anchored WE/electrolyte interface is deduced from the second semi-circle at frequency ($1000\ Hz < f < 1Hz$). The third semi-circle at low frequency (<1 Hz) reveals the ions diffusion in the electrolyte (Jose et al., 2009). Typically for high performing DSSCs, $R_{CT} >> R_T$ and the second semi-circle is much larger than the first. A similar trend is observed in our experiments which is shown in **Figure 6. 12.** Similarly, MPNFs + 0.5 M DSSCs exhibits larger diameter than the pure analogues and passivated DSSCs at lower molar concentrations, thereby, evidencing the suppression of electrons recombination and consequently long τ_n.
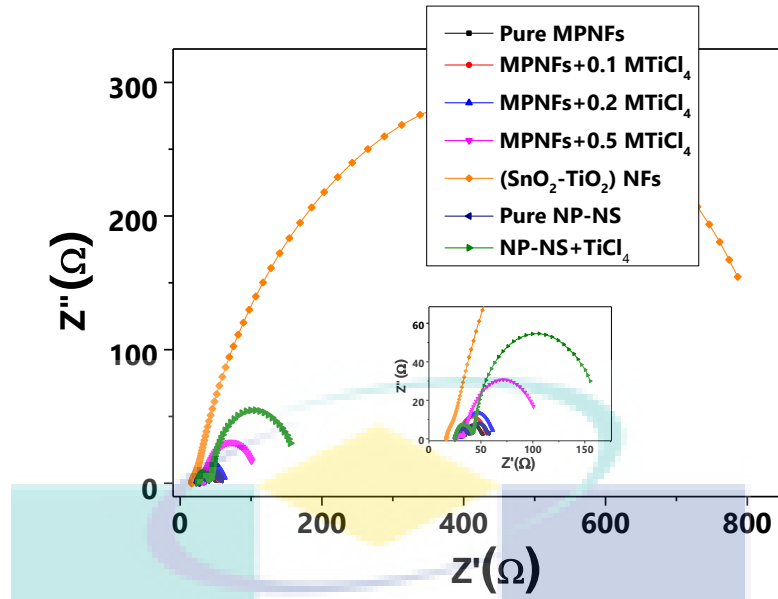
Figure 6.12: Nyquist plots recorded for the pure multifunctional (NPs-NSs) and MPNFs), (0.1-0.5 M TiCl$_4$ post treated MPNFs) and NPs-NSs +TiCl$_4$, and (SnO$_2$-TiO$_2$) NFs.

The τ_n was calculated for the respective DSSCs using mid frequency of the bode-phase plots **(Figure 6.13)** and by using the relation $\tau_n = 1/2\pi f_o$ where f_o is the maximum frequency at the mid peak. The calculated values of f_o were ~18.0, 17.0 ~3.6 and, 12.34, 6.65, 5.88 and 42.8 for NPs-NSs DSSCs, MPNFs DSSCs, NPs-NSs DSSCs+TiCl$_4$ and 0.1-0.5 M TiCl$_4$ DSSCs, respectively and their corresponding τ_n are listed in **Table 6.3**. Long τ_n values for the composites nanostructures shows that the electrons could survive for longer time before recombination which leads to higher J$_{SC}$ and V$_{OC}$ in DSSCs employing them.
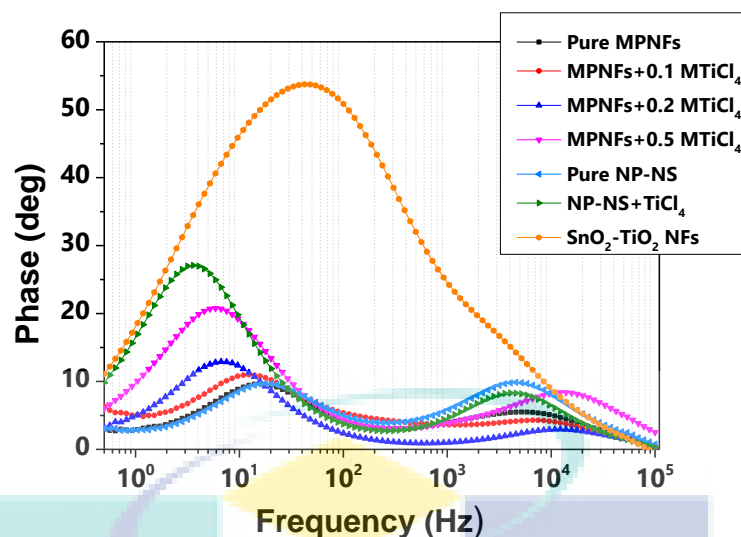
Figure 6.13: Bode phase plots recorded for the pure (multifunctional NPs-NSs and MPNFs), (0.1-0.5 M TiCl$_4$ MPNFs) and multifunctional NPs-NSs +TiCl$_4$, and (SnO$_2$-TiO$_2$) NFs.

To further explore the effect of TiCl$_4$ treated DSSCs and the electrospun (SnO$_2$-TiO$_2$) NFs composite, OCVD measurement was performed. It is useful technique to understand the electrons recombination mechanism and investigate the residual electrons or the built in potential particularly in TiCl$_4$ treated DSSCs. Under light illumination, the device under test attain a state of equilibrium due to the electron injection into MOS thereby raising the Fermi level to its optimum level. However, when an illumination is interrupted, the V$_{OC}$ start decaying with time as can be seen in **Figure 6.14**. The OCVD measurement is performed in the dark so that no electrons could recombine with oxidized dye molecules as the dye is not oxidized in dark, therefore electrons can only recombine with electrolyte species. Due to the recombination, the Fermi level start to move toward lower position, i.e., toward valence band. When all the photo-injected electrons vanishes, the Fermi level touch the valence band of the MOS and results in a zero V$_{OC}$.

136

Table 6.3
Electron life time using OCVD and EIS of DSSCs based on pure (multifunctional NPs-NSs and MPNFs), their composite and composite of (SnO_2-TiO_2) NFs

DSSC/ WE	OCVD (τ_n sec)			EIS (τ_n ms)
	V_{OC} ~0.2V	V_{OC} ~0.3V	V_{OC} ~0.4V	
Pure NPs-NSs	4.8	0.40	0.50	28.0
Pure MPNFs	0.39	0.11	0.05	28.0
MPNFs+0.1 M $TiCl_4$	4.9	0.90	0.14	19.4
MPNFs+0.2 M $TiCl_4$	5.0	1.6	0.84	10.5
MPNFs+0.5 M $TiCl_4$	>100	>100	1.9	9.2
NPs-NSs +$TiCl_4$	>100	16.0	2.5	5.6
(SnO_2-TiO_2) NFs	>100	13.5	3.6	66.5
TiO_2 P25	4.1	1.5	0.8	--

It can be seen from **Figure 6.14** that V_{OC} decays slowly for all passivated and (SnO_2-TiO_2) NFs devices, while there was an abrupt drop in pure SnO_2 multifunctional NPs-NSs and MPNFs. This slower decay observed the passivated DSSCs not only assures that electron could last for long time and consequently long τ_n but also open a new concept that a built in potential is formed between the two MOS having different CB and other physio-chemic properties.

To further study the recombination kinetics in detail, τ_n is derived from OCVD curves by the relation **(Eq. 3.15)** and compared with the V_{OC} **(Figure 6.15)**. At lower range of V_{OC}, the passivated DSSCs (NPs-NSs and MPNFs) with $TiCl_4$ and (SnO_2-TiO_2) NFs composite show very high τ_n compared to the pure counterparts (multifunctional NPs-NSs and MPNFs), respectively. The τ_n calculated from OCVD curves at ~0.2, 0.3, and ~0.4 V are listed in **Table 6.3**. Therefore, the composite DSSCs show significantly higher τ_n than the pure analogues due to the suppression of electron recombination at the SnO_2 WE/electrolyte interfaces.
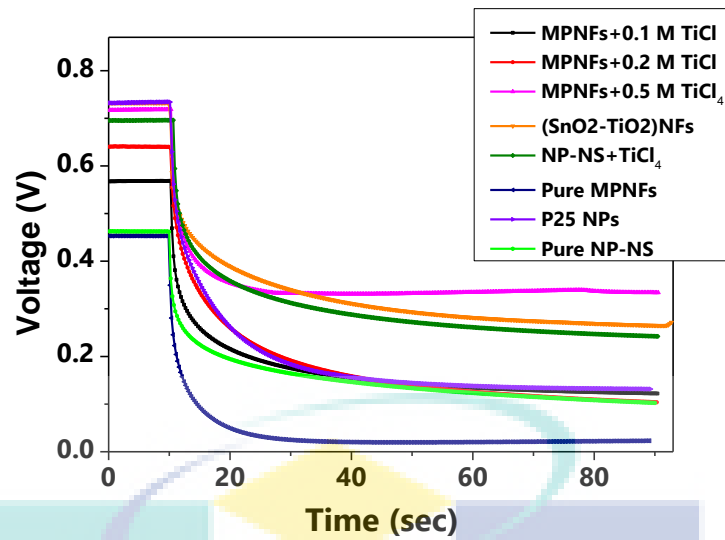
Figure 6.14: OCVD measurement where voltage decaying with the passage of time for pure SnO$_2$ (NPs-NSs and MPNFs), (0.1-0.5 M TiCl$_4$ MPNFs), multifunctional NPs-NSs +TiCl$_4$ and P25 NPs.
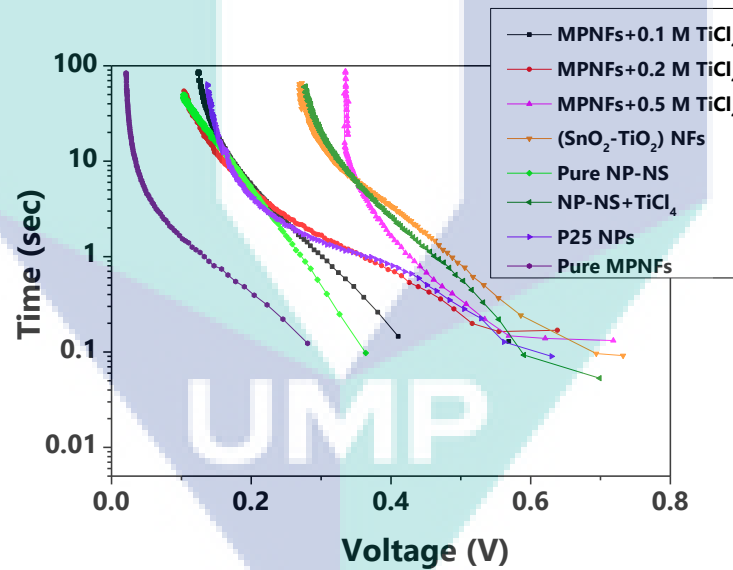
Figure 6.15: Electron life time from OCVD measurement of the pure (NPs-NSs and MPNFs), (0.1-0.5 M TiCl$_4$ MPNFs), multifunctional NPs-NSs +TiCl$_4$ and P25 NPs.

6.5   CONCLUSIONS

Primary issue of pure SnO_2 nanostructures, i.e, inferior V_{OC} and FF are significantly enhanced by compositing with TiO_2 using two different approaches. Initially, pure SnO_2 photoanodes were passivated with aqueous $TiCl_4$ solution with varying molar concentrations which dramatically enhanced the V_{OC} from ~500 to ~730 mV with final η ~8%, however, the FF remained unchanged (~50%) for both the devices. In the next approach, an electrospun NFs composite was developed by chemically combining the inherent feature of the both SnO_2 and TiO_2. The resulted composite significantly improved the FF ~64% comparable to that of a reference TiO_2 based DSSC and also a V_{OC} ~732 mV. This enhancement in PV parameters are due to the suppression of electron recombination, enhanced dye loading and Fermi level shift.

CONCLUSIONS AND RECOMMENDATIONS

7.1   CONCLUSIONS

Broad scope of this study was to develop SnO_2 morphologies to fabricate highly efficient DSSCs on account of its high electron mobility. Experimental results described in Chapters 4, 5, 6 show that the specific objectives outlined in Chapter 1 have been achieved. The novelty of the work is that SnO_2 has been developed as an electrode possessing simultaneously all the outstanding properties (require for any high performance in dye sensitized solar cells) such as high specific surface area; higher crystallinity and mobility superior light scattering. Furthermore, a composite in the SnO_2 – TiO_2 system as nanofibers has been developed possessing favorable conduction band position for high open circuit voltage. Major conclusions are:

(i)   Multifunctional SnO_2 comprising its NPs and nanospheres (NPs-NSs) were developed by hydrothermal reaction at 200 ^{o}C. When used as photoanode in DSSCs, they offered superior light scattering and charge transport properties although it has relatively lower surface area. They showed superior PV parameters with η ~4% (J_{SC} ~17 mA cm^{-2}) compared to the other samples synthesized at lower temperatures (150 and 180 ^{o}C). Electrochemical impedance spectroscopy measurements show that the multifunctional SnO_2 supports longer electron life time and charge transport parameters.

(ii) Next, a series of one-dimensional SnO_2 with varying surface properties were synthesized by electrospinning by controlling precursor concentration in the polymeric solution employed. This procedure identified multiporous nanofibers with surface area as high as 80 m^2/g. The multiporous nanofibers offered a record η ~4.3% (J_{SC} ~18 mA cm^{-2}) when used as a photoanode in DSSCs on account of superior dye-loading and charge transport properties.

(iii) The efficiency achieved in the above two studies are far lower than conventional TiO_2 because the intrinsic limitations in SnO_2 DSSCs, i.e., lower V_{OC} and FF, could not be solved. Towards this end, two approaches were made. In the first approach, TiO_2 particles were grown in SnO_2 multiporous nanofibers. This procedure gave one of the best efficiencies achieved in composite photoanodes employing SnO_2 (η ~8% with J_{SC} ~22 mA cm^{-2}). In the second approach, SnO_2-TiO_2 composite nanofibers were developed by electrospinning, which showed η ~7.9%. Although the second approach offered superior V_{OC} and FF, lower current density limited its performance lower than the first one.

7.2   OUTLOOK AND FUTURE RECOMMENDATIONS

The questions that need to be answered at the end of the study are: *(i) how far the efficiency of SnO_2 dye-sensitized solar cell could be increased? And, (ii) what strategies are required for it?*

Firstly, it is clear that there is a theoretical limits of 31% for a single junction solar cells and the best reported η in DSSCs based on TiO_2 till date is ~14.3% by engineering various parts of the basic embodiment such as photoanodes architecture, sensitizers, electrolyte, and counter electrodes. However, the best performing DSSCs using SnO_2 nanocrystalline as a photoanode resulted a maximum ~3-4% in pure and ~7-8% in a composite with other MOS. This is due to the low CB with respect to the most employed ruthenium based sensitizers (lower V_{OC} and lower FF). Although the present study showed SnO_2 DSSCs simultaneously yielding comparable V_{OC} and FF to those of TiO_2 based analogues, the photocurrent is limited in such devices due to the lower surface roughness. One promising direction in this scenario is to further develop the composite

wires with high surface area and increase the surface roughness. Moreover, multiporous SnO$_2$ nanofibers has a potential application in sensors, catalysis and lithium ion batteries owing to its desirable charge transport properties associated with high specific surface area.
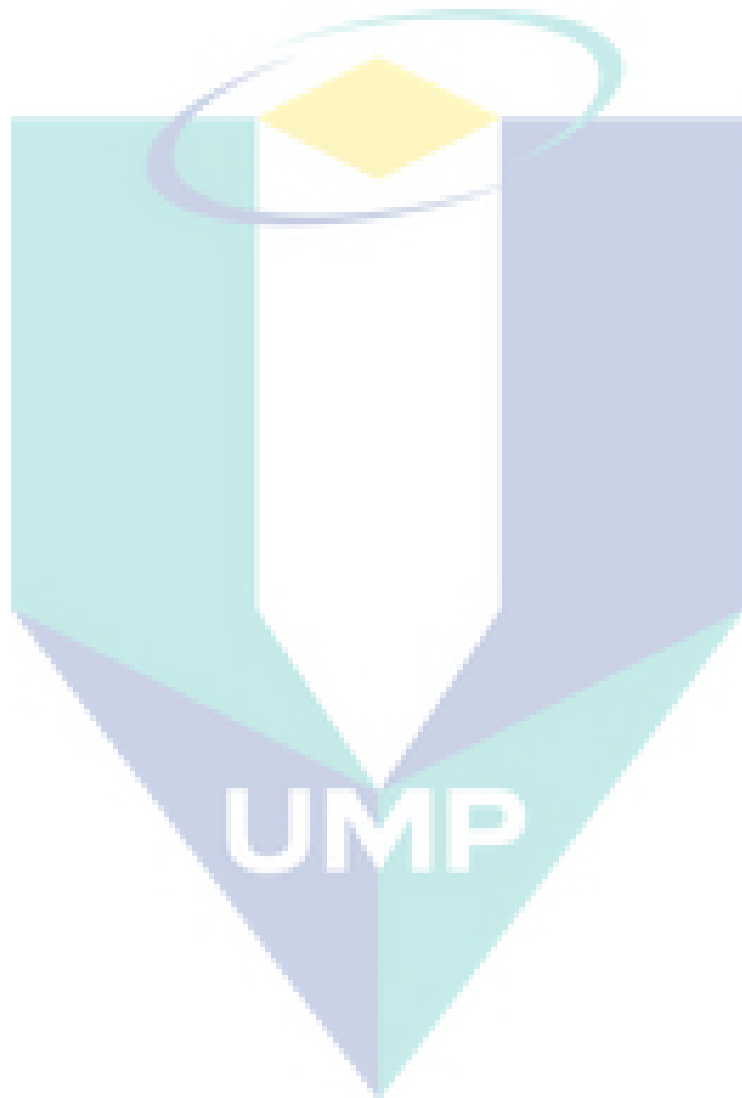
REFERENCES

Ahn, S. H., Kim, D. J., Chi, W. S. and Kim, J. H. (2013). One-dimensional hierarchical nanostructures of TiO_2 nanosheets on SnO_2 nanotub es for high hfficiency solid-state dye-sensitized solar cells. *Advanced Material.* 25(35): 4893-4897.

Anta, J. A., Guillén, E. and Tena-Zaera, R. (2012). ZnO-based dye-sensitized solar cells. *The Journal of Physical Chemistry C*. 116(21): 11413-11425.

Ahn, H.-J., Choi, H.-C., Park, K.-W., Kim, S.-B. and Sung, Y.-E. (2004). Investigation of the structural and electrochemical properties of size-controlled SnO_2 nanoparticles. *The Journal of Physical Chemistry B*. 108(28): 9815-9820.

Ahn, S. H., Kim, D. J., Chi, W. S. and Kim, J. H. (2014). Hierarchical double-shell nanostructures of tio_2 nanosheets on SnO_2 hollow spheres for high-efficiency, solid-state, dye-sensitized solar cells. *Advanced Functional Materials*. 24(32): 5037-5044.

Akilavasan, J., Wijeratne, K., Gannoruwa, A., Alamoud, A. R. M. and Bandara, J. (2014). Significance of $TiCl_4$ post-treatment on the performance of hydrothermally synthesized titania nanotubes-based dye-sensitized solar cells. *Applied Nanoscience*. 4(2): 185-188.

Aponsu, G. M. L. P., Wijayarathna, T. R. C. K., Perera, I. K., Perera, V. P. S. and Siriwardhana, A. C. P. K. (2013). The enhancement of photovoltaic parameters in dye-sensitized solar cells of nano-crystalline SnO_2 by incorporating with large $SrTiO_3$ particles. *Spectrochimica Acta Part A: Molecular and Biomolecular Spectroscopy.* 109(0): 37-41.

Armin, A., Velusamy, M., Wolfer, P., Zhang, Y., Burn, P. L., Meredith, P. and Pivrikas, A. (2014). Quantum efficiency of organic solar cells: electro-optical cavity considerations. *ACS Photonics*. 1(3): 173-181.

Archana, P. S., Jose, R., Vijila, C. and Ramakrishna, S. (2009). Improved electron diffusion coefficient in electrospun tio_2 nanowires. *Journal of Physical Chemistry C*. 113(52): 21538-21542.

Archana, P. S., Naveen Kumar, E., Vijila, C., Ramakrishna, S., Yusoff, M. M. and Jose, R. (2013). Random nanowires of nickel doped TiO_2 with high surface area and electron mobility for high efficiency dye-sensitized solar cells. *Dalton Transaction*. 42(4): 1024-1032.

Arote, S., Tabhane, V., Jadkar, S. and Pathan, H. (2014). Optimization of dye loading time for SnO_2 based Rose Bengal dye-sensitized solar cell. *Indian Journal of Physics.* 88(10): 1067-1071.

Asdim, Manseki, K., Sugiura, T. and Yoshida, T. 2014. Microwave synthesis of size-controllable SnO_2 nanocrystals for dye-sensitized solar cells. *New Journal of Chemistry.* 38(2): 598-603.

Barbé, C. J., Arendse, F., Comte, P., Jirousek, M., Lenzmann, F., Shklover, V. and Grätzel, M. (1997). Nanocrystalline titanium oxide electrodes for photovoltaic applications. *Journal of the American Ceramic Society.* 80(12): 3157-3171.

Bedja, I., Hotchandani, S. and Kamat, P. V. (1994). Preparation and photoelectrochemical characterization of thin SnO_2 nanocrystalline semiconductor films and their sensitization with bis(2,2'-bipyridine)(2,2'-bipyridine-4,4'-dicarboxylic acid) ruthenium(ii) complex. *The Journal of Physical Chemistry*. 98(15): 4133-4140.

Bellan, L. M. and Craighead, H. G. (2011). Applications of controlled electrospinning systems. *Polymers for Advanced Technologies.* 22(3): 304-309.

Becquerel AE. (1839). Recherches sur les effets de la radiation chimique de la lumiere solaire au moyen des courants electriques. *Comptes Rendus de L´Academie des Sciences*. 9(0): 145-149.

Bhande, S. S., Shinde, D. V., Tehare, K. K., Patil, S. A., Mane, R. S., Naushad, M., Alothman, Z. A., Hui, K. N. and Han, S. H. (2014). DSSCs synergic effect in thin metal oxide layer-functionalized SnO_2 photoanodes. *Journal of Photochemistry and Photobiology A: Chemistry*. 295: 64-69.

Bisquert, J. (2002). Theory of the impedance of electron diffusion and recombination in a thin layer. *The Journal of Physical Chemistry B*. 106(2): 325-333.

Birkel, A., Lee, Y.-G., Koll, D., Meerbeek, X. V., Frank, S., Choi, M. J., Kang, Y. S., Char, K. and Tremel, W. (2012). Highly efficient and stable dye-sensitized solar cells based on SnO_2 nanocrystals prepared by microwave-assisted synthesis. *Energy and Environmental Science*. 5(1): 5392-5400.

Bird, R. E., Hulstrom, R. L. and Lewis, L. J. (1983). Terrestrial solar spectral data sets. *Solar* Energy. 30(6): 563-573.

Bisquert, J. (2008). Physical electrochemistry of nanostructured devices. *Physical Chemistry Chemical Physics*. 10(1): 49-72.

Boschloo, G. and Hagfeldt, A. (2009). Characteristics of the iodide/triiodide redox mediator in dye-sensitized solar cells. *Accounts of Chemical Research*. 42(11): 1819-1826.

Brunauer, S., Deming, L. S., Deming, W. E. and Teller, E. (1940). On a Theory of the van der Waals Adsorption of Gases. *Journal of the American Chemical Society.* 62(7): 1723-1732.

Brunauer, S., Emmett, P. H. and Teller, E. (1938). Adsorption of gases in multimolecular layers. *Journal of the American Chemical Society*. 60(2): 309-319.

Cai, N., Moon, S.J., Cevey-Ha, L., Moehl, T., Humphry-Baker, R., Wang, P., Zakeeruddin, S. M. and Grätzel, M. (2011). An organic d-π-a dye for record efficiency solid-state sensitized heterojunction solar cells. *Nano Letters*. 11(4): 1452-1456.

Calogero, G., Bartolotta, A., Di Marco, G., Di Carlo, A. and Bonaccorso, F. (2015). Vegetable-based dye-sensitized solar cells. *Chemical Society Reviews*, 44(10), 3244-3294.

Cavaliere, S., Subianto, S., Savych, I., Tillard, M., Jones, D. J. and Rozière, J. (2013). Dopant-driven nanostructured loose-tube SnO_2 architectures: alternative electrocatalyst supports for proton exchange membrane fuel cells. *The Journal of Physical Chemistry C*. 117(23): 18298-18307.

Chen, D., Huang, F., Cheng, Y.-B. and Caruso, R. A. (2009). Mesoporous anatase TiO_2 beads with high surface areas and controllable pore sizes: a superior candidate for high-performance dye-sensitized solar cells. *Advanced* Materials. 21(21): 2206-2210.

Chae, H., Song, D., Lee, Y.-G., Son, T., Cho, W., Pyun, Y. B., Kim, T.-Y., Lee, J. H., Fabregat-Santiago, F., Bisquert, J. and Kang, Y. S. (2014). Chemical effects of tin oxide nanoparticles in polymer electrolytes-based dye-sensitized solar cells. *The Journal of Physical Chemistry C.* 118(30): 16510-16517.

Chapin, D. M., Fuller, C. S. and Pearson, G. L. (1954). A new silicon p-n junction photocell for converting solar radiation into electrical power. *Journal of Applied Physics.* 25(5): 676-677.

Chappel, S., Chen, S.-G. and Zaban, A. (2002). TiO_2-coated nanoporous sno_2 electrodes for dye-sensitized solar cells. *Langmuir*. 18(8): 3336-3342.

Chen, J., Li, C., Xu, F., Zhou, Y., Lei, W., Sun, L. and Zhang, Y. (2012). Hollow SnO_2 microspheres for high-efficiency bilayered dye sensitized solar cell. *RSC Advances*. 2(19): 7384-7387.

Chen, L., Li, X., Wang, Y., Gao, C., Zhang, H., Zhao, B., Teng, F., Zhou, J., Zhang, Z., Pan, X. and Xie, E. (2014). Low-temperature synthesis of tin dioxide hollow nanospheres and their potential applications in dye-sensitized solar cells and photoelectrochemical type self-powered ultraviolet photodetectors. *Journal of Power Sources.* 272: 886-894.

Chen, W., Qiu, Y. and Yang, S. (2010a). A new ZnO nanotetrapods/SnO_2 nanoparticles composite photoanode for high efficiency flexible dye-sensitized solar cells. *Physical Chemistry Chemical Physics.* 12(32): 9494-9501.

Chen, W., Qiu, Y., Zhong, Y., Wong, K. S. and Yang, S. (2010b). High-efficiency dye-sensitized solar cells based on the composite photoanodes of sno_2 nanoparticles/zno nanotetrapods. *The Journal of Physical Chemistry A*. 114(9): 3127-3138.

Chiba, Y. I., Ashraful. Watanabe, Yuki. Komiya, Ryoichi. Koide, Naoki. Han, Liyuan (2006). Dye-sensitized solar cells with conversion efficiency of 11.1%. *Japanese Journal of Applied Physics*. 45(25): 638-640.

Clifford, J. N., Palomares, E., Nazeeruddin, M. K., Grätzel, M. and Durrant, J. R. (2007). Dye dependent regeneration dynamics in dye sensitized nanocrystalline solar cells: evidence for the formation of a ruthenium bipyridyl cation/iodide intermediate. *The Journal of Physical Chemistry C*. 111(17): 6561-6567.

Cojocaru, L., Olivier, C., Toupance, T., Sellier, E. and Hirsch, L. (2013). Size and shape fine-tuning of SnO_2 nanoparticles for highly efficient and stable dye-sensitized solar cells. *Journal of Materials Chemistry A*. 1(44): 13789-13799.

Dadkhah, M. and Salavati-Niasari, M. (2014a). Controlled synthesis of tin dioxide nanostructures via two simple methods and the influence on dye sensitized solar cell. *Electrochimica Acta*. 129: 62-68.

Dadkhah, M. and Salavati-Niasari, M. (2014b). Dye-sensitized solar cells based on tin dioxide nanoparticles prepared by a facile hydrothermal method. *Materials Science in Semiconductor Processing*. 20: 41-48.

Daeneke, T., Kwon, T.-H., Holmes, A. B., Duffy, N. W., Bach, U. and Spiccia, L. (2011). High-efficiency dye-sensitized solar cells with ferrocene-based electrolytes. *Nature Chemistry*. 3(3): 211-215.

Daeneke, T., Mozer, A. J., Uemura, Y., Makuta, S., Fekete, M., Tachibana, Y., Koumura, N., Bach, U. and Spiccia, L. (2012). Dye regeneration kinetics in dye-sensitized solar cells. *Journal of the American Chemical Society*. 134(41): 16925-16928.

Das, S. and Jayaraman, V. (2014). SnO_2: A comprehensive review on structures and gas sensors. *Progress in Materials Science*. 66: 112-255.

Dalton, P. D., Vaquette, C., Farrugia, B. L., Dargaville, T. R., Brown, T. D. and Hutmacher, D. W. (2013). Electrospinning and additive manufacturing: converging technologies. *Biomaterials Science*. 1(2): 171-185.

Desai, U. V., Xu, C., Wu, J. and Gao, D. (2013). Hybrid TiO_2-SnO_2 nanotube arrays for dye-sensitized solar cells. *The Journal of Physical Chemistry C*. 117(7): 3232-3239.

Diamant, Y., Chappel, S., Chen, S. G., Melamed, O. and Zaban, A. (2004). Core-shell nanoporous electrode for dye sensitized solar cells: the effect of shell characteristics on the electronic properties of the electrode. *Coordination Chemistry Reviews*. 248(13-14): 1271-1276.

Do, D. D., Do, H. D. and Nicholson, D. (2010). A computer appraisal of BET theory, BET surface area and the calculation of surface excess for gas adsorption on a graphite surface. *Chemical Engineering Science*. 65(10): 3331-3340.

Dollimore, D., Spooner, P. and Turner, A. (1976). The bet method of analysis of gas adsorption data and its relevance to the calculation of surface areas. *Surface Technology*. 4(2): 121-160.

Dong, Z., Ren, H., Hessel, C. M., Wang, J., Yu, R., Jin, Q., Yang, M., Hu, Z., Chen, Y., Tang, Z., Zhao, H. and Wang, D. (2014). Quintuple-shelled sno2 hollow microspheres with superior light scattering for high-performance dye-sensitized solar cells. *Advanced Materials.* 26(6): 905-909.

Dou, X., Sabba, D., Mathews, N., Wong, L. H., Lam, Y. M. and Mhaisalkar, S. (2011). Hydrothermal synthesis of high electron mobility Zn-doped SnO_2 nanoflowers as photoanode material for efficient dye-sensitized solar cells. *Chemistry of Materials*. 23(17): 3938-3945.

Docampo, P., Tiwana, P., Sakai, N., Miura, H., Herz, L., Murakami, T. and Snaith, H. J. (2012). Unraveling the function of an mgo interlayer in both electrolyte and solid-state SnO_2 based dye-sensitized solar cells. *The Journal of Physical Chemistry C*. 116(43): 22840-22846.

Dong, P., Pint, C. L., Hainey, M., Mirri, F., Zhan, Y., Zhang, J., Pasquali, M., Hauge, R. H., Verduzco, R., Jiang, M., Lin, H. and Lou, J. (2011). Vertically aligned single-walled carbon nanotubes as low-cost and high electrocatalytic counter electrode for dye-sensitized solar cells. *ACS Applied Materials and Interfaces.* 3(8): 3157-3161.

Duan, Y., Zheng, J., Fu, N., Fang, Y., Liu, T., Zhang, Q., Zhou, X., Lin, Y. and Pan, F. (2015). Enhancing the performance of dye-sensitized solar cells: doping SnO_2 photoanodes with Al to simultaneously improve conduction band and electron lifetime. *Journal of Material Chemistry A*. 3(6): 3066-3073.

Emery, K. (2005). *Measurement and characterization of solar cells and modules*. *Handbook of photovoltaic science and engineering*. DOI: 10.1002/047001 4008.ch16. John Wiley & Sons, Ltd.

El-Etre, A. Y. and Reda, S. M. (2010). Characterization of nanocrystalline SnO_2 thin film fabricated by electrodeposition method for dye-sensitized solar cell application. *Applied Surface Science*. 256(22): 6601-6606.

Elumalai, N. K., Jose, R., Archana, P. S., Chellappan, V. and Ramakrishna, S. (2012). Charge transport through electrospun SnO_2 nanoflowers and nanofibers: Role of surface trap density on electron transport dynamics. *The Journal Physical Chemistry C*. 116(42): 22112-22120.

Eyre, B. L. (1973). Transmission electron microscope studies of point defect clusters in fcc and bcc metals. *Journal of Physics F: Metal Physics.* 3(2): 422-470.

Fabregat-Santiago, F., Garcia-Belmonte, G., Bisquert, J., Zaban, A. and Salvador, P. (2002). Decoupling of transport, charge storage, and interfacial charge transfer in the nanocrystalline tio2/electrolyte system by impedance methods. *The Journal of Physical Chemistry B*. 106(2): 334-339.

Fakharuddin, A., Ahmed, I., Wali,Q., Khalidin, Z.,Yosuff, M., M Jose, R., (2014). Probing electron lifetime and recombination dynamics in large area dye-sensitized solar cells by electrochemical impedance spectroscopy. *Advanced Matererial Research*. 295: 553-558.

Fakharuddin, A., Ahmed, I., Khalidin, Z., Yusoff, M. M. and Jose, R. 2014. Charge transport through split photoelectrodes in dye-sensitized solar cells. *Journal of Applied Physics*. 115(16): 164509-164518.

Fakharuddin, A., Jose, R., Brown, T. M., Fabregat-Santiago, F. and Bisquert, J. (2014). A perspective on the production of dye-sensitized solar modules. *Energy and Environmental Science*. 7(12): 3952-3981.

Ferrere, S., Zaban, A. and Gregg, B. A. (1997). Dye sensitization of nanocrystalline tin oxide by perylene derivatives. *The Journal of Physical Chemistry B*. 101(23): 4490-4493.

Feldt, S. M., Gibson, E. A., Gabrielsson, E., Sun, L., Boschloo, G. and Hagfeldt, A. (2010). Design of Organic Dyes and Cobalt Polypyridine Redox Mediators for High-Efficiency Dye-Sensitized Solar Cells. *Journal of the American Chemical Society*. 132(46): 16714-16724.

Ferber, J., Stangl, R. and Luther, J. (1998). An electrical model of the dye-sensitized solar cell. *Solar Energy Materials and Solar Cells*. 53(1-2): 29-54.

Frenot, A. and chronakis, I. S. (2003). Polymer nanofibers assembled by electrospinning. *Current Opinion in Colloid & Interface Science*. 8(1): 64-75.

Fu, Z., Li, X. and Xu, G. (2014). Novel electrospun SnO_2@carbon nanofibers as high performance anodes for lithium-ion batteries. *Crystal Research and Technology*. 49(7): 441-445.

Fungo, F., Otero, L., Durantini, E. N., Silber, J. J. and Sereno, L. E. (2000). Photosensitization of thin sno_2 nanocrystalline semiconductor film electrodes with metallodiporphyrin. *The Journal of Physical Chemistry B*. 104(32): 7644-7651.

Gao, C., Li, X., Lu, B., Chen, L., Wang, Y., Teng, F., Wang, J., Zhang, Z., Pan, X. and Xie, E. (2012). A facile method to prepare SnO_2 nanotubes for use in efficient SnO_2-TiO_2 core-shell dye-sensitized solar cells. *Nanoscale*, 4(11), 3475-81.

Gao, C., Li, X., Zhu, X., Chen, L., Zhang, Z., Wang, Y., Zhang, Z., Duan, H. andXie, E. (2014). Branched hierarchical photoanode of titanium dioxide nanoneedles on tin dioxide nanofiber network for high performance dye-sensitized solar cells. *Journal of Power Sources*. 264: 15-21.

Ganapathy, V., Kong, E.-H., Park, Y.-C., Jang, H. M. and Rhee, S.-W. (2014). Cauliflower-like SnO_2 hollow microspheres as anode and carbon fiber as cathode for high performance quantum dot and dye-sensitized solar cells. *Nanoscale*.6(6): 3296-3301.

Ghorani, B. and Tucker, N. (2015). Fundamentals of electrospinning as a novel delivery vehicle for bioactive compounds in food nanotechnology. *Food Hydrocolloids*. 51: 227-240.

Godinho, K. G., Walsh, A. and Watson, G. W. (2008). Energetic and electronic structure analysis of intrinsic defects in SnO_2. *The Journal of Physical Chemistry C*. 113(1): 439-448.

Golnaz S, V. S., Robbert G, Pablo D, Ingmar B, Neil P, Azam I and Henry J. S. (2013). *Physical Chemistry Chemistry Physics*. 15: 2075-2080

Grätzel, M. (2009). Recent advances in sensitized mesoscopic solar cells. *Accounts of Chemical Research*. 42(11): 1788-1798.

Kumara G.R., Tennakone, K., Kottegoda, I. R. M., Bandaranayake, P. K. M., Konno, A., Okuya, M., Kaneko, S. and Murakami, K. (2003). Efficient dye-sensitized photoelectrochemical cells made from nanocrystalline tin(IV) oxide-zinc oxide composite films. *Semiconductor Science and Technology*. 18(4): 312-318.

Gray, J. L. (2011). *The Physics of the solar sell. Handbook of photovoltaic science and engineering*. DOI: 10.1002/9780470974704. John Wiley & Sons, Ltd.

Grätzel, M. (2003). Dye-sensitized solar cells. *Journal of Photochemistry and Photobiology*. 4(2): 145-153.

Green, A. N. M., Palomares, E., Haque, S. A., Kroon, J. M. and Durrant, J. R. (2005). Charge transport versus recombination in dye-sensitized solar cells employing nanocrystalline TiO_2 and SnO_2 films. *The Journal of Physical Chemistry B*. 109(25): 12525-12533.

Green, M. A. (2009). The path to 25% silicon solar cell efficiency: History of silicon cell evolution. *Progress in Photovoltaics: Research and Applications*. 17(3): 183-189.

Gregg, B. A. (2003). Excitonic Solar Cells. *The Journal of Physical Chemistry B*. 107(20): 4688-4698.

Gubbala, S., Chakrapani, V., Kumar, V. and Sunkara, M. K. (2008). Band-edge engineered hybrid structures for dye-sensitized solar cells based on SnO_2 nanowires. *Advanced Functional Materials*. 18(16): 2411-2418.

Guo, H., Mao, R., Yang, X., Wang, S. and Chen, J. (2012). Hollow nanotubular SnO_2 with improved lithium storage. *Journal of Power Sources*. 219: 280-284.

Gu, F., Huang, W., Wang, S., Cheng, X., Hu, Y. and Li, C. (2014). Improved photoelectric conversion efficiency from titanium oxide-coupled tin oxide nanoparticles formed in flame. *Journal of Power Sources*. 268: 922-927.

Hagfeldt, A., Boschloo, G., Sun, L., Kloo, L. and Pettersson, H. (2010). Dye-sensitized solar cells. *Chemical Reviews*. 110(11): 6595-6663.

Hagfeldt, A. and Graetzel, M. (1995). Light-induced redox reactions in nanocrystalline systems. *Chemical Reviews*. 95(1): 49-68.

Hara, K., Sato, T., Katoh, R., Furube, A., Ohga, Y., Shinpo, A., Suga, S., Sayama, K., Sugihara, H. and Arakawa, H. (2003). Molecular design of coumarin dyes for efficient dye-sensitized solar cells. *The Journal of Physical Chemistry B*. 107(2): 597-606.

Hattori, S., Wada, Y., Yanagida, S. and Fukuzumi, S. (2005). Blue copper model complexes with distorted tetragonal geometry acting as effective electron-transfer mediators in dye-sensitized solar cells. *Journal of the American Chemical Society*. 127(26): 9648-9654.

Haid, S., Marszalek, M., Mishra, A., Wielopolski, M., Teuscher, J., Moser, J.-E., Humphry-Baker, R., Zakeeruddin, S. M., Grätzel, M. and Bäuerle, P. (2012). Significant improvement of dye-sensitized solar cell performance by small structural modification in π-conjugated donor-acceptor dyes. *Advanced Functional Materials*. 22: 1291-1302.

Han, L., Koide, N., Chiba, Y., Islam, A., Komiya, R., Fuke, N., Fukui, A. and Yamanaka, R. (2005). Improvement of efficiency of dye-sensitized solar cells by reduction of internal resistance. *Applied Physics Letters*. 86(21): 213501.

Hardin, B. E., Snaith, H. J. and Mcgehee, M. D. (2012). The renaissance of dye-sensitized solar cells. *Nature Photonics.* 6(3): 162-169.

Hauch, A. and Georg, A. (2001). Diffusion in the electrolyte and charge-transfer reaction at the platinum electrode in dye-sensitized solar cells. *Electrochimica Acta*. 46(22): 3457-3466.

Hendry, E., Koeberg, M., O'regan, B. and Bonn, M. (2006). Local field effects on electron transport in nanostructured tio$_2$ revealed by terahertz spectroscopy. *Nano Letters*. 6(4): 755-759.

Hendry, E., Wang, F., Shan, J., Heinz, T. F. and Bonn, M. (2004). Electron transport in TiO$_2$ probed by THz time-domain spectroscopy. *Physcal Review B*. 69(8): 081101-081104.

Horiuchi, T., Miura, H., Sumioka, K. and Uchida, S. (2004). High efficiency of dye-sensitized solar cells based on metal-free indoline dyes. *Journal of the American Chemical Society*. 126(39): 12218-12219.

Hossain, M. A., Jennings, J. R., Koh, Z. Y. and Wang, Q. (2011). Carrier generation and collection in cds/cdse-sensitized SnO$_2$ solar cells exhibiting unprecedented photocurrent densities. *ACS Nano*. 5(4): 3172-3181.

Hoshikawa, T., Yamada, M., Kikuchi, R. and Eguchi, K. (2005). Impedance analysis of internal resistance affecting the photoelectrochemical performance of dye-sensitized solar cells. *Journal of The Electrochemical Society*. 152(2): E68-E73.

Huang, Z., Liu, X., Li, K., Li, D., Luo, Y., Li, H., Song, W., Chen, L. and Meng, Q. (2007). Application of carbon materials as counter electrodes of dye-sensitized solar cells. *Electrochemistry Communications*. 9(4): 596-598.

Huo, J., Hu, Y., Jiang, H., Huang, W. and Li, C. (2014). SnO_2 nanorod@TiO_2 hybrid material for dye-sensitized solar cells. *Journal of Material Chemistry A*. 2(22): 8266-8272.

Huang, Z.-M., Zhang, Y.-Z., Kotaki, M. and Ramakrishna, S. (2003). A review on polymer nanofibers by electrospinning and their applications in nanocomposites. *Composites science and technology*. 63(15): 2223-2253.

Imahori, H., Umeyama, T. and Ito, S. (2009). Large π-aromatic molecules as potential sensitizers for highly efficient dye-sensitized solar cells. *Accounts of Chemical Research*. 42(11): 1809-1818.

Inada, H., Kakibayashi, H., Isakozawa, S., Hashimoto, T., Yaguchi, T. and Nakamura, K. (2009). Chapter 4 - Hitachi's development of cold-field emission scanning transmission electron microscopes. *Advances in Imaging and Electron Physics*. 159: 123-186.

Inagaki, M., Yang, Y. and Kang, F. (2012). Carbon nanofibers prepared via electrospinning. *Advanced Materials*. 24(19): 2547-2566.

Ito, S., Makari, Y., Kitamura, T., Wada, Y. and Yanagida, S. (2004). Fabrication and characterization of mesoporous SnO_2/ZnO-composite electrodes for efficient dye solar cells. *Journal of Materials Chemistry*. 14(3): 385-390.

Ito, S., Chen, P., Comte, P., Nazeeruddin, M. K., Liska, P., Péchy, P. and Grätzel, M. (2007). Fabrication of screen-printing pastes from TiO_2 powders for dye-sensitised solar cells. *Progress in Photovoltaics: Research and Applications*. 15(7): 603-612.

Ito, S., Murakami, T. N., Comte, P., Liska, P., Grätzel, C., Nazeeruddin, M. K. and Grätzel, M. (2008). Fabrication of thin film dye sensitized solar cells with solar to electric power conversion efficiency over 10%. *Thin Solid Films*. 516(14): 4613-4619.

Ito, S., Nazeeruddin, M. K., Liska, P., Comte, P., Charvet, R., Péchy, P., Jirousek, M., Kay, A., Zakeeruddin, S. M. and Grätzel, M. (2006). Photovoltaic characterization of dye-sensitized solar cells: effect of device masking on conversion efficiency. *Progress in Photovoltaics. Research and Applications*. 14: 589-601.

Jarzebski, Z. M. and Marton, J. P. (1976). Physical Properties of SnO_2 Materials: I . Preparation and defect structure. *Journal of The Electrochemical Society*. 123(7): 199C-205C.

Jennings, J. R., Liu, Y., Safari-Alamuti, F. and Wang, Q. (2011). Dependence of dye-sensitized solar cell impedance on photoelectrode thickness. *The Journal of Physical Chemistry C*. 116(1): 1556-1562.

Jose, R., Thavasi, V. and Ramakrishna, S. (2009). Metal oxides for dye-sensitized solar cells. *Journal of Americal Ceramics Society*. 92(2): 289-301.

Kakiage, K., Aoyama, Y., Yano, T., Oya, K., Fujisawa, J.-I. and Hanaya, M. (2015). Highly-efficient dye-sensitized solar cells with collaborative sensitization by silyl-anchor and carboxy-anchor dyes. *Chemical Communications.* 51: 15894-15897.

Kawamoto, N., Tang, D.-M., Wei, X., Wang, X., Mitome, M., Bando, Y. and Golberg, D. (2013). Transmission electron microscope as an ultimate tool for nanomaterial property studies. *Microscopy*. 62(1): 157-175.

Kavan, L., O'regan, B., Kay, A. and Grätzel, M. (1993). Preparation of TiO_2 (anatase) films on electrodes by anodic oxidative hydrolysis of $TiCl_3$. *Journal of Electroanalytical Chemistry*. 346(1): 291-307.

Kay, A. and Grätzel, M. (2002). Dye-sensitized core-shell nanocrystals: Improved efficiency of mesoporous tin oxide electrodes coated with a thin layer of an insulating oxide. *Chemistry of Materials*. 14(7): 2930-2935.

Kasaudhan, R., Elbohy, H., Sigdel, S., Hui, Q., Qufu, W. and Qiquan, Q. (2014). Incorporation of nanoparticles into nanofibers for higher efficiency dye-sensitized solar cells. *IEEE Electron Device Letters*. 35(5): 578-580.

Kern, R., Sastrawan, R., Ferber, J., Stangl, R. and Luther, J. (2002). Modeling and interpretation of electrical impedance spectra of dye solar cells operated under open-circuit conditions. *Electrochimica Acta*. 47(26): 4213-4225.

Keis, K., Lindgren, J., Lindquist, S.-E. and Hagfeldt, A. (2000). Studies of the Adsorption Process of Ru Complexes in Nanoporous ZnO Electrodes. *Langmuir*. 16(10): 4688-4694.

Kelly, C. A. and Meyer, G. J. (2001). Excited state processes at sensitized nanocrystalline thin film semiconductor interfaces. *Coordination Chemistry Reviews*. 211(1): 295-315.

Kim, M.-H. and Kwon, Y.-U. (2011). Semiconducting divalent metal oxides as blocking layer material for SnO_2-based dye-sensitized solar cells. *The Journal of Physical. Chemistry C*. 115(46): 23120-23125.

Koo, B.-K., Lee, D.-Y., Kim, H.-J., Lee, W.-J., Song, J.-S. and Kim, H.-J. (2006). Seasoning effect of dye-sensitized solar cells with different counter electrodes. *Journal of Electroceramics*. 17(1): 79-82.

Krishnamoorthy, T., Tang, M. Z., Verma, A., Nair, A. S., Pliszka, D., Mhaisalkar, S. G. and Ramakrishna, S. (2012). A facile route to vertically aligned electrospun SnO_2

nanowires on a transparent conducting oxide substrate for dye-sensitized solar cells. *Journal of Materials Chemistry*. 22(5): 2166-2172.

Kumar, E. N., Jose, R., Archana, P. S., Vijila, C., Yusoff, M. M. and Ramakrishna, S. (2012). High performance dye-sensitized solar cells with record open circuit voltage using tin oxide nanoflowers developed by electrospinning. *Energy &Environmental Science*. 5(1): 5401-5407.

Kumar, A., Santangelo, P. G. and Lewis, N. S. (1992). Electrolysis of water at strontium titanate ($SrTiO_3$) photoelectrodes: distinguishing between the statistical and stochastic formalisms for electron-transfer processes in fuel-forming photoelectrochemical systems. *The Journal of Physical Chemistry*. 96(2): 834-842.

Kusior, A., Klich-kafeL, J., Trenczek-Zajac, A., Swierczek, K., Radecka, M. & Zakrzewska, K. (2013). TiO_2–SnO_2 nanomaterials for gas sensing and photocatalysis. *Journal of the European Ceramic Society*. 33: 2285-2290.

L A Harris, A. and Wilson, R. H. (1978). Semiconductors for photoelectrolysis. *Annual Review of Materials Science*. 8(1): 99-134.

Le Viet, A., Jose, R., Reddy, M. V., Chowdari, B. V. R. and Ramakrishna, S. (2010). Nb_2O_5 Photoelectrodes for dye-sensitized solar cells: choice of the polymorph. *The Journal of Physical Chemistry C*. 114(49): 21795-21800.

Lee, C., Lee, G.W., Kang, W., Lee, D.-K., Ko, M. J., Kim, K. and Park, N.-G. (2010). Suppression of charge recombination rate in nanocrystalline SnO_2 by Thin coatings of divalent oxides in dye-sensitized solar cells. *Bulletin of the Korean Chemical Society*. 31(11): 3093.

Lee, J.H., Park, N.G. and Shin, Y.-J. (2011). Nano-grain SnO_2 electrodes for high conversion efficiency SnO_2-DSSC. *Solar Energy Materials and Solar Cells*. 95(1): 179-183.

Leventis, H. C., O'mahony, F., Akhtar, J., Afzaal, M., O'brien, P. and Haque, S. A. (2010). Transient optical studies of interfacial charge transfer at nanostructured metal oxide/pbs quantum dot/organic hole conductor heterojunctions. *Journal of American Chemical Society*. 132(8): 2743-2750.

Li, K.N., Wang, Y.-F., Xu, Y.-F., Chen, H.-Y., Su, C.-Y. and Kuang, D.-B. (2013). Macroporous SnO_2 synthesized via a template-assisted reflux process for efficient dye-sensitized solar cells. *ACS Applied Materials & Interfaces*. 5(11): 5105-5111.

Li, D. and Xia, Y. (2004). Electrospinning of nanofibers: Reinventing the wheel? *Advanced Materials*. 16(14): 1151-1170.

Li, Z., Zhou, Y., Mao, W. and Zou, Z. (2015). Nanowire-based hierarchical tin oxide/zinc stannate hollow microspheres: Enhanced solar energy utilization efficiency for

dye-sensitized solar cells and photocatalytic degradation of dyes. *Journal of Power Sources*. 274: 575-581.

Li, Z., Zhou, Y., Yu, T., Liu, J. and Zou, Z. (2012). Unique Zn-doped SnO_2 nano-echinus with excellent electron transport and light harvesting properties as photoanode materials for high performance dye-sensitized solar cell. *CrystEngComm*. 14(20): 6462-6468.

Lin, J., Peng, Z., Xiang, C., Ruan, G., Yan, Z., Natelson, D. and Tour, J. M. (2013). Graphene nanoribbon and nanostructured SnO_2 Composite anodes for lithium ion batteries. *ACS Nano*. 7(7): 6001-6006.

Liu, J., Luo, T., Mouli T, S., Meng, F., Sun, B., Li, M. and Liu, J. (2010). A novel coral-like porous SnO2 hollow architecture: biomimetic swallowing growth mechanism and enhanced photovoltaic property for dye-sensitized solar cell application. *Chemical Communications*. 46(3): 472-474.

Liu, M., Yang, J., Feng, S., Zhu, H., Zhang, J., Li, G. and Peng, J. (2012). Composite photoanodes of Zn_2SnO_4 nanoparticles modified SnO_2 hierarchical microspheres for dye-sensitized solar cells. *Materials Letters*. 76: 215-218.

Liu, Z., Pan, K., Liu, M., Wang, M., Lü, Q., Li, J., Bai, Y. and Li, T. (2005). Al_2O_3-coated SnO_2/TiO_2 composite electrode for the dye-sensitized solar cell. *Electrochimica Acta*. 50(13): 2583-2589.

Mahmoud, S. A. and Fouad, O. A. (2015). Synthesis and application of zinc/tin oxide nanostructures in photocatalysis and dye sensitized solar cells. *Solar Energy Material and Solar Cells*. 136: 38-43.

Martinson, A. B. F., Hamann, T. W., Pellin, M. J. and Hupp, J. T. (2008). New architectures for dye-sensitized solar cells. *Chemistry - A European Journal*. 14(15): 4458-4467.

Ma, W., Jiao, Y. and Meng, S. (2014). Predicting energy conversion efficiency of dye solar cells from first principles. *The Journal of Physical Chemistry C*. 118(30): 16447-16457.

Mccann, J. T., Li, D. and Xia, Y. (2005). Electrospinning of nanofibers with core-sheath, hollow, or porous structures. *Journal of Materials Chemistry*. 15(7): 735-738.

Mccusker, L. and Baerlocher, C. (2013). Electron crystallography as a complement to X-ray powder diffraction techniques. *Zeitschrift für Kristallographie - Crystalline Materials.* 288(1): 1-10.

Memming, R. and Schröppel, F. (1979). Electron transfer reactions of excited ruthenium(II) complexes in monolayer assemblies at the SnO_2-water interface. *Chemical Physics Letters*. 62(2): 207-210.

Meyer, G. J. (1997). Efficient Light-to-Electrical Energy Conversion: Nanocrystalline TiO$_2$ Films Modified with Inorganic Sensitizers. *Journal of Chemical Education.* 74(6): 652.

Montanari, I., Nelson, J. and Durrant, J. R. (2002). Iodide electron transfer kinetics in dye-sensitized nanocrystalline TiO$_2$ films. *The Journal of Physical Chemistry B.* 106(47): 12203-12210.

Morkoç, H. & Özgür, Ü. (2009). General Properties of ZnO. *Zinc Oxide.* Wiley-VCH Verlag GmbH & Co. KGaA, DOI: 10.1002/9783527623945.ch1.

Moser, J. (1887). Notiz u¨ber Versta¨rkung photoelektrischer Stro¨me Durch Optische Sensibilisirung. *Monatshefte fu¨r Chemie (Chemical Monthly).* 8(1): 373-3.

Murakami, T. N. and Grätzel, M. (2008). Counter electrodes for DSC: Application of functional materials as catalysts. *Inorganica Chimica Acta.* 361(3): 572-580.

Nazeeruddin, M. K., Péchy, P., Renouard, T., Zakeeruddin, S. M., Humphry-Baker, R., Comte, P., Liska, P., Cevey, L., Costa, E., Shklover, V., Spiccia, L., Deacon, G. B., Bignozzi, C. A. and Grätzel, M. (2001). Engineering of efficient panchromatic sensitizers for nanocrystalline TiO$_2$-based solar cells. *Journal of the American Chemical Society.* 123(8): 1613-1624.

Nazeeruddin, M. K., Kay, A., Rodicio, I., Humphry-Baker, R., Mueller, E., Liska, P., Vlachopoulos, N. and Graetzel, M. (1993). Conversion of light to electricity by cis-X2bis(2,2'-bipyridyl-4,4'-dicarboxylate)ruthenium(II)charge-transfer sensitizers (X = Cl-, Br-, I-, CN-, and SCN-) on nanocrystalline titanium dioxide electrodes. *Journal of the American Chemical Society.* 115(14): 6382-6390.

Nelson, J. and Chandler, R. E. (2004). Random walk models of charge transfer and transport in dye sensitized systems. *Coordination Chemistry Reviews.* 248(13-14): 1181-1194.

Nelson, J. J., Amick, T. J. and Elliott, C. M. (2008). Mass Transport of polypyridyl cobalt complexes in dye-sensitized solar cells with mesoporous TiO$_2$ photoanodes. *The Journal of Physical Chemistry C.* 112(46). 18255-18263.

Niu, H., Zhang, S., Wang, R., Guo, Z., Shang, X., Gan, W., Qin, S., Wan, L. and Xu, J. (2014). Dye-sensitized solar cells employing a multifunctionalized hierarchical SnO$_2$ nanoflower structure passivated by TiO$_2$ nanogranulum. *The Journal of Physical Chemistry C.* 118(7): 3504-3513.

NREL (2015). Best research cell efficiencies *http://www.nrel.gov/ncpv/images /efficiency_chart.jpg*

Nusbaumer, H., Zakeeruddin, S. M., Moser, J. E. and Gratzel, M. (2003). An alternative efficient redox couple for the dye-sensitized solar cell system. *Chemistry.* 9(16): 3756-63.

Ohl RS. (1941). Light sensitive electric device. US Patent 240252..Light-sensitive electric device including silicon. US Patent 2443542.

Olsen, E., Hagen, G. and Eric Lindquist, S. (2000). Dissolution of platinum in methoxy propionitrile containing LiI/I$_2$. *Solar Energy Materials and Solar Cells*. 63(3): 267-273.

Olivier, J. P. (1998). Improving the models used for calculating the size distribution of micropore volume of activated carbons from adsorption data. *Carbon*. 36(10): 1469-1472.

O'regan, B., Gratzel, Michael (1991). A low-cost, high-efficiency solar cell based on dye-sensitized colloidal TiO$_2$ films. *Nature*. 353: 737-740.

Ondersma, J. W. and Hamann, T. W. (2013). Recombination and redox couples in dye-sensitized solar cells. *Chemistry Reviews*. 257(9-10): 1533-1543.

Palomares, E., Clifford, J. N., Haque, S. A., Lutz, T. and Durrant, J. R. (2003). Control of charge recombination dynamics in dye sensitized solar cells by the use of conformally deposited metal oxide blocking layers. *Journal of the American Chemical Society*. 125(2): 475-482.

Pang, H., Yang, H., Guo, C. X. and Li, C. M. (2012). Functionalization of SnO$_2$ photoanode through mg-doping and TiO$_2$-coating to synergically boost dye-sensitized solar cell performance. *ACS Applied Materials & Interfaces*. 4(11): 6261-6265.

Park, J. T., Lee, C. S. and Kim, J. H. (2014). One-pot synthesis of hierarchical mesoporous SnO$_2$ spheres using a graft copolymer: enhanced photovoltaic and photocatalytic performance. *RSC Advances*. 4(59): 31452-31461.

Park, N. G., Schlichthörl, G., Van De Lagemaat, J., Cheong, H. M., Mascarenhas, A. and Frank, A. J. (1999). Dye-sensitized TiO$_2$ solar cells: structural and photoelectrochemical characterization of nanocrystalline electrodes formed from the hydrolysis of TiCl$_4$. *The Journal of Physical Chemistry B*. 103(17): 3308-3314.

Park, N.-G., Kang, M. G., Ryu, K. S., Kim, K. M. and Chang, S. H. (2004a). Photovoltaic characteristics of dye-sensitized surface-modified nanocrystalline SnO$_2$ solar cells. *Journal of Photochemistry and Photobiology A: Chemistry*. 161(2-3): 105-110.

Park, N. G., Kang, M. G., Kim, K. M., Ryu, K. S., Chang, S. H., Kim, D. K., Van De Lagemaat, J., Benkstein, K. D. and Frank, A. J. (2004b). Morphological and photoelectrochemical characterization of core-shell nanoparticle films for dye-sensitized solar cells: Zn−O type shell on SnO$_2$ and TiO$_2$ cores. *Langmuir*. 20(10): 4246-4253.

Parks, G. A. (1965). The isoelectric points of solid oxides, solid hydroxides, and aqueous hydroxo complex systems. *Chemical Reviews*. 65(2): 177-198.

Pelet, S., Moser, J.-E. and Grätzel, M. (2000). Cooperative effect of adsorbed cations and iodide on the interception of back electron transfer in the dye sensitization of nanocrystalline TiO_2. *The Journal of Physical Chemistry B*. 104(8): 1791-1795.

Peng, M., Cai, X., Fu, Y., Yu, X., Liu, S., Deng, B., Hany, K. and Zou, D. (2014). Facial synthesis of SnO_2 nanoparticle film for efficient fiber-shaped dye-sensitized solar cells. *Journal of Power Sources*. 247: 249-255.

Peng, Y., Zhong, J., Wang, K., Xue, B. and Cheng, Y.-B. (2013). A printable graphene enhanced composite counter electrode for flexible dye-sensitized solar cells. *Nano Energy*. 2(2): 235-240.

Perera, K. A. T. A., Anuradha, S. G., Kumara, G. R. A., Paranawitharana, M. L., Rajapakse, R. M. G. and Bandara, H. M. N. (2011). The interconnected $CaCO_3$ coated SnO_2 nanocrystalline dye-sensitized solar cell with superior performance. *Electrochimica Acta*. 56(11): 4135-4138.

Pitarch, A., Garcia-Belmonte, G., Mora-Sero, I. and Bisquert, J. (2004). Electrochemical impedance spectra for the complete equivalent circuit of diffusion and reaction under steady-state recombination current. *Physical Chemistry Chemical Physics*. 6(11): 2983-2988.

Polizzotti, A., Schual-Berke, J., Falsgraf, E. & Johal, M. (2012). Investigating new materials and architectures for Grätzel cells. DOI: 10.5772/28223.

Poudel, P. and Qiao, Q. (2012). One dimensional nanostructure/nanoparticle composites as photoanodes for dye-sensitized solar cells. *Nanoscale*. 4(9): 2826-2838.

Prasittichai, C. and Hupp, J. T. (2010). Surface Modification of SnO_2 photoelectrodes in dye-sensitized solar cells: significant improvements in photovoltage via Al_2O_3 atomic layer deposition. *The Journal of Physical Chemistry Letters*. 1(10): 1611-1615.

Qi, B. and Wang, J. (2013). Fill factor in organic solar cells. *Physical Chemistry Chemical Physics*. 15(23): 8972-8982.

Qian, J., Liu, P., Xiao, Y., Jiang, Y., Cao, Y., Ai, X. and Yang, H. (2009). TiO_2-coated multilayered SnO_2 hollow microspheres for dye-sensitized solar cells. *Advanced Materials*. 21(36): 3663-3667.

Ramasamy, E. and Lee, J. (2010). Ordered mesoporous SnO_2-based photoanodes for high-performance dye-sensitized solar cells. *The Journal of Physical Chemistry C*. 114(50): 22032-22037.

Robertson, N. (2006). Optimizing dyes for dye-sensitized solar cells. *Angewandte Chemie International Edition*. 45(15): 2338-2345.

Rosenbluth, M. L. and Lewis, N. S. (1989). "Ideal" behavior of the open circuit voltage of semiconductor/liquid junctions. *The Journal of Physical Chemistry*. 93(9): 3735-3740.

Rouquerol, J., Avnir, D., Fairbridge, C. W., Everett, D. H., Haynes, J. M., Pernicone, N., Ramsay, J. D. F., Sing, K. S. W. and Unger, K. K. (1994). Recommendations for the characterization of porous solids (Technical Report). *Pure and Applied Chemistry*. 66(8): 1739-1758.

Rudman, R. (1967). X-ray diffraction analysis (continued). Part 4. Powder cameras and techniques. *Journal of Chemical Education*. 44(4): A289.

Rutledge, G. C. and Fridrikh, S. V. (2007). Formation of fibers by electrospinning. *Advanced Drug Delivery Reviews*. 59(14): 1384-1391.

Sawicka, K. and Gouma, P. (2006). Electrospun composite nanofibers for functional applications. *Journal of Nanoparticle Research*. 8(6): 769-781.

Schoonheydt, R. A. (2010). UV-VIS-NIR spectroscopy and microscopy of heterogeneous catalysts. *Chemical Society Reviews*. 39(12): 5051-5066.

Scaife, D. E. (1980). Oxide semiconductors in photoelectrochemical conversion of solar energy. *Solar Energy*. 25(1): 41-54.

Senevirathna, M. K. I., Pitigala, P. K. D. D. P., Premalal, E. V. A., Tennakone, K., Kumara, G. R. A. and Konno, A. (2007). Stability of the SnO_2/MgO dye-sensitized photoelectrochemical solar cell. *Solar Energy Materials and Solar Cells*. 91(6): 544-547.

Shalan, A. E., Rasly, M., Osama, I., Rashad, M. M. and Ibrahim, I. A. (2014). Photocurrent enhancement by Ni_2+ and Zn_2+ ion doped in SnO_2 nanoparticles in highly porous dye-sensitized solar cells. *Ceramics International*. 40(8 part A): 11619-11626.

Shaikh, S. F., Mane, R. S. and Joo, O.-S. (2014a). Mass scale sugar-mediated green synthesis and DSSCs application of tin oxide nanostructured photoanode: Effect of zinc sulphide layering on charge collection efficiency. *Electrochimca Acta*. 147: 408-417.

Shaikh, S. F., Mane, R. S. and Joo, O.-S. (2014b). Spraying distance and titanium chloride surface treatment effects on DSSC performance of electrosprayed SnO_2 photoanodes. *RSC Advances*. 4(68): 35919-35927.

Shang, G., Wu, J., Huang, M., Lin, J., Lan, Z., Huang, Y. and Fan, L. (2012). Facile synthesis of mesoporous tin oxide spheres and their applications in dye-sensitized solar cells. *The Journal of Physical Chemistry C*. 116(38): 20140-20145.

Shang, G., Wu, J., Tang, S., Liu, L. and Zhang, X. (2013). Enhancement of photovoltaic performance of dye-sensitized solar cells by modifying tin oxide nanorods with titanium oxide layer. *The Journal of Physical Chemistry C*. 117(9): 4345-4350.

Shimura, M., Shakushiro, K. and Shimura, Y. (1986). Photo-electrochemical solar cells with a SnO_2-liquid junction sensitized with highly concentrated dyes. *Journal of Applied Electrochemistry*. 16(5): 683-692.

Shozo, Y., Youhai, Y. and Kazuhiro, M. (2009). Iodine/iodide-free dye-sensitized solar cells. *Accounts of Chemical Research*. 42(11): 1827-1838.

Simon Mathew, A. Y., Peng Gao, Robin Humphry-Baker, Basile F. E. Curchod, Negar Ashari-Astani, Ivano Tavernelli, Ursula Rothlisberger, Md. Khaja Nazeeruddin and Gra¨Tzel, A. M. (2014). Dye-sensitized solar cells with 13% efficiency achieved through the molecular engineering of porphyrin sensitizers. *Nature Chemistry*. 6(1861): 242-247.

Sing, K. S. W. (1985). Reporting physisorption data for gas/solid systems with special reference to the determination of surface area and porosity (Recommendations 1984). *Pure and Applied Chemistry*. 02/9783527610044.hetcat0065

Song, H., Lee, K.-H., Jeong, H., Um, S. H., Han, G.-S., Jung, H. S. and Jung, G. Y. (2013). A simple self-assembly route to single crystalline SnO_2 nanorod growth by oriented attachment for dye sensitized solar cells. *Nanoscale*. 5(3): 1188-1194.

Snaith, H. J. and Ducati, C. (2010). SnO_2-based dye-sensitized hybrid solar cells exhibiting near unity absorbed photon-to-electron conversion efficiency. *Nano Letters*. 10(4): 1259-1265.

Snaith, H. J. and Schmidt-Mende, L. (2007). Advances in Liquid-Electrolyte and Solid-State Dye-Sensitized Solar Cells. *Advanced Materials*. 19(20): 3187-3200.

Sun, B., Long, Y. Z., Zhang, H. D., Li, M. M., Duvail, J. L., Jiang, X. Y. and Yin, H. L. (2014). Advances in three-dimensional nanofibrous macrostructures via electrospinning. *Progress in Polymer Science*. 39(5): 862-890.

Szalai, Z., Kiss, K., Jakab, G., Sipos, P., Belucz, B. and Németh, T. (2013). The use of UV-VIS-NIR reflectance spectroscopy to identify iron minerals. *Astronomische Nachrichten*. 334(9). 940-943.

Sun, W., Sun, X., Peng, T., Liu, Y., Zhu, H., Guo, S. and Zhao, X.-Z. (2012). A low cost mesoporous carbon/SnO_2/TiO_2 nanocomposite counter electrode for dye-sensitized solar cells. *Journal of Power Sources*. 201(0): 402-407.

Teh, J. J., Guai, G. H., Wang, X., Leong, K. C., Li, C. M. and Chen, P. (2013a). Nanoporous tin oxide photoelectrode prepared by electrochemical anodization in aqueous ammonia to improve performance of dye sensitized solar cell. *Journal of Renewable and Sustainable Energy*. 5(2): 023120.

Teh, J. J., Ting, S. L., Leong, K. C., Li, J. and Chen, P. (2013b). Gallium-doped tin oxide nano-cuboids for improved dye sensitized solar cell. *ACS Applied Materials & Interfaces*. 5(21): 11377-11382.

Tennakone, K., Jayaweera, P. and Bandaranayake, P. (2003). Dye-sensitized photoelectrochemical and solid-state solar cells: charge separation, transport and recombination mechanisms. *Journal of Photochemistry Photobiology A: Chemistry*. 158(2): 125-130.

Thapa, A., Zai, J., Elbohy, H., Poudel, P., Adhikari, N., Qian, X. and Qiao, Q. (2014). TiO_2 coated urchin-like SnO_2 microspheres for efficient dye-sensitized solar cells. *Nano Research*. 7(8): 1154-1163.

Thavasi, V., Singh, G. and Ramakrishna, S. (2008). Electrospun nanofibers in energy and environmental applications. *Energy and Environmental Science*. 1(2): 205-221.

Tiwana, P., Docampo, P., Johnston, M. B., Snaith, H. J. and Herz, L. M. (2011). Electron mobility and injection dynamics in mesoporous ZnO, SnO_2, and TiO_2 films used in dye-sensitized solar cells. *ACS Nano*. 5(6): 5158-5166.

Van De Lagemaat, J., Park, N. G. and Frank, A. J. (2000). Influence of electrical potential distribution, charge transport, and recombination on the photopotential and photocurrent conversion efficiency of dye-sensitized nanocrystalline TiO_2 solar cells: A study by electrical impedance and optical modulation techniques. *The Journal of Physical Chemistry B*. 104(9): 2044-2052.

Vogel, R., Hoyer, P. and Weller, H. (1994). Quantum-sized PbS, CdS, Ag_2S, Sb_2S_3, and Bi_2S_3 particles as sensitizers for various nanoporous wide-bandgap semiconductors. *The Journal of Physical Chemistry*. 98(12): 3183-3188.

Wali, Q., Fakharuddin, A., Ahmed, I., Ab Rahim, M. H., Ismail, J. and Jose, R. (2014). Multiporous nanofibers of SnO_2 by electrospinning for high efficiency dye-sensitized solar cells. *Journal of Material Chemistry A*. 2(41): 17427-17434.

Wang, C.-L., Liao, J.-Y., Zhao, Y. and Manthiram, A. (2015a). Template-free TiO_2 hollow submicrospheres embedded with SnO_2 nanobeans as a versatile scattering layer for dye-sensitized solar cells. *Chemical Communication*. 51(14): 2848-2850.

Wang, Q., Ito, S., Grätzel, M., Fabregat-Santiago, F., Mora-Seró, I., Bisquert, J., Bessho, T. and Imai, H. 2006. Characteristics of high efficiency dye-sensitized solar cells. *The Journal of Physical Chemistry B*. 110(50): 25210-25221.

Wang, Y.-F., Li, X.-F., Li, D.-J., Sun, Y.-W. and Zhang, X.-X. (2015b). Controllable synthesis of hierarchical SnO_2 microspheres for dye-sensitized solar cells. *Journal of Power Sources*. 280: 476-482.

Wang, Y.-F., Zhao, W.-X., Li, X.-F. and Li, D.-J. (2015c). Engineered Interfacial and configuration design of double layered SnO_2@TiO_2-ZnO nanoplates ternary heterostructures for efficient dye-sensitized solar cells. *Electrochimica Acta*. 151: 399-406.

Wang, H. and HU, Y. H. (2012). Graphene as a counter electrode material for dye-sensitized solar cells. *Energy and Environmental Science*. 5(8): 8182-8188.

Wang, H., Li, B., Gao, J., Tang, M., Feng, H., Li, J. and Guo, L. (2012). SnO_2 hollow nanospheres enclosed by single crystalline nanoparticles for highly efficient dye-sensitized solar cells. *CrystEngComm*. 14(16): 5177-5181.

Wang, M., Chamberland, N., Breau, L., Moser, J.-E., Humphry-Baker, R., Marsan, B., Zakeeruddin, S. M. and Grätzel, M. (2010). An organic redox electrolyte to rival triiodide/iodide in dye-sensitized solar cells. *Nature Chemistry*. 2(5): 385-389.

Wang, P., Klein, C., Moser, J.-E., Humphry-Baker, R., Cevey-Ha, N.-L., Charvet, R., Comte, P., Zakeeruddin, S. M. and Grätzel, M. (2004). Amphiphilic ruthenium sensitizer with 4,4'-Diphosphonic Acid-2,2'-bipyridine as anchoring ligand for nanocrystalline dye sensitized solar cells. *The Journal of Physical Chemistry B*. 108(45): 17553-17559.

Wang, P., Zakeeruddin, S. M., Comte, P., Charvet, R., Humphry-Baker, R. and Grätzel, M. (2003a). Enhance the performance of dye-sensitized solar cells by co-grafting amphiphilic sensitizer and hexadecylmalonic acid on TiO_2 nanocrystals. *The Journal of Physical Chemistry B*. 107(51): 14336-14341.

Wang, P., Zakeeruddin, S. M., Moser, J. E., Nazeeruddin, M. K., Sekiguchi, T. and Gratzel, M. (2003b). A stable quasi-solid-state dye-sensitized solar cell with an amphiphilic ruthenium sensitizer and polymer gel electrolyte. *Nature Materials*. 2(6): 402-7.

Wang, Q., Moser, J. E. and Grätzel, M. (2005). Electrochemical impedance spectroscopic analysis of dye-sensitized solar cells. *The Journal of Physical Chemistry B*. 109(31): 14945-14953.

Wang, X., He, G., Fong, H. and Zhu, Z. (2013a). Electron transport and recombination in photoanode of electrospun TiO_2 nanotubes for dye-sensitized solar cells. *The Journal of Physical Chemistry C*. 117(4): 1641-1646.

Wang, Y.-F., Li, K.-N., Wu, W.-Q., Xu, Y.-F., Chen, H.-Y., Su, C.-Y. and Kuang, D.-B. (2013b). Fabrication of a double layered photoanode consisting of SnO_2 nanofibers and nanoparticles for efficient dye-sensitized solar cells. *RSC Advances*. 3(33): 13804-13810.

Wenger, S., Bouit, P.-A., Chen, Q., Teuscher, J., Censo, D. D., Humphry-Baker, R., Moser, J.-E., Delgado, J. L., Martín, N., Zakeeruddin, S. M. and Grätzel, M. (2010). Efficient electron transfer and sensitizer regeneration in stable π-extended tetrathiafulvalene-sensitized solar cells. *Journal of the American Chemical Society*. 132(14): 5164-5169.

Wu, M., Lin, X., Guo, W., Wang, Y., Chu, L., Ma, T. and Wu, K. (2013). Great improvement of catalytic activity of oxide counter electrodes fabricated in N_2

atmosphere for dye-sensitized solar cells. *Chemical Communications*. 49(11): 1058-1060.

Wu, M. and Ma, T. (2014). Recent progress of counter electrode catalysts in dye-sensitized solar cells. *The Journal of Physical Chemistry C*. 118(30): 16727-16742.

Xu, X., Qiao, F., Dang, L., Lu, Q. and Gao, F. (2014). Porous tin oxide nanosheets with enhanced conversion efficiency as dye-sensitized solar cell electrode. *The Journal of Physical Chemistry C*. 118(30): 16856-16862.

Yang, H. X., Qian, J. F., Chen, Z. X., Ai, X. P. and Cao, Y. L. (2007). Multilayered nanocrystalline SnO_2 hollow microspheres synthesized by chemically induced self-assembly in the hydrothermal environment. *The Journal of Physical Chemistry C*. 111(38): 14067-14071.

Yang, X., Yanagida, M. and Han, L. (2013). Reliable evaluation of dye-sensitized solar cells. *Energy and Environmental Science*. 6(1): 54-66.

Yarin, A. L. (2011). Coaxial electrospinning and emulsion electrospinning of core-shell fibers. *Polymers for Advanced Technologies*. 22: 310-317.

Yang, H., Li, P., Zhang, J. and Lin, Y. (2014a). TiO_2 compact layer for dye-sensitized SnO_2 nanocrystalline thin film. *Electrochimica Acta.* 147: 366-370.

Yang, J., Bao, C., Zhu, K., Yu, T., Li, F., Liu, J., Li, Z. and Zou, Z. (2014b). High catalytic activity and stability of nickel sulfide and cobalt sulfide hierarchical nanospheres on the counter electrodes for dye-sensitized solar cells. *Chemical Communications*. 50(37): 4824-4826.

Yi-zhou zhang, H. P., Yanqiu S, Wen-Yong L, Ang W, Wei H. (2013). Porous tin oxide nanoplatelets as excellent-efficiency photoelectrodes and gas sensors. *International. Journal of. Electrochemical. Science.* 8(3): 3371-3378.

Yue, G., Wu, J., Lin, J.-Y., Xiao, Y., Tai, S.-Y., Lin, J., Huang, M. and Lan, Z. (2013). A counter electrode of multi-wall carbon nanotubes decorated with tungsten sulfide used in dye-sensitized solar cells. *Carbon*. 55: 1-9.

Yu, H., Bai, Y., Zong, X., Tang, F., Lu, G. Q. M. and Wang, L. (2012). Cubic CeO_2 nanoparticles as mirror-like scattering layers for efficient light harvesting in dye-sensitized solar cells. *Chemical Communications*. 48(59): 7386-7388.

Zaban, A., Greenshtein, M. and Bisquert, J. (2003). Determination of the electron lifetime in nanocrystalline dye solar cells by open-circuit voltage decay measurements. *ChemPhysChem*. 4(8): 859-864.

Zekry, Z. and Eldallal, G. (1988). Effect of MS contact on the electrical behaviour of solar cells. *Solid-State Electronics*. 31(1): 91-97

Zhang, Q. and Cao, G. (2011). Nanostructured photoelectrodes for dye-sensitized solar cells. *Nano Today*. 6(1): 91-109.

Zheng, H., Tachibana, Y. and Kalantar-Zadeh, K. (2010). Dye-sensitized solar cells based On WO_3. *Langmuir*. 26(24): 19148-19152.

Zhou, Y., Xia, C., Hu, X., Huang, W., Aref, A. A., Wang, B., Liu, Z., Sun, Y., Zhou, W. and Tang, Y. (2014). Dye-sensitized solar cells based on nanoparticle-decorated ZnO/SnO_2 core/shell nanoneedle arrays. *Applied Surface Science*. 292: 111-116.

Zhu, T. & Gao, S.-P. (2014). The stability, electronic structure, and optical property of TiO_2 polymorphs. *The Journal of Physical Chemistry C*. 118: 11385-11396

Zukalová, M., Zukal, A., Kavan, L., Nazeeruddin, M. K., Liska, P. and Grätzel, M. (2005). Organized mesoporous TiO_2 films exhibiting greatly enhanced performance in dye-sensitized solar cells. *Nano Letters*. 5(9): 1789-1792.
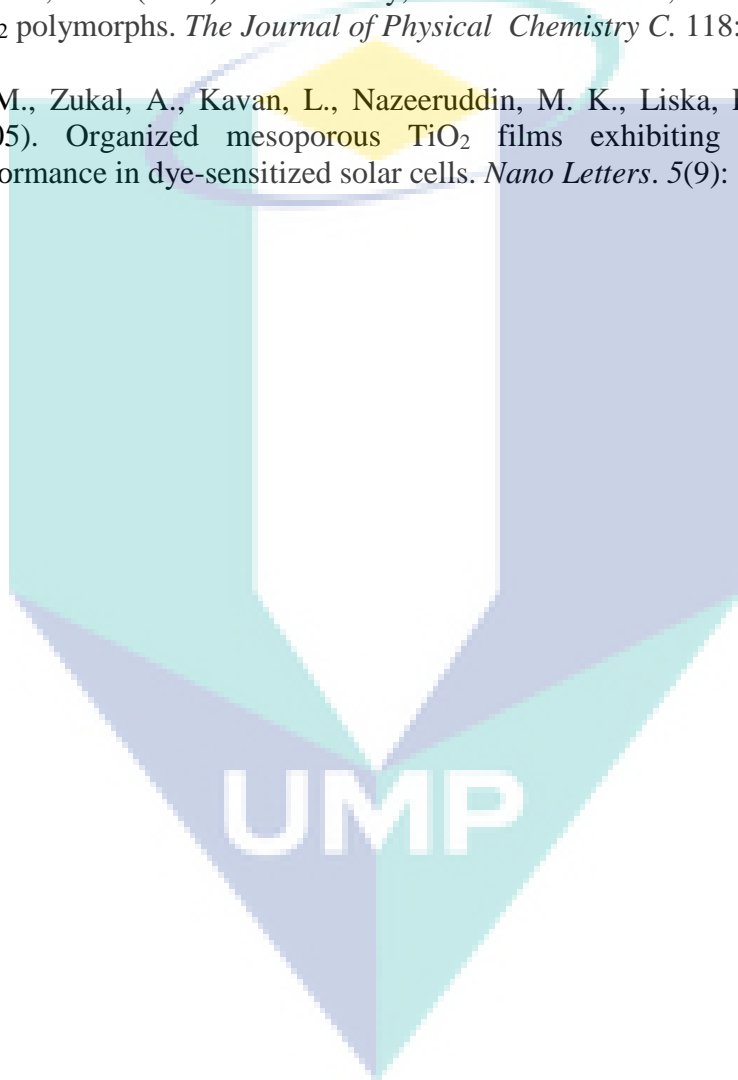
ACHIEVEMENTS

Wali Q., Fakharuddin A., Ahmed I., Hasbi Mohd. Ab R., Ismail J., R. Jose. (2014). Multiporous nanofibers of SnO_2 by electrospinning for high efficiency dye-sensitized solar cells. *Journal of Material Chemistry A*. 2(41): 17427-17434.

Wali Q., Fakharuddin A., Yaseen A., R. Jose. (2015). One pot synthesis of multi-Functional tin oxide nanostructures for high efficiency dye-sensitized solar cells. *Journal of Alloys &* compounds. 646: 32-39.

Wali Q., Fakharuddin A., R. Jose. (2015). Tin oxide as a photoanode for dye-sensitized solar cells: current progress and future challenges. *Journal of Power Sources*. 293: 1039-1052.

Wali Q., Zinab H., N. A Manshor. Fakharuddin A., R Jose. (2016). SnO_2-TiO_2 hybrid nanofibers for efficient dye-sensitized solar cells. *Journal of Solar Energy*. **132**: 395–404

Fakharuddin, A.; I. Ahmed; **Q. Wali.;** Khalidin, Z.; Yusoff, M. M.; R. Jose. (2014). Probing electron lifetime and recombination dynamics in large area dye-sensitized solar cells by electrochemical impedance spectroscopy. *Advanced Material Research.* 295: 553-558.

Ahmed I., Fakharuddin A., **Wali Q**., Zainun A. R., Ismail J., R. Jose. (2015). Mesoporous titania-vertical nanorods films with interfacial engineering for high performance dye-sensitized solar cells. *Nanotechnology.* 26: 105401.

Fakharuddin A., Di Giacomo F., Ahmed I., **Wali Q**., Brown T.M., R. Jose. (2015). Role of morphology and crystallinity of nanorods and planar electron transport layer on long term durable performance of perovskite solar cells. *Journal of Power Sources.* 283: 61-67.

Fakharuddin A, Palma A. L., Di Giacomo F., Matteocci F., **Wali Q.;** Rauf, M; J. Di Carlo A., Brown T.M., and Jose R. (2015). Solid-state perovskite solar modules by vacuum-vapor assisted sequential deposition on Nd:YVO4 laser patterned rutile nanorods Vertical TiO_2 . *Nanotechnology.* 26: 494002.

CONFERENCE AND WORKSHOPS

Jose Rajan, Qamar Wali Azhar Fakharuddin Naveen Kumar Elumalai Jamil Ismail. (7 & 8 October 2015). Nanoparticles, nanowires, nanoflowers, nanotubes, and multichannel nanotubes of SnO_2 for renewable energy applications. *International Tin Chemical & Solder Conference and Exhibition*. Hotel Istana, Kuala Lumpur, Malaysia

Qamar Wali. (6-7th October 2015). Electrospun nanofibers for energy applications International. Workshop on electrospinning: Research, management and commercialization. Shah Alam convention centre, Selangor, Malaysia.

Qamar Wali. (24 & 25th January 2015). Tin Oxide multichannel nanotubes for solar cells application. National conference for post graduate research. Universiti Malaysia Pahang.

PATENTS

Qamar Wali, A. Fakharuddin, R. Jose, Z. M. M. Yusoff. (2014). SnO_2 multichannel nanotubes. **PI 2015702458.**

OTHER AWARDS

Qamar Wali. (2014). Nanostructure electrodes for dye sensitized solar cells. Three minute (3MT) thesis competition. *Univesiti Malaysia Pahang*

Qamar Wali. (2015). Let the Sun shine: Today for perovskite solar cells. Malaysian three minute (3MT) thesis competition. *Univesiti Malaysia Pahang*

Qamar Wali. (2015). Let the Sun shine: Today for perovskite solar cells. Malaysian three minute (3MT) thesis competition. *Univesiti Technology Malaysia*

Qamar Wali, Azhar Fakharuddin, Mohd Hasbi Ab Rahim, Jamil B Ismail, Mashitah Mohd Yusoff, Rajan Jose. (2014). Multichannel tin oxide nanotubes. *Creation innovation, technology & research exhibition,* Universiti Malaysia Pahang. (**Gold Medal**)

Qamar Wali, Azhar Fakhruddin, Mohd Hasbi Ab Rahim, Jamil Ismail, Mashitah M. Yusoff Jose Rajan. (8-10th May 2014). Multichannel tin oxide nanotubes for electronic applications. *25th International invention, innovation & technology exhibition*, Kuala Lumpur Malaysia. (**Gold Medal**)

Qamar Wali, Azhar Fakhruddin, Mohd Hasbi Ab Rahim, Jamil Ismail, Mashitah M. Yusoff, Jose Rajan. (2015). Solartins. *British Invention show*, *Barbican Convention Center London*, (**Gold Medal + double Gold Medal**)